EXPERIMENTAL INVESTIGATION OF THERMAL CONDUCTION AND RELATED PHENOMENA IN A LASER HEATED PLASMA

by

David Reynolds Gray, B.Sc., A.R.C.S.

February, 1979

A thesis submitted for the degree of Doctor of Philosophy of the University of London and for the Diploma of Membership of the Imperial College.

Blackett Laboratory,
Imperial College,
London SW7.

To my parents

ABSTRACT

Thermal conduction in plasmas is of major importance especially in controlled nuclear fusion studies. Direct measurements are rare.

When the temperature gradient in a plasma becomes large enough classical thermal conduction (Heat flux $q = -k\nabla \underline{T}$) no longer applies and it is thought that q is limited to some fraction of the free streaming limit $q_m = nkT_e(2kT_e/\pi m_e)^{0.5}$

The main experiment is the heating of a z-pinch plasma - 6.10^{16} cm^{-3}/4eV - by a fast rising (~ 1ns.), intense (~ 3.10^{11} Wcm^{-2}) carbon dioxide laser pulse. Electron temperature and density in time and space are diagnosed by ruby laser scattering. The profiles obtained were consistent with a flux limited to ~ 3% of the free streaming limit.

Ion acoustic turbulence is observed along the temperature gradient. It is shown that the observed turbulence level is consistent with the heat flux limitation. At electron densities > 10^{17} cm^{-3} backscattered light is observed from the plasma whose growth rate implies that it is Brillouin scattered.

Some comments are made on the breakdown of Spitzer's thermal conductivity formula when q becomes large.

ACKNOWLEDGEMENTS

This research was performed while I was a member of the Plasma Physics Group at the Blackett Laboratory. I would like to thank all members of this group for many stimulating discussions. In particular I would like to thank:

J.D. KILKENNY for his relentless interest in this work, for many helpful suggestions and for the calculation of the fractional fluctuation level of Chapter 7.

A.E. DANGOR (my supervisor) for his direction in the early stages of this work.

M.G. BROWN for advice on computational matters.

J. WESTLAKE for construction and maintenance of the ruby laser system.

The bulk of the experimental work was done using a CO_2 laser system at the Atomic Weapons Research Establishment, Aldermaston. I would therefore like to acknowledge the help of the following people:

P.T.G. FLYNN for making the experiment possible.

P. BLYTH and D. HULL for the development and running of the CO_2 laser system.

E. THORNTON for advice on calorimetry and fast transients.

The experiment was completed while the author was a recipient of a Northern Ireland Department of Education research studentship. The data reduction and computer modelling were completed while a research assistant at the Rutherford Laboratory where the author is presently doing further research.

Also I would like to thank G. Hale for being my dearest friend and providing emotional support.

Finally, I would like to thank S. Cowen for the typing of this manuscript.

CONTENTS

LIST OF SYMBOLS

ENGLISH

a	acceleration
$\underline{B}$	magnetic field
$\underline{B}_\phi$	poloidal magnetic field
$\underline{E}$	electric field
$\underline{E}_0$	electric field of laser
E_∞	ionization energy
e	charge on the electron
$f(v)$	velocity distribution function
f	fraction of free streaming limit to which heat flux is limited
FWHM	full width half maximum
I_0	laser intensity
j	current density
k	wave number or absorption coefficient
k_0	incident laser wave number $(= 2\pi/\lambda_0)$
k_B	Boltzmann's constant
k_D	Debye wave no. $= 2\pi/\lambda_{De}$
L	temperature gradient scale length
L_n	density gradient scale length
m_e	electron mass
m_i	ion mass
n_e	electron density
n_i	ion density
n_c	critical density
p	principal quantum number
P	pressure
P_r	radiation pressure
P_{th}	thermal pressure

LIST OF SYMBOLS continued...

P_L	laser power
q	electron heat flux
$\underline{q}_{max.}$	free streaming limit to heat flux
q_i	ion heat flux
r	radius
RMS	root mean square
s	multiplier to thermal conduction coefficient
$S_e(k)$	total scattered light in the electron feature
$S_i(k)$	total scattered light in the ion feature
S_{ith}	expected thermal level for $S_i(k)$
S_{io}	observed level for $S_i(k)$
t	time
T_e	electron temperature
T_i	ion temperature
T_H	hot electron temperature
U	internal energy (e.g. $= {}^3/_2\, n_e k_B T_e$)
v	velocity
v_{ia}	ion acoustic velocity
v_r	ripple velocity in laser electric field
v_{th}	electron thermal velocity
v_{the}	electron thermal velocity
v_{thi}	ion thermal velocity
w	multiplier to the absorption coefficient
z	ion charge
z_{eff}	effective charge state of the plasma

GREEK

α	laser scattering parameter

LIST OF SYMBOLS continued...

γ	ratio of specific heats
γ_{iaL}	Landau damping rate
γ_{coll}	collisional damping rate
δ	displacement of laser focal spots
$\Delta\lambda$	wavelength displacement
Δt	timestep
ε_o	permittivity of free space
θ	angle
$K_{(e)}$	classical thermal conduction coefficient
$K_\perp$	thermal conduction coefficient across a magnetic field
λ_o	laser wavelength
λ_D	debye length
λ_{De}	debye length
λ_e	electron collisional mean free path
ν_{ei}	electron-ion collision frequency
ν^*	anomalous collision frequency
ρ	mass density
σ_p	plasma cross-section for scattering of light
σ_T	Thomson cross-section
τ_c	a characteristic time
τ_{TC}	thermal conduction-characteristic time
τ_H	laser heating-characteristic time
τ_{eq}	equilibration-characteristic time
τ_m	mass motion-characteristic time
τ	containment time
ϕ_i	angle between light ray and plasma vacuum boundary
ω_o	laser frequency
ω_R	ripple frequency in laser electric field

LIST OF SYMBOLS continued...

ω_D	frequency bandwidth of detector

MATHEMATICAL

$\nabla \underline{T}$	temperature gradient
∇n	density gradient
∇P	pressure gradient
$\ln \Lambda$	collision integral

CHAPTER 1

1. INTRODUCTION

The thermal conductivity of a plasma is a fundamental parameter. Theoretical models to date[1,2,3,4.] are only valid for small (1st order) perturbations to the electron velocity distribution function, f(v). (i.e. small temperature gradients).

When a thermal gradient is set up in a plasma the hottest electrons are the least collisional and tend to leave the hot region. To maintain charge neutrality a return current of cold electrons flows back into the hot region. The theory for electrical conduction in the presence of a weak electric field $\underline{E}$ is linked to that for thermal conduction in the presence of a small temperature gradient $\nabla\underline{T}$:-

$$\underline{j} = \sigma\underline{E} + \alpha\nabla\underline{T} \qquad (1\text{-}1)$$

$$\underline{q} = -\beta\underline{E} - k\nabla\underline{T} \qquad (1\text{-}2)$$

where j is the current density and q is the thermal flux. If a current is induced in a plasma due to an applied electric field then a temperature gradient will occur since the least collisional electrons will tend to flow. However, $\underline{j} = 0$ in the experiment described here.

When $\nabla\underline{T}$ becomes large, the heat flux has an upper limit, q_{max}, called the free streaming limit:-

$$q_{max.} = \tfrac{1}{4}\, n\bar{c}\ (2kT_e) = nkT_e(2kT_e/\pi m_e)^{0.5} \qquad (1\text{-}3)$$

i.e. all the electrons are moving down the temperature gradient with their thermal velocity.

When a plasma carries a heat flux there is an associated skewing of the velocity distribution function f(v) with $\partial f/\partial v$ going positive near zero velocity. Fig. (1-1) shows a schematic of a distribution function which is carrying a heat flux q.

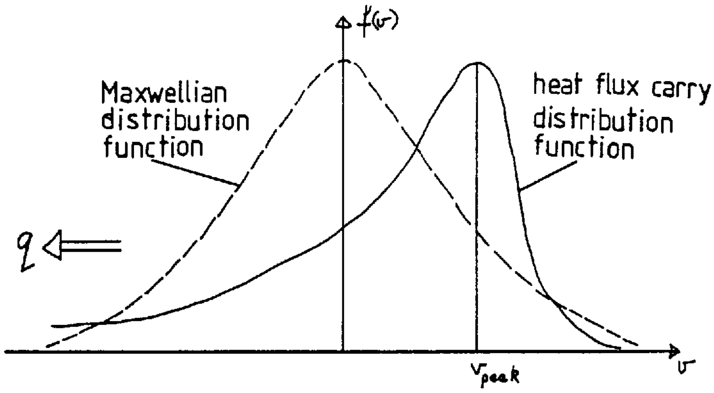

Fig. (1-1)

The size of the perturbation to the distribution function is given by λ_e/L where L is the scale length for the temperature gradient ($= |T_e/\nabla T_e|$) and λ_e is the electron collisional mean free path. Following Spitzer[3] we use $\lambda_e = v_{th} / \nu_{ei}$ where[6]

$$\nu_{ei} = \frac{1}{\varepsilon_0^2 \, 3\pi^{\frac{1}{2}}} \frac{e^4}{m_e^2} n_i \left(\frac{2k_B T_e}{m_e}\right)^{-3/2} \ln \Lambda$$

So numerically:

$$\lambda_e/L = 2.292 \; 10^{13} \; (T_e | \nabla T_e |)/(n_i \ln \Lambda)$$

with T_e in eV and n_i in cm^{-3}. Thus for j = 0,

$$q/q_{max} \propto \lambda_e/L$$

and a more highly perturbed velocity distribution carries a larger flux.

There are important consequences of the shift in the peak of the distribution function shown in Fig. (1-1). When $v_{peak} > v_{ia}$ energy is transferred from electrons travelling at velocities around v_{ia} into ion-acoustic waves by inverse Landau damping[7]. This is because if $\partial f/\partial v$ is positive around v_{ia} then there are more electrons travelling faster than v_{ia} than electrons travelling slower than v_{ia}. Trapping of electrons in the fields of the ion acoustic waves means a net energy flow from the electrons to the waves. If $T_e >> T_i$ then $v_{ia} >>$ the ion thermal velocity and the ion acoustic waves are lightly ion-Landau damped.

D.W. Forslund[8] calculates the threshold for the amplification of ion-acoustic waves by the electrons in the skewed velocity distribution. However, he uses the distribution functions of Spitzer and Härm[5] and the work is applicable only to small λ_e/L. Manheimer[9] starts by adopting an assumed form for the velocity distribution which gives agreement with computer simulations and calculates the reduction in the thermal conductivity due to the presence of ion acoustic turbulence. Physically a high turbulence level reduces the thermal conductivity because the electric fields of the ion acoustic waves scatter the electrons carrying the thermal energy. (i.e. the collision frequency is increased). The work of Forslund and of Manheimer is compared in detail with the results of this thesis in Chapter 7.

This work is an extension of a near classical conduction experiment[10] at Imperial College which had a $(\lambda_e/L)_{max} \sim 0.04$. This was induced by focussing a 20MW, 70 ns CO_2 laser pulse into a homogeneous z-pinch plasma of $n_e \sim 8.10^{16}$ cm^{-3}, $T_e \sim 5eV$ and $z_{eff} \sim 1$. Using the same preformed plasma, $(\lambda_e/L)_{max.}$ has been increased to ~ 0.48 by using a 250MW, 3 ns CO_2 laser pulse at A.W.R.E. Aldermaston. The spectra of incoherent light scattered by plasma electrons in the focus of a ruby laser were used as the principal diagnostic in both experiments. This technique gave n_e and T_e in time and space as well as information on plasma waves.

2. HISTORICAL PERSPECTIVE

To illustrate a raison d'être for the experiment λ_e is $\gtrsim L$ in the following plasmas.

(a) Naturally Occuring Plasmas

(i) Solar Corona

At about 2.5 solar radii from the sun's centre, in the equatorial plane, estimates for L range from 0.003 to 0.1 A.U. while λ_e = 0.002 A.U.[11]
(1 A.U. = distance from the earth to the sun).

(ii) Solar Wind

Forslund[8] quotes $\lambda_e/L \sim 0.5$ in the solar wind near the earth.

(b) Laser Produced Plasmas

I. Introduction

The potential of a laser produced thermonuclear plasma as a controlled energy source has greatly enhanced interest in this field. The importance of thermal conductivity in this context will now be discussed.

There are two essential conditions which must be satisfied in a thermonuclear reactor: (a) An ion ignition temperature is dictated by a balance of reaction cross-sections and bremsstrahlung power losses. This is typically T_i > 5keV for the deuterium-tritium reaction (DT) and T_i > 100keV for the deuterium-deuterium (DD) reaction. (b) The Lawson Criterion[12] sets a lower limit on $n_i\tau$ (where n_i = ion density and τ = the containment time) for a net power output from a reactor. This "breakeven" condition is typically $n_i\tau > 10^{14}$ for the DT reaction and $n_i\tau > 10^{16}$ for the D-D reaction.

It is thought that these criteria can be met by focussing intense laser light onto a DT filled glass sphere ($\sim$ 100μm diameter). The incidence of the laser light on the sphere causes a rapid surface ablation which provides the pressure to produce a spherical implosion. Spherical compression[13] reduces the minimum pellet mass and laser energy required for efficient thermonuclear burn because: a) the burn efficiency (i.e. the burn rate x the confinement time) is proportional to the density - radius product (ρr); b) For large ρr only the centre of the compressed core need be ignited as the α-particle reaction products will ignite the surrounding fuel; and c) Compression heats the ions while plasma absorption of laser light primarily heats the electrons.

Effective compression may be attained by either: (a) Using a structured laser pulse which produces a series of shocks all of which coalesce near the pellet centre (sometimes called singular compression); (b) Using a longer lower intensity laser pulse to freely accelerate the dense plasma front like a rocket rather than to shock it[88].

For a highly compressed pellet initially ignited over a volume with dimensions of the α-particle range, the α-particle energy deposition produces a rapid temperature rise with a corresponding very rapid rise in the thermonuclear reaction rate. The α-particle range then exceeds the dimensions of the initial reacting region and energy is deposited in the adjacent relatively cold fuel, causing it to ignite. The result is the formation of a spherically expanding burning front which expands into the rest of the fuel at supersonic speed, igniting it before appreciable hydrodynamic rarefaction can occur[14].

Fig. (1-2) shows a schematic of an implosion soon after the start of the laser pulse. Laser light is reflected at the critical surface defined by an electron density:

$$n_c = \omega_o^2 m_e \varepsilon_o / e^2 \qquad (1\text{-}4)$$

i.e. where $\omega_o = \omega_{pe}$. For $n_e > n_c$, the real part of the refractive index becomes negative and light cannot propagate. As will be explained below the dominant laser light absorption mechanisms deposit energy near $n_e = n_c$.

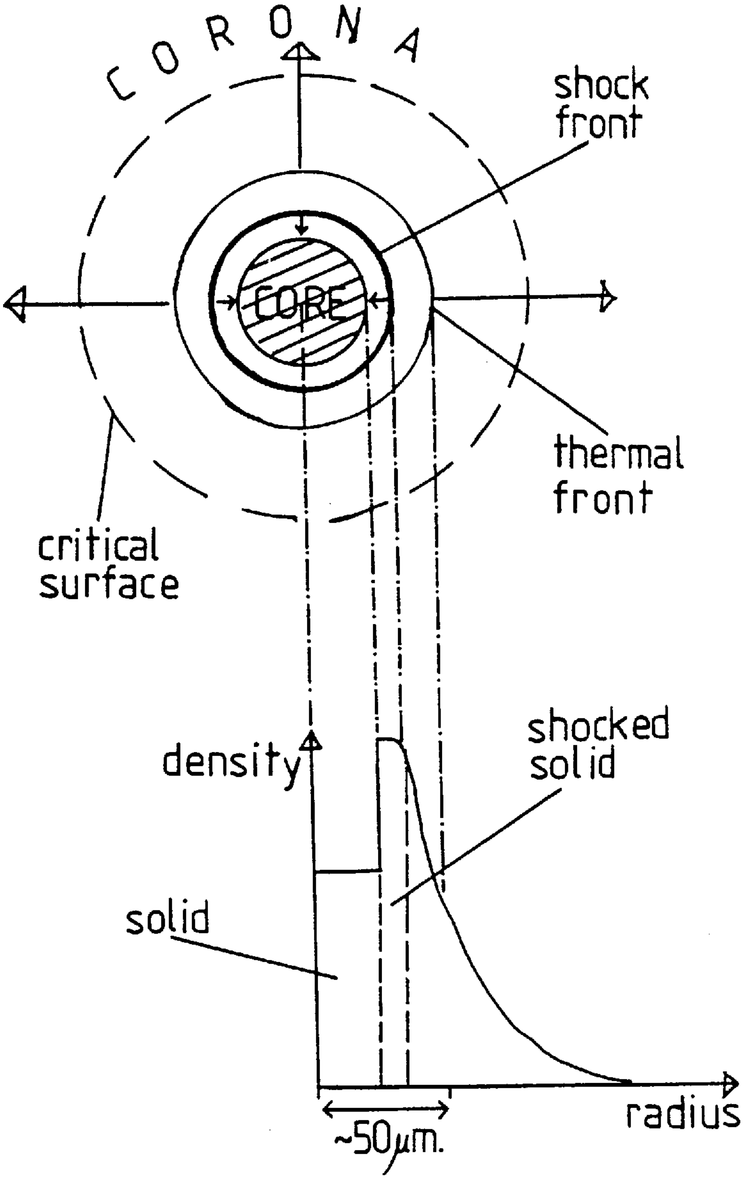

Fig. (1-2)

Schematic of a laser-induced implosion.

However, material is heated well beyond the critical density due to the penetration of the high density region by a thermal conduction wave with energy carried by electrons. A rapid penetration of the thermal front assumes a high thermal conductivity (often Spitzer's[3] - coefficient $k_e \propto T_e^{5/2}$) which allows the thermal wave to move ahead of the hydrodynamic rarefaction wave. (The rarefaction wave moves at the sound speed). Ahead of the conduction wave, material is compressed by a shock driven by the pressure in the laser deposition region. Behind the rarefaction wave, the density drops rapidly due to hydrodynamic expansion.

The pressure during the implosion arises primarily from the removal of material at the surface of the dense compressed DT as a result of energy transport from the laser deposition region to the region of compression. Clearly, an understanding of the coupled mechanisms of energy absorption and thermal transport is required to achieve good compressions.

II. Absorption of Laser Light

(i) Inverse bremsstrahlung

Here, the electrons oscillate in the electric field of the laser light and transfer their energy to the plasma collisionally. However, for the laser intensities now attainable ($> 10^{16}$ Wcm^{-2}) the ripple velocity, v_r, of electrons in the laser electric field, E_0, ($v_r = |eE_0/m_e\omega_0|$) becomes $\gg v_{the}$ (the electron thermal velocity) and the collision frequency drops making inverse bremsstrahlung absorption ineffective[15].

(ii) Parametric Processes

These occur when the laser frequency is in resonance with existing, or stimulated waves in the plasma. The interacting waves must satisfy both an energy and a momentum relation:

$$\omega_{laser} = \omega' + \omega'' + \ldots\ldots \qquad (1\text{-}5)$$

$$k_{laser} = k' + k'' + \ldots\ldots \qquad (1\text{-}6)$$

where ω' etc. may be plasma or electromagnetic waves. This coupling of the laser light with plasma waves gives rise to absorption (the so-called parametric decay and oscillating two-stream instabilities near $n_e = n_c$), stimulated Raman and Brillouin backscattering and harmonic generation (principally at $2\omega_o$ and $^3/_2\ \omega_o$). In the presence of a density gradient, conditions (1-5) and (1-6) are only satisfied over a limited distance. Convection of energy by wave propagation out of the matched regions means that the thresholds for the instabilities are directly related to the density gradient scale length[16], $L_n = n_e/\nabla n_e$. This scale length is shortened by the radiation pressure of the laser light. Steepening of the electron density profile has been theoretically investigated[17] and experimentally observed[18,19]. Attwood et al.[18] looked at the density profile interferometrically with a space-time resolution of 1μm. and 15ps. For $\lambda = 1.06\mu m$ illumination of a 41μm. diameter spherical glass microshell at a peak intensity $I_o \sim 3.\ 10^{14}\ Wcm^{-2}$ they observed supercritical ($l \sim 8\mu m.$) and subcritical ($l \sim 6\mu m$) density shelves with a rapid rise ($l \sim 1.6\mu m$) up to the critical density. Here, l is the e-folding density scale length. In the above experiment they estimated the ratio of radiation to thermal pressure to be $P_r/P_{th} \sim 0.2$.

They also irradicated plane targets and observed that for $I_o > 10^{14}$ Wcm^{-2} plasma was forced out of the focal spot region leaving a large scale hole (~ 30μm.). For $I_o > 10^{15}$ Wcm^{-2} they observed a small scale rippling in the density. The latter is attributable to hot spots in the beam when $P_r \sim P_{th}$.

From the same plasma, in another paper,[20] a streak camera was used to time resolve the backscattered light. For $I_o > 10^{16}$ Wcm^{-2} they found that the backscattering switched off after the peak of the laser pulse. They proposed that the momentum deposition accompanying the light reflection steepened the density profile sufficiently to turn off the Brillouin backscattering.

Currently, at $I_o \sim 10^{15} \rightarrow 10^{16}$ Wcm^{-2} an absorption of ~ 15% is used at Lawrence Livermore[21] as the fraction due to ion density fluctuations driven by the laser light near $n_e = n_c$.

(iii) Resonance Absorption

If focussed light is incident over a range of angles to the density gradient, it is refracted as shown in Fig. (1-3)[22]

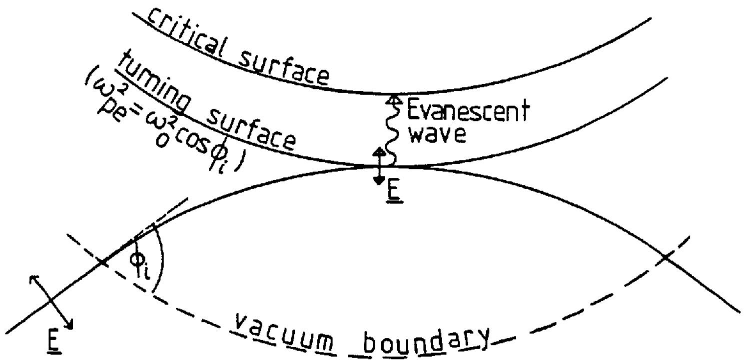

Fig. (1-3).

For light polarised in the plane of incidence (p polarisation), the electric field (E) tunnels through to the critical surgace where it resonantly drives charge density fluctuations. There is an optimum angle for absorption determined by minimising the tunnelling distance and maximising the component of $\underline{E}$ along $\nabla \underline{n}_e$. This is given by $\sin \phi_i \approx (k_0 L)^{-1/3}$ where k_0 is the free space wave number of the incident light and L is the density scale length.

From theory and simulations, Forslund et al.[23] have found resonance absorption weakly temperature dependent. For $k_0 L = 12.5$, they found the absorption (for optimum angle) unchanged at ~ 50% for $T_e = 2.5$ and 50 keV. (See Fig. 1, ref. 23). At low incident intensities - $P_L \lambda_0^2 < 2.10^6$ W (i.e. $< 2.10^{12}$ Wcm^{-2} for 10μm. light) - they noted generation of a plasma wave at $n_e = n_c$ which propagated towards lower densities. Landau damping of this wave produced a hot electron tail on the velocity distribution (See Fig. 3(c), ref. 23). At higher intensities, $P_L \lambda_0^2 > 2.10^6$ W, the laser electric field accelerated electrons locally to high energy with relatively little energy going into an intermediate plasma wave. The electrons travelled outwards at speeds up to 5% c, were reflected at the low density electron sheath by space charge effects and returned to higher density. Almost all the absorbed energy went into the hot electron tails. Although the hot electrons do not necessarily have a Maxwellian distribution the term "hot electron temperature" (T_H) is still used to give an idea of the energy in the tail. They estimated that for $k_0 L \approx 12.5$:-

$$T_H(\text{keV}) \approx 0.01\, \lambda_0(\text{cm.}) \sqrt{P_L}(\text{Wcm}^{-2}).$$

which is in reasonable agreement with current X-ray determinations of T_H.

Resonance absorption has been experimentally investigated by tilting targets and measuring the differences in absorption by calorimetry. Manes et al.[24] at the Lawrence Livermore Laboratory observed a clear absorption maximum for p-polarised light but not for s-polarised light. ($\lambda_0 = 1.06\mu m$; $I_0 \sim 10^{16}$ Wcm^{-2}). These results have recently been further discussed by Thomson et al.[21] and correlated with the density profile measurements of Attwood et al.[18] To explain the absolute value and angular dependence of the absorption they included laser driven ion density fluctuations, resonance absorption and enhanced resonance absorption due to "hot spot" rippling of the critical density surface. A remaining discrepancy of 10% between theory and experiments was tentatively attributed to absorption due to self-generated magnetic fields.

In complete contrast, Bodner et al.[25, 26] at NRL using $\lambda = 1.06\mu m$. and $I_0 \sim 10^{16}$ Wcm^{-2} observed absorptions up to 70% which were independent of both polarisation and angle of incidence. This anomalously high absorption was attributed to the existence of ion-acoustic turbulence driven by the thermal conduction return current[9]. Later work at NRL[27] quotes a 40 to 50% absorption but the fraction due to resonance absorption was still unknown.

With the exception of the NRL work, the two dominant absorption mechanisms (i.e. parametric and resonance) deposit most of absorbed laser energy in non-Maxwellian hot electron tails near the critical density surface. The existence of "hot" and "cold" electrons has been used to explain the observed "two temperature" X-ray spectra[28,29,20] (bremsstrahlung emission) and the generation of fast ions[30,28,29,20] (these hot ions may be generated by acceleration through the ambipolar potential which builds up quickly as electrons try to leave the target). Direct observation of high energy (i.e. > 30 keV) electron emission spectra has also been made[20].

III. Thermal Conduction

The use of Spitzer type thermal conduction to model energy transport by hot electrons is clearly a bad approximation. There is now experimental evidence (though indirect) that the hot electrons can heat the pellet ahead of the compression front of Fig. (1-2). This is called "exploding-pusher" compression[31]. Comparisons between the measured compressed core density and computer simulations have shown that a multigroup diffusion treatment[32] of the hot electron transport must be used to explain the observations. In particular, computations show that this pre-heating of the core can reduce the compressed core density by an estimated factor of 60. This is borne out by experiments at the Rdtherford Laboratory[29]. In a theoretical paper, Anisimov et al.[33] see a reduction in fusion yield for $\emptyset > 0.1$ where $\emptyset$ = (the energy transferred to the target by fast electrons)/(the absorbed laser energy). They apply a 3% flux limit and see an increased yield and compression. This was attributed to the flux limit reducing the pre-heating. It is not obvious, however, that a one parameter inhibition of the flux adequately deals with a two temperature plasma.

Experimental investigations of thermal transport in solid target experiments is complicated by the coupling of the absorption and conduction mechanisms. A well resolved knowledge of the heated electron distribution functions has not yet been claimed. However, flux limits to thermal conduction have been inferred from thin foil burnthrough experiments. Malone et al.[34] inferred a 3% → 10% flux limit on the burn through of a thin CH_2 foil using the fractional light transmission, the magnitude of the fast ion emission and the electron temperature from the bremsstrahlung emission. Pearlman and Anthes[35] in a similar experiment saw the fractional transmission fall by an order of magnitude as the incident flux was increased from 10^{13} to 10^{14} Wcm^{-2}.

Yaakobi and Bristow[36] observed X-ray line emission from glass targets coated with a thin aluminum overlay. Above a critical aluminium thickness no more silicon lines were seen. Their calculations implied considerable axial heat conduction inhibition plus evidence for lateral inhibition attributed to $\nabla \underline{T} \wedge \nabla \underline{n}$ magnetic field generation. Similar burn through experiments on thin foils and aluminium coated microballoons have recently been performed at the Rutherford Laboratory and also provide evidence for thermal conduction inhibition (to be published). Campbell et al.[37] looked at the energy in fast ions and using energy balance arguments deduced a flux limitation due to ion turbulence. Ripin et al.[38] at NRL found evidence for conduction inhibition by magnetic fields and it is interesting that they again emphasize their non-observation of supra-thermal electrons. Mead et al.[28] and Haas et al.[20] at the Lawrence Livermore Laboratory saw high energy X-rays implying suprathermal electrons. The spatial extent of their X-ray emission was too small to be explained with turbulence limited conduction alone suggesting that magnetic fields were present.

Magnetic fields have been observed using Faraday rotation techniques in plane target experiments.[39,40,41] These fields may be generated by $\nabla \underline{T} \wedge \nabla \underline{n}$ effects[42,43,44] and by resonance absorption.[45,46]

Various theoretical papers have calculated a limitation to the heat flux. Bickerton[47] and Mishin[48] independently derived a limit of $f \sim (m_e/m_i)^{\frac{1}{2}}$ for $T_e \gg T_i$ and a distribution function skewed such that $v_{peak} > v_{ia}$. Morse and Nielson[49] found a 6% flux limit to collisionless thermal conduction in 1-D. Manheimer[9] calculated the reduction to the classical (e.g. Spitzer) conduction coefficient due to ion turbulence using a empirically justified distribution function. His results were consistent with the Malone et al.[34] experiment and are also used later in this thesis.

More recently Mason[50] has shown that cold thermal return currents and thermoelectric field enhancement by suprathermal electron currents can reduce and even reverse the thermal transport in laser targets absorbing $I_0 > 10^{15}$ Wcm^{-2} of 1.06μm light. Elimination of $\underline{E}$ from equations (1-1) and (1-2) gives:-

$$\underline{q} = -(k - \alpha/\sigma)\nabla\underline{T} \;-\; \beta/\sigma\,\underline{j} \qquad (1\text{-}7)$$

In the presence of suprathermal currents Mason shows that the second term in equation (1-7) can dominate the first, quenching or reversing the heat flow.

3. CONCLUSION

Thermal conduction down large temperature gradients has yet to be correctly treated theoretically. Experimental investigation of the thermal transport in laser/solid target experiments is indirect and complicated by the many phenomena occuring and in particular the existance of a hot body of non-thermal electrons.

The experiment described in this thesis was designed to isolate thermal conduction as the dominant physical mechanism occuring under conditions of large λ_e/L in a background thermal plasma. By avoiding the extra complications of incompletely understood phenomena such as suprathermal electrons and anomalous absorption it was possible to make a definitive measurement of the thermal conductivity and absorption.

This was done by using a CO_2 laser to heat a plasma which initially was homogeneous and effectively unmagnetised. The plasma density (at ~ $10^{16} \rightarrow 10^{17}$ cm^{-3}) was about two orders of magnitude below the critical density for CO_2 laser light (~ 10^{19} cm^{-3}). This meant that most of the anomalous absorption mechanisms did not occur and that the absorption was small enough to approximate temperature invariance along the CO_2 laser beam making the computer modelling of the experiment a one-dimensional problem. The peak CO_2 laser intensity used was large enough to put the thermal conduction outside the realm of first order theory while small enough to make the saturation of inverse bremsstrahlung and the ponderomotive force minor effects.

The thermal conductivity and the absorption were deduced by comparing the measured temporal evolution of the electron temperature at four radial displacements from the CO_2 laser beam with the results of a computer simulation. By fitting the computer results within the experimental errors it was possible to define a range of allowed values for the conductivity and absorption.

In Chapter 2, the equipment and how it was used in the experiment is described.

In Chapter 3, the reduction of the raw data to obtain the electron temperature vs. time at different radial distances from the CO_2 laser beam axis is described. Observations of low frequency turbulence along the temperature gradient and backscattering at plasma densities $> 10^{17}$ cm^{-3} are also given.

Chapter 4 describes the computer simulation.

Chapter 5 gives the fitting of the computer output within the experimental errors.

Chapter 6 discusses the breakdown of first order theory for large λ_e/L.

In Chapter 7 the results and their significance are discussed.

The role of the author in this work.

The experiment described here was large enough to require the support of people other than myself (see Acknowledgements). The CO_2 laser used was built at A.W.R.E. However, it was not suitable for immediate coupling to a plasma so my work on parasitic oscillations and focal spot measurements is described. The Z-pinch plasma device and the computer simulation were inherited and therefore only my modifications to the computer program are described in detail. Section 4 of Chapter 7 is based on work by J.D.Kilkenny. With the above qualifications this thesis is solely due to the author.

CHAPTER 2

DESCRIPTION OF THE EXPERIMENT

1. INTRODUCTION

The background plasma used was a preformed z-pinch discharge in hydrogen giving $n_e \sim 6\ 10^{16}$ cm^{-3} and $T_e \sim 4eV$ for 1μs.

To prevent conduction increasing the scale length for the temperature gradient, a fast rising ($\overset{<}{\sim}$1ns) laser heating pulse was used. The CO_2 laser pulse length was variable from ~2→20ns and measurements were taken with both short and long pulses. Care was taken in obtaining good calibrations for the incident power and for the focal spot size.

The definitive diagnostic of laser scattering was used to observe the spatial and temporal evolution of n_e and T_e and to look for enhanced ion acoustic wave activity. The resolution in space (~150μm) and time (~1.2ns) was sufficient to give non-smeared spectra.

Fig. (2-1) shows the CO_2 and ruby lasers and the z-pinch plasma source.

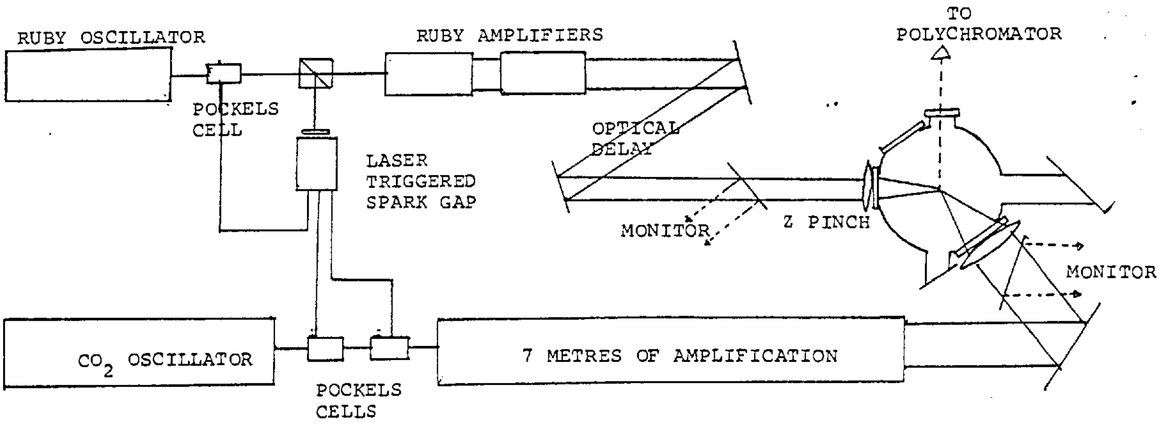

Fig. (2-1) A schematic of the experimental layout.

The experimental equipment is now described in sections as follows:

Section 2:

Firstly the CO_2 laser system as constructed at A.W.R.E. is briefly described. Secondly, the application of the CO_2 laser to the experiment is described. This included energy measurements, suppression of parasitic oscillations caused by the z-pinch input optics and focal spot measurements.

Section 3:

The ruby laser was home made and therefore a detailed description of it is given here. The imaging of ruby light into the plasma and the measurement of the ruby focal spot are also described.

Section 4:

A résumé of the plasma source is given.

Section 5:

To the author's knowledge this experiment was the first to make laser scattering measurements with a 1ns time resolution. This section describes how the problems of synchronisation and time resolution were tackled.

Section 6:

This section describes how the experiment's principal diagnostic (laser scattering) works.

Section 7:

This section shows the geometrical arrangement of the plasma, the CO_2 laser beam (and its diagnostics), the ruby laser beam (and its diagnostics) and the spectrometer recording the scattered light.

2. CO_2 LASER (AWRE)

(i) General Details of Laser

The experimental set up is shown in Figs. (2-2) and (2-3). The laser was constructed from 1m double discharge TEA modules of the Dumanchin[51] type, there being 2 in the driver section and 5 acting as amplifiers.

The oscillator cavity was formed by a 10M radius of curvature (100%R) and a 60% reflecting plane output mirror separated by 2.8m. A low pressure (∿5 Torr) D.C. discharge cell, operating just below its self-lasing threshold in this cavity, preferentially excited a single longitudinal mode during the gain switching of the TEA oscillator.[92] Thus, the nanosecond temporal structure due to mode-beating was eliminated from the (∿50ns FWHM) gain switched pulse and a reproducible output could be switched out by the electro-optic gate. A single transverse mode was selected using an intracavity aperture. The oscillator was horizontally polarised by having 3 KCl windows at Brewsters angle within the cavity. Spectral Analysis showed that lasing occurred on the P(20), P(18) and P(16) lines of the $00^01 - 10^00$ transition.

The electro-optic gate consisted of two 10 x 10 x 50mm gallium arsenide Pockels Cells (PC1 and PC2) pulsed to their half-wave voltage (∿ 14kV) by using 2 outputs of a 5-channel laser triggered spark gap fired by the ruby laser. The cable to the second pockels cell was longer by the optical path difference between the cells. The pockels cells were designed as strip transmission lines which had a characteristic impedance of 100Ω and the voltage pulse was propagated along the direction of the laser.

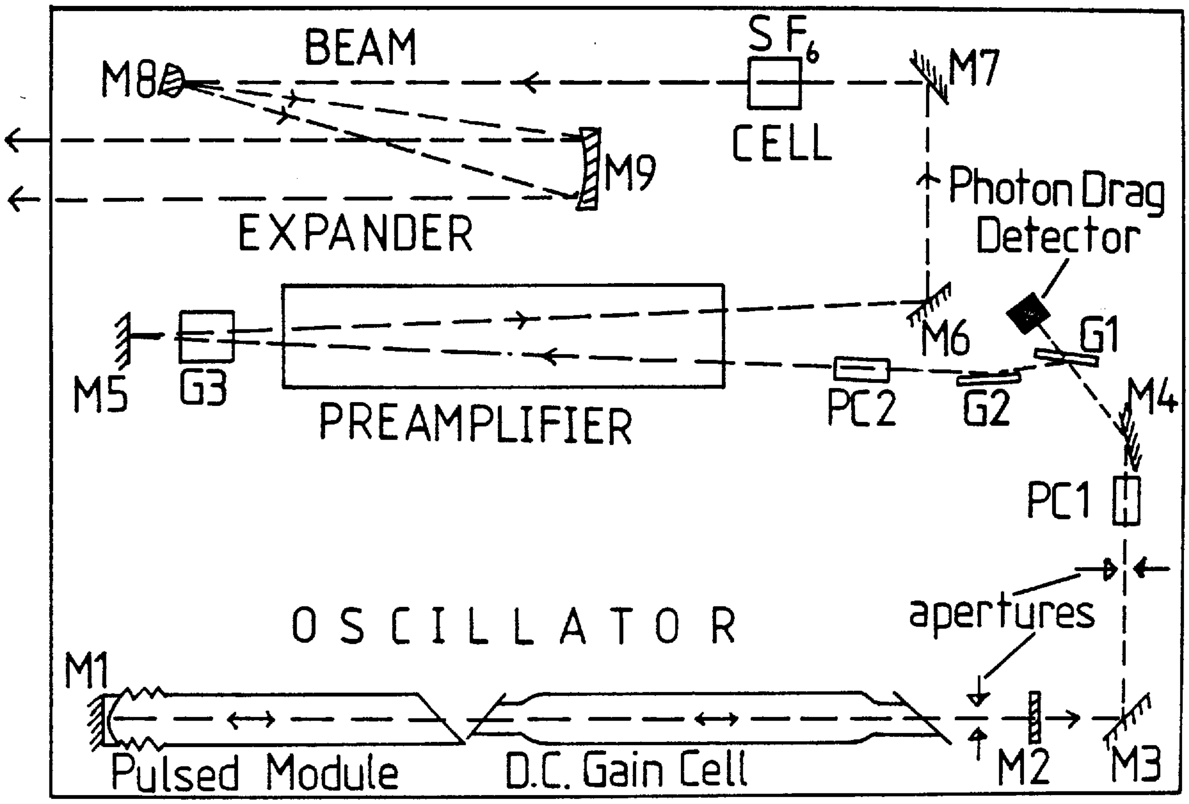

Fig. (2-2) Driver Section - CO_2 Laser.

M1, M3 → 9.......100% Reflecting Mirrors; M2....60%;

G1 → 3.......Germanium plates at Brewster's Angle

PC1,2.......GaAs Pockels Cells.

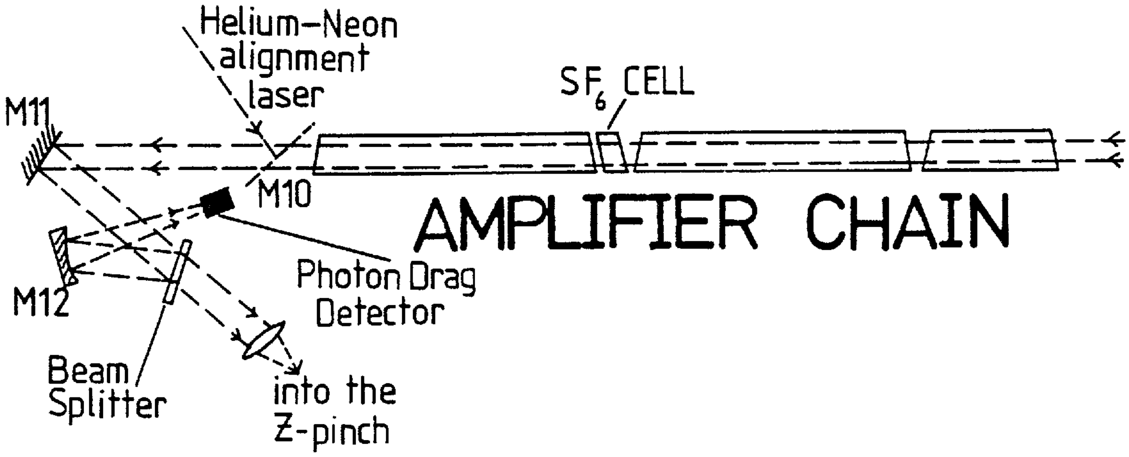

Fig. (2-3) Amplifier Section - CO_2 Laser.

Maximum open-time duration was limited to ∿ 30ns, because of tracking down the sides of the crystals. Short pulses were obtained by closing the second pockels cell using a shorted termination. During energy/power calibrations, secondary pulses, switched out ∿ 20ns after the first pulse due to voltage reflections, had to be eliminated. This was done by closing the first pockels cell using an adjustable air spark gap placed in the cable connecting it to the laser triggered spark gap.

Uncoated Germanium plates at Brewsters angle were used in reflection as crossed polarisers to the unswitched laser output. Perfect polarisation was not achieved due to beam divergence and optical surface quality.

Two pockels cells were used to reduce the breakthrough; i.e. leakage of oscillator pulses through the closed electro-optic gate. This was thought to be due mainly to residual birefringence in the Pockels cells reducing the extinction ratio of the crossed polarisers. Two saturable absorber cells containing a few-torr of SF_6 reduced this breakthrough even further to ∿ 2 mJ for powers ∿1 GW onto a calorimeter at the end of the chain. (Measurements D. Hull and P. Blyth).

Photo (2-1) shows sample CO_2 laser burn marks on polaroid

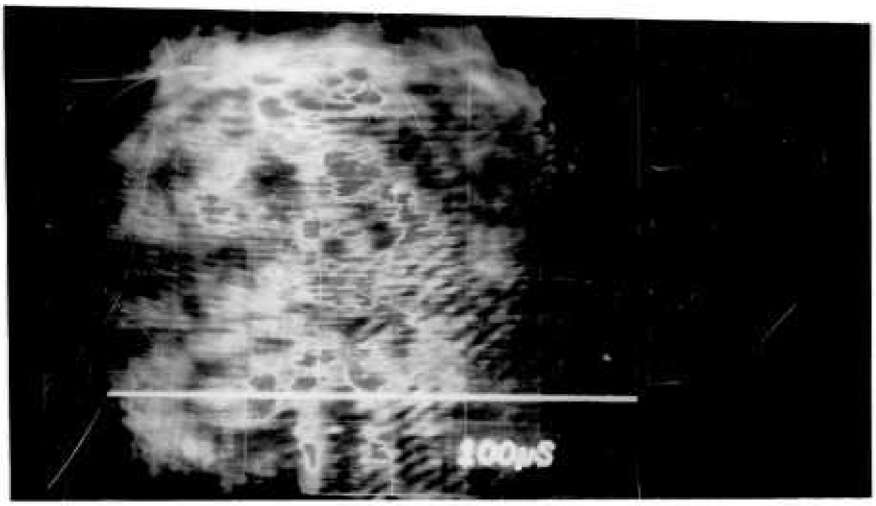

Photo (2-1) CO_2 laser burn marks on polaroid showing:- right...the oscillator output and left...the output at the end of the amplifier chain. (Magnification = 1 to 1)

(ii) Applying the laser to the Experiment

(a) Calorimetry

Because of the importance of a good energy/power calibration for the heating pulse in the plasma absorption/conduction experiment, two calorimeters of different design were used:

(α) "Perspex" Calorimeter

This was a thermocouple device constructed by E. Thornton of AWRE which made a differential measurement with respect to background temperature by having 2 copper backed perspex absorbers (5 x 5 cms) only one of which is hit by the laser. Calibration was achieved by passing a known current I for time t. Voltage readout from a thermocouple was onto a pen recorder.

(β) "Jen-Tec" Calorimeter ED500

These commercial calorimeters came with a calibration chart. Voltage readout was onto a scope. This calorimeter was used during most of the experiment for convenience.

(b) Power Calibrations

The pulse shape and thus power calibrations were taken for each experimental run using a Rofin 7412 photon drag detector monitored on a Tektronix 7904 scope with 7A19 plug-in (total convoluted rise time 1.2ns).

(c) Precautions taken for good calibrations

(α) The linearity of the power detector was checked against the joulemeter with increasing laser power. A saturation level of 150mV was found.

(β) No secondary pulses from laser. The spark gap mentioned previously was inserted in the lead to PC1 to prevent voltage reflections reopening the electro-optic gate.

(γ) The gain in amplifiers was kept low enough to make the parasitic plus breakthrough energy negligible. (Tilting of the joulemeter off normal incidence was found to be effective in reducing the parasitic energy).

(d) Elimination of parasitic oscillations

Although, as mentioned in part (i), powers >1GW were obtainable onto a calorimeter at the end of the chain, this power level was not obtainable onto a plasma. This was because a resonator was formed using surfaces of the z-pinch input optics and other surfaces in the amplifier chain. With a small signal gain ~10^6 in the amplifiers, irreproducible parasitic oscillations built up before the main pulse time, perturbing the plasma, depleting the gain in the amplifiers and sometimes affecting the gain switching of the oscillator. A disc of diameter 9mms. was inserted near the back focus of the z-pinch input lens in an attempt to reduce the number of possible reflection paths. However, this was not found to be very effective. The usefulness of SF_6 as a saturable absorber was investigated. The Jen-Tec ED500 Joulemeter was placed at the end of the amplifier chain angled so that reflections from its face were outside the aperture of the amplifiers. The gain in the amplifier chain was changed by varying the voltage on the energy storage capacitors between 50kV and 60kV. The oscillator was fired but the electro-optic switch was left closed i.e. breakthrough was included. Observations were:

α) A definite threshold charging voltage (i.e. gain) was found for the build-up of parasitics.

β) This threshold changed from day to day.

γ) There was an optimum pressure of SF_6 since this gas also acted as an attenuator for the main pulse.

Overall, the best conditions useable were found to be ∿10 Torr in the first cell (beam area ∿0.5cm^2, cell length ∿1 cm) and ∿2 Torr in the second cell (beam area ∿25 cm^2, cell length ∿5 cms). With the lens in position, the wavelength of these parasitic oscillations was investigated by sending light from the small beam expander mirror onto the slit of an infra-red spectrometer. This instrument was principally designed for CW CO_2 lasers with direct visible readout from a wavelength scale on a fluorescent screen.

Observations were:

α) With the SF_6 cells evacuated the 10.6μm (P20) line was clearly observed and there was sufficient energy to burn polaroid on the entrance slit.

β) With 10 Torr SF_6 in the second cell the 10.6μm line was no longer observed but a polaroid burn was still obtained.

It was assumed that the instrument was too insensitive to register the lasing occuring on the other branches of the transition. Thus SF_6 only acts as a saturable absorber for 10.6μm and parasitics were building up on the 9.6μm lines. Energy coupling between the rotational levels of the CO_2 molecule then allowed gain depletion. The photon drag detector monitoring the unswitched part of the oscillator pulse indicated that when the amplifiers were fired at high gain the magnitude of the oscillator pulse was irreproducibly reduced. This has been observed elsewhere[52] but never with the oscillator isolated by an electro-optic gate!

In the absence of any known wideband saturable absorber it was decided to optimise the power output by varying the time of firing of the amplifiers. This was a compromise between running early when the gain was low but before appreciable parasitics had built up.

At the end of the experiment a gain-time curve of the double-pass amplifier in the driver stage firing at 58kV was measured using photon drag (power) detectors. This is shown in Fig. (2-4) with the arrow indicating the gain at which the main experiment was run.

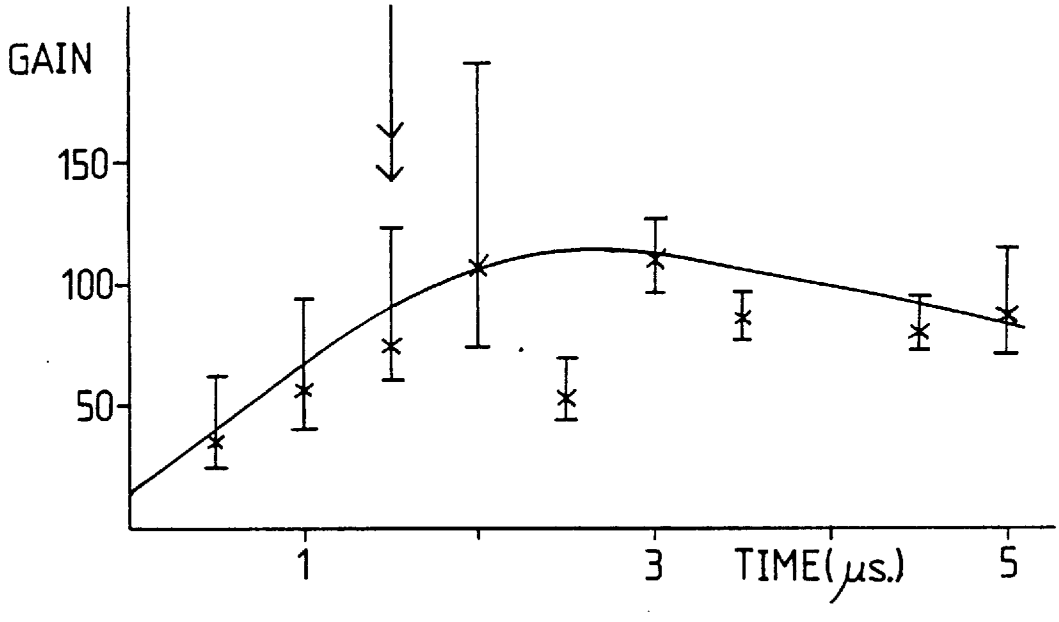

Fig. (2-4) CO_2 Amplifier Gain Time Curve.

(iii) Measurement of the focal spot size

(a) Description of the method used

A good measurement of the size of the focal spot was important because the intensity onto plasma scales as (spot diameter)$^{-2}$. Initially the spot size was recorded on "thermofax" burn paper, this being simplest.

However, the linearity and dynamic range of this medium is very poor. Fig. (2-5) shows measurements of spot diameter and focal area taken from the burn patterns used to focus the input lens. This was a KCl doublet of 17cms. focal length. Note the slightly astigmatic focus.

To get a more quantitative result the focus was scanned across a Stanley Knife blade under vacuum. The experimental set-up is shown in Fig. (2-6).

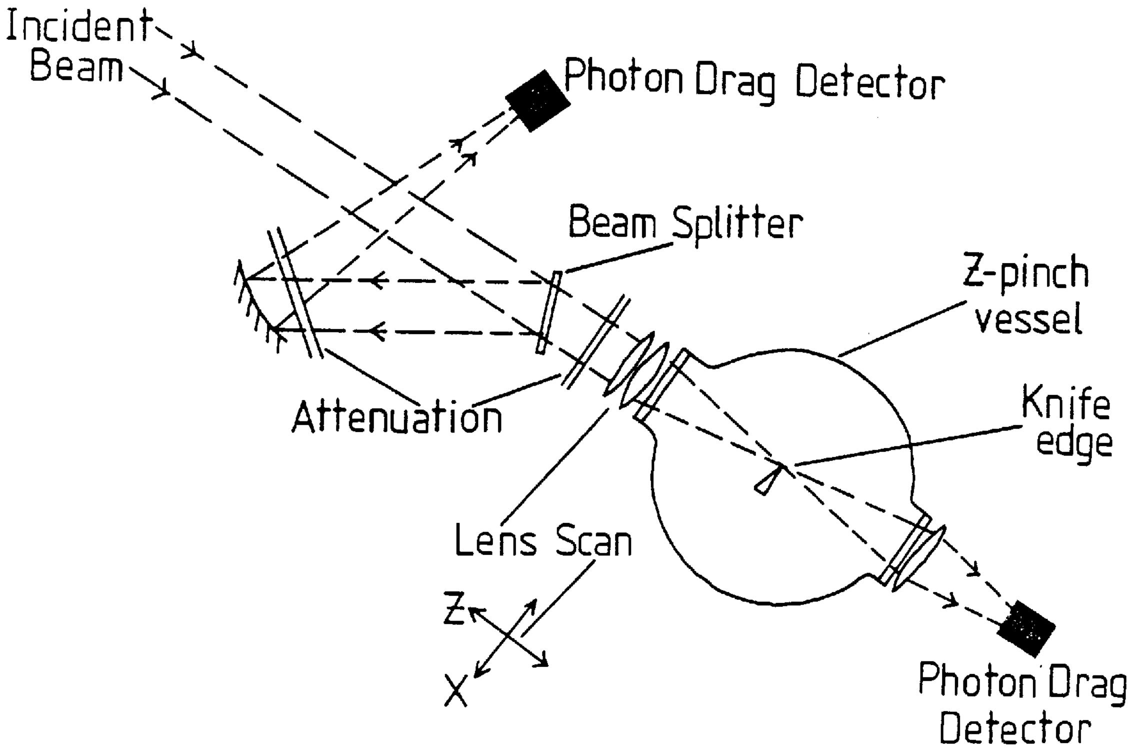

Fig. (2-6) Measurement of the CO_2 laser focal spot size.

The amplifiers were fired hard as in the main experiment to include any thermal lensing in the measurement. It was necessary to attenuate the incident beam to avoid blade damage. This was achieved by only switching one pockels cell and by placing Mylar attenuators (of fine enough quality so as not to distort the beam) at the second SF_6 cell and after the beam splitter in Fig. (2-6). An initial experiment using joulemeters proved unsatisfactory due to blade damage

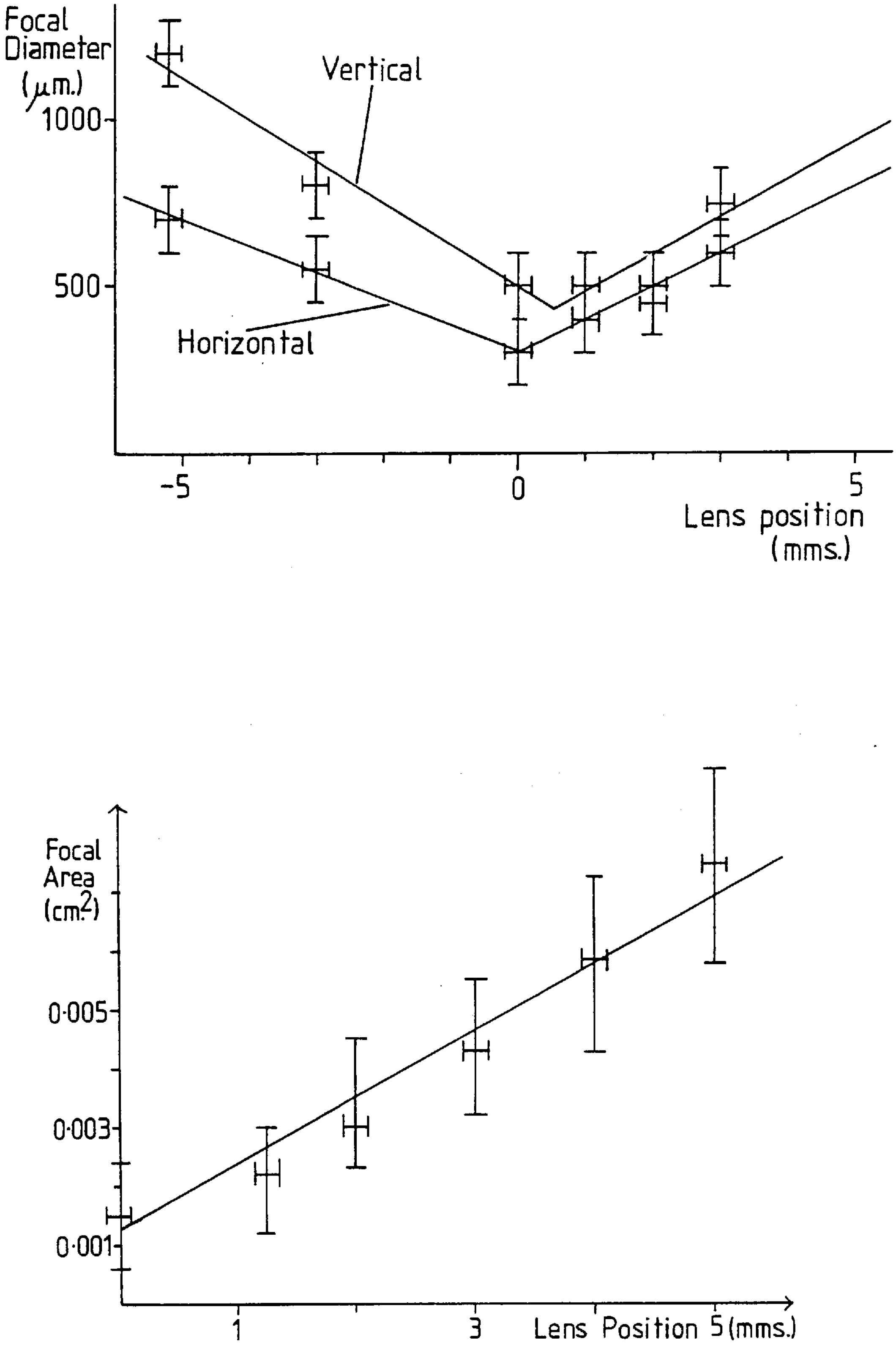

Fig. (2-5) Burn paper measurements of the CO_2 laser focussing.

and the inclusion in the measurement of energy after the main heating pulse time. Thus photon drag detectors were used. The focus was scanned by moving the lens along z and x as indicated in Fig. (2-6). Diffraction effects due to the straight edge were unimportant since all the transmitted light was imaged inside 4mm. of an 8mm. aperture photon drag detector. The fractional transmission was measured by normalising signals to photon drag 1. This is shown in Fig. (2-9). Constancy of transmission while varying lens x-position (i.e. area of photon drag 2 used) was checked with the blade removed. The blades used in the joulemeter and power detector experiments are shown edge to edge in Fig. (2-7).

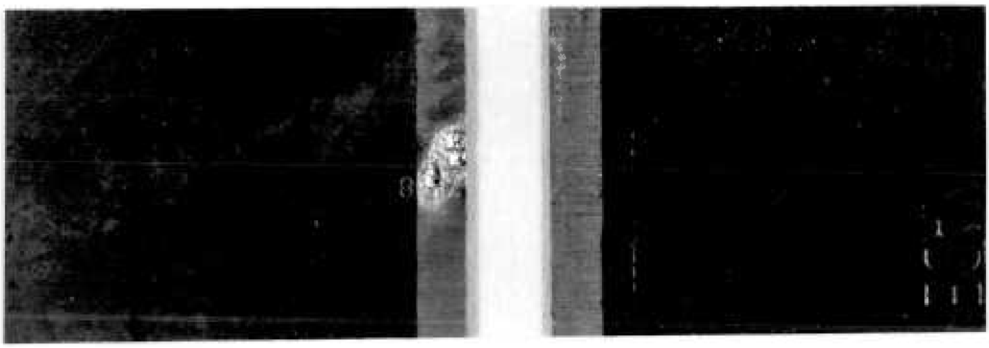

Fig. (2-7) Left....the damaged blade from the first experiment.
Right...the undamaged blade from the second experiment.

(b) Results and Interpretation

Fig. (2-8) shows the geometry of the blade intersecting the focus.

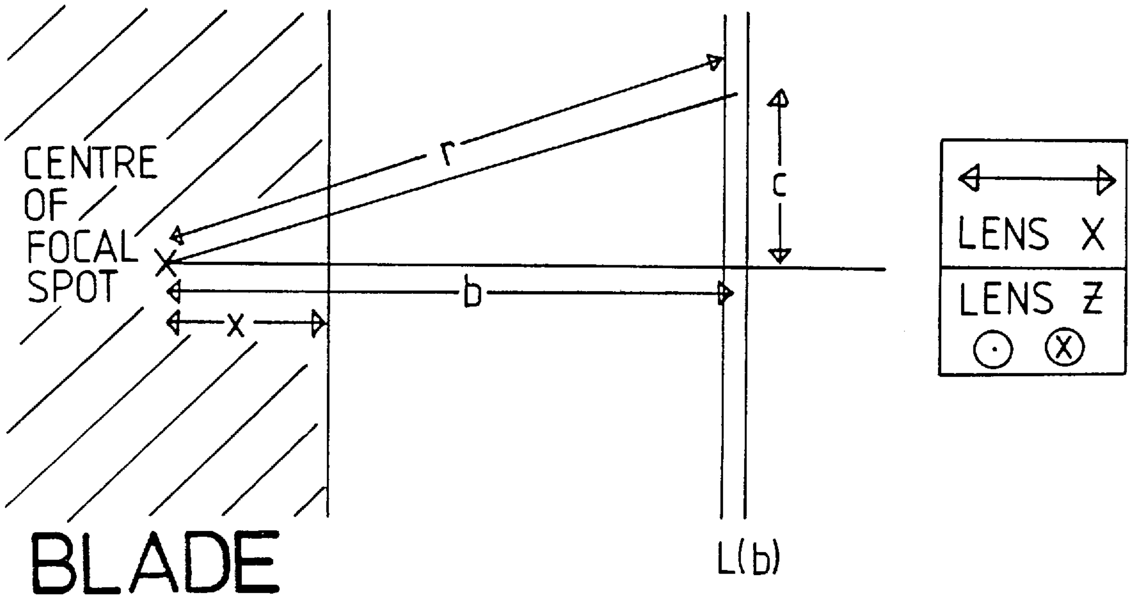

Fig. (2-8)

At this position the measurement integrates all the light from b = x to ∞.

We define:

$$J(b) = \int_{-\infty}^{\infty} f(b^2 + c^2)^{\frac{1}{2}}\, dc$$

we measure:

$$I(x) = \int_{x}^{\infty} J(b)\; db$$

A Gaussion focal spot is assumed reasonable in an aberration limited focus:

$$f(b^2 + c^2)^{\frac{1}{2}} = f(r) = Ae^{-r^2/L^2}$$

$$I(x) = A \int_{x}^{\infty} e^{-\,b^2/L^2} \int_{-\infty}^{\infty} e^{-\,c^2/L^2}\; db\; dc$$

$$= A \int_{-\infty}^{\infty} e^{-\,c^2/L^2}\; dc \left[\int_{0}^{\infty} e^{-\,b^2/L^2}\; db - \int_{0}^{x} e^{-b^2/L^2}\; db \right]$$

This is now reducible using the tabulated error function:

$$\int_{-\infty}^{\infty} e^{-c^2/L^2} \, dc = L\sqrt{\pi} \quad ;$$

$$\int_{0}^{g} e^{-t^2} \, dt = \frac{\sqrt{\pi}}{2} \, \mathrm{erf}(g)$$

$$I(x) = \frac{AL^2\pi}{2} \left[1 - \mathrm{erf}\left(\frac{x}{L} \right) \right] .$$

By varying the $^1/_e$ point of the Gaussian (i.e. $x = L$), it was possible to fit the transmission function, $I(x)$, to the experimental results. Measurements were taken for three lens Z positions (-1, 0, and +1 mm.) and the central (0) position was found to have the sharpest cut-off in transmission. Fig. (2-9) shows that $150 \lesssim L \lesssim 200\mu$m fitted the position of sharpest cut-off. This spot size was limited by the incident beam divergence, the focal length of the z-pinch input lens and imperfections in the input optics. The input optics were F/3.4.

(iv) Attenuation of Pinch Input Optics

The input power photon drag detector was calibrated with the ED500 Joulemeter placed between the beam splitter and lens shown on Figs. (2-3) and (2-6). Thus corrections had to be made for the z-pinch input optics to give the power onto plasma.

(a) Focal Plane Stop:

This was disc of 9 mms. diameter held centrally on the beam axis and just inside the back focus of the main lens by fine wires. To calculate the transmission the beam intensity was assumed to fall off as a Gaussian with a $^1/_e$ point at the edge

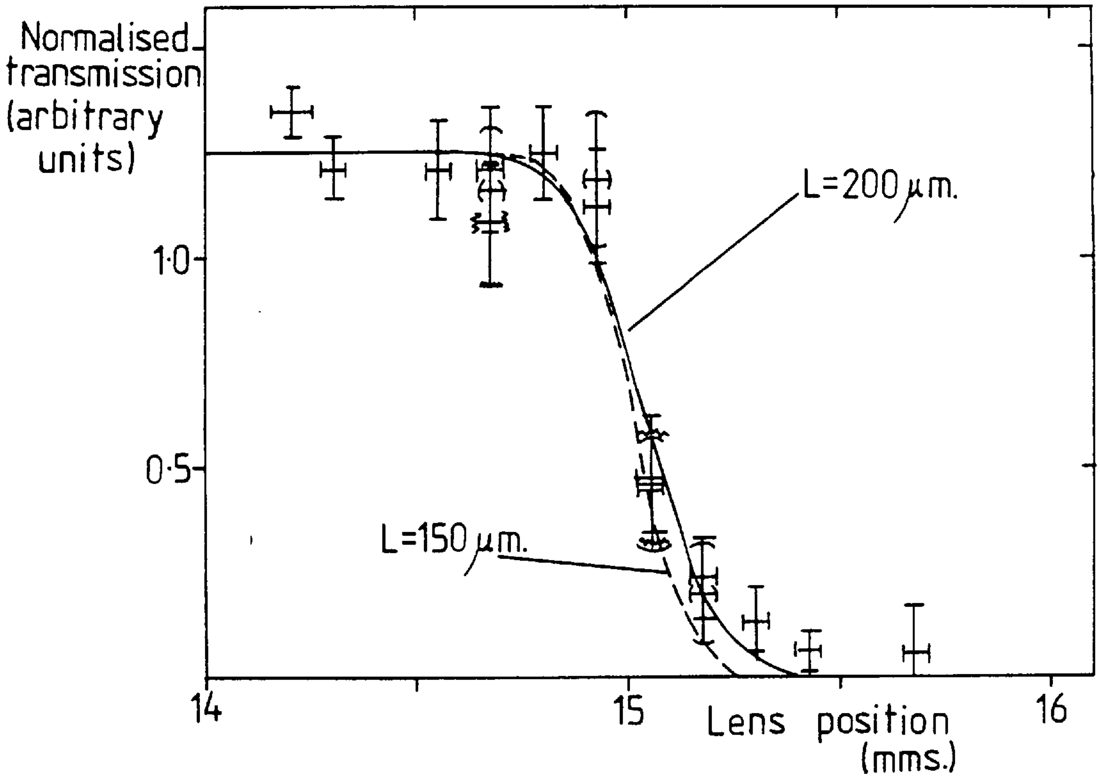

Fig. (2-9) Normalised transmission results for the sharpest cut-off position with fits of I(x) for L = 200μm (solid line) and L = 150μm (dotted line). Overlaid shots at the same lens x position indicate the shot to shot reproducibility.

of the burn mark, and the beam cut-off at the limit of the amplifier aperture. The ratio of the energy obscured by the 9mm disc to the total beam energy gave a fractional transmission of 0.80.

(b) Lens:

With the optical absorption of KCl = .002/cm at 10.6μm, only reflection losses contributed significantly. For normal incidence the reflection loss is 17% for 4 surfaces (n_{KCl} = 1.55).

(c) Pinch Input Windows:

Initially the transmission of the discharge-dirtied input windows was measured using a mechanically-chopped CW CO_2 laser. However, discrepancies were found between the CW and short pulse high-power transmission of some polythene attenuators which were being used to avoid joulemeter damage. Thus it was decided to reproduce the experimental situation for this measurement, using a 3ns laser pulse as shown in Fig. (2-10)

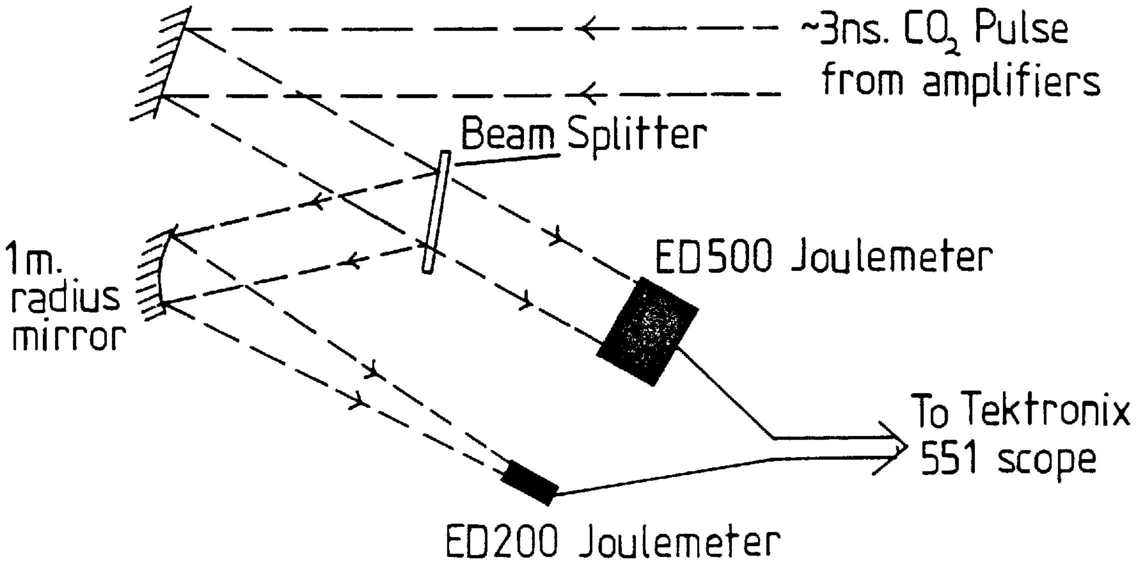

Fig. (2-10)

The ED500 Joulemeter had a large enough aperture to measure the whole beam. A 1m radius gold mirror imaged the whole beam onto the ED200 normalisation joulemeter. Both clean and discharge dirtied windows were measured by insertion in front of the ED500 joulemeter. A number of normalisation (no window present) shots were taken to check for drift. The linearity between voltage ranges on the scope was also checked.

Windows were 5cm. diameter x 9mm. NaCl discs. A clean window was used at the beginning of an experimental run and the number of plasma discharges until its removal was recorded. A linear rate of deposition of material/shot was assumed and confirmed by agreement of rates on comparison of different runs. The decrease in fractional transmission (incident energy/transmitted energy)/shot was found to be $6.3\ 10^{-4}$/shot for the low density ($6.10^{16}cm^{-3}$) pinch and $5.9\ 10^{-3}$/shot for the higher density ($2.10^{17}cm^{-3}$) pinch.

Thus with a measured transmission of 91% for a clean window and knowing the plasma discharge number the power onto plasma was:
(Power from photon drag calibration) x 0.80 For focal plane stop
x 0.83 For lens x (<0.91) According to discharge number .

3. RUBY LASER SYSTEM

(i) General Details of Laser

The diagnostic laser had to provide enough light in a small focal spot to allow scattered spectra to be measured above the light emission of the plasma. This laser was home made and thus a detailed description of it is given.

The oscillator, electro-optic switch and the two amplifiers are shown in Fig. (2-11). These were mounted on a heavy steel table for stability.

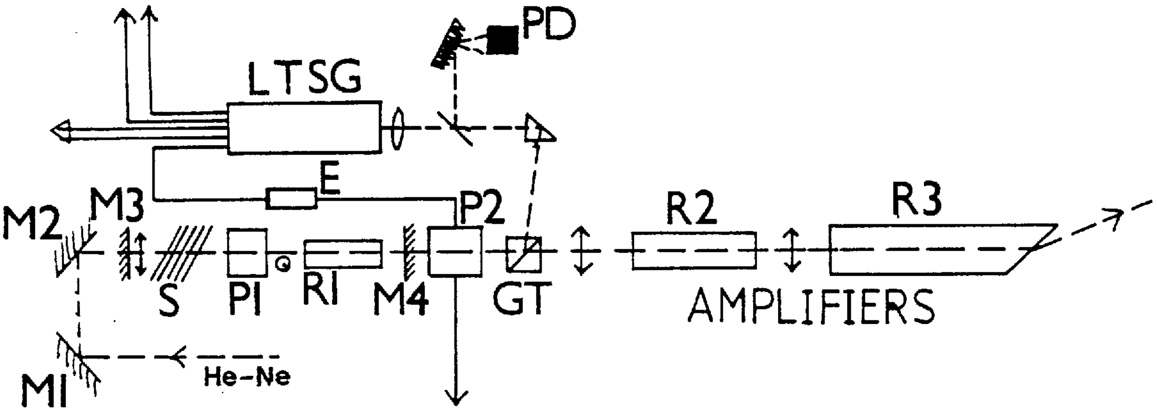

Fig. (2-11) The ruby laser system. M1 → 3.....100% mirrors; M4.....30% mirror; He-Ne.....Helium-neon alignment laser; S.....Stack Plate Polariser; P1 → 2.....Pockels cells; GT.....Glan-Taylor polariser; PD.....Photodiode; LTSG.....Laser triggered spark gap; E.....Electrical attenuator; R1.....ruby rod ($^3/_{16}$" x 4"); R2.....ruby rod ($^9/_{16}$" x 4"); R3.....ruby rod ($\frac{3}{4}$" x 9").

The oscillator was run multimode in a plane-plane cavity and half-wave Q switched. A horizontally polarised output of typically 1J in a pulse of 20ns (FWHM) was obtained with a jitter measured to be 5ns over tens of shots. An external electro-optic switch gated a short pulse from the Q switched pulse. This consisted of a KD*P fast risetime Pockels cell (Electro-optics Ltd. PC125), a Glan-Taylor prism and a laser triggered spark gap[53] (LTSG). The Glan-Taylor polariser was orientated to deflect horizontally polarized light upwards. A total internally reflecting prism (TIR) and a 15cm lens focussed the beam on one electrode of the LTSG. The LTSG was designed as a 10Ω transmission line feeding five 50Ω coaxial cables and held off 27kV across a 0.7 → 1.0 mm electrode spacing in 10kTorr of nitrogen. Optical attenuation in front of the 15cm lens controlled the time of breakdown. Two of the 13.5kV outputs provided the half-wave voltage for the CO_2 pockels cells. Another, attenuated by x 0.5, allowed the external ruby pockels cell (PC125) to rotate the light's polarisation to vertical and thus pass through the polariser and into the amplifiers.

Fig. (2-12) shows amplifier gain versus total energy in flash lamp capacitor banks. This data was taken with the 20ns oscillator pulse by placing a mica half-wave plate before the Glan-Taylor polariser and using a joulemeter to monitor the unamplified and amplified energy. The results shown were taken at the time of maximum gain which was 1.1ms after triggering of the flash lamps for both amplifiers. The error bars represent the shot to shot reproducability.

(ii) Divergence + Beam Spread

The oscillator divergence was measured from the diameter of the burn pattern at the focus of a 3m lens to be 2.3 mrad full angle.

The beam spread after the second amplifier was measured from two burn marks to be 6 mrad full angle. This was thought to be due to the second amplifier ruby crystal acting as a weak diverging lens.

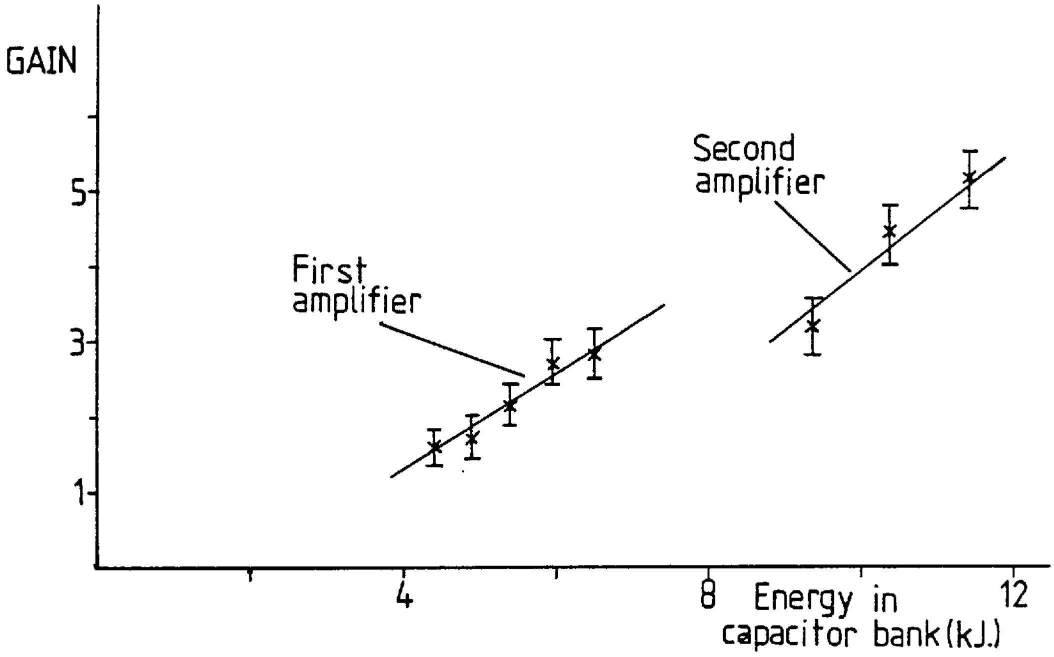

Fig. (2-12) Gain of the Ruby Amplifiers

(iii) Imaging of light onto the plasma

As explained later in the section on synchronisation the ruby oscillator had to be physically near the CO_2 oscillator. This placed it 19m from the z-pinch. The optics imaging the light into the plasma were chosen for reasons of availability, maximum collection of light and smallest focal spot. These are shown Figs. (2-13a) and (2-13b). Fig. (2-13b) was a modification of the direction of the scattering vector, discussed later. The output end of the 2nd amplifier was Brewster angled to avoid parasitic oscillations and refracted the beam upwards. Thus the polarisation was twisted by 20^o from the vertical when T1R1 returned the beam to a horizontal direction. This meant that the Thomson scattered light was reduced by $100\ (1 - \cos 20^o)\% = 6\%$.

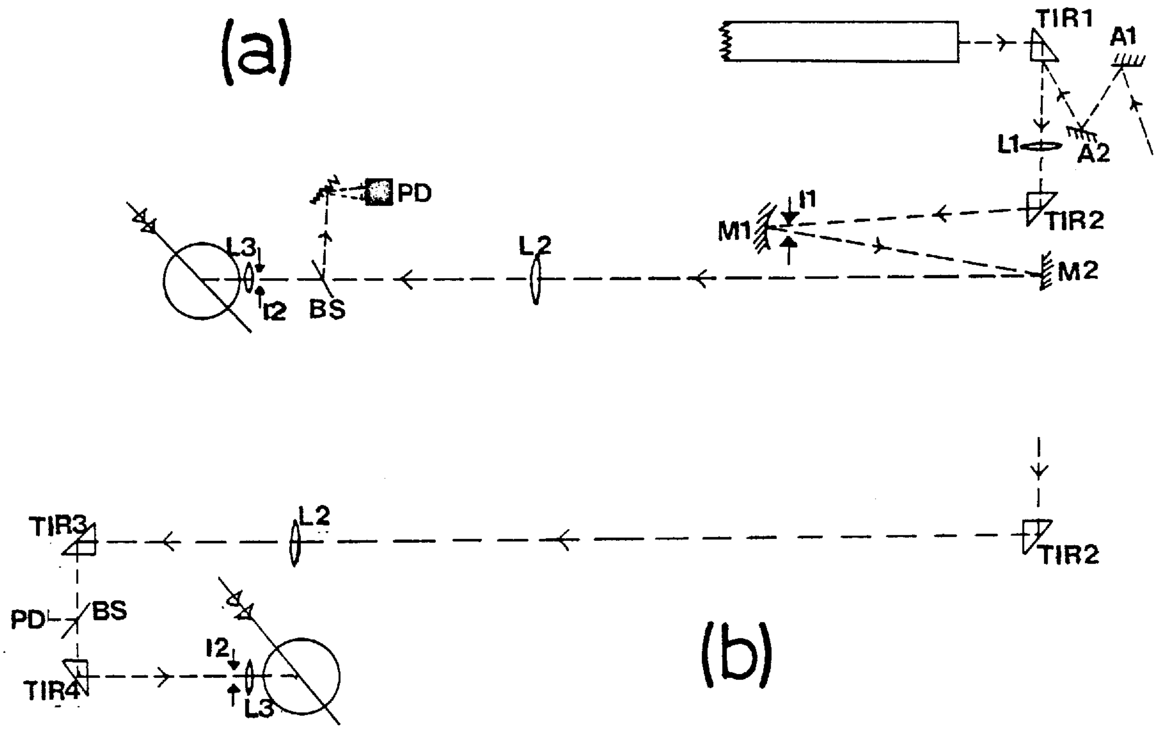

Fig. (2-13) Ruby laser relay optics. TIR1 → 4.....total internal reflection prisms; L1 → 2.....3m lenses; A1 → 2, M2.....100% reflecting plane mirrors; M1.....100% reflecting 3m radius of curvature mirror; I1 → 2.....apertures; PD.....photodiodes; L3.....15cm focal length lens; BS.....glass beam splitter.

A He-Ne alignment laser reflected off the output surface of TIR1 was made co-axial and co-linear with two polaroid burn marks separated by ~ 7 m. These are shown in Fig. (2-14). A pinhole was made through the centre of the near burn mark so that the ruby laser had only to be fired twice. The silvered alignment mirrors A1 and A2 were then iterated to send the He-Ne through the pinhole onto the centre of the far burn.

The relay optics were then centred using the He-Ne. The beam was always sent through the optic axis of a lens to minimise dispersion between the He-Ne (6328 Å) and ruby (6943 Å) beams. Finally alignment was confirmed on the pinch input window and at the focus of the 15cm lens in the pinch vacuum vessel. A few percent of the incident beam was directed onto a diffuser by the glass beam splitter. This diffuser was viewed by an ITL S20 vacuum photodiode and a pin diode. The vacuum photodiode had a red filter and N.D. filters giving a few volts (saturation at ~ 30V) into 50Ω of a 7A19 plug-in on a Tektronix 7904 scope. This gave a convoluted risetime of ~ 850ps. The pindiode was allowed to saturate at ~ 15V giving a sharply rising pulse used to trigger the oscilloscopes.

The vacuum photodiode was calibrated by recording the energy incident at the z-pinch input on a Laser Instrumentation model 152 joulemeter. Running the amplifiers close to the limit of flash tube shattering as in the main experiment (Amp 1 - 6.5kJ, Amp 2 - 13kJ) the peak power was ~ 50MW. The peak power immediately after the 2nd amplifier was ~ 500MW. The energy transmission of TIR1 was measured to be ~ 70% and that of L1 to be ~ 85%. These losses cannot be due only to reflection but there must be bulk absorption in the glass. Thus 4 prisms and 2 lenses give a relay system transmission of ~ 17% in reasonable agreement with the power measurements.

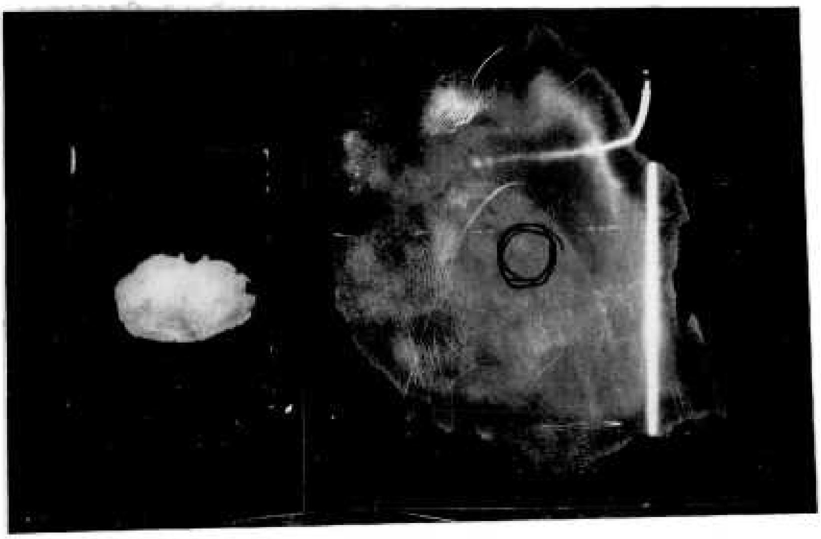

Fig. (2-14) Ruby laser alignment burn marks at amplifier output (left) and ~ 7m further on (right). N.B. Relay optics not present.

(iv) Measurement of the ruby focal spot size

The diagnostic laser had to have a sufficiently small focal spot to resolve the spatial features of the heating. While setting-up and focussing, burn marks on blue-inked card were used to estimate the spot diameter. As discussed for the CO_2 laser, burn patterns are not a definitive measurement and indeed the diameter of the bleached area increased with increasing incident energy.

A better measurement was obtained by imaging in strips, the light, Rayleigh scattered by CO_2 gas from the focus as shown in Fig. (2-15).

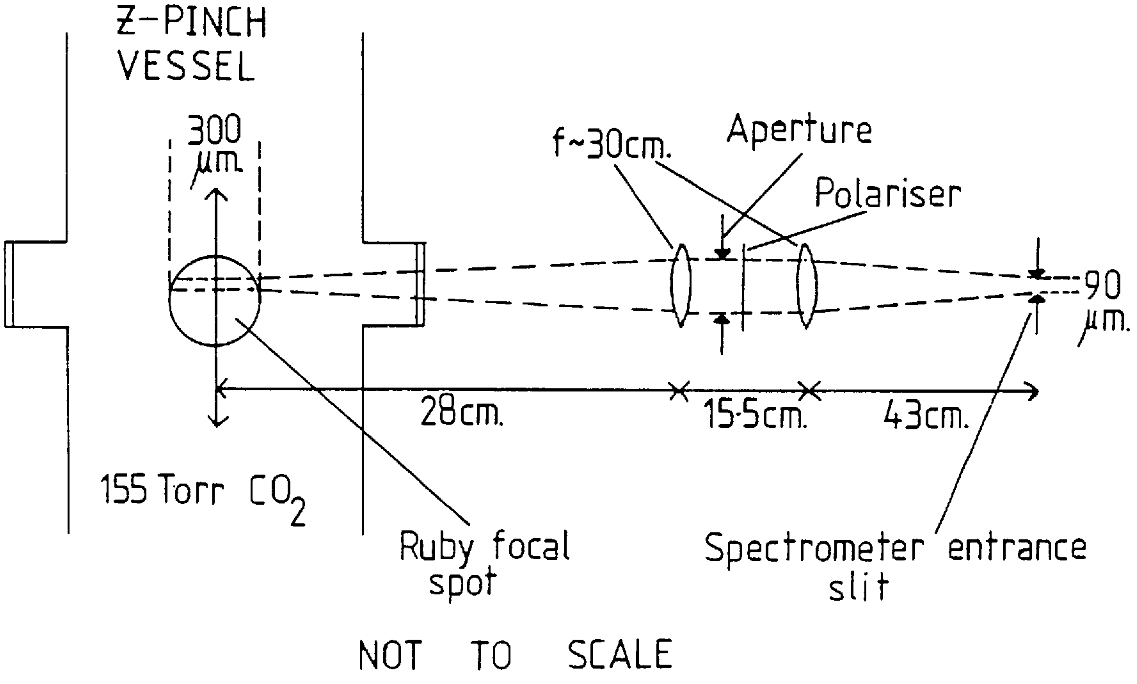

Fig. (2-15) Rayleigh scattering from the ruby focal spot.

The slit was ¾mm wide x 90μm high and the imaging optics had a measured magnification of 1.45. The resolution of these optics was <u>at least</u> 80μm. This was measured by illuminating a ruled graticule at the focal spot position from a tungsten ribbon lamp and observing the image on the slit. The C31024A photomultiplier used in the main experiment viewed the exit slit of the spectrometer (which was tuned to 6943Å). The ruby laser was fired at full power as in the main experiment. 155 Torr CO_2 in the vacuum vessel gave sufficient scattered light and laser induced gas breakdown did not occur. The scan across the focal spot was achieved by moving the 15cm ruby focussing lens. With a total movement ~ 0.5mm in a total aperture of ~ 5cms lens characteristics were assumed constant. The parasitic* light level was checked to be << the Rayleigh scattered light level at all the lens positions used by taking shots with the z-pinch vessel evacuated. The photomultiplier signals were normalised to the input power recorded on the vacuum photodiode. Fig. (2-16) shows the raw data.

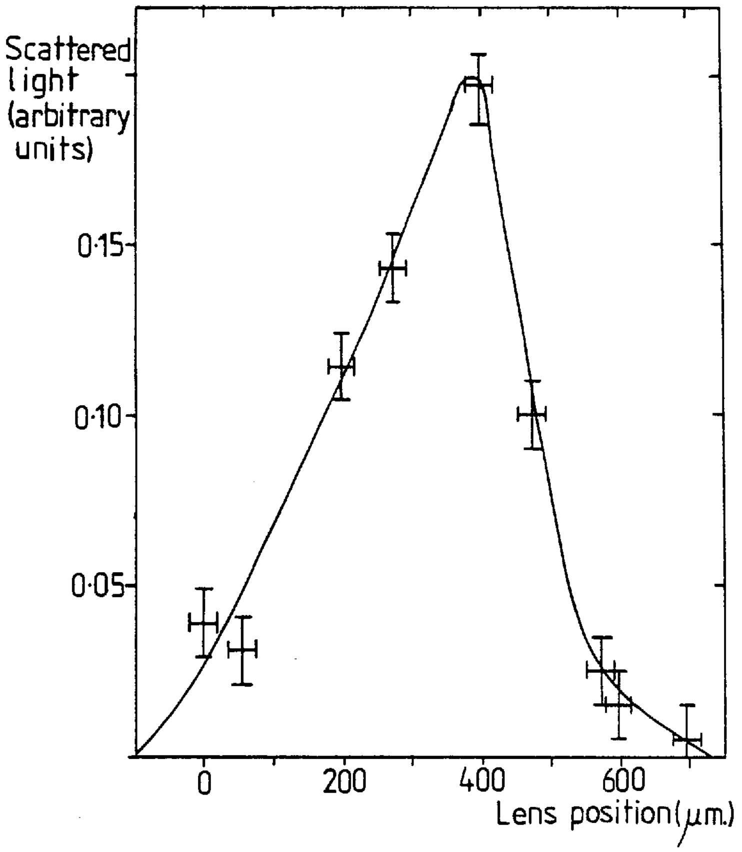

Fig. (2-16)
Vertical scan through ruby focal spot. The vertical error bars represent the shot to shot reproducibility.

---

* Parasitic light is stray light usually scattered by the apparatus.

Abel Inversion of Data

If it is assumed that the intensity is radially symmetric then the measurements may be Abel Inverted.[54]

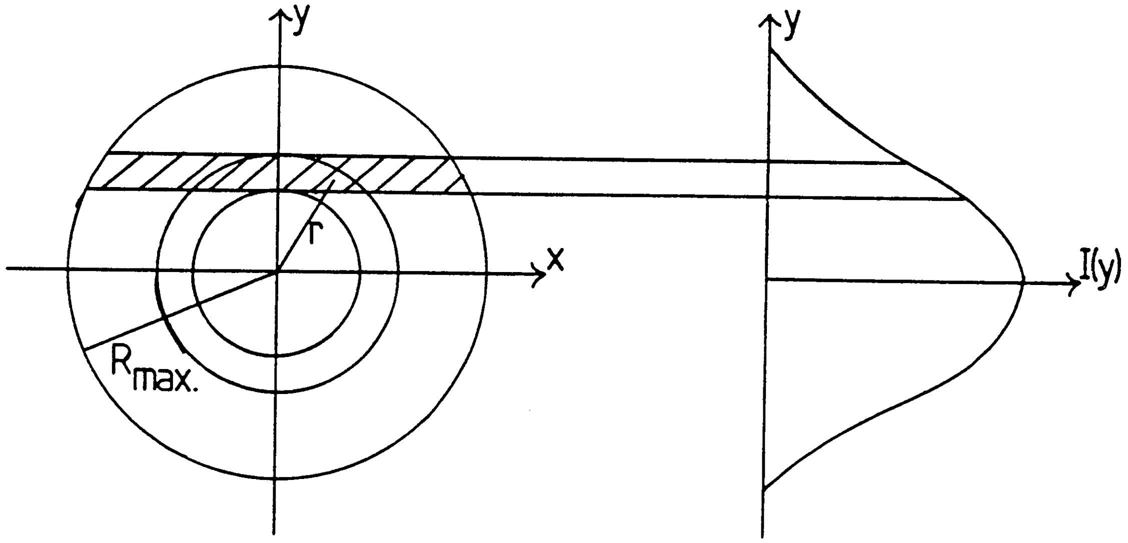

Fig. (2-17) Abel Inversion Geometry.

I(y) and y represent the Normalised scattering and lens position respectively of Fig. (2-15) If J(r) describes the radial intensity in the focal spot then:

$$I(y) = 2 \int_{y}^{R_{max}} \frac{r\,J(r)\,dr}{(r^2 - y^2)^{\frac{1}{2}}} \qquad (2\text{-}1)$$

and using the Abel Inversion:

$$J(r) = -\frac{1}{\pi} \int_{r}^{R_{max}} \frac{I'(y)\,dy}{(y^2 - r^2)^{\frac{1}{2}}} \qquad (2\text{-}2)$$

Equ. (2-2) was numerically integrated using Simpson's Rule:

$$J(r) = -\frac{1}{\pi} \quad I'(y) \int \frac{dy}{(y^2-r^2)^{\frac{1}{2}}} - \iint \frac{dy}{(y^2-r^2)^{\frac{1}{2}}} I''(y)\,dy \quad \Bigg|_{y = r}^{y = R_{max.}}$$

$$\int \frac{dy}{(y^2-r^2)^{\frac{1}{2}}} = \log_e \left(y + (y^2-r^2)^{\frac{1}{2}}\right)$$

y was then numerically scanned in small enough steps (1000 steps) to make:

$$\int_{\substack{\text{over} \\ \text{1 step}}} I''(y)\, dy \ll I'(y) \quad \text{at that step.}$$

Thus

$$J(r) = -\frac{1}{\pi} \sum_{n=0}^{1000} I'(y_n) \left\{ \log_e \left(y_n + \Delta + \sqrt{(y_n + \Delta)^2 - r^2} \right) - \log \left(y_n + \sqrt{y_n^2 - r^2} \right) \right\}$$

where $y_0 = r$, $y_{1000} = R_{max}$ and $\Delta = (R_{max} - r)/1000$

This expression then gave J(r) by using values of r from 10μm out to R_{max}. A copy of the fortran program used is given in Appendix A. The numerical accuracy of the program was checked by putting J(r) = r in equ. (2-1) which then becomes a known integral. Values of I(y) fed into the program reproduced J(r) = r to an accuracy of 5% at worst.

Fig. (2-16) indicated that the focal spot was slightly assymmetric and thus 21 values of I(y) from either side of the maximum were inverted. Fig. (2-18) shows the results

This gave an average $^1/_e$ point at 150μm. The measured half divergence angle of the oscillator was 1 mrad which would give a $^1/_e$ point at 150μm. Thus the measured 150μm is due to the ruby oscillator.

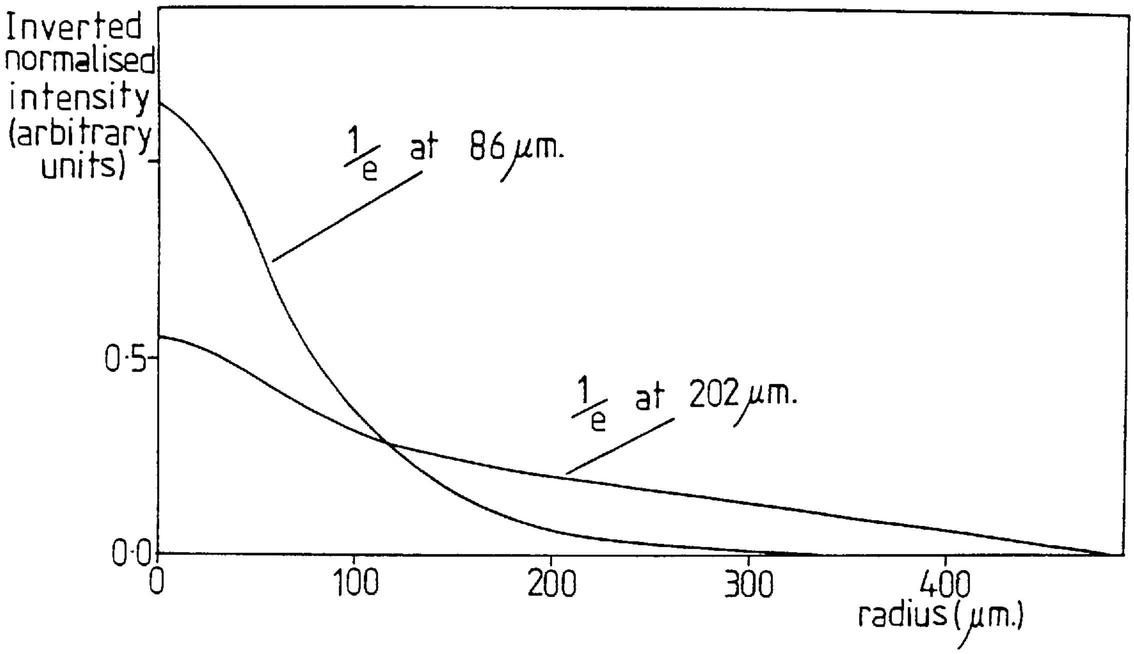

Fig. (2-18) Abel inversion of data from Fig. (2-16). The 86μm result was from the sharp side of Fig.(2-16) and the 202μm result from the other side.

4. THE Z-PINCH PLASMA

The development of the z-pinch plasma is described in detail in the Ph.D. Thesis of M.S. White[55]. M.S. White also thoroughly diagnosed the plasma by laser scattering, emission spectroscopy, streak photography and magnetic probes. Laser scattering showed that during the pinch phase there was a 1μs period when the electron density and electron temperature were approximately constant. From the ionization rates and the Saha equation the plasma must be more than 99% ionized. The photographic diameter of the pinch was large, 3cm compared with the 1-mm scale length of the heating experiment. Finally, with the magnetic probe at a position 2mm away from the pinch axis the value of the Hall parameter (electron cyclotron frequency/collision frequency) was 0.15. Thus on the length scale (1mm) and timescale (10ns.) of the heating experiment, the z-pinch plasma was essentially homogeneous, constant and unmagnetised. The electron-drift velocity of the pinch current and the local $\underline{j} \wedge \underline{B}$ forces were also found negligible for the dynamics of the heating experiment. This is discussed in more detail in Chapter 4.

The initial electron density could be increased by increasing the hydrogen filling pressure and/or the charging voltage on the 1.08mF capacitor bank. In the present work two principal settings were used namely, 200mT; 2kV giving 6.10^{16} cm^{-3}, 4eV; and 650mT, 3kV giving $2\ 10^{17}$ cm^{-3}; 5eV. The shot-to-shot reproducibility of these initial conditions was checked with the multi-channel laser scattering system using a 20 ns ruby pulse. To maintain good reproducibility, clean electrodes and a clean pyrex vacuum vessel were found to be important.

5. SYNCHRONISATION AND TIME RESOLUTION

Fig. (2-19) shows the triggering time sequence in the experiment. The coarse triggering up to time F was performed with delay units containing thyratrons with an inherent jitter ~ 5 → 10 ns. The jitter in the ruby laser(F→G) was measured to be 5 ns over tens of shots. The CO_2 laser jitter (EG) was 30 ns under optimum conditions. For optimum reproducibility of the CO_2 laser power the time (G) at which the half-wave voltage is applied to the Pockels cells should co-incide with the time of the peaks of the oscillator pulses. However, the CO_2 laser jitter was $\geq$ the temporal length of the ruby Q-switched pulse. Therefore the LTSG was triggered from the ruby laser pulse. A routine check of this coarse synchronisation was made using a Tektronix 551 oscilloscope and power detectors which monitored the unswitched parts of the laser pulses.

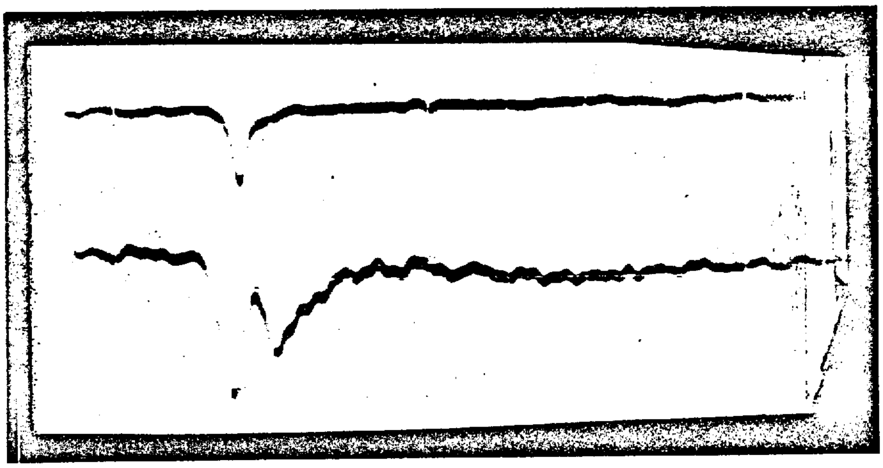

Fig. (2-20) Coarse synchronisation monitor. Upper trace........ unswitched ruby pulse; lower trace.....unswitched CO_2 laser pulse.

The root mean square variation in the time between the start of the CO_2 laser pulse and the opening of the electro-optic gate was found to be ~ 30ns on a typical run. Gain saturation in the final CO_2

FIG. (2-19) TRIGGERING TIME SEQUENCE

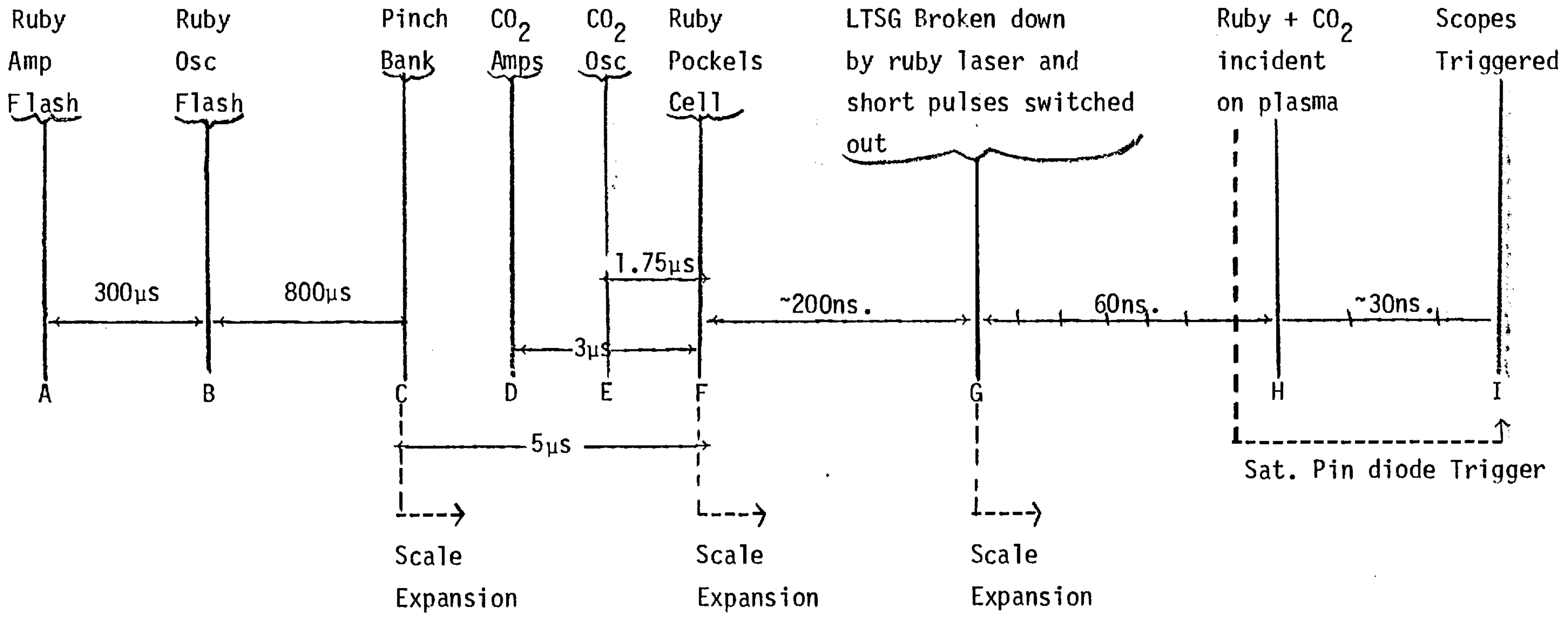

Times

A and B → F : Gain build-up in ruby rods.

C → F : Pinch Formation time.

D + E → G : CO_2 circuitry electrical risetime and gain build-up time.

F → G : ruby laser pulse build-up time in cavity.

G → H : transit of light to plasma.

H → I : cable delay to scopes.

laser amplifiers helped to reduce the variation of the CO_2 laser intensity at the z-pinch. (The overall intensity variation was typically 20% RMS).

The time between the breakdown of the LTSG and the arrival of the two laser pulses at the z-pinch was controlled only by the length of cables to the Pockels cells and the optical flight paths to the z-pinch. Thus with a constant alignment of the ruby laser and CO_2 laser relay optics the synchronisation of the switched pulses was constant. The LTSG broke down on the rising edge of the ruby pulse and thus to open the electro-optic gate near the peak of the ruby pulse the cable length to the ruby Pockels cell had to be < 5ns. This constrained the ruby pulse to have an optical flight path not less than that of the CO_2 pulse. This placed the ruby laser oscillator ~ 19 m from the z-pinch.

Another consideration was minimisation of cable lengths to prevent degradation of the LTSG voltage pulse risetime. Fig. (2-21) shows a measurement of the LTSG voltage pulse after propagation through the X2 attenuator and the ruby laser Pockels cell.

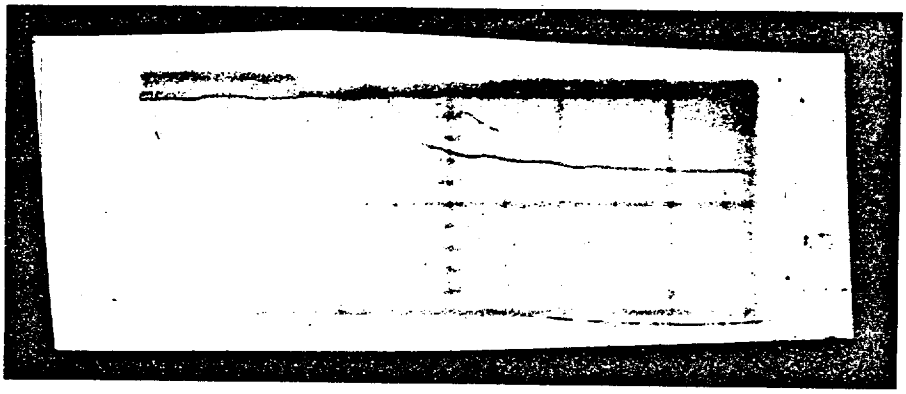

Fig. (2-21) Voltage pulse on ruby Pockels cell. (2 ns/division)

This was taken with a current shunt and a Tetronix 519 oscilloscope (risetime 300ps). The performance of the current shunt[56] was investigated by observing nanosecond voltage pulses on a Textronix 7904 oscilloscope (risetime 800ps) both, through the current shunt, and through 300ps risetime Textronic co-axial attenuators. Using the attenuators, the pulse rose to 90% in 1.2ns. Through the current shunt the pulse rose sharply to 70% in 1.2ns whereupon the slope changed and it rose to 90% in a further 1ns. Thus the plateau on the pulse in Fig. (2-21) may be a function of the shunt. However, evidence for the existence of a voltage ramp after an initial sharp rise is given by the tail on a short ruby pulse observed on the vacuum photodiode and a Tektronix 519 near the z-pinch. An example for a shorted termination 4.5 cms. from the Pockels cell is shown in Fig. (2-22).

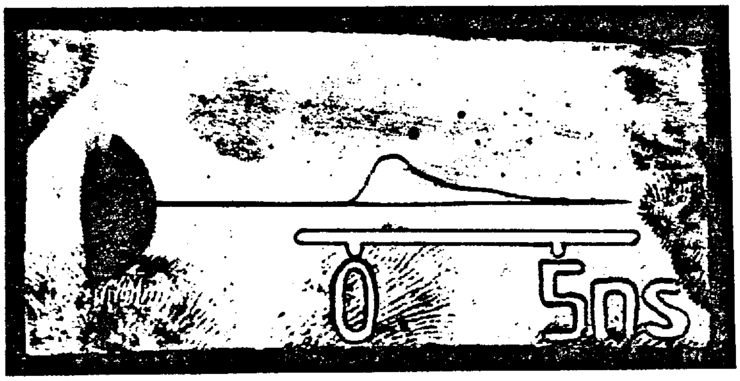

Fig. (2-22) Ruby laser pulse switched with a 4.5cm stub. (FWHM = 1.7ns).

The sweep calibration drawn on Fig. (2-22) was checked by reflecting pulses from a known length of 50 Ω cable. The peak amplitude of the pulse (and the FWHM) increased with increasing shorted termination lengths indicating a modulation depth less than 100% in the electro-optic switch.

It was initially planned to perform the experiment by recording a full scattered spectrum per shot using an existing bank of 8 ns risetime photomultipliers and to obtain time resolution by using a short ruby pulse. The temporal evolution of the spectrum would then be obtained by changing the relative timing of the CO_2 and ruby laser pulses. However, better time resolution was provided using half a Q-switched ruby pulse and a single 1.2 ns (10 → 90%) risetime photomultiplier (RCA C31024A). Then, the full temporal evolution in a single spectral interval was obtained per shot. Expense prevented the purchase of enough photomultipliers to take a full spectrum per shot.

To switch-out half a Q switched ruby laser pulse a 50 Ω termination on the end of a long cable was substituted for the shorted termination. Switch-out modulation was observed to be ~ 100%. Note that synchronisation of the two laser pulses was still essential to define a time zero for the laser scattering.

The electrical outputs of the vacuum photodiode and photomultiplier were recorded on Tektronix 7904/7844 oscilloscopes with 7A19 plug-ins (Risetimes 0.8 ns). The time resolution of the RCA C31024 A photomultiplier was checked on Rayleigh scattering by using a fast rising ruby laser pulse. Fig. (2-23) shows that its risetime was ~ 1ns.

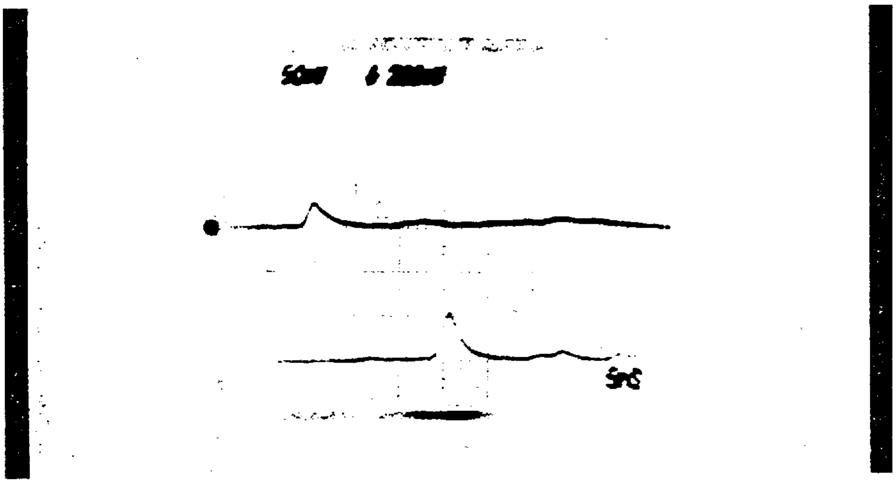

Fig. (2-23) Upper trace.....Vacuum photodiode (risetime ~ 300ps)
Lower trace.....fast photomultiplier (risetime ~ 1.2ns)
Oscilloscope.....Tektronix 7844 (risetime ~ 0.8ns)
Sweep Rate 5ns/division.

6. LASER SCATTERING AS A DIAGNOSTIC

If practically feasible, laser scattering is the most definitive of all optical plasma diagnostics. The scattered spectra can yield not only n_e, T_e and T_i but also information on plasma wave activity, magnetic fields and impurity content.

(a) Theory

I will now give a simplistic résumé of the theory[57].

Suppose that a monochromatic plane wave of amplitude E_0, propagation vector k_0 and angular frequency ω_0, is passing through a plasma such that $\omega_{pe} << \omega_0$. When the amplitude of oscillation of the re-radiating electrons is very small compared with the emitted wavelength then we can use the dipole approximation to calculate the field in the wave zone. Most of the light is transmitted through the plasma but a small fraction, given by the Thomson cross-section (6.65 10^{-25} cm^2/electron), n_e and T_e, is incoherently re-radiated in a dipole distribution.

The acceleration of the electrons under the action of the above laser light is:

$$a = -(^e/m) \; E_0 \; \cos \{\underline{k_0} \cdot \underline{r}_j (t) - \omega_0 t\}$$

Note that the acceleration depends upon time implicitly through the variation $\underline{r}_j(t)$ of the position vector of the electron with time as well as explicibly through the phase factor $\omega_0 t$. Hence, the Fourier analysis of this acceleration will also contain in addition to the frequency ω_0, frequencies characteristic of the electron motion in the absence of the radiation field. The light scattered by the electron will thus contain these additional frequencies as well as the incident frequency; this is the essential property of the scattering process that is of interest for plasma diagnosis.

When the electric fields due to the dipole emissions of each electron are summed at a detector far outside the plasma, it is found that electrons giving rise to the same phase (i.e. constructively interferring) lie on planes spaced by integer multiples of $2\pi/\underline{k}_{scatt}$. Here, $\underline{k}_{scatt}$ is the differential scattering vector shown in Fig. (2-24)

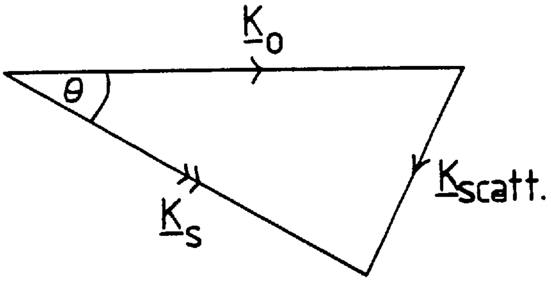

Fig. (2-24) $\underline{k}_0$ - incident laser propagation vector
$\underline{k}_s$ - scattered light propagation vector.

At visible frequencies $h\nu \ll mc^2$ and we consider only elastic scattering i.e. $|k_0| = |k_s|$. Thus:

$$|\underline{k}_{scatt}| = (4\pi/\lambda_0) \sin \theta/2.$$

So by fixing an incident laser wavelength λ_0 and a scattering angle θ we select the spatial Fourier component of the electron density distribution whose wave number is $|\underline{k}_{scatt}|$. For electrons on planes not separated by $2\pi|\underline{k}^{-1}_{scatt}|$ the scattered light from these electrons would not be in phase at the detector and the scattered intensity would be the same as if the electrons were randomly distributed.

Selecting the spatial Fourier component of the electron density distribution determines the frequency spectrum that will be observed at the detector.

α = scale length for scattering/plasma debye length = $1/k\lambda_D$

When $\alpha >> 1$, ($k^{-1} >> \lambda_D$), electron plasma waves of wavelength $2\pi\ k^{-1}$ modulate the number of electrons on the planes and peaks (sidebands) appear in the scattered spectrum.

When $\alpha << 1$, ($k^{-1} << \lambda_D$), all electron plasma waves are heavily Landau damped and the spectrum simply shows the component of the electron velocity distribution parallel to $\underline{k}$.

The light scattered by the ions is down by a factor of $(m_e/m_i)^2$ over the electrons. However, a low frequency "ion feature" is formed by the slow movement of the electron shielding cloud surrounding each ion. When $\alpha << 1$, the scale length for scattering is inside the shielding cloud ($2\pi k^{-1} << \lambda_D$) and the proportion of light scattered into this ion feature is small as expected.

The mathematical statement of the above is given in Evans and Katzenstein[57] as follows. (A Maxwellian velocity distribution is assumed). The plasma cross-section (σ_p) differs from the Thomson cross-section (σ_T) :-

$$\sigma_p = \sigma_T \int S(k,\omega)d\omega$$

where $S(k,\omega)$ is the form factor given by:-

$$S(k,\omega)d\omega = \Gamma_\alpha\ (x_e)\ dx_e + Z\ \left(\frac{\alpha^2}{1+\alpha^2}\right)^2 \Gamma_\beta\ \ (x_i)\ dx_i,$$

$$\beta^2 = Z\ \left(\frac{\alpha^2}{1+\alpha^2}\right)\ {}^{T_e}/_{T_i}\ , \quad \Gamma_\alpha\ (x) = \frac{\exp(-x^2)}{|1+\alpha^2 W(x)|^2}\ ,$$

$$W(x) = 1 - 2x \ \exp(-x^2)\int_0^x \exp(p^2)\, dp - i\pi^{\frac{1}{2}}\, x \exp(-x^2)$$

Here, the spectral function $S(k,\omega)$ has been divided into an electron feature $\Gamma_\alpha(x_e)$ and an ion feature $\Gamma_\beta(x_i)$ using the Salpeter approximation. The basis of this approximation is the large disparity in the scale of the dimensionless frequency variables $x_e = \Delta\omega/k_{scatt}\, v_{the}$ and $x_i = \Delta\omega/k_{scatt}\, v_{thi}$. Thus, the electron spectrum has a frequency scale kv_{the}, the characteristic Doppler shift at the electron thermal speed ($\Delta\lambda_c \sim 70$ Å in this experiment) and the ion spectrum has a frequency scale kv_{thi}, the characteristic Doppler shift at the ion thermal speed ($\Delta\lambda_c \sim 1.6$ Å in this experiment). Note that the analytic form $\Gamma(x)$ of the two spectra is the same, although they differ in amplitude and in the value of the parameter α. The spectral shape for ions and electrons is shown in Fig. (2-25) taken from Salpeter[58](1960).

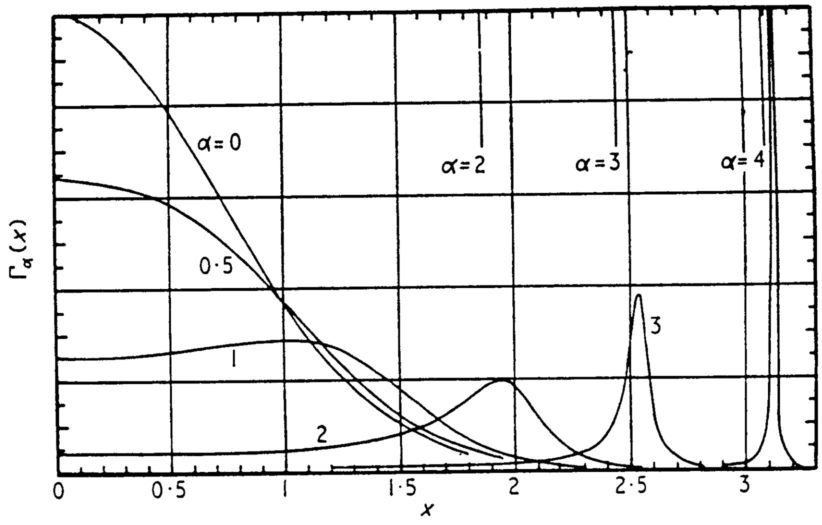

Fig. (2-25)

When $\alpha \ll 1$ ($k^{-1} \ll \lambda_D$), $\Gamma_\alpha(x) \rightarrow e^{-x^2}$ and so reflects the assumed Maxwellian distribution of velocities. As α increases, a resonance in the denominator of $\Gamma_\alpha(x)$, caused by the Complex function $W(x)$, increasingly dominates the exponential numerator.

The assumptions of the Salpeter approximation exclude a resonance in the ion term. The quoted restriction is $\beta < 3.45$ which can be rephrased as a limitation on T_e/T_i:

$$(T_e/T_i)_{max.} < 11.9\ (1 + \alpha^2)/Z\alpha^2.$$

The total scattered light in the electron and ion spectra is obtained by integrating the spectral function over frequency:

$$S_e(k) = {}^1/_1 + \alpha^2 \ \left[\text{Electron feature contribution}\right] \tag{2-3}$$

$$S_i(k) = {}^{z\alpha^4}/(1 + \alpha^2)\ \{1 + \alpha^2(1 + z\ T_e/T_i)\} \left[\text{Ion feature contribution .}\right] \tag{2-4}$$

Note that $S_i(k) \to 0$ as $\alpha \to 0$ as commented on above.

(b) Practical Considerations

(i) Plasma Heating

It is essential that the probe beam does not perturb the plasma. Kunze[59] (1965) gives an expression for the fractional increase in electron temperature neglecting thermal conduction:

$$\frac{\Delta T_e}{T_e} = 5.32.10^{-7}\ \left(\frac{nz}{T_e{}^{3/2}}\right)\ \lambda^3$$

$$\{1 - \ \exp\ (-h\nu/\omega)\}\ I_0\Delta\tau$$

in the following units: n_e - cm^{-3}; T_e - eV; λ - cm; I_o - Wcm^{-2}; $\Delta\tau$ - s; $h\nu$ - eV. This expression gives $\Delta T_e/T_e \sim 0.2$ for the experimental conditions of this experiment. The experimental result to be presented for δ = 1.2 mms in Chapter 3 confirms that the diagnostic was not perturbing the plasma.

(ii) Plasma light

The photomultiplier detection system introduces shot noise. For a Poissonian distribution the noise on N electrons emitted from the photo cathode is $\sqrt{N}$. To see a good Thomson scattered signal above the shot noise generated by the background continium emission of the plasma it is necessary to maximise the total light level and in particular the ratio of the Thomson scattered light to the continium emission.

Shot noise gave the principal contribution to the error bars (~10%) on the scattered spectra of this experiment.

(iii) Stray light ("Parasitic")

Typically, only ~10^{-10} of the incident light energy is Thomson scattered into the solid angle viewed by the detector. Stray light scattered by the apparatus can easily swamp the Thomson scattered signals unless it is discriminated against. Thus, precautions were taken to optically isolate the laser beam path and the viewing path. The exiting ruby laser beam was absorbed in a dyed-glass dump placed far from the scattering region. This was Chance-Pilkington OB10 blue glass orientated at Brewster's angle to the plane-polarised laser beam to minimise reflections. The spectrometer also looked into a blue glass dump. High divergence rays in the input beam which might scatter off the periphery of the input port were removed by the iris I2 shown in

Fig. (2-13).

With a scattering angle of 90^0, these simple precautions gave a stray light level from 5 x to 10 x down on the Thomson scattering in the spectrometer channel centred at the laser wavelength. The stray light is, of course, concentrated at the laser wavelength and was orders of magnitude down on the Thomson scattering in the electron feature due to the spectral contrast of the monochromater.

(iv) Rayleigh Calibration

The ratio of the Thomson to the Rayleigh cross-sections for various gases is accurately known. Thus, by taking scattering measurements from a known pressure of neutral gas (bound electrons) before and after taking scattering measurements on the plasma (free electrons), the sensitivity of the system can be measured and checked for drift. The total Thomson scattered light together with the system sensitivity gives a cross-check on the electron density obtained from the spectral shape of the electron feature.

A number of measurements at increasing gas pressure also provides a convenient check on photomultiplier linearity.

(v) Fitting of Salpeter Curves to Observed Spectra

The plasma parameters (n_e and T_e) were obtained from the measured electron spectrum by finding the best fit theoretical curve. The method used is described by Kunze[59].

The spectral curves $\Gamma_\alpha(x)$ for various α have already been described in this section:

$$\Gamma_\alpha(x) = \frac{\exp(-x^2)}{|1 + \alpha^2 W(x)|^2} \qquad \text{where } x = \Delta\omega/kv_{e \text{ or } i}$$

In application, the curves for various α, could be redrawn vs. the measurement parameter $\Delta\lambda$ instead of the normalised $\Delta\lambda/T_e^{\frac{1}{2}}$ scale. A particular electron temperature, T_{e1} say, and scattering angle θ must be chosen. The spectra for any other electron temperature T_{e2}, but the same α, can now be obtained simply by multiplying the wavelength scale with a factor given by the square root of the temperature ratio - i.e. all points of equal intensity on the curves of equal α, but varying T_e now have a wavelength relationship:

$$T_{e2}/T_{e1} = (\Delta\lambda_2/\Delta\lambda_1)^2$$

Also:

$$\alpha \propto \sqrt{n_e/T_e}$$

Therefore

$$n_{e2}/n_{e1} = (\Delta\lambda_2/\Delta\lambda_1)^2$$

These multiplication relations are transformed to linear displacements when the spectra are plotted vs. $\log_{\text{anything}} \Delta\lambda$. Now spectra of the same α but different n_e and T_e merge into each other simply by a horizontal displacement and only one universal set of theoretical spectra is required. The set of normalised spectra produced by Kegel[60] have been used in this experiment. These spectra were plotted for $\theta = 90^0$, $n_e = n_{cal}$ and $T_e = T_{cal}$. The above multiplication relations transform to:

$$(n_e'/n_{cal}) = (T_e'/T_{cal}) = \text{antilog}_{10}\, 2D$$

where $D = \log_{10} \Delta\lambda' - \log_{10} \Delta\lambda_{cal}$

D was read directly from the overlaid scales of the theoretical and measured spectra.

N.B. These spectra may also be used for any scattering angle θ' by application of the correction.

$$(T_e'/T_{cal}) = (\Delta\lambda'/\Delta\lambda_{cal})^2(\sin 45^\circ/\sin {}^{\theta'}/_2)^2$$

7. THE INTERACTION REGION

Fig. (2-26) shows the initial experimental layout around the plasma. The measurements of the focal dimensions of the two lasers have already been described in sections 2 and 3. Two lenses (nominally 30cms. focal length) imaged the light scattered at 90^0 onto the entrance slit of the spectrometer with a measured magnification of 1.45. The iris(I1) was closed to match the f number of these optics to that of the spectrometer. This was a protection against the stray light described in section 6. The polaroid, orientated to pass the vertically polarised scattered light increases the scattered to plasma light ratio by a factor of 2.

The spectrometer could be used either as a polychromator with an insertable mirror feeding light into eight RCA 7265 photomultipliers (~8ns risetime) or as a monochromator with an RCA C31024A photomultiplier (~1ns risetime). By Rayleigh scattering the ruby laser beam (~0.1 Å width) in CO_2 gas and scanning the spectrometer around 6943 Å an instrumental FWHM of 13 Å was measured. (The FWHM was limited by the input and output slit widths and the dispersion of the diffraction grating). This 13 Å setting was a compromise between light detectability and spectral resolution. The spectrometer was calibrated using a mercury lamp and a helium-neon laser.

The spectrometer entrance aperture was defined both horizontally and vertically. The de-magnified image of this aperture (set typically at : 370μm high x 600μm wide) together with the focal waist of the ruby laser formed a "scattering box" in the plasma. This region is shown in Fig. (2-27) in schematic form.

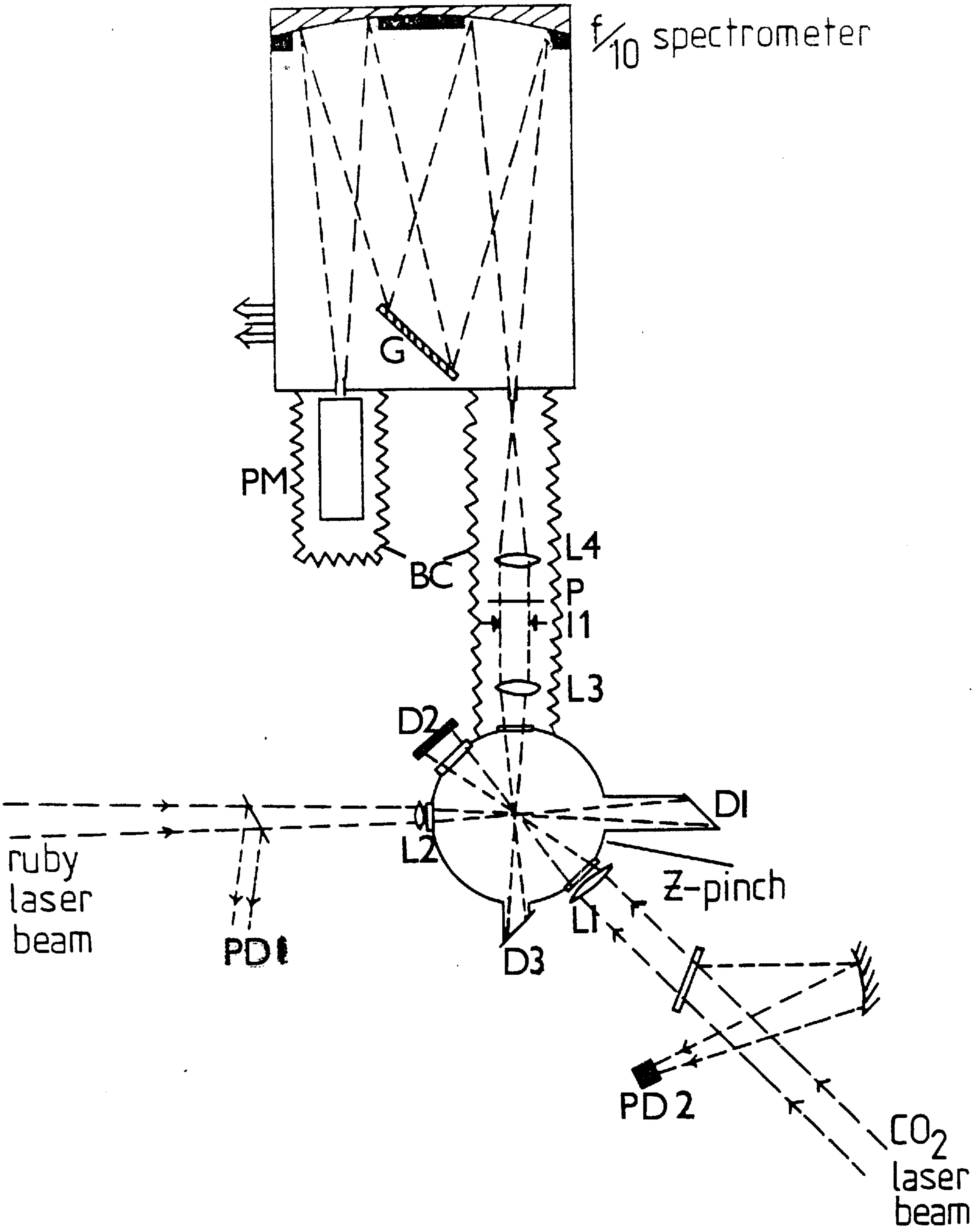

Fig. (2-26) The interaction region. L1....F/3.4 KCl doublet; L2....15cm. focal length quartz lens; L3,L4....30cm. focal length relay optics; P....polariser; I1....aperture; BC....Black Cloth tunnel to exclude stray light; D1,D3....Brewster-angled blue glass light absorbers; D2....CO_2 laser beam dump; PD1....photodiodes; PD2....photon drag detector; G....blazed diffraction grating; PM....RCA C31024A photomultiplier.

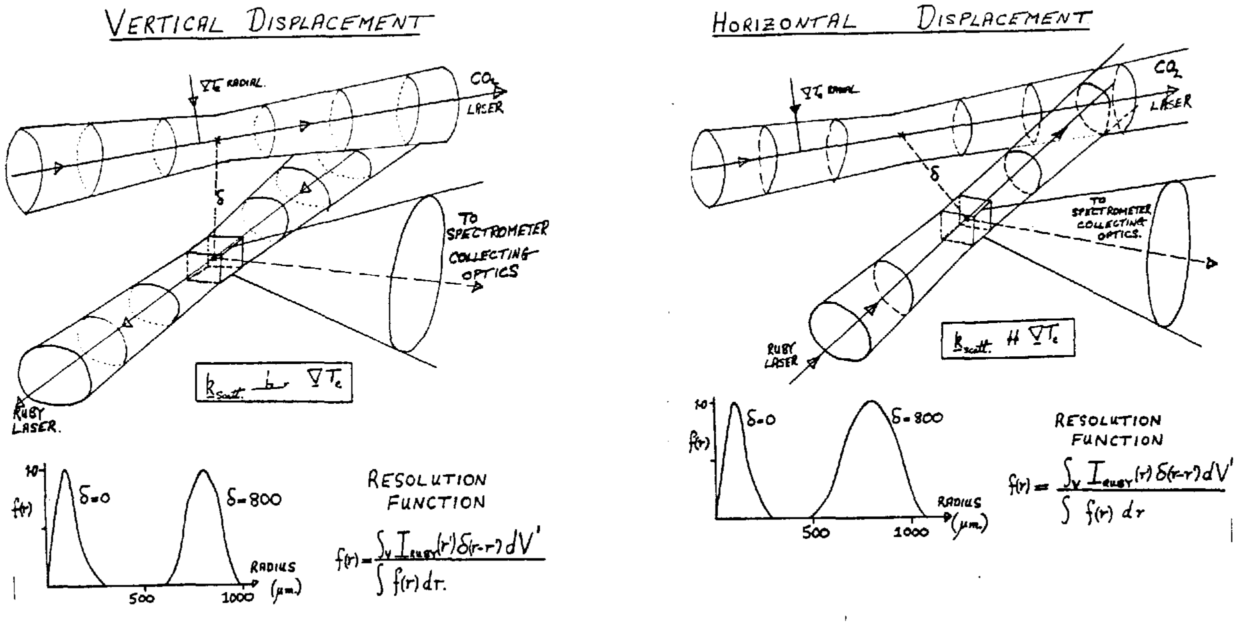

Fig. (2-27) Schematic of the focal regions inside the z-pinch plasma.

Here the homogeneous plasma dimensions and the CO_2 laser absorption length are both >> the length scale for the experiment. These facts together with the f/4 focussing of the CO_2 laser meant that the temperature and density gradients along the CO_2 laser beam were negligible. Thus, there was cylindrical symmetry about the CO_2 laser beam axis and a radial temperature gradient. Fig. (2-27a) shows the initial set-up corresponding to Fig. (2-26). Here, the differential scattering vector $\underline{k}_{scatt}$ (see Fig. (2-24)) is perpendicular to $\nabla \underline{T}_e$ for both horizontal and vertical displacements. Fig. (2-27b) shows a later modification where the direction of the ruby laser was reversed with the ruby laser dump now on the left in Fig. (2-26). Now, with $\underline{k}_{scatt}$ parallel to $\nabla \underline{T}_e$ for horizontal displacements the scattering measurements were sensitive to plasma waves propagating along $\nabla \underline{T}_e$.

In section 3, the radial fall-off of the ruby laser intensity was measured. ($I_{ruby}(r')$ in Fig. (2-18)). Thus we may define resolution functions, f(r), for different displacements, δ, of the focal spots. These resolution functions take account of the fact that the more intense regions in the ruby laser focus contribute more to the observed scattering. The numerical calculations of these resolution functions and their use to spatially weight the computed radial temperature profiles for comparison with the experimental results is described in Chapter 4.

The displacement δ of the focal spots was set by scanning the CO_2 laser focussing lens. With maximum total movements of ~1mm. across a lens aperture of ~10cms. perturbations to the focussing were negligible. Correct relative alignment of all the optics in Fig. (2-26) was a crucial and difficult adjustment. First, the co-incidence of the ruby laser and its alignment helium-neon laser was checked in the focal plane. Then, the spectrometer input optics were adjusted so that the focussed helium-neon laser spot was central (by eye) on the input aperture of the spectrometer. This now defined in space the position of the "scattering box". The CO_2 laser focus was then coarsely aligned using a semi-coincident helium-neon laser. Dispersion in the KCl optics meant that the helium-neon laser was defocussed in the focal plane of the CO_2 laser. The final alignment was set by making burn marks on "thermofax" heat sensitive paper. The side facing the ruby laser was covered with black ink to achieve a burn. Each time a new adjustment to the CO_2 focal spot position was made the new target was positioned inside the vacuum vessel using a micrometer and viewing the helium-neon spot (on the ruby beam) throught the spectrometer entrance aperture. For a given displacement several such back to back burn patterns were taken to establish the setting error in δ which was typically ±100μm.

CHAPTER 3

THE EXPERIMENTAL RESULTS

1. INTRODUCTION

In this chapter the experimental results and their reduction from the raw data is described. Section 2 shows a sample of the raw data and how it was measured. In Section 3, the electron feature spectra (which gave the electron temperatures and densities) are shown for different displacements (δ) from the CO_2 laser axis. The Rayleigh calibration of the scattering system gave a second measurement of the electron density. This is described in Section 4. Section 5 shows the electron temperatures and densities at different times as derived from the electron feature spectra of Section 3. Section 6 discusses the low frequency ion feature part of the laser scattering. This was not spectrally resolved but the total scattered light in the feature at $\delta = 0$ was enhanced above the thermal level indicating low frequency turbulence in the focal spot region. Section 7 shows some electron feature spectra obtained at a plasma density $> 10^{17}$ cm^{-3}. Section 8 describes the backscattering seen at densities $> 10^{17}$ cm^{-3}.

2. SAMPLE RAW DATA

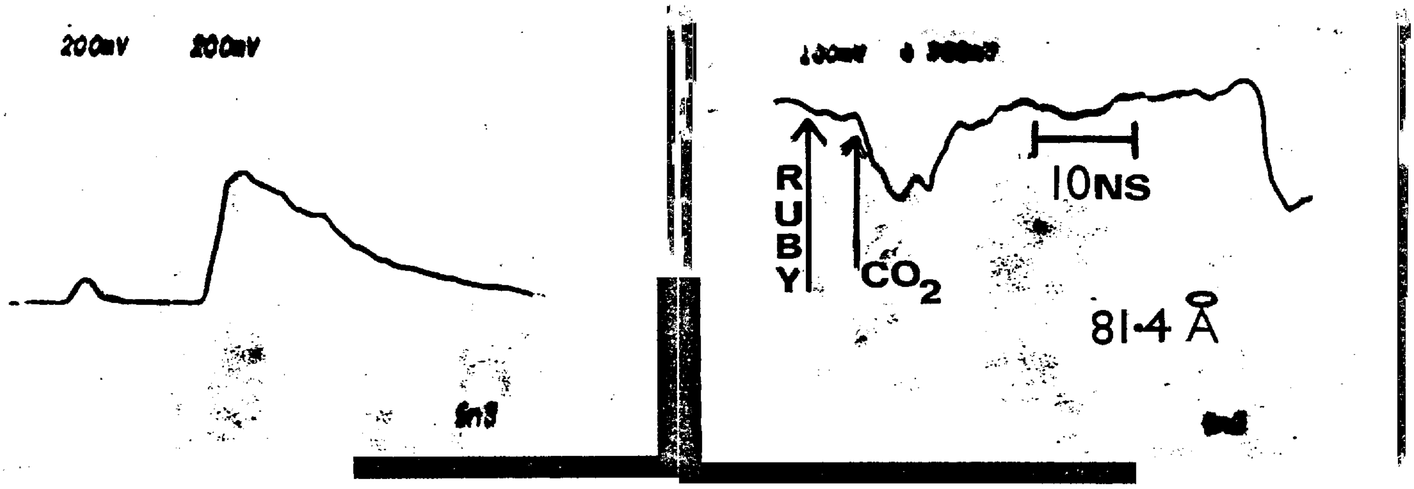

(a) (b)

Fig. (3-1) Oscilloscope traces for a single shot into a plasma with initial conditions of $n_e = 6.10^{16}$ cm^{-3}, T_e = 4eV.

(a) The CO_2 and ruby laser pulses respectively.

(b) The photomultiplier signal with timing marker at the end of the trace.

(Tektronix 7904 oscilloscopes on 5ns/division, adding signals from type 7A19 vertical amplifiers).

Fig. (3-1)(a) shows the CO_2 and ruby laser pulses. The temporal separation of the rising edges of these pulses (which was set using cable delays) was always constant within measurement error (~ 0.5ns) thus confirming the accuracy of the synchronisation technique. The relative timing of the CO_2 and ruby laser pulses at the centre of the z-pinch plasma was 4.5 ± 0.25 ns as shown on Fig. (3-1)(b). This was deduced by measuring the optical and electrical transit times between the detectors and the plasma and the detectors and the oscilloscope respectively.

Fig. (3-1)(b) shows the Thomson scattered light in the spectral interval centred at 81.4 Å to the blue of 6943 Å. The negative going spike at the end of the trace is a delayed timing marker generated by dividing the ruby fast photodiode signal in a matched GHz T-piece and delaying the signal in a cable. When the spectrometer is centred at the ruby laser wavelength (i.e. observing the ion feature or Rayleigh scattering) the photomultiplier signal starts abruptly at the time indicated by the arrow. The result shown was taken at a displacement, $\delta = 0 \pm 100\mu m$ and, at $\Delta\lambda = 81.4$ Å into the electron feature, it is only when the CO_2 laser beam heats the plasma and the electron temperature rises that light begins to be scattered at this wavelength. (At low α, the spectral shape is generated by Doppler shifting of the dipole emission due to the electron velocities. Thus, the appearance and disappearance of scattered light at $\Delta\lambda \sim 80$ Å somewhat illustrates the electron heating and cooling.) The noise on this trace is the photomultiplier "shot noise". The shot noise spike on the cooling edge of the heating again confirms the 1ns time resolution. Note, from Fig. (3-1(a)), that the electrical noise level is negligible.

By normalising the photomultiplier signal to the photodiode signal at selected instants from the start of the ruby pulse, a time history of the Thomson scattering at 81.4 Å is generated. Then, from sets of data taken at other wavelengths time resolved spectra are obtained.

When the CO_2 laser was not fired the constancy of the normalised scattering from the now unperturbed plasma was checked. Temporal variations in the ruby laser focal plane intensity distribution and in the plasma conditions were thus ruled out.

3. THE ELECTRON FEATURE SPECTRA (i) $\delta = 0$

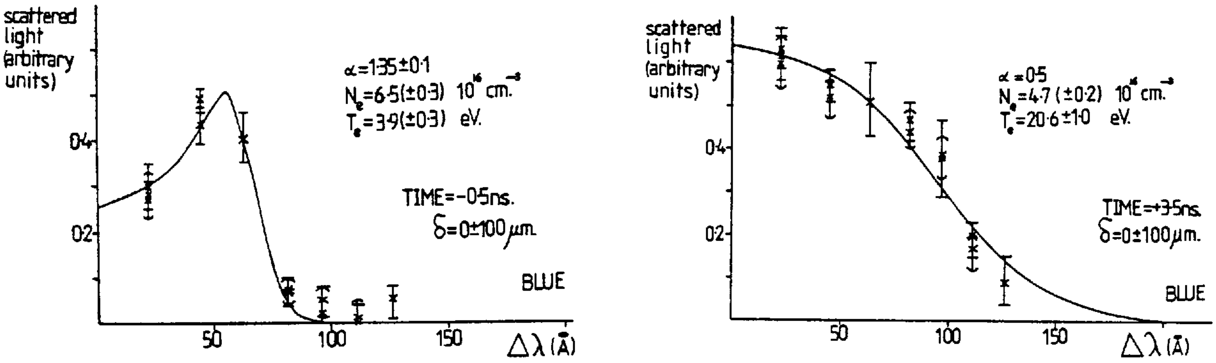

Fig. (3-2) (a) (b)

Fig. (3-2) shows some electron feature spectra obtained by the method just described. The timing shown is relative to the start of the CO_2 laser heating pulse. Thus the spectrum of Fig.(3-2(a)) defines the initial conditions in the plasma and Fig. (3-2(b)) is near the peak temperature. The differential scattering vector was parallel to the induced temperature gradient. The measurement was centred on the CO_2 laser beam axis to the shown accuracy. At zero displacement no assymmetry between the red and blue electron spectra is expected because of the cylindrical symmetry about the CO_2 laser beam axis. Thus, the thermal electron motion towards and away from the spectrometer inside the "scattering box" would be symmetric. Also, the rippling of electrons in the CO_2 laser light ($\omega_R \sim 10^5$ GHz i.e. $\tau_c \sim 10^{-6}$ns) was outside the bandwidth of detection ($\omega_D \sim 1$GHz i.e. $\tau_c \sim 1$ns.). Spectra were taken in the blue as the quantum efficiency of the photomultiplier photocathode increased with frequency.

Note that at many spectral positions the results of several shots have been overlaid and indicate that reproducibility was good.

The solid curves are the best fit Salpeter curves. The good fits obtained at this displacement confirm that here the electron velocity distribution was close to Maxwellian. The fits were obtained by normalising the observed spectra to their peak value, plotting them vs. $\log_{10} \Delta\lambda$ and overlaying the theoretical spectra produced by Kegel[60]. The electron density and temperature were then deduced as described in Chapter 2. The error bars on temperature and density came from the marginal fits when the theoretical spectra ran along the extremities of the error bars on the measured spectra. The upper error bar of the temperature came from the lowest α spectrum marginally fitable. It was found that lower α spectra gave the largest allowable positive displacement D. From Chapter 2:

$$(T_e/T_{cal}) = \text{antilog}_{10}(2D).$$

Similarly, the lower temperature error bar was the highest α marginal fit with the largest negative displacement. The measured parameter of system sensitivity was used to further define α and D as will be described in part 4 of this chapter.

(ii) $\underline{\delta \approx 400\mu\text{m}.}$ (In the horizontal plane).

At this displacement, the scattering box was centred near the edge of the focal spot where large thermal fluxes were expected. With $\underline{k}_{scatt}$ $||$to $\nabla \underline{T}_e$ the assymmetry between the red and blue sides of the electron spectrum was investigated. However, a power supply fault prevented the full E.H.T. being applied to the ruby photodiode to which the Thomson scattered light was normalised. Saturation in the ruby photodiode was indicated by the non-constancy of the normalised scattering from an unperturbed plasma and from CO_2 gas (Rayleigh scattering). The peak signal level was also down by ~ 30% from normal running conditions. Thus the absolute light level was not measured. However, within the assumption that the ruby pulse was reproducible, spectral shapes measured at various times from the start of the ruby pulse were still meaningful. (The RMS variation of the peak ruby intensity was 7% over all the shots of the previous run {δ = o}). Fig. (3-3) shows two spectra obtained at δ = 400μm.

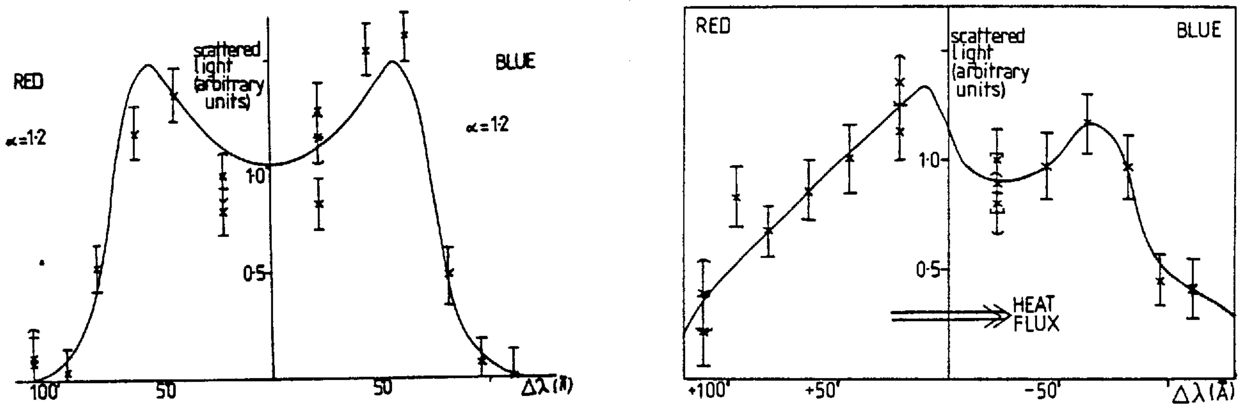

(a) (b)

Fig. (3-3) (a) Electron spectrum 0.5ns. before start of the CO_2 laser pulse at δ = 400μm.

(b) Electron spectrum 3.5ns. after the start of the CO_2 laser pulse.

Note that the shot-to-shot reproducibility was much worse than the δ = o data because of the above normalisation error. The initial conditions defined by Fig. (3-3)(a) had a best symmetric fit of $\alpha = 1.2$ giving $n_e = 6.10^{16}$; T_e = 5eV. At times after the start of the CO_2 laser pulse the observed red and blue spectra did not fit the Salpeter curves and were assymmetric.

Fig. (3-3)(b) shows the spectrum near the time of peak flux.

Although, no theoretical scattering spectra for suitable non-thermal plasmas are obtainable in the literature, when α becomes $\lesssim 0.5$ the electron spectrum reflects the electron velocity distribution. There is no evidence for an electron wing (i.e. any scattering on a scale length $> \lambda_D$) on the red side indicating $\alpha \lesssim 0.5$. With $\underline{k}_{scatt}$ anti-parallel to the temperature gradient, the direction of the heat flux in corresponding electron velocity space is shown. It is thus conceivable that the peak at $\Delta\lambda \sim 10$ Å is the doppler shifted scattering from a return current of cold electrons.

(iii) $\delta \sim 800\mu m$. (In the horizontal plane).

At this displacement, spectra were also taken to the red and blue of 6943 Å. $\underline{k}_{scatt}$ was now parallel to $\nabla \underline{T}_e$ i.e. the CO_2 focal spot was displaced in the horizontal plane to the spectrometer side of the scattering box.

Fig. (3-4) shows the spectra obtained at three different times with respect to the start of the CO_2 laser pulse. The density and temperature conditions change much less dramatically than at $\delta \approx 0\mu m$. At early times, the red and blue symmetry was good (Figs. (3-4)(a) and (b)). Later in time, marginally different α's (and D's) fitted to the red and blue. The density and temperature conditions were then taken as the RMS of the maximum and minimum conditions considering both sides of the spectrum.

(iv) Summary of all other experimental runs.

The above displacements of 0, 400 and 800μm in the horizontal plane illustrate the method used and the most interesting features of the spectra obtained at the lower z-pinch density.

Other experimental runs were performed:

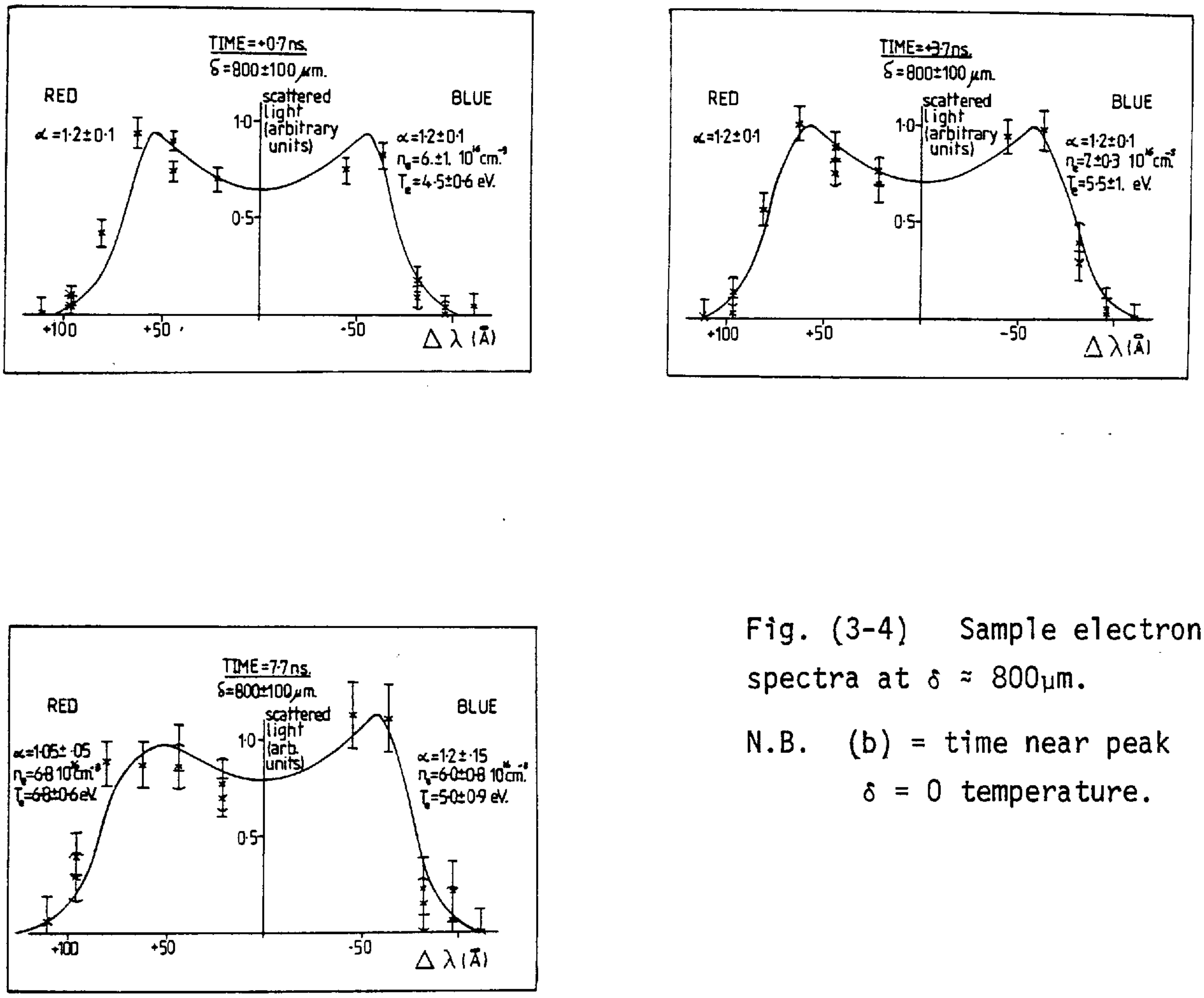

Fig. (3-4) Sample electron spectra at $\delta \approx 800\mu m$.

N.B. (b) = time near peak $\delta = 0$ temperature.

(a) Displacements in the vertical plane. This ensured $\underline{k}_{scatt} \perp_r \nabla \underline{T}_e$

(b) $\underline{k}_{scatt} \| \underline{k}_{CO_2}$. This meant $\underline{k}_{scatt} \perp_r \nabla \underline{T}_e$ for horizontal and vertical displacements. There were early results and the ruby photodiode signal was displayed on the same scope as the photomultiplier signal. Consequently, the shot noise errors were almost double those on later runs and the data was weak i.e. the error bars on the temperature measurements were large.

(c) A long CO_2 laser pulse (1ns. risetime with a 20ns. falltime) was used. It was useful to look at the heating with more absorbed energy on a longer timescale.

(d) A higher initial plasma density (> 10^{17} cm^{-3}) was used. Non-thermal spectra were obtained as described in part 7 of this chapter.

TABLE (3-1) lists all the runs performed:-

Run	Initial Conditions		$k_{scatt.}$	δ (μm.)	FWHM CO_2 laser pulse (ns)	Average peak CO_2 laser intensity (MW)	RMS deviation peak CO_2 intensity (MW)
	n_e ($10^{16}cm^{-3}$)	T_e (eV)					
1	6.3	3.6	$\parallel \nabla T_e$	0±100 (H)	2.5	236	54
2	7.2	4.3	$\parallel \nabla T_e$	800±100 (H)	2.5	270	61
3	7.0	3.9	$\parallel \nabla T_e$	1250±100 (H)	2.5	383	27
4	7.5	4.5	$\parallel \nabla T_e$ $\perp \nabla T_e$	400± 50 (H) 300± 50 (H)	2.5	257	64
5	5.6	3.0	$\perp \nabla T_e$	350± 50 (V)	2.5	409	92
6	3.8	3.8					
7	5.5	5.1		650± 50 (V)			
8	6.8	4.8	$\perp \nabla T_e$	400± 50 (V)	12.5	200	38
9				700± 50. (V)			
10	10.3	5	$\parallel \nabla T_e$	0±100	2.5	275	51
11	15.8	5	$\perp \nabla T_e$	300±100 (V)	2.5	241	54

Table (3-1) In the column giving the focal spot displacement (δ), the H or V refers to a horizontal or vertical displacement respectively. Runs 5, 6, 7, 8, 9 and 11 were taken with the scattering geometry of Fig. (2-27)(a). Subsequently, the direction of the ruby laser was reversed and runs 1, 2, 3, 4 and 10 were taken with the scattering geometry of Fig. (2-27)(b).

4. RAYLEIGH CALIBRATION

As described in Chapter 2, by filling the pinch vacuum vessel with various pressures of clean CO_2 or N_2 gas the scattering system sensitivity may be calibrated. As the laser bandwidth is << the spectrometer bandwidth, Rayleigh scattering was also used to centre the spectrometer on 6943 Å and to check its bandwidth before taking data.

At the end of a run a second Rayleigh calibration was performed. This in general indicated a slight fall in sensitivity due to the discharge dirtying of the windows described in Chapter 2. The spectra were corrected as a linear fall-off in sensitivity/shot. Corrections were also made for the spectral variation of the photomultiplier photocathode response. This was ~ 10% over 100 Å as measured on a standard lamp.

The value of electron density obtained from summing the total scattered light in the electron feature (allowing for spectrometer bandwidth) and using Equ. (2-3) agreed with that obtained from the curve fitting to the spectra shape.

Late in time as the ruby laser intensity decayed the scattered light/shot rise ratio became smaller. Thus the error bars on the spectra increased at these times. The fact that the electron density obtained from curve fitting be consistent with the system sensitivity was used to reduce the error bars on the n_e and T_e results. In other words, certain α, D combinations gave spectra which fitted inside the measured error bars but gave too high or low a value for the electron density as determined by the Rayleigh calibration. These spectra were thus rejected as non-fits. This process was automated by inputing the spectral shapes for different α's as data in a computer program and then numerically integrating for different shifts (D). A listing of this program is given in Appendix B.

5. ELECTRON DENSITY AND TEMPERATURE EVOLUTION

Fig. (3-5) shows the time evolution of T_e and n_e at $\delta = 0 \pm 100\mu m$. The CO_2 laser pulse is also shown on the T_e plot. For all the shots required to obtain the shown temperature evolution, the CO_2 laser pulse had a mean peak intensity of 236 MW on plasma with a RMS deviation of 54 MW.

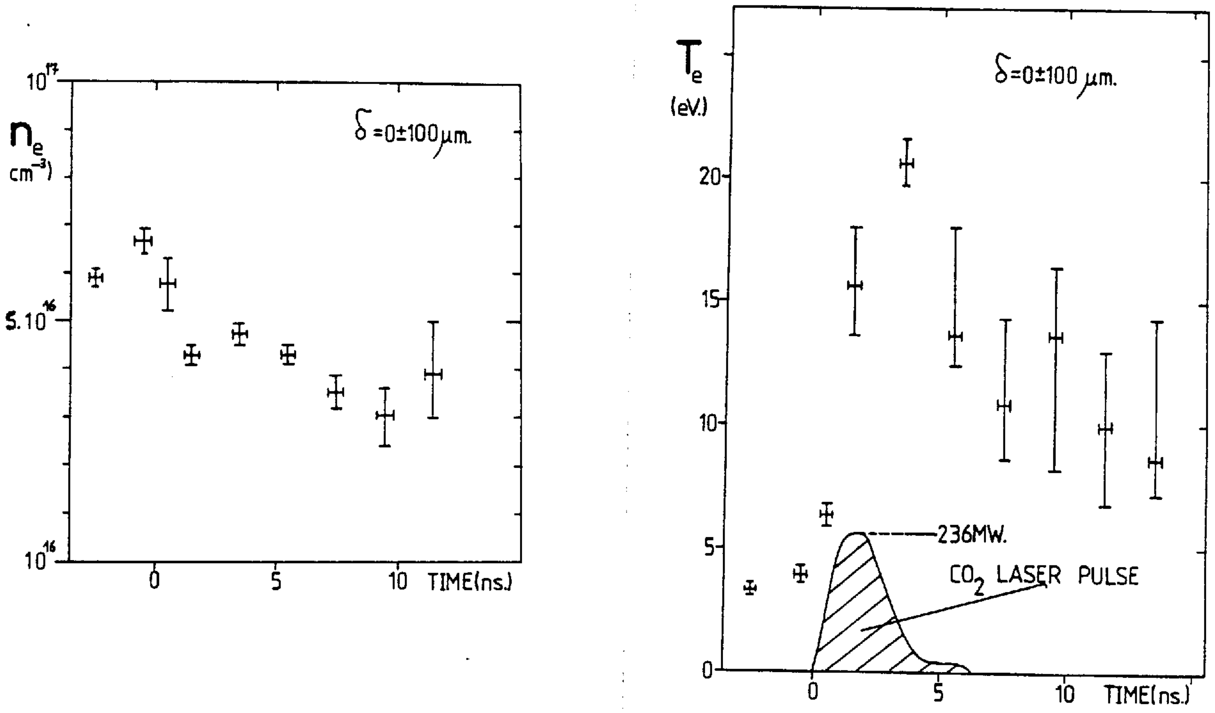

Fig. (3-5)

Looking at the T_e vs. time plot note that the result on the rising edge of the heating (t = 1.5ns.) has a large error bar. This is attributed to the fact that at this time the electron temperature changed significantly within the achieved time resolution. A poor spectral fit was thus obtained. Late in time the error bars increase because of a low scattered light/shot noise ratio. A further point is that lower α spectra give a more sensitive determination of T_e. When $\alpha << 1$ the electron feature reflects the electron velocity distribution and is

Gaussian for a Maxwellian distribution. Its $^1/e$ point depends on T_e:-

$$\Delta\lambda = 27.52 \sin \theta/2 \sqrt{T_e} \ \mathring{A} \qquad (3\text{-}1)$$

where θ = scattering angle and T_e is in eV. In contrast, when $\alpha > 1$ the spectrum exhibits a sharp feature due to co-operative scattering from electron plasma waves. The wavelength shift of the electron wing, in the region $0.6 < \alpha < 2.0$, is:-

$$\Delta\lambda = 2.05 \ 10^{-7} \sqrt{n_e} \ \mathring{A} \qquad (3\text{-}2)$$

with n_e in cm^{-3}. Fitting of the α parameter which is T_e and n_e dependent still of course gives a temperature measurement:

$$\alpha = 1.056 \ 10^{-8} \ (n_e/T_e)^{\frac{1}{2}}$$

with n_e - cm^{-3}; T_e - eV; $\theta = 90^0$, $\lambda_0 = 6943 \ \mathring{A}$

These facts explain why the error bar at peak temperature (t = 3.5ns.) is small. When the computer simulation is fitted to these results in Chapter 5, it will be seen that this point is important in the conduction measurement.

Fig. (3-6) shows the heating at $\delta = 800 \pm 100\mu m$.

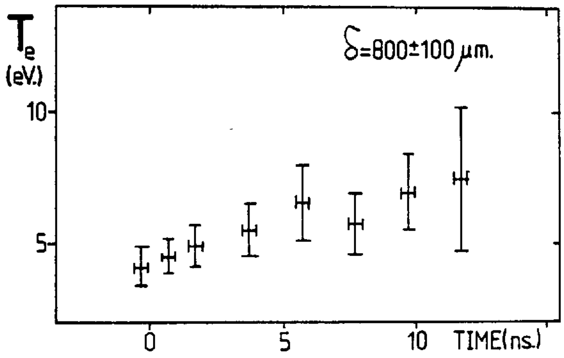

(Fig. (3-6)

The results of the other runs will be shown on comparison with the computer results in Chapter 5.

6. THE ION FEATURES

The spectral shape of the ion feature was not resolved by the 13 Å bandwidth spectrometer. However, by subtracting the stray light and electron feature contributions from the observed scattering with the spectrometer centred on 6943 Å, the total scattered light in the ion feature (S_{io}, say) was obtained. As described in section 4., the total scattered light in the electron feature gave an electron density that agreed with that determined from the spectral shape of the electron feature. The spectral shapes obtained were also consistent with Maxwellian velocity distributions. In other words the electron feature scattering was thermal (at $\delta = 0$ and 800μm.)

Using equations (2-3) and (2-4) it is possible to define a thermal level (S_{ith}, say) for the total scattered light in the ion feature.

$$S_{ith} = (\Sigma_{\text{spectrometer bandwith}} \text{ light in the electron feature}). \frac{S_i(k)}{S_e(k)}$$

where:
$$\frac{S_i(k)}{S_e(k)} = \frac{Z\alpha^4}{1 + \alpha^2\ (1+ZT_e/T_i)}$$

It was found that the observed total scattered light in the ion feature (S_{io}) was enhanced above the thermal level (S_{ith}) at $\delta = 0 \pm 100\mu m$. as shown in Fig. (3-7).

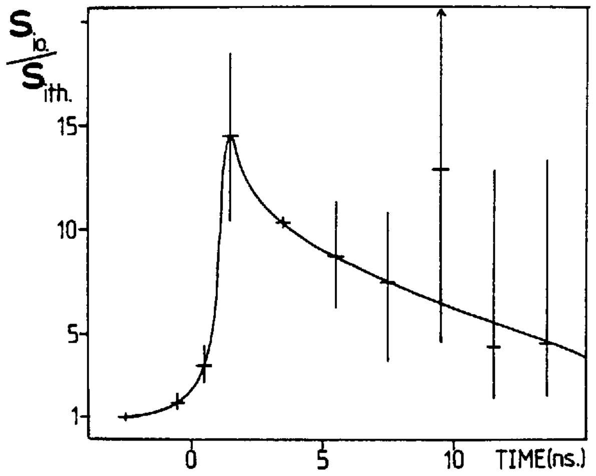

Fig. (3-7) Enhancement above thermal of the total scattered light in the ion feature at $\delta = 0 \pm 100\mu m$.

Time zero is, as before, the incidence of the CO_2 laser pulse on the plasma. This result indicates low frequency turbulence > 10X the thermal level starting on incidence of the CO_2 laser pulse and staying on after it has switched off.

At $\delta = 400\mu m$. the non-thermal electron spectra and the photodiode fault meant that S_{ith} was ill-defined.

Fig. (3-8) shows the turbulence level at $\delta = 800 \pm 100\mu m$.

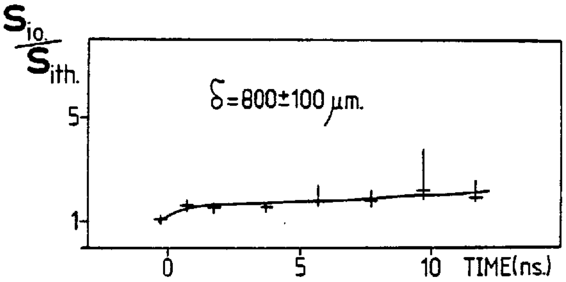

Fig. (3-8) Error bars are taken from the worst case of the red and blue electron feature spectra.

The turbulence is thus highest in the CO_2 laser focal spot region. The interpretation of this as ion-acoustic turbulence driven by the cold electrons returning to the hot region to maintain charge neutrality is discussed in Chapter 7.

7. THE SPECTRA AT HIGHER PINCH DENSITIES

Highly non-thermal spectra were obtained when the initial pinch density was > 10^{17} cm^{-3}. The spectra obtained were also less reproducible than those obtained at the lower pinch density. Fig. (3-9) shows the spectra obtained at $\delta = 0 \pm 100\mu m$. at different times relative to the start of the CO_2 laser pulse with $\underline{k}_{scatt}$ parallel to $\nabla \underline{T}_e$

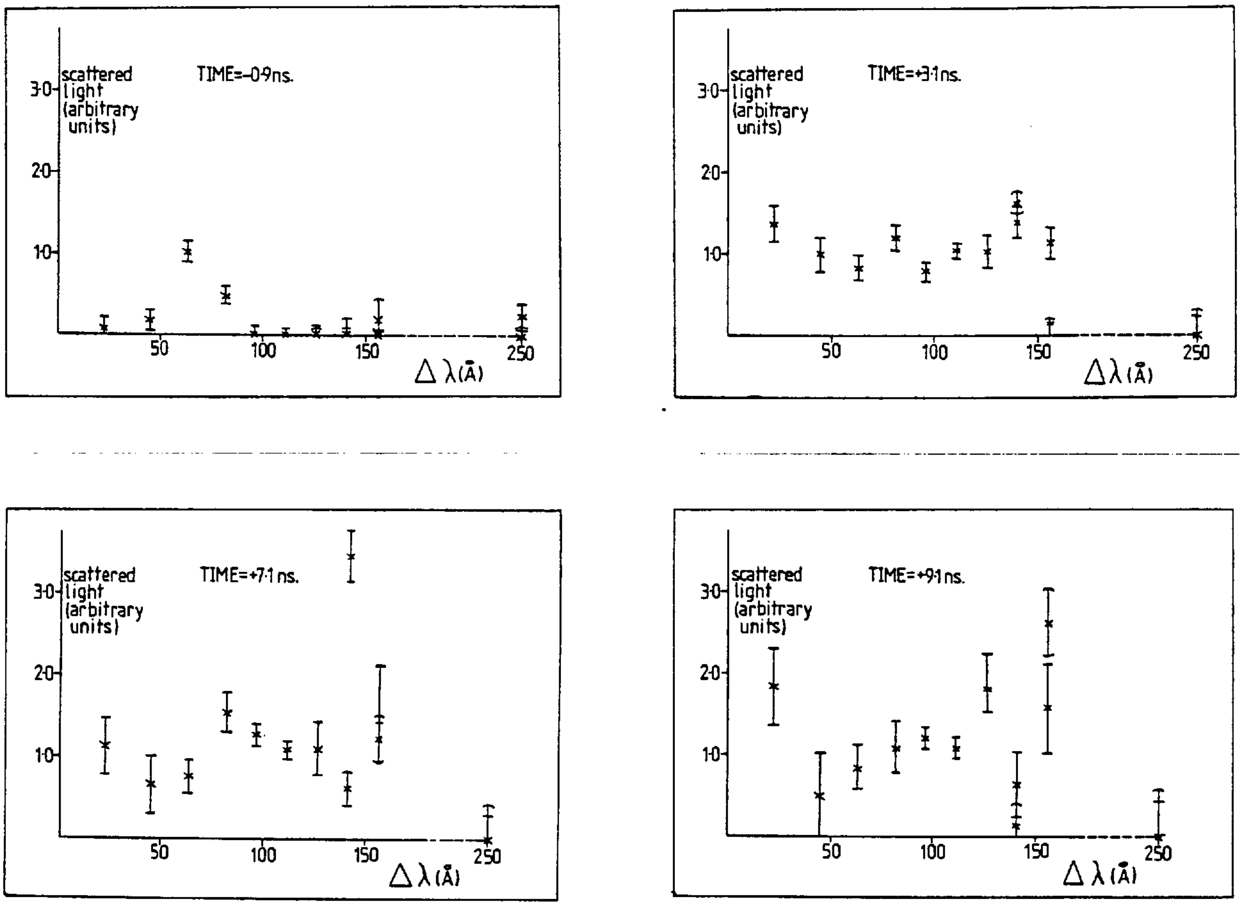

Fig. (3-9) Electron feature spectra (in the blue) at $\delta = 0 \pm 100\mu m$. (Run 10..........Table (3-1)).

Before the start of the CO_2 laser (i.e. TIME = -0.9ns.) there is an electron wing in the spectrum. If $0.6 < \alpha < 2$ we can use equation (3-2) to determine the initial plasma density. For $\Delta\lambda_{wing} = 66$ Å this gave $n_e = 1.03\ 10^{17}\ cm^{-3}$. After the start of the CO_2 laser pulse, the increase in the total scattered light and the peaks in the spectrum are evidence for high frequency turbulence. However, these spectra were not quantitatively interpretable.

Fig. (3-10) shows the spectra obtained at $\delta = 300 \pm 100\mu m$. with $\underline{k}_{scatt}$ perpendicular to $\nabla \underline{T}_e$

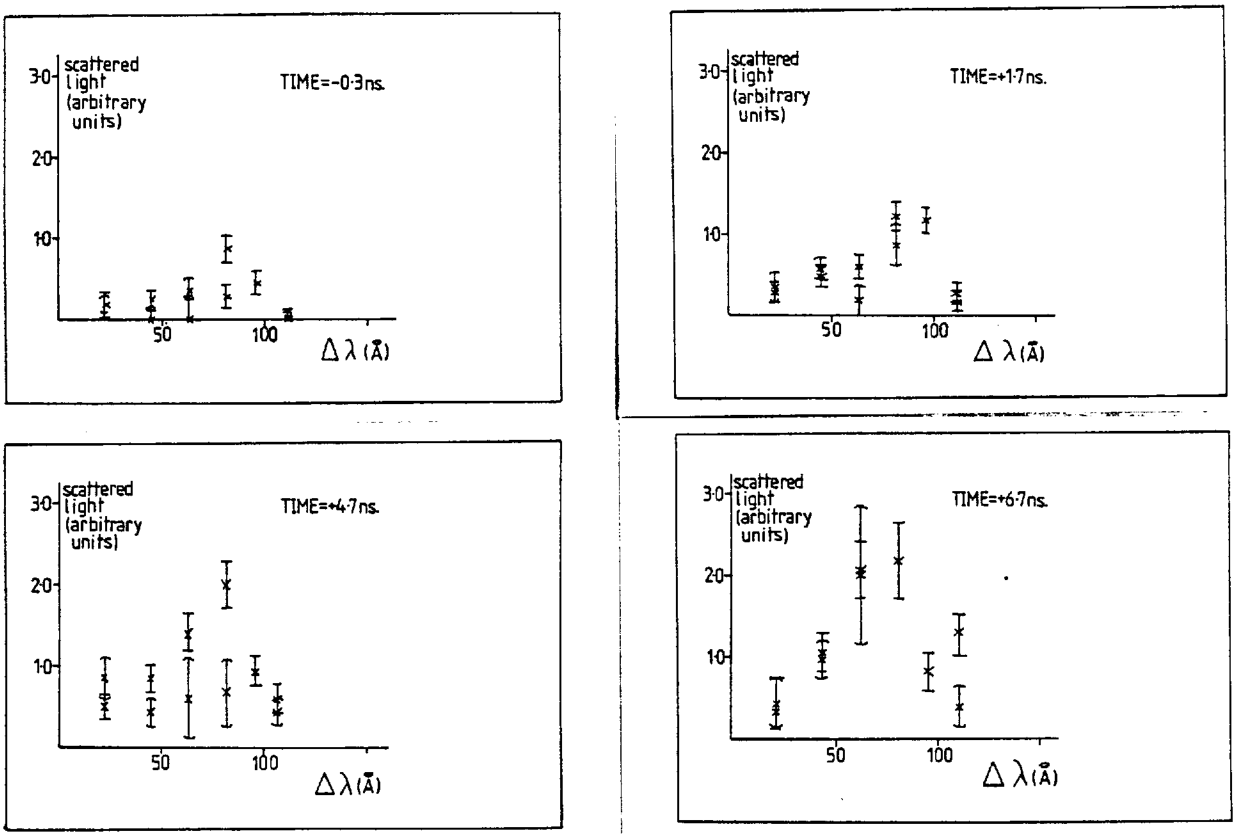

Fig. (3-10) Electron feature spectra (in the blue) at $\delta = 300 \pm 100\mu m$. (Run 11..........Table (3-1)).

The spectrum at TIME = -0,3ns. with $\Delta\lambda_{wing}$ = 81 Å, gave an initial electron density = $1.6\ 10^{17}\ cm^{-3}$. The total scattered light was again enhanced after the start of the CO_2 laser pulse but in this case the peaks were around $\Delta\lambda_{wing}$ rather than at higher frequencies.

The non-thermal nature of these electron spectra prevented the deduction of a thermal level for scattering in the ion feature.

8. BACKSCATTERING

Backscattered light from the plasma was investigated. A schematic of the experimental set-up is shown in Fig. (3-11).

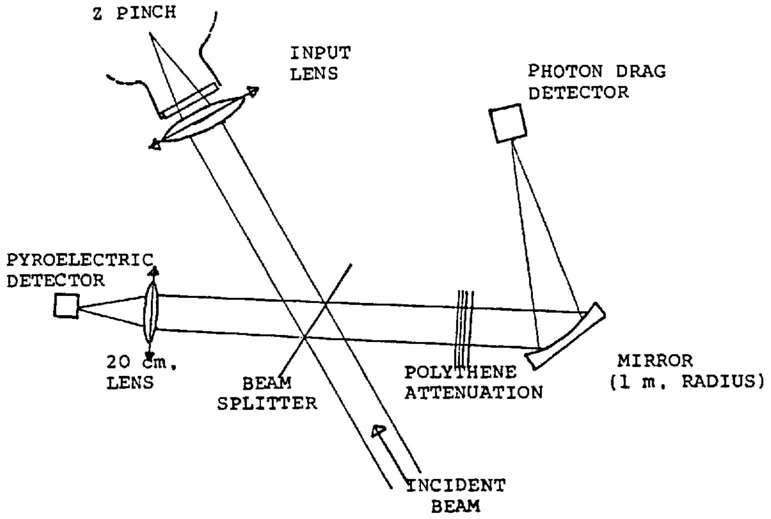

Fig. (3-11) Layout of the detectors in the backscatter experiment.

A 20ns. CO_2 laser pulse of peak intensity 300 MW was used. The incident power monitor was a Rofin 7412 photon drag detector, risetime 1ns. and the backscattering monitor a Molectron P5E pyroelectric detector, risetime 0.6ns. Both pulses were monitored on a Tektronix 7844 oscilloscope giving a time resolution of ~ 1ns. Due to the small sensitive area ($1mm.^2$) of the pyroelectric detector specular reflections from optical components and dielectric reflection from the plasma boundary were discriminated against since they were not imaged onto the detector. In the case of mis-alignment onto a specular reflection the pyroelectric detector signal had the same temporal shape as the incident pulse.

Backscattering was only detectable at pinch densities > 10^{17} cm^{-3} and was typically 300kW for 300 MW incident laser power.

Fig. (3-12) shows one result obtained.

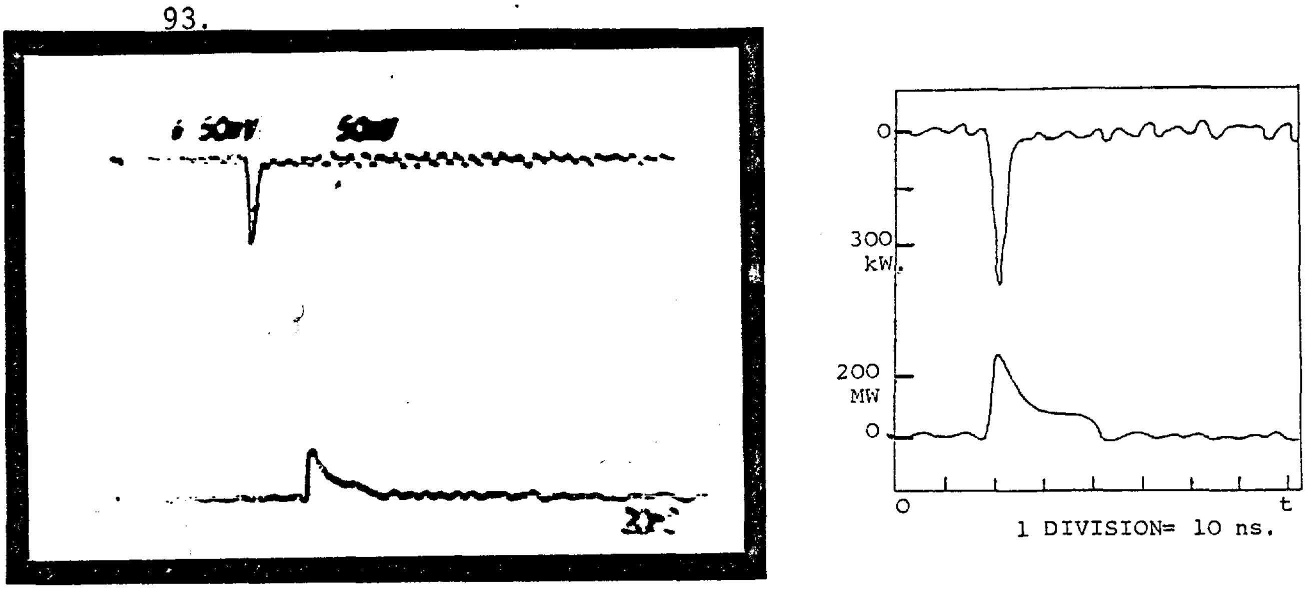

Fig. (3-12) (a) Scope trace of detector signals: Upper trace...... Pyroelectric detector; Lower trace.......Photon Drag detector.

(b) Tracing of scope picture with power calibrations for the detectors.

From timing calibrations, the backscattered light starts at the same time as the CO_2 laser pulse to within 1ns.

The measured temporal shapes of the incident and backscattered signals are convolutions of their optical temporal shapes and the detector response function. We can say however that the growth and decay times of the backscattering are $\leq$ 1ns.

Fig. (3-13) shows a plot of ln (Power backscattered) vs. incident power taken at different times during the pulse indicating an exponential growth from a thermal level, P_N say.

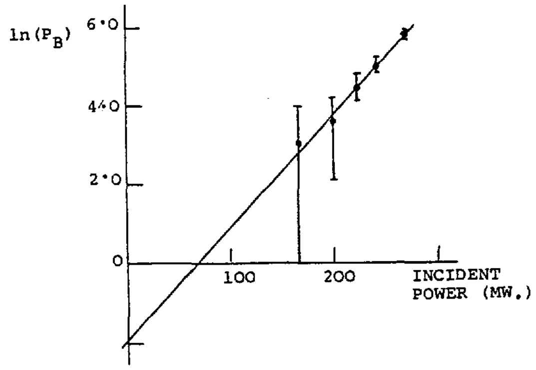

Fig. (3-13)

On three consecutive shots, the experimental value of the exponent at peak intensity was 7.9, 5.2 and 4.8. These results are compared with both a coherent wave theory[61,62] and a random phase theory[62,63] of stimulated Brillouin and Raman scattering in Chapter 7.

CHAPTER 4

COMPUTER MODELLING OF THE EXPERIMENT

1. INTRODUCTION

The one-dimensional two-temperature fluid code used to model the experiment was developed by M.S. White[55]. In this chapter I give a brief description of the code and the modifications that were made to it in the course of this work.

2. THE VALIDITY OF A ONE-DIMENSIONAL MODEL

To a good approximation, the experiment was cylindrically symmetric around the axis of the CO_2 laser beam and axially invariant along it. Thus the use of a one-dimensional model was possible.

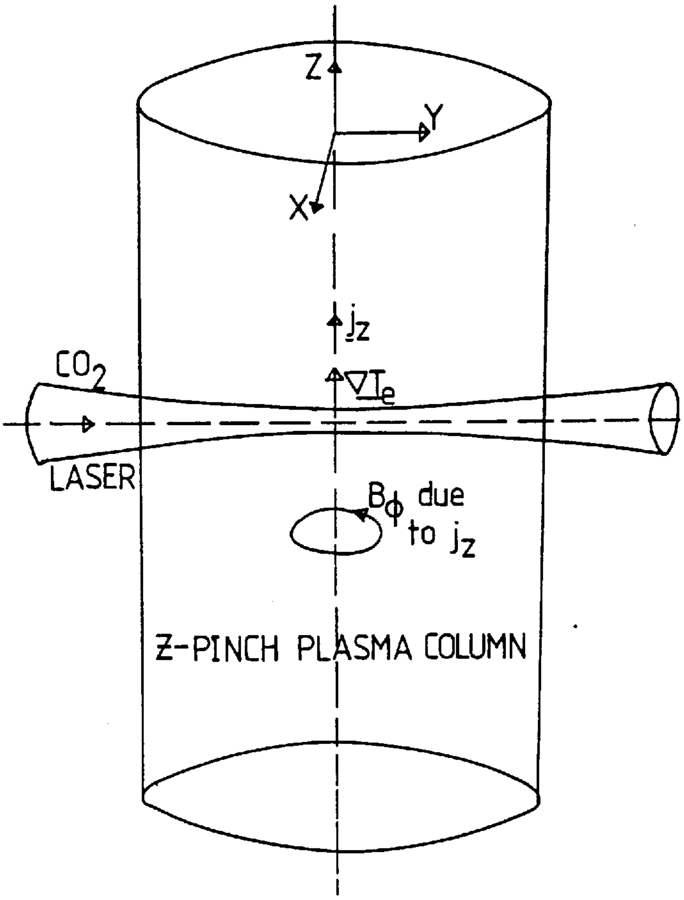

Fig. (4-1) Shows the geometry of the CO_2 laser beam and the Z-pinch plasma column. The cylindrically symmetric/axially invariant approximation was good because:

(i) The effect of the Z-pinch $B\phi$ on the thermal conduction was small.

(ii) The focussing and absorption of the CO_2 laser beam was weak so that radial conduction dominated over axial conduction.

(iii) The plasma dimensions were very much greater than the scale lengths for the experiment.

These assumptions may be justified as follows:

i) Neglect of the pinch magnetic field

a) Effect on thermal conductivity

Magnetic probe measurements[64] indicated that near the pinch axis at the experimental time the field was $B_\phi \sim 0.05$ Tesla. The cross-field thermal conductivity (K) differs from the zero field case (K) by a factor $(1 + \omega_B^2 \tau_c^2)^{-1}$, where ω_B = electron cyclotron frequency = $1.76\ 10^{11}$ B (Tesla) rad/sec and τ_c = electron collision time = $3.42\ 10^5\ T_e^{3/2}\ (n_i\ \ln\Lambda)^{-1}$sec. The calculated reductions in the transport coefficients at $n_i = 6.10^{16}\ cm^{-3}$; B = 0.05T are :- T_e = 20eV - 20%, T_e = 15eV - 12%; T_e = 10eV - 4%; and T_e = 5eV - 0.5%. The region of maximum heat flux was near the edge of the CO_2 laser focal spot ($\delta \sim 400\mu m.$) where temperatures were found to be a maximum of 13eV. Exactly on the pinch axis at $\delta = 0$, $B_\phi \rightarrow 0$ and thus the error involved in neglecting B_ϕ is estimated at ~ 10%.

b) Effect on plasma motion

In Chapter 3, it was seen that the electron density changed little in comparison to the electron temperature. Since all scale lengths in the experiment (typically > 100μm) were >> the debye length (typically ~ 0.1μm.) the plasma remained quasi-neutral and mass motion was restricted to the ion-acoustic velocity (typically $4.10^6\ cms^{-1}$). On the nanosecond experimental timescale thermal conduction was then the dominant mechanism.

Note that the force from the pressure gradient (due to the laser induced temperature gradient) is >> the $\underline{j}_z \wedge \underline{B}_\phi$ force constricting the plasma. Using, $P = nk\ (T_e + T_i)$ and a gradient of 20eV to 4eV over 800μm. at ~ $6.10^{16}\ cm^{-3}$ we have $\underline{\nabla P \sim 2.10^8 Nm^{-3}}$.

The current density ($\underline{j}_z$) was estimated from the measured 30kA total current[55], the 3.5 cm pinch diameter and a factor of two was included to account for axial current peaking[66]. Thus we have

$\underline{j}_z \wedge \underline{B}_\phi \sim 3.10^6\ \mathrm{Nm}^{-3}$, i.e. $<< \nabla\underline{P}$.

ii) Neglect of variations along the CO_2 laser beam

The plasma is about two orders of magnitude underdense for the CO_2 laser light (i.e. $n_e/n_c \sim 0.01$) and absorption is small. The intensity e-folding distance for 10μm. light is ~ 60cms. at $6.10^{16}\ cm^{-3}$; 4eV and ~ 500cms. at $6.10^{16} cm^{-3}$; 20eV. Axial intensity variations due to absorption in the 3cm long plasma were therefore negligible.

Axial temperature gradients due to the f/4 focussing of the heating pulse were investigated in retrospect by varying the spot size in the completed program. Table 4-1 compares axial and radial temperature gradients in computer runs using absorption/conduction conditions which fitted the experimental results.

δ = 0μm.

Time (ns)	2	4	7
Axial	8	1	1
Radial	0	0	0

δ = 400μm.

Time (ns)	2	4	7
Axial	1	2	2
Radial	600	500	125

Table 4-1 Temperature gradients (eV/cm) at radial displacements of 0 and 400μm from the CO_2 laser beam axis.

Note that the dominant conduction was radial near the edge of the focal spot ($\delta \approx 400\mu m$) as expected.

iii) Assumption that the background plasma was constant and homogeneous

Laser scattering measurements on the un-heated Z-pinch plasma[55] showed that the plasma density and temperature conditions were stable for ~1μs. Streak photography indicated that the pinch diameter was ~ 3cm.

The maximum ion sound speed was ~ 50μm ns^{-1} (5.10^4 ms^{-1}) so that on the 10ns experimental timescale density perturbations should be restricted to ~ 500μm. Also, no temperature changes were observed further than 1mm from the CO_2 beam axis. Therefore, on the experimental time and space scales, the background plasma was effectively constant.

We may also neglect local changes in the ohmic heating of the Z-pinch due to the laser induced heating. The 30kA current, driven by a voltage $\lesssim$ 2kV (the large voltage drop at the electrodes has here been neglected) in the 30cm long plasma column of diameter 3cms. gives an over estimate of 2.10^5 Wcm^{-3} for the ohmic heating. In comparison, the laser heating input was ~ 5.10^9 Wcm^{-3} at 6.10^{16} cm^{-3}; 4eV and ~ $6\ 10^8$ Wcm^{-3} at 6.10^{16} cm^{-3}; 20eV. The laser heating thus dominated.

Convective heat transport due to the Z-pinch current was also small. This current, $j_z = n_e\ e\ U_z$. At 6.10^{16} cm^{-3}; 30kA over 3cms, gives an electron drift velocity of U_z ~ 3.2μm ns^{-1} ($3.2\ 10^3$ ms^{-1}). This was << the ion sound speed and also made the plasma effectively stationary over the 10ns experimental timescale.

3. IONIZATION STATE AND THE IMPURITY LEVEL OF THE PLASMA

The computer calculations assume that at the time of the conduction experiment, the plasma is fully ionized and that the effective charge (Z_{eff}) = 1. These assumptions are justified below.

a) Ionization state

In a hydrogen plasma of ~ 6.10^{16} cm^{-3}; 4eV the excited energy levels of principal quantum number (p) $\gtrsim 7$ are in the continuum as the depression of the ionization potential is ~ 0.3eV. (The Inglis-Teller limit for the merging of excited levels by the Stark effect is 10^{17} cm^{-3} for p = 7[65]). The density is low by a factor ~ 6 for complete local thermodynamic equilibrium to exist[55]. In his thesis[55] M.S. White used the modified quasi-steady state populations of McWhirter and Hearn[66] to calculate the densities of unionized hydrogen atoms with electrons in levels p = 1 to 6. For a hydrogen plasma of $n_e = 8.10^{16}$ cm^{-3}; T_e = 5eV, he found that $n_{total}(p = 1 \text{ to } 6)/n_e \sim 9.10^{-5}$ so that atomic particles were negligible and the Z-pinch plasma was fully ionized.

b) Impurity level

The Z_{eff} of the plasma is an important parameter as it enters directly into the thermal conduction equation. An upper limit to Z_{eff} was determined by statically filling the Z-pinch (as opposed to a continuous flow of hydrogen in normal operation) and measuring the pressure rise after firing. For an initial filling pressure of 200 mT hydrogen, the post-firing pressure stabilised at ~ 300mT in about two minutes. This pressure rise is attributed to impurities from the walls (oxygen) and electrodes (copper) of the discharge.

It is likely that most of this pressure rise came from the brass electrodes and there is insufficient time for any copper from the electrodes to reach the centre of the pinch by the time of the experiment.

However, as a worst case, the complete pressure rise was attributed to oxygen contamination. The populations of oxygen atoms in different ionization states have been calculated by using Jordan's results[67] for plasmas in steady state coronal equilibrium. At $T_e = 4eV$, he finds that $O^+/\text{all } O = 25\%$; $O^{2+}/\text{all } O = 74\%$; $O^{3+}/\text{all } O < 0.3\%$. This equilibrium of ionization states is density independent. However, the time to establish this equilibrium is determined by the ionization rates (S) for $O \rightarrow O^+$ and $O^+ \rightarrow O^{2+}$. From Johnson and Hinnov[68], the ionization rate for $H \rightarrow H^+$ at $n_e \sim 10^{16} \rightarrow 10^{17}$ cm^{-3} and $T_e \sim 3eV$ is $S \approx 8.10^{-10}$ cm^{-3} s^{-1}. At an electron density of 6.10^{16} cm^{-3}, this gives an ionization e-folding time of $(Sn_e)^{-1} \approx 20ns$. The ionization rates for non-hydrogenic ions such as oxygen are not explicitly available but one may expect the rates for $O \rightarrow O^+$ and $H \rightarrow H^+$ to be comparable. (The ionization energy for $H \rightarrow H^+$ is 13.595 eV and for $O \rightarrow O^+$ is 13.614 eV).

The ionization rates for different hydrogenic levels scale as[69]:-

$S \propto \exp\{(z^2E_H/n'^2 - E_\infty)/kT_e\}$ where E_∞ = the ionization energy of the level; z = effective charge; n' = principal quantum number of the level where radiative decay is about as likely as collisional excitation. Since for oxygen $n' \gg 2$, we can estimate that the rate for $O^+ \rightarrow O^{2+}$ is $\sim \exp(-E_\infty{}^{2+}/kT)/\exp(-E_\infty{}^{+}/kT)$ X the rate for $O \rightarrow O^+$ (i.e. rate for $H \rightarrow H^+$). With $E_\infty{}^{2+} = 35.1$ eV and $E_\infty{}^{+} = 13.6$ eV this gives an estimated e-folding time of 4 μs for $O^+ \rightarrow O^{2+}$, at a temperature of 4 eV and a density of 6.10^{16} cm^{-3}.

From the bremmstrahlung continuum emission observed on a photomultiplier of the laser scattering system, an appreciable electron density exists in the pinch for ~ 1.5μs before the experimental time.

Thus we may expect that ~ 30% of the O^+ present will be ionized to

O^{2+} at the experimental time. The pressure rise after firing the statically filled pinch gave an upper limit of 50% to the oxygen contamination. The upper limit to the Z_{eff} was therefore 1.10 from the above calculations. Note that with a photon energy of $h\nu \sim 0.12eV$ at 10μm, photo-ionization was unimportant.

It is also necessary to consider what happens to Z_{eff} when the CO_2 laser heats the plasma to 20eV and how any increase in Z_{eff} affects the thermal conduction. Using Jordan's[67] results again we find that given sufficient time to ionize, the distribution of ionization states at 20eV will be:- O^{3+}/all O = 3%; O^{4+}/all O = 42%; O^{5+}/all O = 48%; O^{6+}/all O = 4%. As before we may deduce the ionization rates from Johnston and Hinnov[68]. At $n_e = 10^{16} \rightarrow 10^{17}$ cm^{-3} and $T_e = 20eV$ the ionization e-folding time for H to H^+ is ≈ 0.4 ns and hence for O^+ to O^{2+} is ≈ 1.2 ns; for O^{2+} to O^{3+} ≈ 3.2 ns and O^{3+} to O^{4+} is ≈ 9.9 ns. Looking at the time history of the heating and cooling shown in Fig. 3-5 it is seen that the temperature rises to 20eV in ~ 3 ns and falls to <10eV in a further 5 ns. Thus a reasonable estimate for the ionization state at peak temperature is 25% of the oxygen present in O^{3+} and 75% in O^{2+}. This gives $Z_{eff} = 1.4$.

Spitzer and Harm[5] included the variation of Z_{eff} in their calculation of the thermal conductivity. The plasma thermal conductivity coefficient (K_L)differs from that of a Lorentz gas (K_n) as : $K = \delta_T \varepsilon K_L$. The values for δ_T and ε for Z = 1, 2, 4, 16 and ∞ are given in table III of Spitzer and Härm's paper. The conductivity varies with Z as $\delta_T \varepsilon/Z$. Table 4-2 shows $\delta_T \varepsilon/Z_{eff}$ vs. Z_{eff}.

Z_{eff}	1	2	4	16
$\delta_T \varepsilon/Z_{eff}$	0.094	0.073	0.051	0.002

Table 4-2

Thus a $Z_{eff} < 2$ has a minor effect on the classical thermal conductivity.

An experimental measurement of Z_{eff} is also given by the total scattered light in the ion feature. D.E. Evans has made numerical calculations of the scattering from multi-component plasmas[70] which showed that

(a) the effect of varying the concentration of an O^{n+} ion was equivalent to varying Z_{eff}.

(b) use of $Z = Z_{eff}$ in the formula for the total scattered light in the ion feature (equation 2-4 in this thesis) is an underestimate of the scattering.

Looking back to the ion feature measurements shown in figures (3-7) and (3-8), one sees that the enhancement, before incidence of the CO_2 laser pulse is very small. Putting the upper and lower error bar values into equation (2-4) and taking Z_{eff} as a variable to explain the small enhancement one gets $Z_{eff} = 1.18 \begin{smallmatrix} +0.18 \\ -0.05 \end{smallmatrix}$ as an overestimate.

One may also use Evans' results to show that the observed enhancement of the ion feature cannot be due to an increase in Z_{eff} due to the heating. From Fig. 2 of his paper it is seen that for $T_e/T_i = 5$, the total scattered light in the ion feature increases by less than 8% as Z_{eff} increases from 1.01 (0.2% O^{8+}) to 1.70 (10% O^{8+}).

4. CHARACTERISTIC TIMESCALES

It is useful to compare the characteristic timescales of the important mechanisms of the experiment through some simplistic calculations i.e. uncoupling all the equations and considering the given process in isolation.

a) Thermal Conduction

If we combine the empirical law : $\underline{q} = -K\nabla \underline{T}$ with the conservation (continuity) of energy: $\partial U/\partial t + \nabla.q = 0$
we get the one dimensional heat diffusion equation:

$$^{3}/_{2}\, n_e\, \partial T_e/\partial t = -K_e\, \partial^2 T_e/\partial x^2 \qquad (4\text{-}0)$$

Spitzer[3] gives the coefficient as

$$K_e = 4.67\ 10^{-12}\ T_e^{5/2}\ \ /\ Z\ \ln\Lambda\ \ \text{cal s}^{-1}\ \text{deg}^{-1}\ \text{cm}^{-1}$$

which converts to $K_e = 2.05\ 10^{22}\ T_e^{5/2}\ /\ Z\ \ln\Lambda\ \text{cm}^{-1}\ \text{s}^{-1}$ with T_e in eV.

Writing the heat diffusion equation with characteristic parameters ($T_e = T\theta$, $t = \tau_{TC}\ \alpha$, $x = L\ \phi$ where $\theta \sim \alpha \sim \phi \sim 1$) we have:-
$\tau_{TC} = {}^{3}/_{2}\ n_e\ Z\ \ln\Lambda\ L^2/(2.05\ 10^{22}\ T^{\ 5/2})$ s

Taking 20eV to 4eV over 800μm at 6.10^{16} cm^{-3} we get $L = |T_e/\nabla T_e|$ $\sim$ 0.06 cm and with a mean $T_e \sim$ 12eV and $Z \sim 1$ this gives

$\underline{\tau_{TC} \sim 0.25\ \text{ns}.}$

b) Convective Motion

The laser generated temperature gradient leads to a pressure gradient in the plasma. The simple scalar pressure may be written: $P = n_e k_B T_e + n_i k_B T_i$. We define a scale length for the pressure gradient as $L_P = |P/\nabla P|$. Using again T_e = 20eV to 4eV over 800μm at $n_e = n_i =$

6.10^{16} cm^{-3} and assuming no equilibration we get $L_P = 0.12$ cms.

We take for the ion sound speed $v_s = 9.79\ 10^5\ \sqrt{T_e}$ cms^{-1} and define the characteristic time for mass motion of the plasma as : $\tau_m = L_P/v_s$. Thus $\tau_m \sim$ 35 ns at 12eV and ~ 27 ns at 20eV.

c) Equilibration

From the NRL plasma formulary the equilibration time between electrons and ions is:-

$$\begin{aligned}\tau_{eq} &= 5.55\ 10^{18}\ m_e(T_e)^{3/2}\ /\ (\sqrt{m_i}\ n_i\ \ln\Lambda)\ s\\ &= 7.32\ 10^{-10}\ (T_e)^{3/2}\ s \quad \text{at } 6.10^{16}\ cm^{-3}\\ &\sim 6\ ns \quad \text{at} \quad 4eV \quad \text{(initial conditions)}\\ &\sim 65\ ns \quad \text{at} \quad 20eV \quad \text{(hottest conditions)}.\end{aligned}$$

d) Laser Heating

The characteristic time (τ_H) here is the CO_2 laser pulse width (~3 ns). However, since the plasma absorption coefficient scales as $T_e^{-3/2}$, the laser pulse risetime (~1 ns) is also important.

e) Conclusion

The above timescales are estimates since the governing equations are in fact coupled. We can see however, that $\tau_{TC} \ll \tau_m$ and that thermal conduction dominates over convection. In summary:-

$$\tau_{TC} < \tau_H \ll \tau_{eq} \sim \tau_m.$$

5. THE APPLICABILITY OF THE FLUID EQUATIONS

A fundamental question which arises is the accuracy of a fluid description in this case. Let L and τ be a distance and a time over which macroscopic plasma parameters (such as n_e, T_e, v_e; if definable) change appreciably. The most stringent requirements for the applicability of a fluid model then are:-[71]

(i) $\tau >> \tau_c$ - where τ_c is the time for the distribution of particle velocities to become randomised to a Maxwellian.

(ii) $L >> \lambda_e$ - where λ_e is the electron mean free path. i.e. the fluid parameters (n_e, T_e, v_e) should not change appreciably in the volume-time element over which they are defined.

Using the results of Chapter 3 we find that $(\tau_{ei})_{max}$ ~ 87ps while $(\tau)_{min}$ ~ 1ns. However, the smallest length scale around is $L = |T_e/\nabla T_e|$, giving $(\lambda_e/L)_{max.}$ ~ 0.22 (using 20eV to 4eV over 800μm. at 6.10^{16} cm^{-3}) and anticipating later computer results reaches ~ 0.5 in localised regions. Condition (ii) is therefore marginal.

We can see however, that this does not exclude the use of a fluid model by looking at the equations in detail.

The macroscopic fluid equations used are the continuity, momentum and energy equations. These are derived by taking the first, second and third moments of the Boltzmann equation for the distribution function $f_k(t,\underline{r},\underline{w})$:-

$$\partial f_k/\partial t + \underline{w}.\ \nabla_r f_k + {}^{q_k}/_{m_k}\ (\underline{E} + \frac{\underline{w} \wedge \underline{B}}{c}).\ \nabla_w f_k = \left.\frac{\partial f_k}{\partial f}\right|_{\text{collisions}} \qquad (4\text{-}1)$$

where $\underline{w}$ is the microscopic velocity, and q_k and m_k are the k species charge and mass. Equation (4-1) is microscopic and independent of the fluid conditions (i) and (ii).

(4-1) x $\int m_k \, d\underline{w}$ gives conservation of mass:-

$$\partial/\partial t \; \rho_k + \underline{\nabla} \cdot \; (\rho \underline{v}_k) = 0 \tag{4.2}$$

(4-1) x $\int m_k \, w_k \, d\underline{w}$ gives the momentum equation:-

$$\begin{aligned} &\partial/\partial t \; (\rho_k \underline{v}_k) + \underline{\nabla} \cdot \; (\rho_k \underline{v}_k \underline{v}_k + \underline{\underline{P}}_k) \\ &- n_k q_k \; (\underline{E} + \underline{v}_k \wedge \underline{B}/c) = \Sigma_i \underline{D}_{ki} \end{aligned} \tag{4.3}$$

where $\underline{\underline{P}}_k$ = the stress tensor = $\int m_k \, (\underline{w} - \underline{v}_k)(\underline{w} - \underline{v}_k) \, f_k d\underline{w}$ and $\underline{\underline{D}}_{ki}$ = the momentum exchange from species i to species k.

(4-1) x $\int m_k \, \underline{w}_k \, \underline{w}_k \, d\underline{w}$ gives the energy equation:-

$$\begin{aligned} &\partial/\partial t \; (\tfrac{1}{2}\rho_k \, v_k^2 + U_k) + \underline{\nabla} \cdot \; (\tfrac{1}{2}\rho_k \, v_k^2 \, \underline{v}_k + U_k \, \underline{v}_k + \\ &\underline{\underline{P}}_k \cdot \underline{v}_k + \underline{q}_k) - n_k q_k \, \underline{E} \cdot \underline{v}_k \\ &= \Sigma_i \, \xi_{ki} + E_{laser} \end{aligned} \tag{4.4}$$

where U_k = the internal energy = $\int \tfrac{1}{2} m_k \, (\underline{w} - \underline{v}_k)^2 \, f_k \, d\underline{w}$
$= {}^{3}/{}_{2} \, n_k \, k_B \, T_k$
and q_k = the heat flux = $\int \tfrac{1}{2} m_k \, (\underline{w} - \underline{v}_k)^2 (\underline{w} - \underline{v}_k) \; f_k \, d\underline{w}$

ξ_{ki} = energy exchange from species i to species k. E_{laser} = source term due to inverse bremsstrahlung absorption.

These equations were simplified as follows:-

(a) For the electron species equation (4-4) reduces directly to the internal energy equation since $U_e \gg \tfrac{1}{2}\rho_e \, v^2$. The maximum fluid velocity is the ion sound speed maximum i.e. 5.10^4 ms^{-1}.

Therefore $U_e/\frac{1}{2}m_e\, n_e\, v^2_{max} = 3kT_e/m_e\, v^2 \sim 10^3$ at 4eV. We also have $\frac{1}{2}\rho_e\, v^2\underline{v} << U_e\, \underline{v}$ in the divergence term.

For the ions, however, $\frac{1}{2}\rho_i\, v^2 \sim U_i$ due to the larger ion mass. We eliminate the kinetic energy of motion by taking equation (4-4) and adding to it $\frac{1}{2}v_k^2$ times equation (4-2) and subtracting $\underline{v}_k$ times equation (4-3). Hence:-

$$\partial U_k/\partial t + \nabla . \quad (U_k\, \underline{v}_k + \underline{q}_k) \quad + \quad (\underline{\underline{P}}_k . \nabla) . \, \underline{v}_k$$

$$= \Sigma_k\, (\xi_{ki} - \underline{D}_{ki} . \underline{v}_k) \tag{4.5}$$

using $\nabla . (\underline{\underline{P}}_k . \underline{v}_k) = \underline{v}_k\ \nabla . (\underline{\underline{P}}_k) \quad + \quad (\underline{\underline{P}}_k . \text{grad}) . \, \underline{v}_k$

On the timescale of this experiment, equilibration is small and the ion temperature remains almost homogeneous/isotropic and so $\nabla . (\underline{\underline{P}}_i) \sim 0$. Thus the $(\underline{\underline{P}}_k \, . \, v_k)$ form may be retained inside the divergence bracket.

In the previous experiment of M.S. White et al., $\nabla . \underline{P}_i \nsim 0$ as equilibration was important. However, from computer results I estimate that $\left\{ v_k\ \nabla .\ \underline{P}_k \ / \ (\underline{P}_k . \text{grad})\ v_k \right\}_{\text{maximum}}$ was $\lesssim 10\%$ due to the small temperature gradient involved. However, in the presently proposed laminar flow experiment (see Chapter 7) the above manipulation may become severely inexact.

(b) From the cyclindrical symmetry:

$$\partial/\partial z \ = \ \partial/\partial\phi = 0, \quad \text{so } \nabla \equiv (\partial/\partial r,\ 0,\ 0)$$
$$v\phi \ = \ v_z = 0, \quad \text{so } \underline{v} \equiv (v_r,\ 0,\ 0) = (v,\ 0,\ 0).$$

Deb

(c) Because the debye length << any scale lengths we have quasi-neutrality - i.e. $n_e = n_i = n$ and $v_e = v_i = v$. Thus we may reduce the two fluid equations to a one-fluid, two-temperature model - i.e. one continuity equation, one momentum equation and two energy equations.

(d) From condition (b), the pressure tensor is scalar

$$\underline{\underline{P}}_k \rightarrow P_k = nk_B T_k, \quad \nabla . \underline{\underline{P}}_k \rightarrow \nabla P_k$$

(e) The Lorentz force terms involving the self-consistent electric and magnetic fields may be neglected. From Ohm's Law:- $\underline{j} = {}^{1}/_{\eta} \; (\underline{E} + \underline{v} \wedge \underline{B})$ We use Spitzer's[3] resistivity (with T_e in eV):-

$$\eta = 6.53 \; 10^3 \; \ln \Lambda \; / \; (1.16 \; 10^4 \; T_e)^{3/2} \quad \Omega\text{-cm}$$

Then taking 30X2 kA over a 2.5 cm diameter pinch we get:-

$|\underline{E} + \underline{v} \wedge \underline{B}| = 2852 \text{ Vm}^{-1}$, giving a Lorentz force ~ 2.7 10^7 Nm^{-3}.

In the momentum (4-3) and energy (4-4) equations we compare the Lorentz terms with $\nabla . \underline{\underline{P}}_k$ which equals ∇P_k in our case. Taking as before 20eV to 4eV over 800µm at $6.10^{16} \text{ cm}^{-3}$ we have $\nabla P \sim 2.10^8 \text{ Nm}^{-3}$.

(f) The thermal conductivity ∝(species mass)$^{-\frac{1}{2}}$ so that $q_i/q_e = 2.3 \; 10^{-2}$ for the same temperature gradient. However, to neglect q_i in equation (4-4) we need:-

$$q_i << U_i \underline{v}_i + \underline{\underline{P}}_k . \underline{v}_i$$

i.e. $q_i << {}^{5}/_{3} \; nkT_i \; (kT_e/m_i)^{\frac{1}{2}}$

i.e. the "ion free streaming limit".

The thermal conductivity $\propto(\nu_{ei})^{-1}$. ν_{ei} is enhanced by ion acoustic turbulence (see Chapter 3 and 7) and the above inequality satisfied.

Equations (4-2,-3,-4) may therefore be written:-

$$\partial n/\partial t = - \nabla . (n\underline{v}) \qquad (4.6)$$

$$\partial g/\partial t = - \nabla . (g\underline{v}) - \nabla (P_e + P_i) \qquad (4\text{-}7)$$

$$\partial U_e/\partial t = - {}^{5}/_{3} \; \nabla . (U_e \underline{v}) - \nabla . \underline{q}_e + E_{laser} - \xi \qquad (4\text{-}8)$$

$$\partial U_i/\partial t \; = \; - \; 5/3 \; \nabla.(U_i\underline{v}) + \xi \qquad (4\text{-}9)$$

$$\xi = U_e - U_i/\tau_{eq} \qquad \underline{g} \; = \; n(m_e + m_i)\,\underline{v}$$

The important feature of the experiment governing the accuracy of these equations is that thermal conduction dominated over convective motion. This is shown by the experimental results where the electron density changed slowly compared with the electron temperature (Fig. 3-5) and by the timescale calculations of the last section. In effect, if we had had a very short laser pulse so that $\tau_H << \tau_{TC}$, the experiment would have been impulse heating followed by thermal diffusion from the focal spot region. The electron energy equation (4-8) is the dominant one.

As explained in Chapter 1, the heat flux, q_e, is not well defined when $\lambda_e/L \gtrsim 0.02$ which is when theoretical derivations of the thermal conductivity are invalid. Thus q_e was artificially modified in the program either using the empirical law $q_e = -K_e\nabla T_e$ and reducing K_e, or putting an upper limit on q_e at some fraction of the free streaming limit. The latter modification simulated turbulence limited heat flow since the heat flux was only restricted in regions of large temperature gradient.

It is also important to note from Chapter 3 that theoretical scattering spectra based on Maxwellian velocity distributions closely fitted the experimental data at all positions except near the edge of the focal spot. Thus the macroscopic parameters of velocity and temperature were definable over most regions. Equations (4-6) and (4-7) are therefore expected to reasonably approximate the small rarefaction occuring.

6. CODING OF THE FLUID EQUATIONS

The equations (4-6 to 4-9) were solved on an Eulerian spatial mesh cylindrically symmetric about the CO_2 laser beam axis. The main mesh was of constant spacing D and labelled so that the radius at the point J was $r(J) = (J-1)D$. Time progressed in fixed timesteps Δt so that $t = N\Delta t$. An auxiliary mesh, ½ integer in J and N, was used in the finite difference calculations.

a) Numerical Solution Scheme and Stabilities[72]

The two step Lax-Wendroff (TSLW) numerical scheme integrated the continuity and momentum equations. This is a time and space centred two step scheme accurate to terms of order $(\Delta t)^2$.

For advective equations the scheme should be stable for timesteps:-

$\underline{\Delta t < 0.5\ D/v}$ where v is the maximum advective velocity. With $D \sim 10\mu m$ and $v \sim 50\mu m\ ns^{-1}$ (ion sound speed) this gives $\Delta t < 0.1$ ns i.e. ~ 100 solution steps to calculate 10 ns.

However, the stability criterion is more stringent for a diffusion problem as in the thermal conductivity:-

$\underline{\Delta t < 0.5\ D^2/W}$ where W is the diffusion coefficient. From equation (4-0)

$$W = \frac{K_e}{1.5n_e} = \frac{2.05\ 10^{22}}{1.5}\ T_e^{5/2}\ /(n_e \ln \Lambda)$$

$$= 5.8\ 10^7\ cm^2\ s^{-1} \quad \text{at 20eV;} \quad 6\ 10^{16}\ cm^{-3}$$

thus $\Delta t < 8.6\ 10^{-15}$ s and ~ 10^6 timesteps would be needed to keep this explicit method stable. (Remember that $\tau_{TC} \ll \tau_m$). This problem was overcome by treating the thermal conduction separately from the heat input, convection and equipartion. i.e. Equation 4-7 was solved as two separate equations:-

$$\partial U_e/\partial t = -\frac{5}{3} \nabla . (U_e \underline{v}) + E_{laser} - \xi \qquad (4\text{-}10)$$

and $$\partial U_e/\partial t = -\nabla . q_e \qquad (4\text{-}11)$$

The now purely convective equations (4-6, 4-7, 4-9, 4-10) were solved by the explicit TSLW system. On the same timestep equation (4-11) was modelled by an assymmetric implicit scheme which was unconditionally stable. Thus initially the equations handling the laser absorption, the equipartion to the ions and the convective transport were solved with the thermal transport switched off. The thermal diffusion equation (4-11) then allowed the temperature profile to redistribute itself over space by thermal conduction. This is summarised in the flow diagram in Fig. 4-2.

b) Coding of the Convective Equations

The equations (4-6, 7, 9, 10) all have a common form:

$$\frac{\partial X}{\partial t} = -\nabla . (X\underline{v}) + S \qquad (4\text{-}12)$$

where X is the generalised variable, and S represents a composite source term.

Integrating equation (4-12) over a volume element ΔV, and applying the divergence theorem, leads to

$$\frac{\Delta X}{\Delta t} \Delta V = -\oint_A X\underline{v}.d\underline{A} + \int_{\Delta V} S dV$$

where A represents surface area, and Δ denotes finite differences. Hence

$$\Delta X = -\frac{\Delta t}{\Delta V} \{(X\underline{v}.\underline{A})_{out} - (X\underline{v}.\underline{A})_{in}\} + S\Delta t \qquad (4\text{-}13)$$

FIG. 4.2

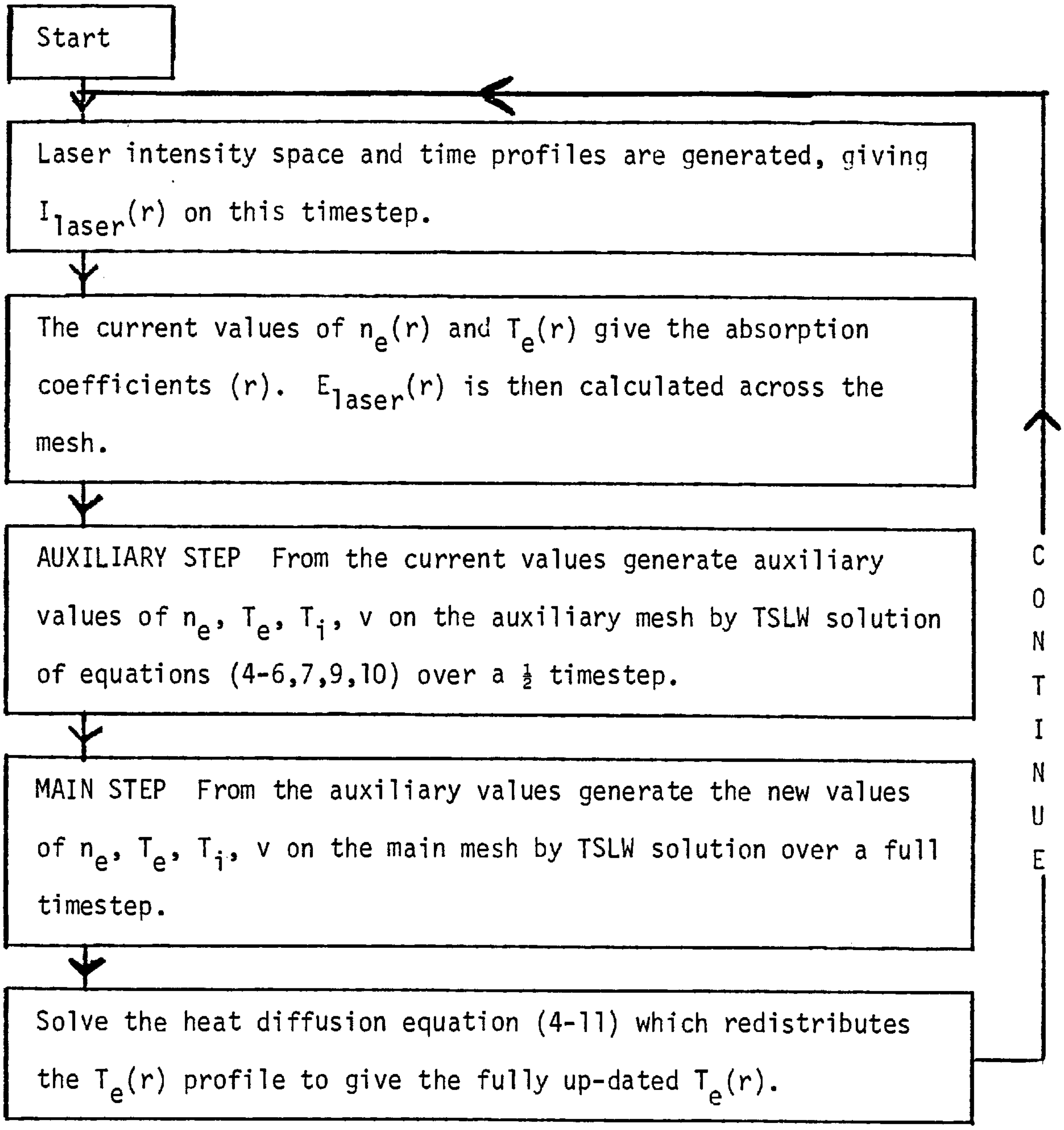

Laser intensity space and time profiles are generated, giving $I_{laser}(r)$ on this timestep.

The current values of $n_e(r)$ and $T_e(r)$ give the absorption coefficients (r). $E_{laser}(r)$ is then calculated across the mesh.

AUXILIARY STEP From the current values generate auxiliary values of n_e, T_e, T_i, v on the auxiliary mesh by TSLW solution of equations (4-6,7,9,10) over a ½ timestep.

MAIN STEP From the auxiliary values generate the new values of n_e, T_e, T_i, v on the main mesh by TSLW solution over a full timestep.

Solve the heat diffusion equation (4-11) which redistributes the $T_e(r)$ profile to give the fully up-dated $T_e(r)$.

Equation (4-13) states that X, the change in X over the time Δt, is equal to the time integrated source in the volume element plus the inward flux of X minus the outward flux of X. Then:-

$$X_{new} = X_{old} + S\Delta t - {}^{\Delta t}/_{\Delta V} \; \{(X\underline{v}.\underline{A})_{out} - (X\underline{v}.\underline{A})_{in}\} \qquad (4\text{-}14)$$

Equation (4-14) was then used to write the continuity, momentum, and energy equations (less the thermal diffusion) in finite difference form using the two step Lax-Wendroff scheme.

c) Coding of the thermal diffusion equation

Since the convection was dealt with above, here we take $\partial n/\partial t = 0$ and using $q_e = \sigma\, T_e^{5/2}\, \nabla T_e \,/\, \ln\Lambda$ and equation (4-11) we have:

$$\frac{\partial U_e}{\partial t} = 1.5\, n\, k_B\, \frac{\partial T_e}{\partial t} = \nabla.\left(\frac{\sigma}{\ln\Lambda}\; T_e^{5/2}\; \nabla T_e\right) \qquad (4\text{-}15)$$

This equation was solved using a mixture of an explicit $T_e^{N+1} = f(T_e^{N})$ and an implicit $T_e^{N+1} = f(T_e^{N+1})$ formalism:

$$T_e^{N+1} = (1-\theta)\; f(T_e^{N}) + \theta\; f(T_e^{N+1})$$

where $0 < \theta < 1$. Setting $\theta = \frac{1}{2}$ is called the Crank-Nicholson method and gives good accuracy while $\theta \rightarrow 1$ is the most stable case.

An implicit solution method on a 1-D spatial mesh of length J implies the solution of J simultaneous linear equations. We can write these simultaneous equations in matrix form and in a 1-D problem the matrix will be tri-diagonal i.e. only elements along the three leading diagonals will be non-zero. This is because the temperature at point J is strongly coupled to the temperature at points J ± 1 and much more weakly coupled to more distant points. The simultaneous equations may be solved by inverting the tri-diagonal matrix or, as here, algebraically.

Starting with the outer boundary condition at J = J_{max} and using the previous timestep values for the temperature, a set of recurrence operators may be defined in a "downscan" across the mesh to J = 1. These recurrence operators relate the temperature values on adjacent mesh points. Then in an "upscan" from J = 1 to J_{max} and starting with the inner boundary temperature at J = 1 the new timestep values for the temperature are derived across the mesh. This is described in depth in reference 72.

In particular, here we want to write equation (4.15) in the form:

$$A(J)\ T_{e\ J+1}^{\ N+1} + B(J)\ T_{e\ J}^{\ N+1} + C(J)\ T_{e\ J-1}^{\ N+1} = D(J)$$

where the coefficients A,B,C,D are known functions of the variables at the old timestep (N). The recurrence operators X and Y may then be defined (on a downscan):

$$X(J-1) = - C(J) / \{A(J)X(J) + B(J)\}$$

$$Y(J-1) = \{D(J) - A(J)Y(J)\}/\{A(J)X(J) + B(J)\}$$

The new temperature distribution may then be derived (in an upscan):

$$T_{e\ J+1}^{\ N+1} = X(J)\ T_{e\ J}^{\ N+1} + Y(J) \qquad (4\text{-}16)$$

Returning to the heat diffusion equation (4-15) it is integrated over a volume element and the divergence theorem is applied:

$$1.5\ nk_B\ \frac{\Delta T_e}{\Delta t}\ \Delta V = \left[- \frac{A'\ \sigma\ T_e^{2.5}}{\ln \Lambda}\ \nabla T_e \right]_{out} - \left[\frac{A'\ \sigma\ T_e^{2.5}}{\ln \Lambda}\ \nabla T_e \right]_{in} \qquad (4.17)$$

The $T_e^{2.5}$ term meant that equation (4-17) did not have the desired tri-diagonal form. Following common procedure the old timestep(N) value was used for the $T_e^{2.5}$ term while the ∇T_e term remained implicit (time - N+1). The calculations were then repeated until the solution converged.

A three level temperature system was defined for this purpose:-

$T(J) = T_J^N$ the old timestep electron temperature, updated for heating and convection and <u>not</u> updated for thermal diffusion.

$T1(J) = T_J^{N+1}$ the solution for the electron temperature after each iteration, so the converged T1(J) was the final solution for the diffused temperature.

$Tk(J) = T_{J-\frac{1}{2}}^{N+\frac{1}{2}}$ from the solution for T1(J) on the <u>preceding</u> iteration loop, before convergence was achieved, this intermediate level temperature was defined on the auxiliary mesh.

Fig. 4-3 gives a flow diagram for the thermal diffusion method.

d) <u>Application of a flux limit</u>

A subroutine (LIMTER) was used to artificially impose an upper limit on the heat flux at all times and all spacial positions. It is called at the start of the main timeloop and generates a modifying factor MODFAC (J) across the mesh. This factor multiplies the Spitzer conductivity constant everywhere it appears in the solution of the thermal diffusion:-

$$\text{MODFAC (J)} \propto 1/(\lambda_e/L) \propto 1/T_e\nabla T_e$$

The heat flux $q_{spitzer} \propto T_e^{2.5}\nabla T_e$

$\therefore$ MODFAC x $q_{spitzer} = q_{program} \propto T_e^{1.5}$

MODFAC (J) = 1, if $q_{spitzer} <$ ARTLIM q_{max} where $q_{max} = nkT_e\ (2kT_e/\pi m_e)^{0.5}$.

FIG. 4.3

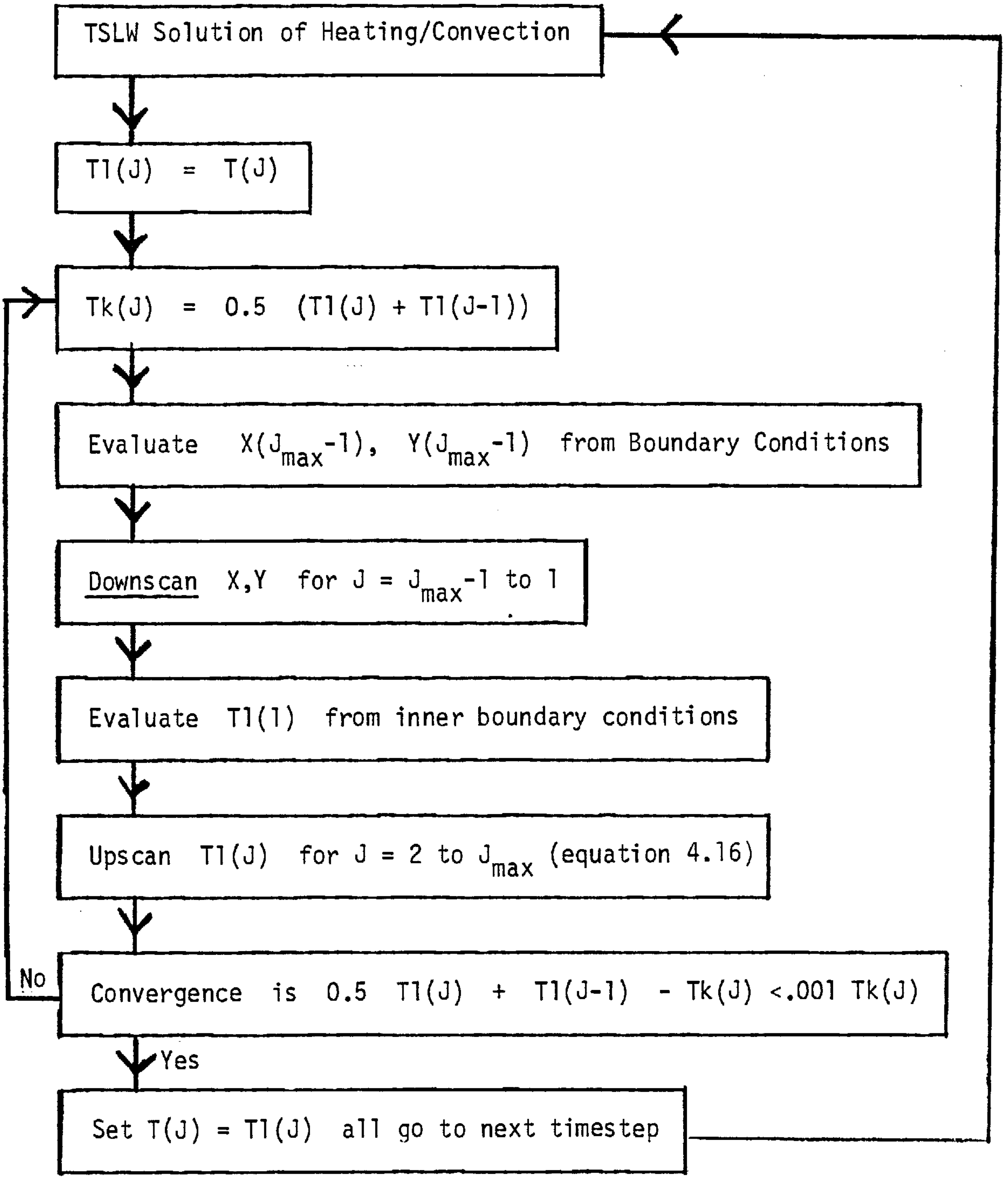
TSLW Solution of Heating/Convection
T1(J) = T(J)
Tk(J) = 0.5 (T1(J) + T1(J-1))
Evaluate X(Jmax-1), Y(Jmax-1) from Boundary Conditions
Downscan X,Y for J = Jmax-1 to 1
Evaluate T1(1) from inner boundary conditions
Upscan T1(J) for J = 2 to Jmax (equation 4.16)
No
Convergence is 0.5 T1(J) + T1(J-1) - Tk(J) <.001 Tk(J)
Yes
Set T(J) = T1(J) all go to next timestep

Here, ARTLIM was an input parameter and the fraction of the free streaming limit to which the heat flux was constrained.

MODFAC (J) = L/λ_e . ARTLIM/X, if $q_{spitzer} > \text{ARTLIM}.q_{max}$.
where $X = L/\lambda_e$ when $q_{spitzer} = q_{max}$.

A second diagnostic subroutine (FLMOD) printed out $q_{program}/q_{max}$. at selected time and space points. This checked that the heat flux was being limited by LIMTER in the regions of large λ_e/L.

7. MODIFICATIONS TO THE ORIGINAL PROGRAM

a) Conduction and Absorption Coefficients

The important parameters of thermal conductivity and inverse bremsstrahlung absorption coefficient were checked first. The units used in the program are MKS throughout with the temperature in ^{o}K.

The thermal conductivity constant agreed with that due to Spitzer[3]. As already described, this constant could be artificially varied by a multiplication factor (SPIFAC). Also, the absolute value of the flux could be limited to some fraction (ARTLIM) of the free streaming limit.

The inverse bremsstrahlung absorption coefficient, however, was found to be in error. With T_e in eV and n_e in cm^{-3}, the absorption coefficient used by M.S. White was:

$$k_{MSW} = 6.99\ 10^{-36}\ n_e^{\ 2}\ T_e^{\ -1.5}\ \ln\Lambda\ (1-{}^{n_e}/_{n_c})^{\frac{1}{2}}\ cm^{-1}$$

This was quoted as being due to Heald and Wharton[73] who derived it from the imaginary part of the refractive index.

Firstly, there are two errors in k_{MSW}

(a) The references of Heald and Wharton, Hora and Wilhem[74] and Billman and Stallcop[75] all give (9.8 ± 0.1) 10^{-36} for the constant above.

(b) As pointed out by Johnston and Dawson[76] there has been a common error in high-frequency power absorption formulae. When $\omega_{laser} >> \omega_{p_e}$, $\Lambda = v_T/\omega_{laser}p_{min}$ and not $v_T/\omega_{p_e}p_{min}$ where v_T = electron thermal velocity and p_{min} = the minimum impact parameter for electron-ion collisions. (This is because the relevant range of collision times is p_{min}/v_T up to $1/\omega_{laser}$ and not up to $1/\omega_{pe}$. Collisions on a time scale slower than $1/\omega_{laser}$ do not contribute to the absorption). Thus the absorption coefficients given in

Hora and Wilhelm[74] are wrong. In the present experiment with $n_e/n_c \sim 10^{-2}$ the correct ln Λ is ~ 2.3 times smaller than used by M.S. White. Secondly, as pointed out by Billman and Stallcop at temperatures $\leq$ 5eV, quantum mechanical corrections to the absorption coefficient become important and the correct expression is:-

$$k_{QM} = 1.77\ 10^{-35}\ n_e^{\ 2}\ T_e^{\ -1.5}\ (1-{}^{n_e}/_{n_c})^{-\frac{1}{2}}\ g\ \text{cm}^{-1}$$

where $g = g\ (\lambda,\ T_e)$ is the free-free Gaunt factor. Fig. (4-4) shows the classical and quantum mechanical absorption coefficients from the paper of Billman and Stallcop[75] at 6 10^{16} cm^{-3} and 1 → 19 eV.

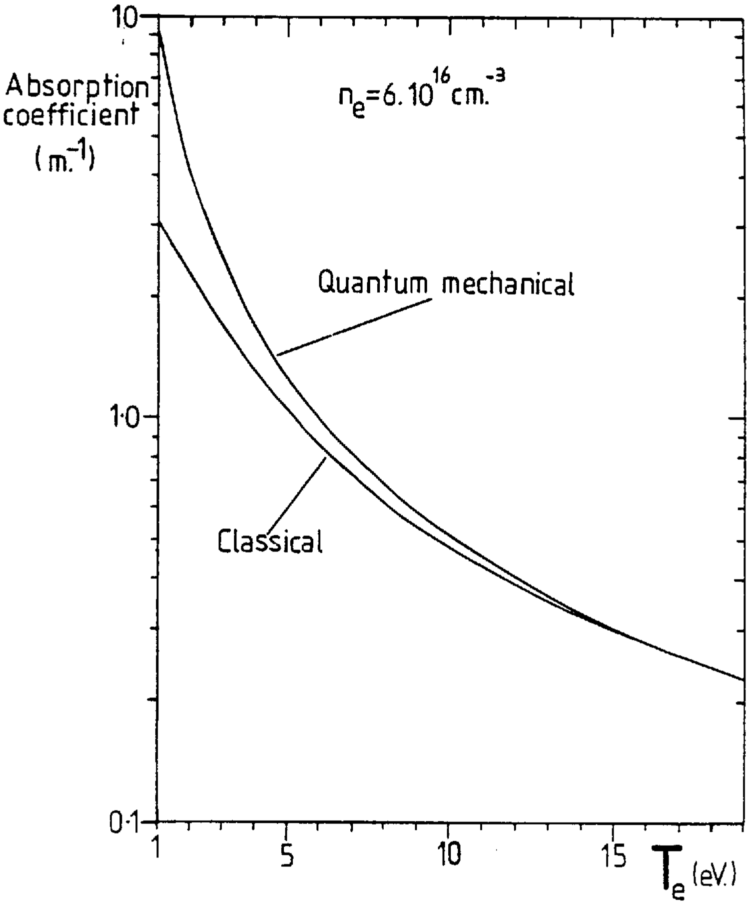

Fig. (4-4)

Variation with temperature of the absorption coefficient for a hydrogen plasma (Z=1)(n_e=6.10^{16} cm^{-3}).

The correct k_{QM} was written into the program replacing k_{MSW}. This was found to make little change to the final result, the peak temperature at the centre remaining unchanged to 0.3%. This is due to cancelling errors from the use of the incorrect ln Λ and constant in k_{MSW} and the dominance of the $T_e^{-1.5}$ variation in both expressions.

The k_{MSW} absorption coefficient was then retained since the use of k_{QM} necessitated the calculation of g across the mesh at each timestep and was expensive on computer time.

The strong field saturation of inverse bremsstrahlung[77] is allowed for in the code by using:

$$k = {}^{k_{MSW}}\!\Big/\!\left(1 + {}^{3}\!/_{2}\,\left({}^{v_o}\!/_{v_{th}}\right)^2\right)$$

where v_o = electron ripple velocity in the laser electric field = $25.6 \sqrt{I}\,\lambda_o$ cms^{-1} where I is in Wcm^{-2} and λ_o in μm. Here the ripple velocity has been taken as additive to the thermal velocity in reducing the collision frequency and thus the absorption:

$$k \propto \nu_{ei} \propto T_e^{-3/2} \propto (v_o \cos \omega t + v_{th})^{-3}$$

The program printed out this $1 + {}^{3}\!/_{2}\,(v_o/v_{th})^2$ reduction to the absorption on selected timesteps. On the computer run which gave the best fit to the experimental results, the peak value of this reduction was 1.49 and the peak temperature at the centre was reduced by 9.5% (24.5 eV to 22.1 eV).

b) Inclusion of the Ponderomotive Force

The ponderomotive force which acts on the electrons arises when there is a gradient in the electric field of the laser light[17]. The force on a single electron may be written:-

$$f = -\,(e^2/2m\omega^2)\ \nabla < E^2 >$$

$$= -\,\tfrac{1}{4}\, m_e\, \nabla(v_r^{\,2}).$$

In the absence of any significant density gradients then the body force/unit volume = $-\frac{1}{4}\, nm_e\, \nabla\, v_r^{\,2}$. The pressure force = $-\,\nabla p_e$ where $p_e = nm_e\, v_{th}^{\,2}$.

$\therefore$ Ponderomotive force/pressure force ~ $\frac{1}{4}\,\nabla(v_r^{\,2})/\nabla(v_{th}^{\,2})$.

Thus, this effect is likely to become important at high intensities when $v_r \sim v_{th}$

Using: $v_r^{\,2} = (e^2/m^2\omega^2)\ 2\ Z_o\ I(r,t)$

where $Z_o = \sqrt{\mu_o/\varepsilon_o} \simeq 377$

$\therefore$ Force/unit volume = $-(ne^2\ Z_o/2m\omega^2)\nabla I(r,t)$

$= (Z_o\ e^2/m\omega^2)\ n_o(r/r_o^{\,2})\ I(r)$

where $I(r) = I_o \exp(-r/r_o)^2$ has been used.

This extra contribution was then included in the solutions of all the momentum equations.

$$\partial/\partial t(gv) = (Z_o e^2/m\omega^2)\ n\ (r/r_o^{\,2})\ I(r)\ +\ \text{other terms}$$

$$\therefore \quad \delta(gv) = (\text{CONJ}).\ \Delta t\ .\ J\ .\ I(J).\ n(J)$$

where CONJ = $Z_o e^2/m\omega^2 r_o^{\,2}$

After insertion of the ponderomotive force correction, the simulation was rerun for the same conditions: SPIFAC = 1, ARTLIM = 1, n_e initial = 6.5 10^{16} cm^{-3}, T_e initial = 4eV, peak laser power = 500MW and the $^1/_e$ point of the focal spot at a radius of 200μm.

Overall, T_e was unchanged to <2% and n_e to $\lesssim$10%

c) The CO_2 laser power in space and time

The spatial distribution of power in the focal spot of the heating laser was made Gaussian following the measurements described in Chapter 2. A radial $^1/_e$ point of 200μm (JZERO = 11 for D = 2. E-5) was used. The effect of using a $^1/_e$ point of 150μm is discussed later.

A subroutine, PTIME, simulated the temporal variation of CO_2 laser power. Fig. (4-5) shows how the pulse was modelled.

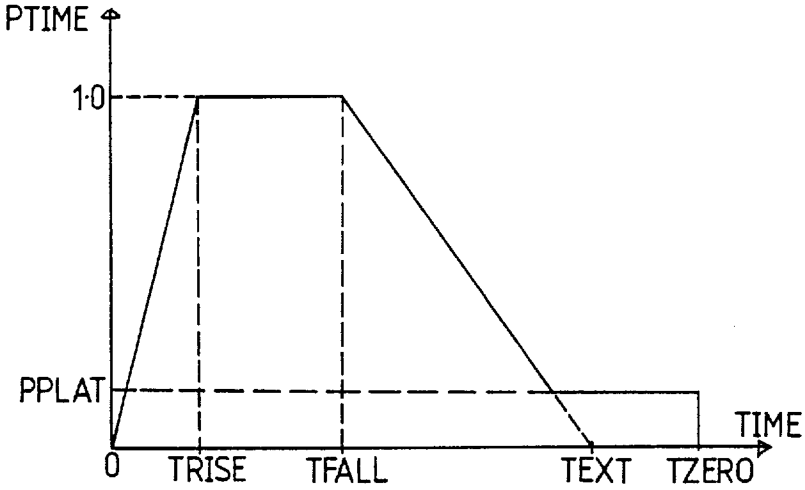

Fig. (4-5) CO_2 laser pulse temporal shape

For the short laser pulse used: TRISE = 1ns, TFALL = 2ns, TEXT = 4.2ns, TZERO = 6ns and the tail PPLAT = 0.1. For the longer laser pulse: TRISE = 1ns, TFALL = 2ns, TEXT = 24ns, TZERO = 25ns and PPLAT = 0.1.

Since it was possible that TRISE was detector bandwidth limited programs were also run with TRISE = 0.5ns. These are discussed later.

d) Spatial weighting of output arrays

The computer output gave n_e, T_e, v_e, T_i every 40μm (radially) for 10ns. To compare these arrays with the experimental results the application of the laser scattering diagnostic was also simulated. The Abel inversion of Chapter 2 gave a measure of the radial intensity in the focal waist of the ruby laser. Thus we may allow for the fact that the more intensely illuminated regions of plasma contribute more to the observed scattering. We calculate normalised resolution functions for displacements in the vertical and horizontal planes:- $f(r,\delta)$. For different displacements δ of the "scattering box" from the CO_2 laser axis this function describes the radial sensitivity of the diagnostic. We may define:

$$f(r,\delta) = \int_V I_{ruby}(r')\,\delta(r-r')\,dV'$$

where we are integrating the (Gaussian) ruby laser intensity over the scattering box volume V'. r' is measured from the ruby laser axis and r from the CO_2 laser axis. Then we may determine what the measured electron temperature (say) should be at various displacements:

$$T_e(\delta) = \frac{\int T_e(r)\, f(r,\delta)\, dr}{\int f(r,\delta)\, dr} \qquad (4\text{-}18)$$

where $T_e(r)$ is the program output. This process is repeated every ns to 10ns. The function $\delta(r-r')$ is different for horizontal and vertical displacements:-

(i) Horizontal Displacement

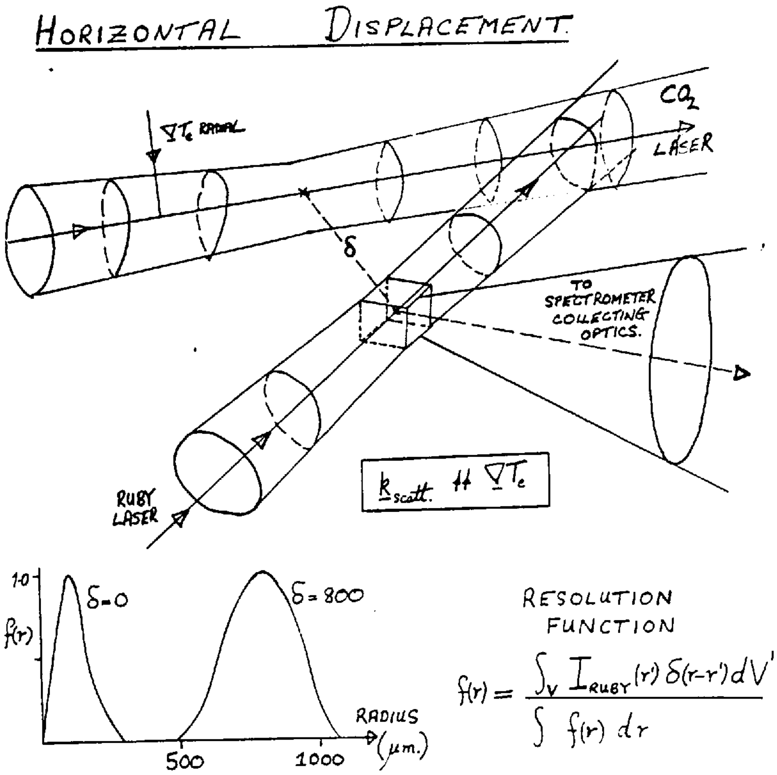

Fig. (4-6)

We define cartesian co-ordinates x, y and z centred on the scattering box and calculate the radius from the CO_2 laser axis in terms of δ, x, y, z. The geometry in the horizontal plane is:

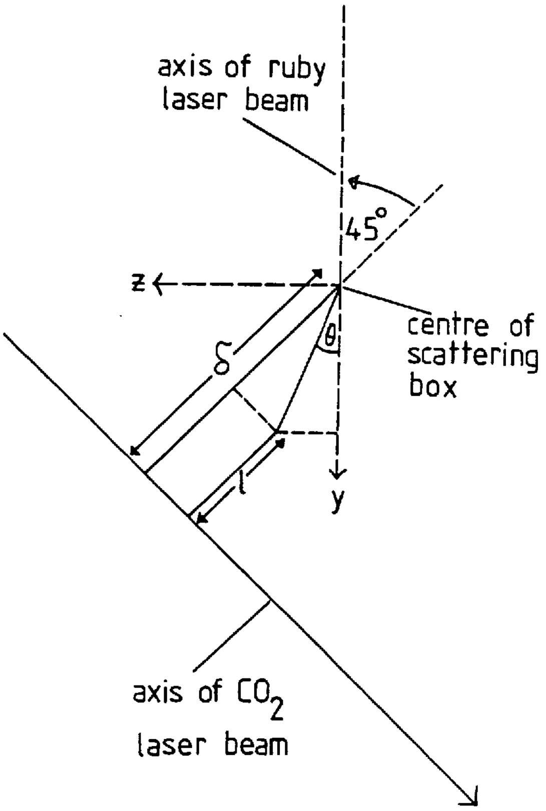

Fig. (4-7)

The distance l to the point, (x = o, y, z)

$= \delta - \sqrt{y^2 + z^2}\ \cos(45 - \theta)$

$= \delta - (y + z)/\sqrt{2}$

The radial distance r_h to the point (x, y, z)

$= \sqrt{x^2 + l^2} \quad = \sqrt{x^2 + (\delta - (y+z)/\sqrt{2}\,)^2}$

Subroutine RUBY now calculates $f(r_h, \delta)$ by summing over x, y, z (to the limits of the scattering box) with each incremental volume weighted as a Gaussian fall-off from the box centre in the x and z directions. The point of maximum scattering sensitivity depends on the number of incremental volumes available at a given radius (r_h) and the ruby laser intensity in those volumes. This explaines why the resolution function for δ = 0 shown in Fig.4-6 does not peak on the CO_2 laser axis.

(ii) Vertical Displacement

The rather longer calculation of r_v is omitted here for brevity. (It involves a transformation of co-ordinates).

$$r_v = \sqrt{(\delta-x)^2 + (y+z)^2/2}$$

Note that $r_v = r_h$ when $\delta = 0$.

Subroutine RUBY also calculates $f(r_v,\delta)$

The main program then calculates $T_e(\delta)$ for horizontal and vertical displacements according to equation (4-18).

N.B. The above corrections ignore the variation in the total scattered light in the electron feature $S_e(k)$ due to variations in the α ($\propto 1/T_e^{\frac{1}{2}}$) across the spatial resolution. $S_e(k) = 1/(1 + \alpha^2)$ and hotter regions scatter more light into the electron feature. From later computer results, the peak value of $\Delta S_e(k)/S_e(k)$ is ~ 30% over 200µm around δ = 300µm. However, at δ = 0 and 800µm where the most important experimental/computer comparisons were made $\Delta S_e(k)/S_e(k) < 3\%$ over 200µm.

8. SUMMARY OF COMPLETE PROGRAM

START Read in initial conditions n_e, T_e, T_i, v, ARTLIM, SPIFAC, LASER POWER, JZERO.

Calculate total energy (ETOT) and particles (NTOT) for conservation test.

Start main time loop

i) Subroutine LIMTER calculates the flux limiting factor MODFAC (J) using the previous timestep results.

ii) Subroutine FLMOD checks q/q_{max}.

iii) Input energy density from CO_2 laser, ELAS (J), from Gaussian focal spot, subroutine PTIME, and absorption coefficient.

iv) TSLW calculations of convective equations.

v) Particle conservation tests (NTOT).

vi) Solution of Thermal Diffusion by iteration in an assymmetric implicit scheme.

vii) Energy conservation test (ETOT).

viii) Store output at selected steps in 2D (space-time) < arrays.

ix) Continue - repeat all on next timestep or exit.

Write out 2D arrays (n_e, T_e, T_i, v).
Subroutine Ruby spatially weights output from 2D arrays.

END

A complete listing of the program is given in Appendix C.

SAMPLE OUTPUT

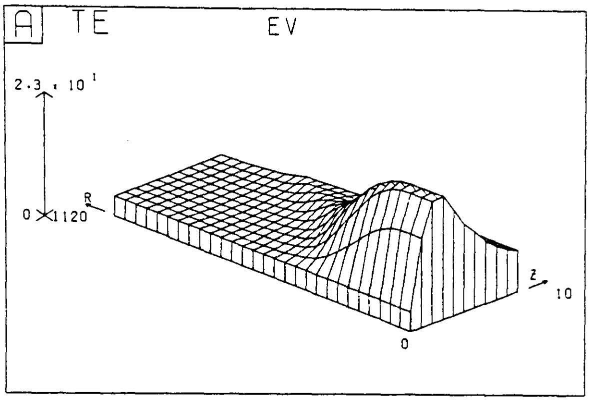

A Electron Temperature

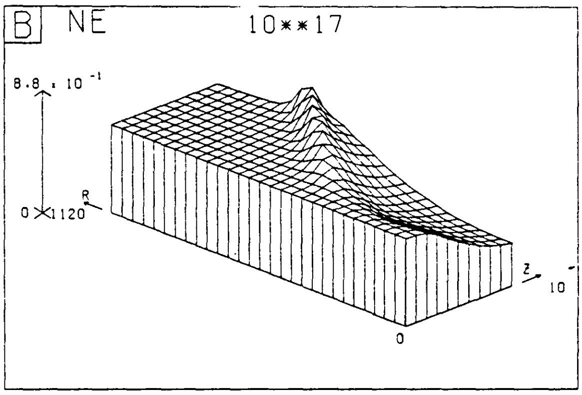

B Electron Density

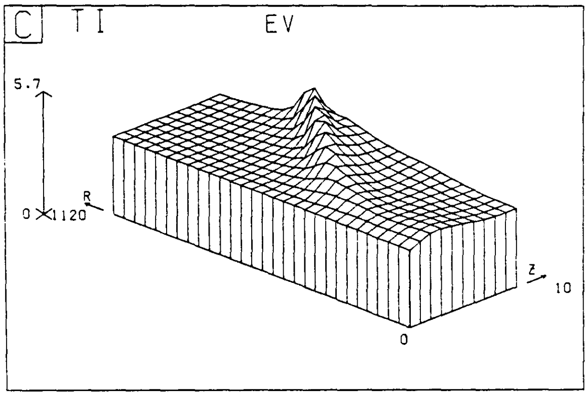

C Ion Temperature

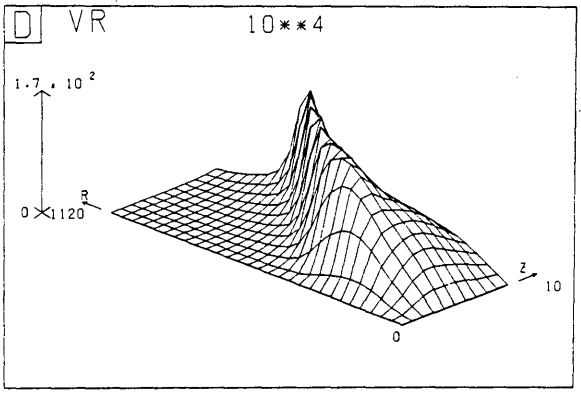

D Radial Fluid Velocity

Program conditions. ARTLIM = 0.03, SPIFAC = 1.0,

ABSORPTION = Classical, Peak CO_2 laser intensity = 236MW.

TRISE = 1ns, TFALL = 2ns, TEXT = 4.2ns, TZERO = 6ns, PPLAT = 0.1, (i.e. short laser pulse length), JZERO = 11, (i.e. CO_2 laser focal spot has a $^1/e$ radial point at 200μm.), initial electron density = $6.3\ 10^{16}\ cm^{-3}$, initial electron temperature = 3.6 eV;

In the plots shown time varies with Z from 1 to 10ns and the radial distance from the CO_2 laser beam axis with R from 0 to 1120μm.

CHAPTER 5

COMPARISON OF SIMULATION AND EXPERIMENT

1. INTRODUCTION

The main aim of this comparison was to find the absorption/ conduction conditions in the program which best fitted the experiment. The artificial multiplier of the absorption (incident power) we shall now call w and that of the conductivity coefficient s (SPIFAC in the program). The variable flux limit (ARTLIM in the program) we now call f.

In this chapter the computer results are drawn as two solid lines for each displacement. These two lines represent the simulated temporal evolution of n_e or T_e after spatially weighting the results for the laser scattering diagnostic at the given displacement ± the alignment setting error. The program could correct for both horizontal and vertical displacements. Measurement of the displacement and its setting error was described in Chapter 2 Part 7. Separate computer runs were preformed using the correct initial conditions for each displacement as given in Table (3-1). This table also gives the scattering vector direction ($|| \nabla T_e$ or $\perp_r \nabla T_e$).

The effects of using a CO_2 laser focal spot size of 150μm (to $^1/e$ point of a Gaussian) and a pulse risetime of 0.5ns were also investigated to account for possible experimental measurement error.

2. δ = 0, 300 and 800μm.; SHORT CO_2 LASER PULSE

The best fit to these experimental results was obtained with w = 1, s = 1, f = 0.03 i.e. classical absorption with the thermal conductivity obeying Spitzer's law except where the heat flux was locally limited to 3% of the free streaming limit. The experimental/computational comparison of the electron temperature is shown in Fig. (5-1). Also shown for the central position, Fig. (5-1a), are computations for f = 0.01 and f = 1.0 to show the sensitivity of the method.

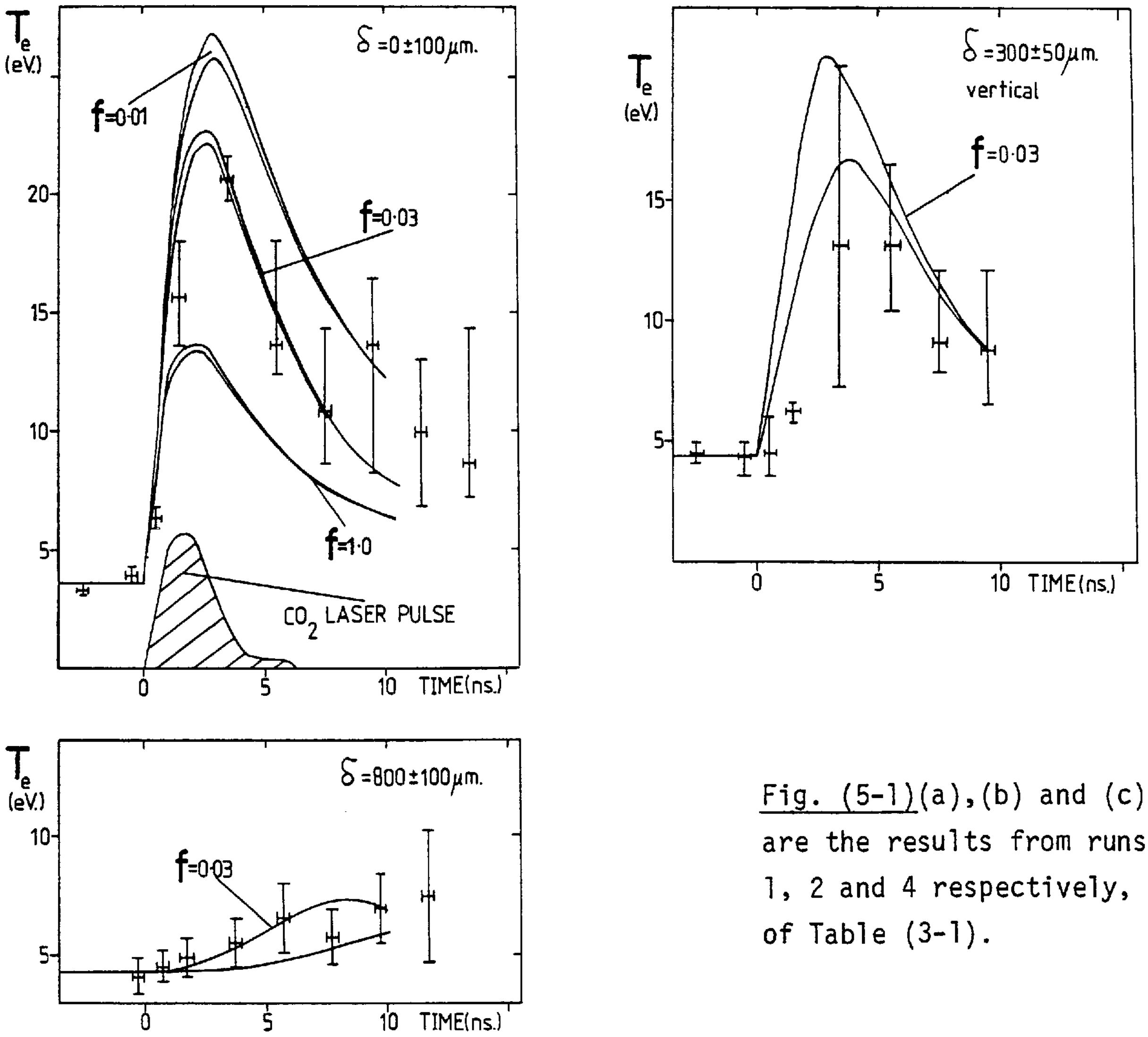

Fig. (5-1)(a),(b) and (c) are the results from runs 1, 2 and 4 respectively, of Table (3-1).

Fig. (5-1a) shows the experimentally measured CO_2 laser pulse profile in time, defining time zero as the start of this pulse. This time origin will be used throughout this chapter.

The peak power used in a given computational run is given in Table (3-1).

Fig. (5-2) shows the temporal evolution of the electron density at $\delta = 0 \pm 100\mu m$.

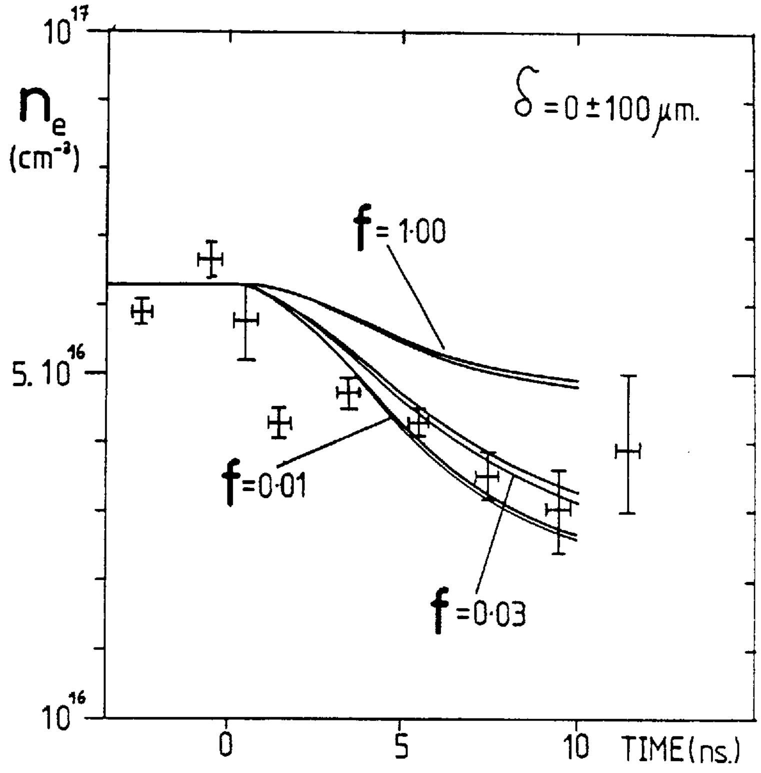

Fig. (5-2)
Electron density results from run 1.

The experimental results are compared with simulations for f = 0.01, 0.03 and 1.00 showing that f = 0.03 is a reasonable fit for the density also. Note that the point at t = 1.5ns is a poor fit for both the T_e and n_e results. As described in Chapter 3, the experimental data is weak at this time due to the plasma conditions changing rapidly inside the temporal resolution of ~1ns.

Programs were also run at $\delta = 0 \pm 100\mu m$ with a CO_2 laser pulse risetime of 0.5ns and a focal spot of 150μm. The 0.5ns risetime run increased the peak temperature by < 2%. The smaller focal spot size increased the peak temperature at the centre by 15% but the points on the falling edge of the temperature (t = 3.5 → 9.5ns) still fitted within experimental error.

Because of the large error bars on the $\delta = 300 \pm 50\mu m$ data, the results at $\delta = 0 \pm 100\mu m$ and $\delta = 800 \pm 100\mu m$ were principally used to define a region of absorption/conduction (w, f or s) space where the computational results fitted the experimental results. The computational/experimental comparison measured both the absorption and conduction as follows. The experimental results at $\delta = 0 \pm 100\mu m$ (most importantly the peak temperature obtained on axis) could theoretically be fitted by increasing (decreasing) the conduction and absorption indefinitely; i.e. the same peak temperature at the centre is obtained for a higher (lower) absorption by having a greater (smaller) conduction of energy out of the focal region. There comes a point however, when increasing (decreasing) the absorption and conduction makes the temperature at $\delta = 800 \pm 100\mu m$ too high (low).

Thus by requiring the computational results at ± the alignment setting error to fall inside the experimental error bars, it was possible to say that a computer run with a certain (w, f) combination was a fit while another computer run with another (w, f) combination was a non-fit. Comparisons where the computational results were close to the error bar limits, were called marginal fits. As an illustration a marginal fit for high absorption (w)/conduction (f) is shown in Fig. (5-3)(a) and a marginal fit for low absorption/conduction is shown in Fig. (5-3)(b).

Similarly, the results at $\delta = 800 \pm 100\mu m$ could be fitted by decreasing (increasing) absorption if the conduction were increased (decreased). However, the temperature at the centre quickly becomes too low (high). The non-fits for these cases are shown in Fig. (5-4).

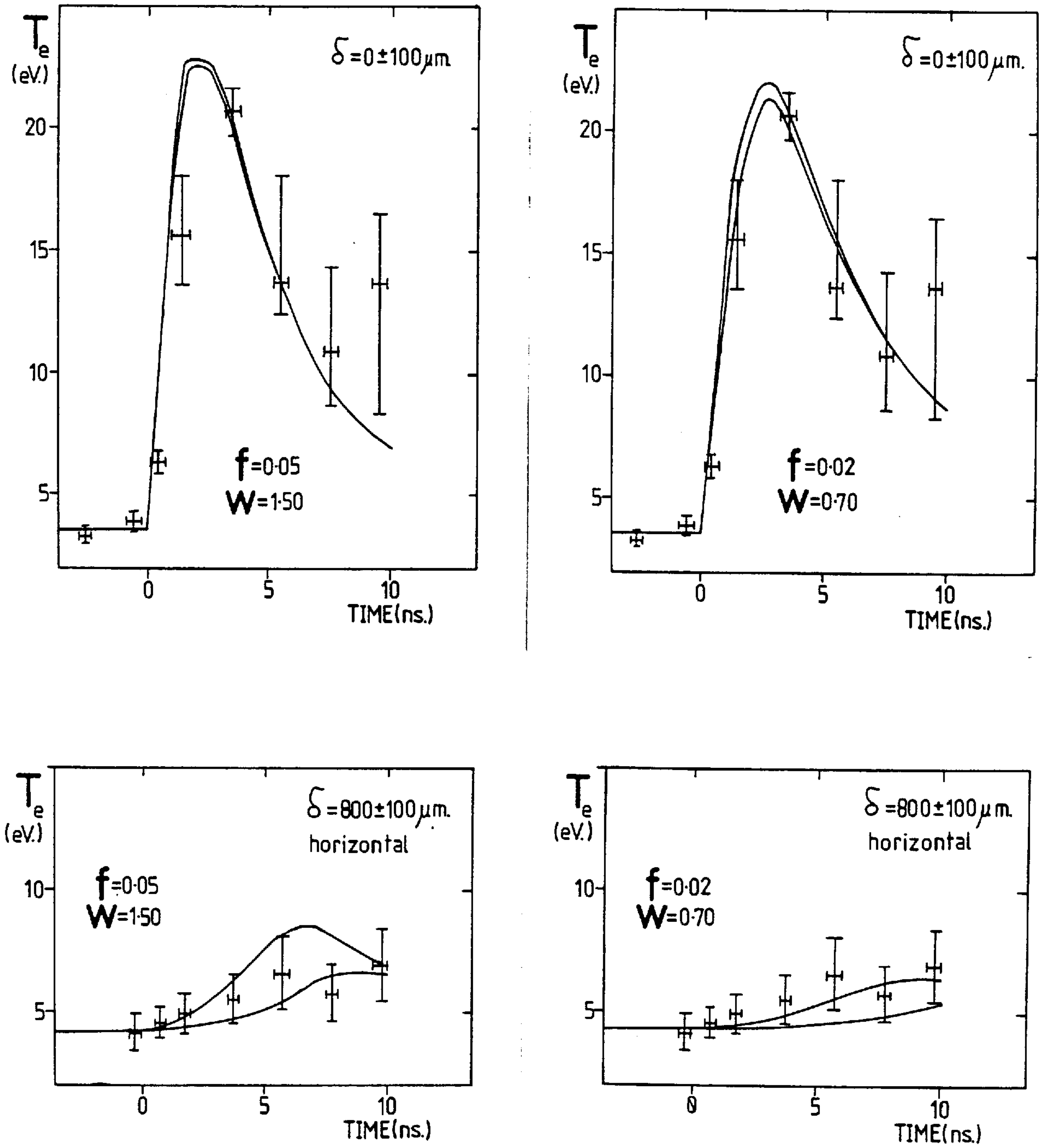

Fig. (5-3) (a) (b)

In this way, by running simulations for a large number of combinations of w and f an allowed region of absorption/conduction space was determined. This is shown in Fig. (5-5).

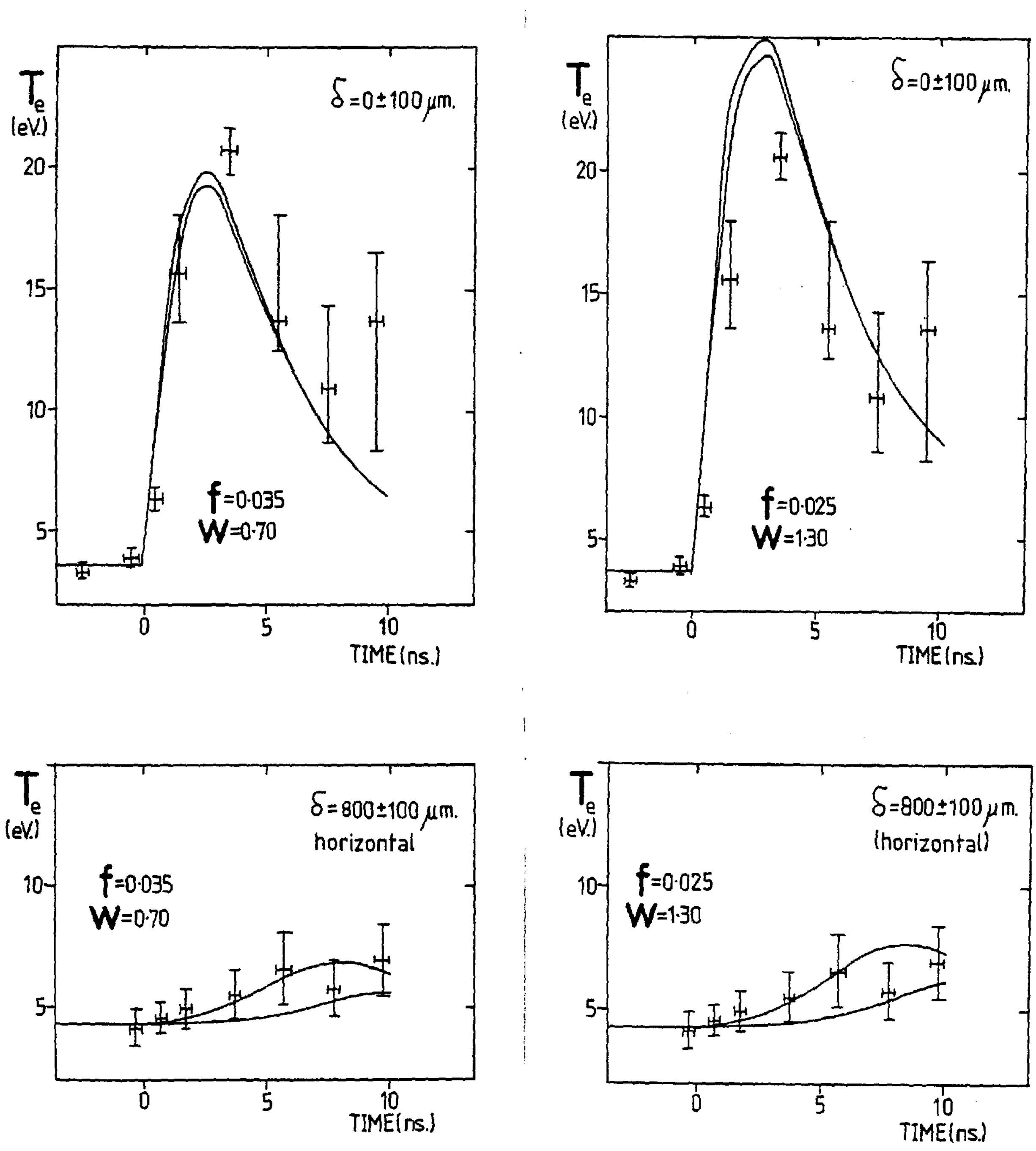

Fig. (5-4) (a) (b)

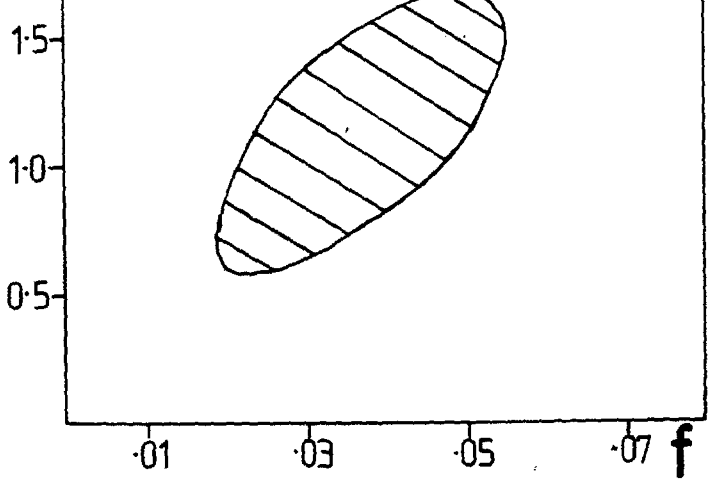

Fig. (5-5)

Attempts were also made to fit the results in (w,s,f = 1) space i.e. applying no flux limit but varying the absorption and conductivity constants. This was much less successful with only one marginal fit obtained at (w = 1.4, s = 0.065, f = 1) as shown in Fig. (5-6).

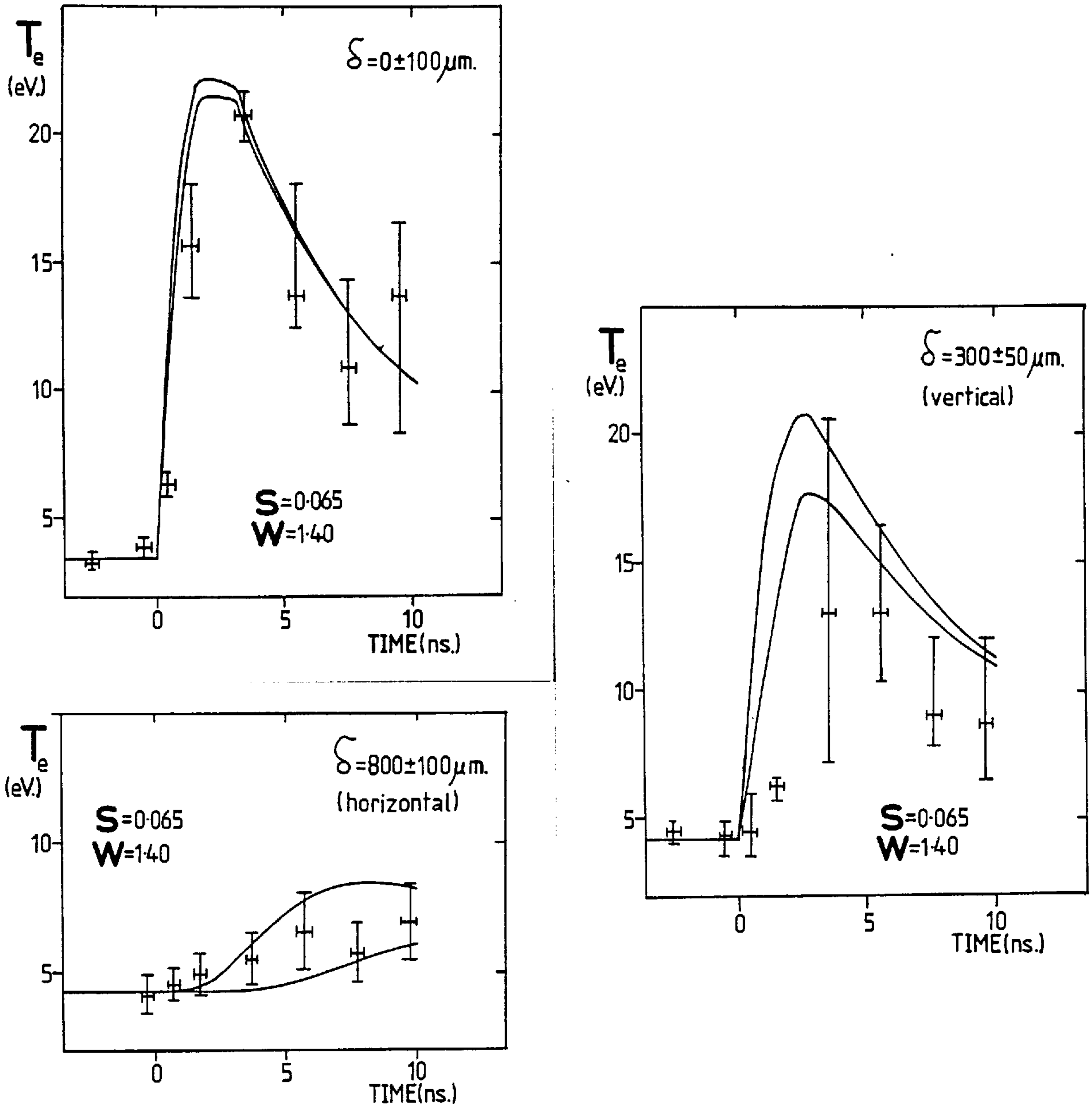

Fig. (5-6) The singular fit obtained in (w,s,f = 1) space.

In this run, subroutine FLMOD indicated a maximum value of 6% for q/q_{max}. The following runs were definite non-fits:

(w = 1.0, s = 0.05), (w = 1.7, s = 0.05), (w = 1.0, s = 0.10) and (w = 1.7, s = 0.10). Thus the region in (w,s) space where experimental/computational agreement was obtainable was much smaller than in (w,f) space. The proposition that the application of a flux limit (f) is more physically correct than a simple blanket reduction of the conductivity coefficient (s) will be discussed in Chapter 7.

3. δ = 400 and 700μm.; LONG CO_2 LASER PULSE

A long heating pulse was used to look for any experimental/computational temporal inconsistencies in the method. The fit obtained for (w = 1.0, f = 0.04, s = 1.0) is shown in Fig. (5-7).

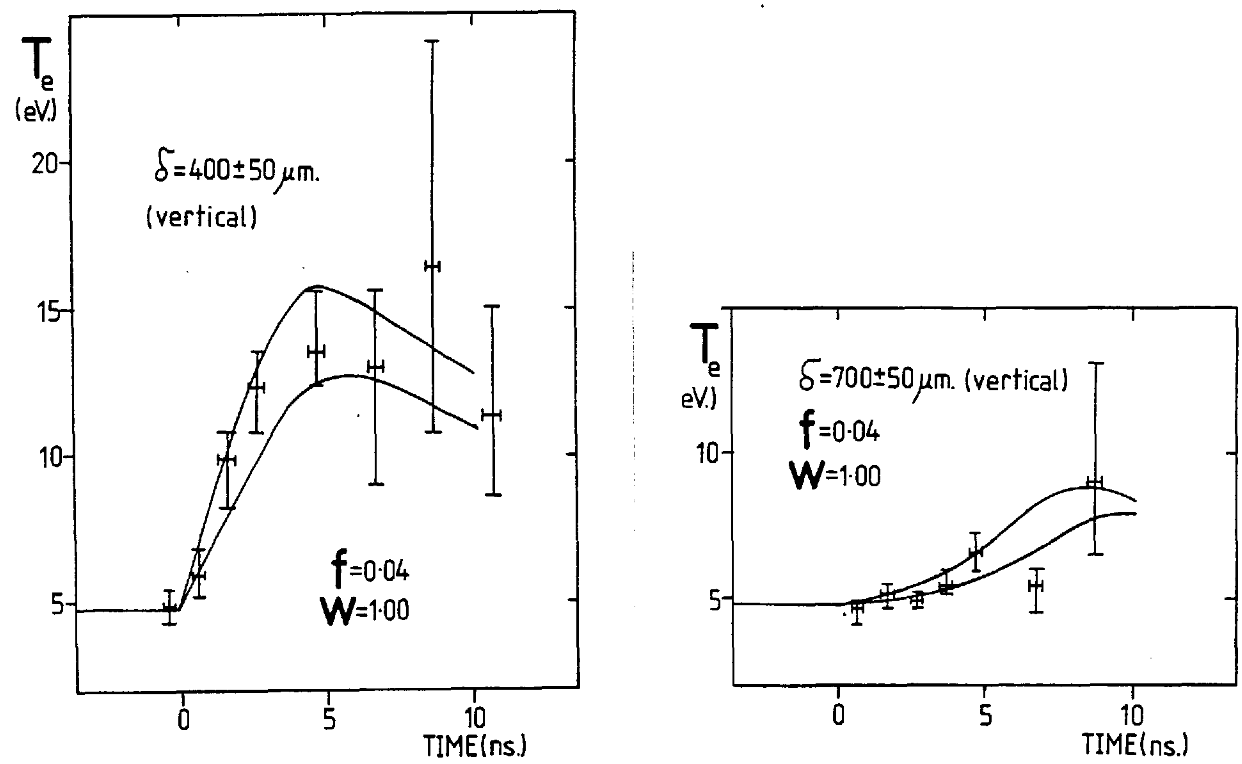

Fig. (5-7) Fit to data from runs 8 and 9 of Table (3-1).

Fig. (5-8) shows the experimental and computational CO_2 laser pulses used for the above simulation.

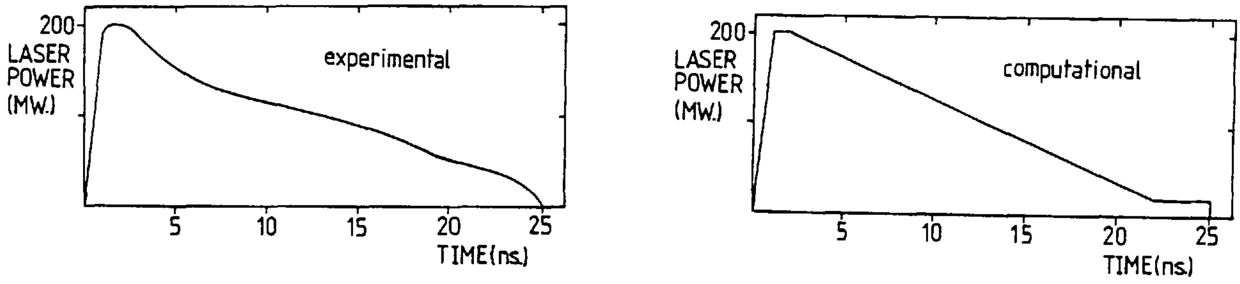

Fig. (5-8)

The allowed region of (w,f,s = 1) space for this 12.5ns (FWHM) pulse data found by the method described in section 2. of this chapter is shown in Fig. (5-9).

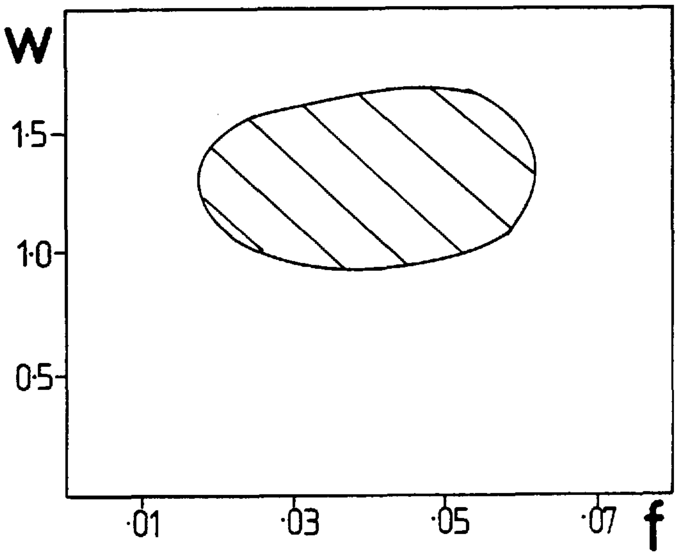

Fig. (5-9)

A run was also performed for (w = 1.4, f = 1, s = 0.065) which was a definite non-fit as shown in Fig. (5-10).

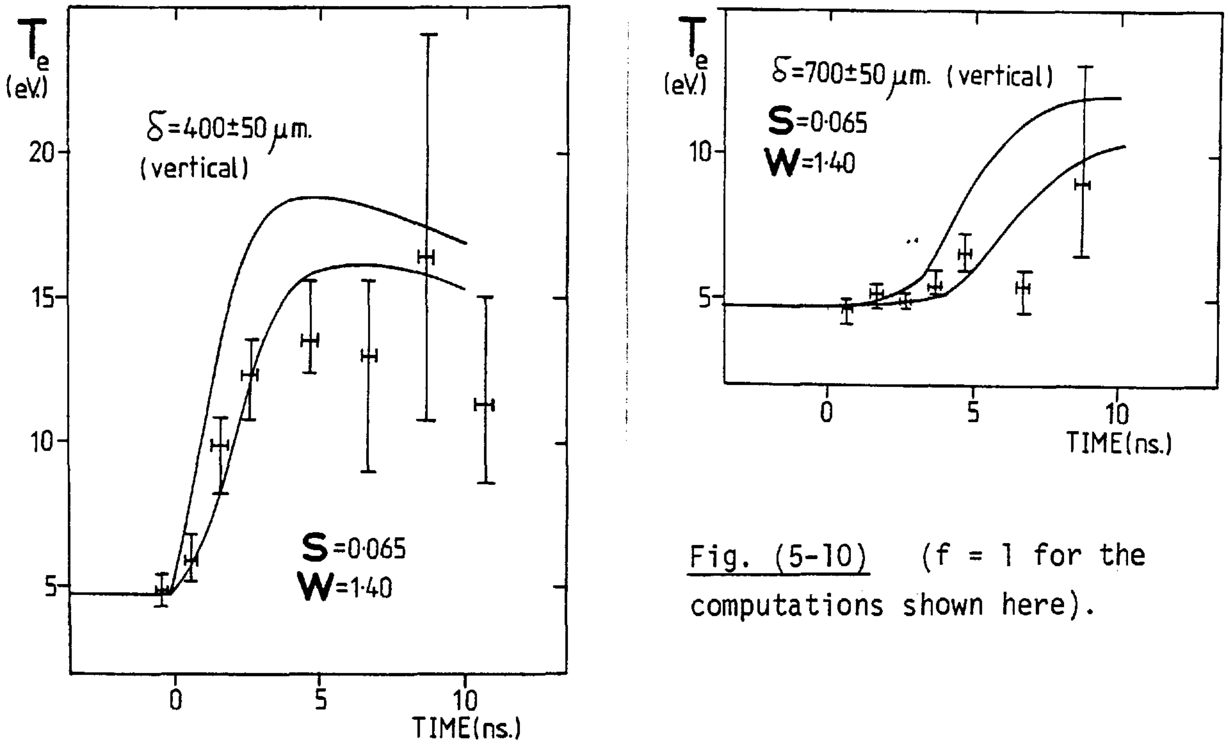

Fig. (5-10) (f = 1 for the computations shown here).

Thus the allowed regions of (w,f) space for the 2.5ns and 12.5ns (FWHM) heating pulses overlapped while the singular point fitable in (w,s) space for the 2.5ns pulse did not fit the 12.5ns pulse data.

4. EARLY RESULTS; δ = 350, 350 and 650μm. SHORT PULSE

These early results were taken with the photomultiplier (scattered light) and photodiode (incident light) signals on the same oscilloscope trace. This meant that the shot noise errors on the spectra for this data were larger by a factor of two than those used for the data of Section 2. Also, at the time these results were taken the available CO_2 laser power was high, peaking at ~ 400MW. No region of (w,f) space could be found where the simulation fitted the results at all displacements. The results near the edge of the focal spot (δ = 350μm) were fitable with (w = 0.625, f = 0.001) as shown in Fig. (5-11).

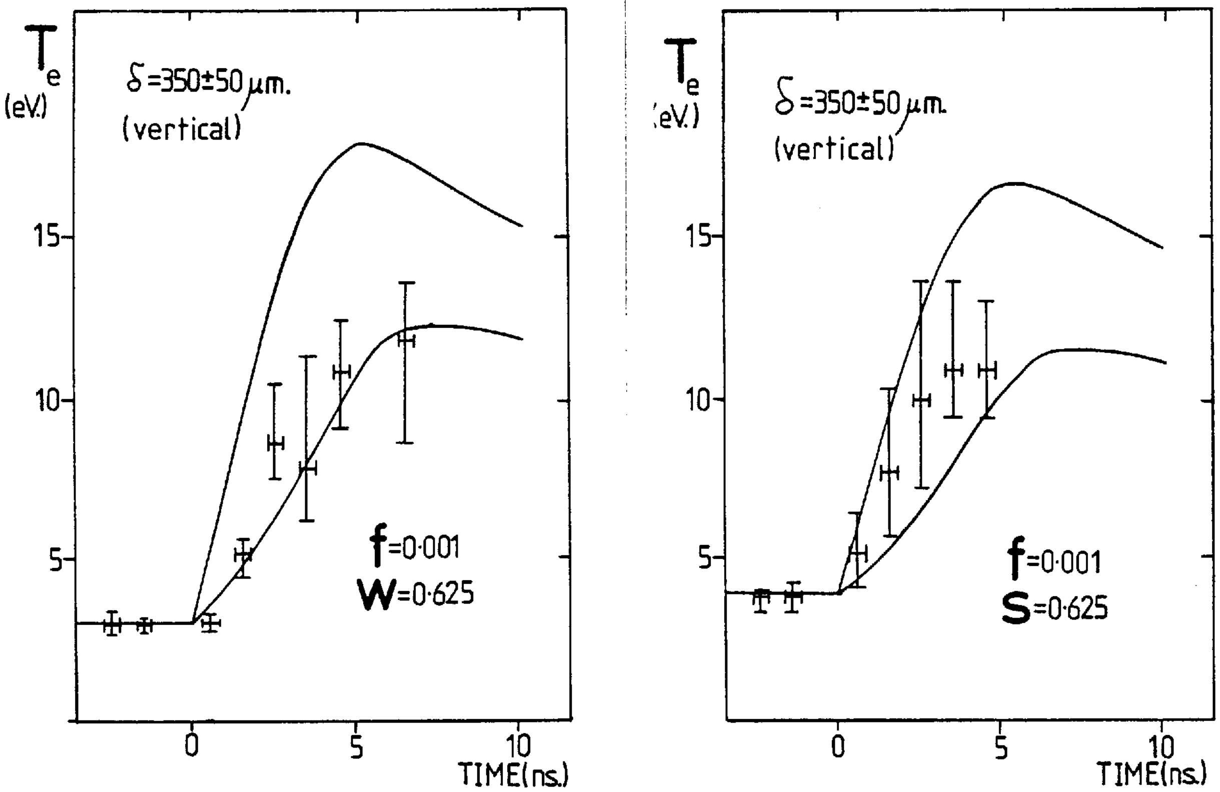

Fig. (5-11) Fit obtained to data from runs 6 and 5 of Table (3-1).

The 640μm results needed more conduction and fitted at (w = 0.625, f = 0.08) as shown in Fig. (5-12).

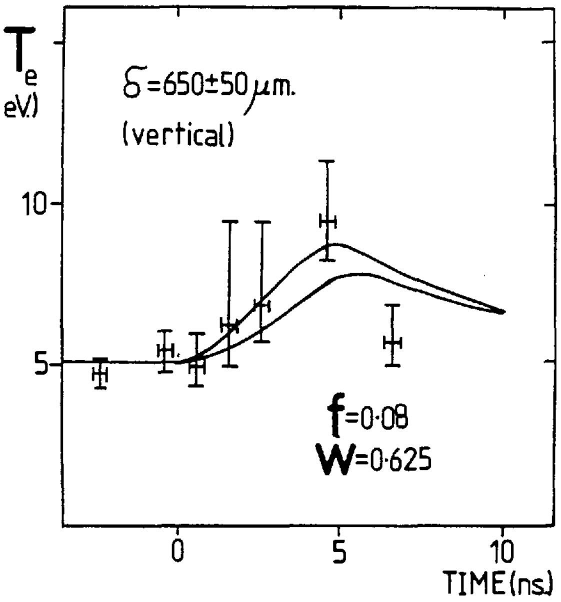

Fig. (5-12) Fit to data from run 7 of Table (3-1).

5. SUMMARY

The essential results of the experiment are the allowed (w,f) space regions of Figs. (5-5) and (5-9). These show reasonable agreement between the 3ns and 20ns pulse results. From these plots we can see that the experiment is best represented by classical inverse bremsstrahlung absorption with thermal conduction modelled classically up to a (2 → 5)% flux limit.

Modelling the thermal conduction simply with a reduced conduction coefficient - i.e. in $(w,s,f = 1)$ space - was much less successful giving a nearest fit to the 3ns data with $s = 0.065$, $w = 1.4$ and $f = 1$. These conduction/absorption conditions did not fit the 20ns data.

Finally, some early low grade results were included in section 4. These results needed a flux limit of 0.1% near the focal spot edge but a flux limit of 8% further out. No consistent explanation has been found for this.

CHAPTER 6

SPITZER'S THEORY AND ITS BREAKDOWN

1. INTRODUCTION

This chapter is included to illustrate the lack of any rigorous theory for heat conduction down large temperature gradients. In particular, Spitzer's first-order perturbation theory is shown to be inadequate when $\lambda_e/L \geqslant 0.02$ due to the dominance of second-order terms. The theory is briefly outlined to illustrate where these second-order terms are neglected and why the derived perturbed electron distribution function is unphysical. This chapter is based on the papers of Cohen et al.[78] and Spitzer et al.[5] They used a Fokker-Planck collision term and applied numerical methods to determine the perturbation to a Maxwellian velocity distribution in the presence of an electric field and a temperature gradient but in the absence of a magnetic field.

Other workers have considered the presence of a magnetic field. Landshoff[1] calculated the conduction coefficients at right angles to the magnetic field using an analytic expansion of the collision term in the Boltzmann equation. Braginskii[2] used a derivation similar to that of Chapman and Cowling[81]. Shkarofsky[4] solved the Fokker-Planck equation analytically. Robinson and Bernstein[79] calculated the transport coefficients of a fully ionized plasma in a magnetic field using variational principles. They give a lengthy tabulation of the transport coefficients for all magnetic fields. Shkarofsky, Robinson and Bernstein[80] simplified the tabulations of Robinson and Bernstein.

2. OUTLINE OF THE THEORY OF SPITZER ET AL.[5,78]

The starting point is the familiar Boltzmann equation:-

$$\delta f_r/_{\delta t} + \Sigma_i \; v_{ri} \frac{\delta f_r}{\delta x_i} + \Sigma_i \; F_{ri} \frac{\delta f_r}{\delta v_{ri}} = \Sigma_s \left(\frac{\delta_e f_r}{\delta t} \right)_s \quad (6\text{-}1)$$

This equation describes the rate of change of the velocity distribution function, f_r, for particles of type r interacting with particles of type s. The Σ_i is over the three co-ordinate directions and the Σ_s (species) includes s = r.

Energy transport through the plasma occurs despite the collision term $\Sigma_s(\frac{\delta_e f_r}{\delta t})_s$. There are four scale lengths which are important for this term:-

(α) b_o - the collision parameter for the 90^o single collision deflection of an electron by a stationary ion.

(β) d - the mean distance of an electron to its nearest neighbour.

(γ) h - the Debye shielding length.

(σ) λ - the mean free path for a net 90^o deflection.

In the Z-pinch plasma (and in most plasmas) it is true that: $b_o \ll d \ll h \ll \lambda$. Let us call the impact parameter b and consider:-

(i) $b < b_o$ - these "close" encounters give large deflections and are relatively infrequent.

(ii) $d > b > b_o$ - these "distant" encounters produce smaller deflections and are much more frequent.

(iii) $h > b > d$ - simultaneous encounters are now taking place between more than two particles but it is argued that the formulae for successive two-body encounters are still valid.

(iv) $b > h$ - outside the Debye sphere electrons are being scattered by the electric fields of organised oscillations (the single electrons are now being screened.)

Table 1 of Cohen et al.[78] gives the cumulative mean-square deflection for various impact parameters and shows that in a gas of charged particles multiple distant encounters are more important than close encounters. Collisions with $b < b_0$ are then not considered (inaccuracy ~10%). For $b > h$, charged particles are mutually electrically screened and the interaction is between a single electron and plasma oscillations. This interaction is weak and neglected (inaccuracy ~ $\ln[h/b_0]$ ~ 10%). Given the above approximations, subsequent collisions are independent events and describable as a Markoff process (e.g. Brownian motion). A Fokker-Planck collision term was then used:-

$$(\delta fe/_{\delta t})_s = - K(f_r f_s) \tag{6-2}$$

Following Chapman and Cowling[81], a perturbation method was used:-

$$f_r = f_r^{(0)} + f_r^{(1)} \tag{6-3}$$

and $$f_r^{(1)}(x) = f_r^{(0)}(x) \; D_r(x) \; \cos\theta \tag{6-4}$$

where $x = (mv^2/2kT_e)^{\frac{1}{2}}$ (a dimensionless parameter), $f^{(0)}(x)$ is a Maxwellian and θ is the angle between the direction of particle motion and $\nabla \underline{T}_e$ and $\underline{E}$. Substituting equations (6-2) and (6-3) into (6-1) they get:-

$$f_r^{(0)}\left\{\frac{m_r v_r^2}{2kT} - \frac{5}{2}\right\} \Sigma_i \, v_{ri} \, \frac{\delta T}{T\delta x_i} - f_r^{(0)} \frac{eZ_r}{kT}$$

$$\Sigma_i \; E_i \, v_{ri} + \Sigma_s K\,(f_r^{(1)} f_s^{(0)}) + \Sigma_s K\,(f_r^{(0)} f_s^{(1)}) = 0 \tag{6-5}$$

where they have neglected the second-order terms in $\{f^{(1)}\}^2$ and

$\underline{v}. \nabla f^{(1)}$. Note also that this equation is true for constant pressure. Substituting for the collision terms in equation (6-5) using equation (6-4) they get a second-order differential equation for the perturbation function D(x):-

$$D^{11}(x) + P(x)\, D^{1}(x) + Q(x)\, D(x) = R(x) + S(x) \qquad (6\text{-}6)$$

Equation (6-6) is solved numerically. The coupled effects of electric field and temperature gradient occur in the R(x) term:-

$$R(x) = \text{function } (x) \,.\, A + \text{Function } (x) \,.\, B$$

where

$$A = -(2kT_e)E \,/ 2\pi e^3\, n_e \ln \Lambda \qquad (6\text{-}7)$$

and

$$B = 2k^2 T_e\, |\nabla T_e| / \pi e^4\, n_e \ln \Lambda \qquad (6\text{-}8)$$

Tables I and II in Spitzer et al.[5] give the solutions for the perturbation function D(x) in the form of $zD_E(x)/A$ and $zD_T(x)/B$.

3. EXAMINATION OF THE PERTURBED DISTRIBUTION FUNCTIONS

By numerically integrating the perturbed distribution function for a non-current carrying plasma with a temperature gradient, the region of velocity space where the heat flux is carried was established. Let us call:

$$zD_E(x)/A = P_E(x)$$

and

$$zD_T(x)/B = P_T(x)$$

Then from equations (6-3) and (6-4) we have for a perturbed distribution function:-

$$f_p(x) = f^{(0)}(x)\left\{1 + \left[AP_E(x) + BP_T(x)\right] \cos\theta/z\right\} \qquad (6\text{-}9)$$

$f_p(x)$ was investigated under the following conditions:-

(i) $z = 1$

(ii) In a non-current carrying plasma $j = 0 = \sigma\underline{E} + \alpha\nabla\underline{T}_e$. From equations (6-7) and (6-8) and Spitzer et al.[5] this defines $A = 0.3517B$ for $z = 1$. Subsequently, increasing perturbations will now be labelled in terms of this B parameter (Note $\lambda_e/L = 0.748B$).

(iii) Directions of $\theta = 0^0$ and 180^0 only are used. This is a simplification justified since the dominant conduction is along $\nabla\underline{T}_e$.

(iv) The energy flux transported is calculated by multiplying the velocity distribution function by x^5. The energy flux $\propto \int_{-\infty}^{+\infty} \frac{1}{2}mv^2 v \cos\theta\, f(v)\, v^2 \sin\theta d\theta d\phi dv$.

An unperturbed (i.e. Maxwellian) distribution function carried no net heat flux i.e.:-

$$\int_{-\infty}^{\infty} x^5 \; f^{(0)}(x)\; dx = 0.$$

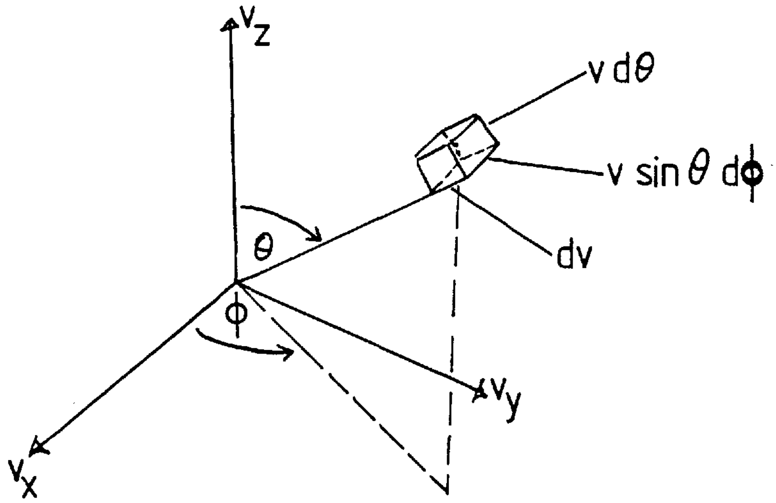

The net heat flux is carried by the perturbation function $\left[AP_E(x) + BP_T(x)\right] e^{-x^2}$ which adds to the Maxwellian in the $\theta = 0^o$ direction and subtracts from it in the $\theta = 180^o$ direction. Thus the flux carried in different regions of velocity is given by the function:

$x^5 \left[AP_E(x) + BP_T(x)\right] e^{-x^2}$. A calculation of this function using the tabulations of Sptizer et al.[5] is shown in Fig. (6-1)(a).

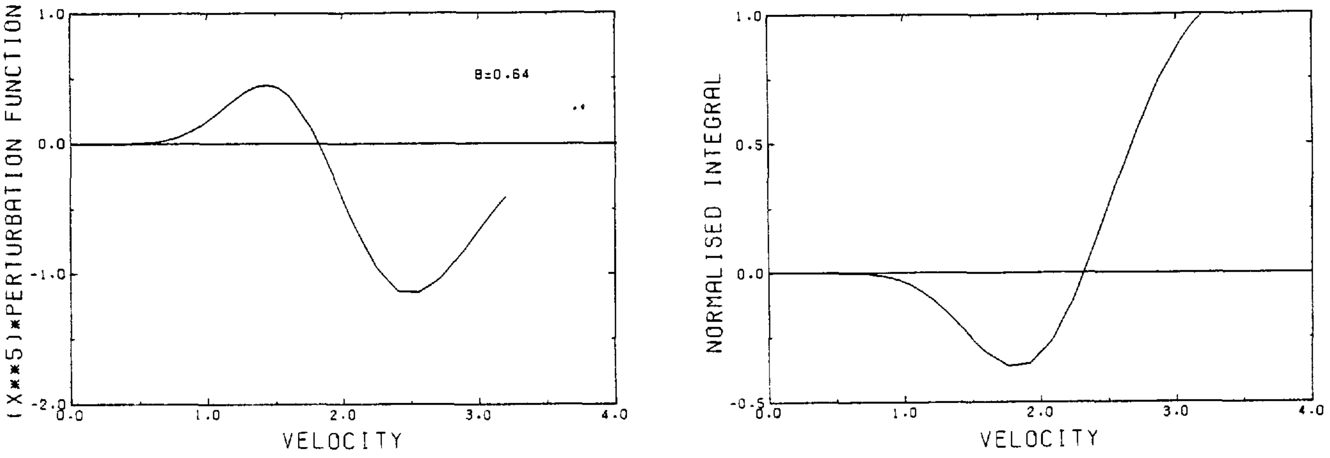

Fig. (6-1) (a) (b)

The B value here affects only the amplitude and not the functional dependence of these plots. The initial positive swing in Fig. (6-1)(a) is attributable to a net energy carried up the temperature gradient by electrons returning to maintain charge neutrality.

The "normalised" integral shown in Fig. (6-1)(b) is defined as:-

$$\int_0^x x^5 \left[AP_E(x) + BP_T(x)\right] e^{-x^2} dx \Big/ \int_0^\infty x^5 \left[AP_E(x) + BP_T(x)\right] e^{-x^2} dx$$

Fig. (6-1)(b) shows that the net energy flux is carried by electrons with velocities of 2 to 3 times v_{the}.

The perturbed distribution functions ($f_p(x)$ in Equation (6-9)) were then calculated for various B values. These are shown in Fig. (6-2) on a logarithmic scale. Note that for $B > 0.02$ the distribution function swings negative on the positive x side. (This is denoted by a * on the diagram). This surprisingly low value of the perturbation parameter arises because heat flux is a high moment of the distribution function. The interpretation of this non-physical behaviour of these distribution functions is that the second-order terms which were neglected in the derivation of equation (6-5) become important for $B > 0.02$. The negative swing of the distribution function in the velocity direction along $\nabla \underline{T}_e$ means that the derived (1st-order) conduction coefficient has been an over-estimate of the conductivity. However, whether the perturbation function should be modified in both velocity directions is not yet clear.

Note that the lack of a return current shift in the peak of the distribution functions of Fig. (6-2) was because only directions of $\theta = 0^0$ and 180^0 were considered. The computer program used to calculate the distribution functions and fluxes from the values for $D_E(x)$ and $D_T(x)$ is listed in Appendix D.

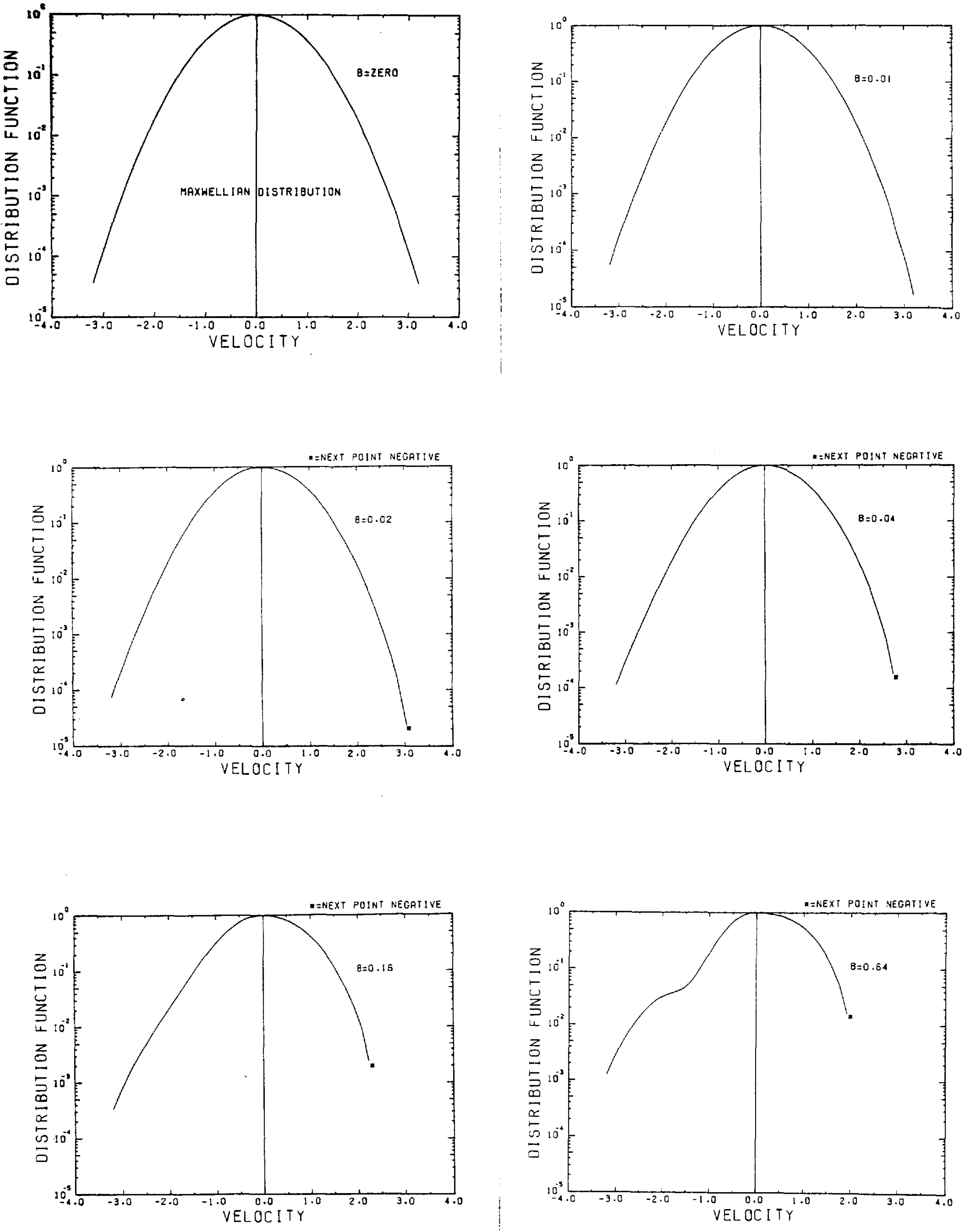

Fig. (6-2) Perturbed distribution functions from Spitzer et al.[5] for increasing B values.

CHAPTER 7

DISCUSSION OF THE RESULTS

1. INTRODUCTION

The essential results are summarised and discussed in this chapter. The determined conduction/absorption values are shown to be reasonable in the presence of the observed turbulence level. In the light of the results of this thesis, the previous work of M.S. White[55] is discussed and future work is outlined.

2. THE CONDUCTION/ABSORPTION SPACE FITS

It was found in Chapter 5 that the application of a flux limit rather than a blanket reduction of the conductivity constant in the computer program gave the most consistent and best agreement with the experiment. In particular, comparing the 3ns and 20ns data it was found that fits were obtained by varying the absorption and the flux limit, but could not be obtained by varying the absorption and the conductivity coefficient.

In Chapter 6, Spitzer's theory[5] was found incorrect for $\lambda_e/L \gtrsim 0.02$. In the present experiment $(\lambda_e/L)_{max.} \simeq 0.5$ (See Fig. 7-2) and no (w,s,f = 1) space fit is therefore expected.

In the previous low power experiment by M.S. White et al.,[10] matching of experimental and computational results for temperature gradients characterised by $\lambda_e/L \lesssim 0.04$ gave the result (w = 1, s = 0.4 ± 0.2). In Fig. (7-1) White's results are compared with simulations when the conductivity is flux limited. It is seen that in this case, the simulations are a poor fit to the data.

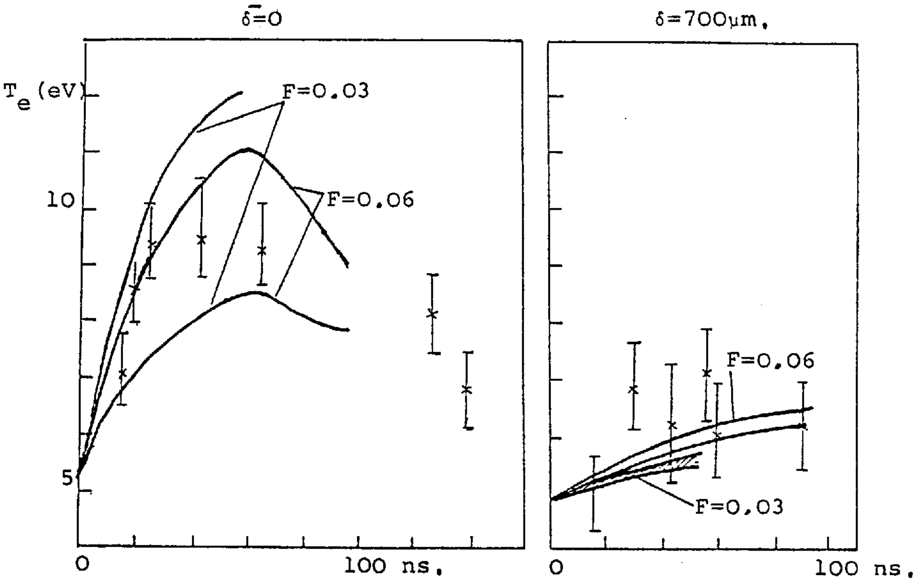

Fig. (7-1) Comparison of White's data with simulations for (w = 1, s = 1, f = 0.03 and 0.06).

3. THE OBSERVED TURBULENCE

The observation of low frequency turbulence in the focal spot region was described in Chapter 3, part 6. This ion acoustic turbulence is presumed to be driven by the cold electron return current. The reason for this is as follows.

Stimulated Brillouin backscattering may be ruled out as the source of the turbulence because no backscattered light was observed at the lower pinch densities and the ion feature enhancement (Fig. 3-7) lasted for longer than the CO_2 laser pulse (Fig. 3-5). In part 6 of this chapter the ion-acoustic damping rate is given and with $k \sim k_D$, $T_e \sim 4T_i \sim 16eV$ the Landau damping rate is $\sim 1.43\ 10^{11}\ s^{-1}$

For increasing T_e/T_i, ion-acoustic waves become weakly ion Landau damped ($v_{ia} >> v_{thi}$) and have a phase velocity $<< v_{the}$. Thus they can easily be driven unstable by a small distortion in the velocity distribution function. Forslund[8] gives a threshold for the heat flux instability in equation 16 of his paper. For our conditions, this gives $\lambda_e/L = 0.6$ for $T_e/T_i = 5$ which is close to observed maximum of $\lambda_e/L \sim 0.5$. Using the computer output from the best fit to the 3ns pulse data (w = 1, s = 1, f = 0.03), λ_e/L vs. radius at various times has been calculated and is shown in Fig. (7-2). Thus, λ_e/L is largest near the edge of the focal region at ~ 2ns. It is presumed that the instability switches on locally within the radial width of the $\delta = 0$ function and not within the width of the $\delta = 800\mu m$ function. However, no hard quantitative work may be persued here as the distribution functions on which Forslund's[8] threshold calculations are based become unphysical when $\lambda_e/L \geq 0.02$.

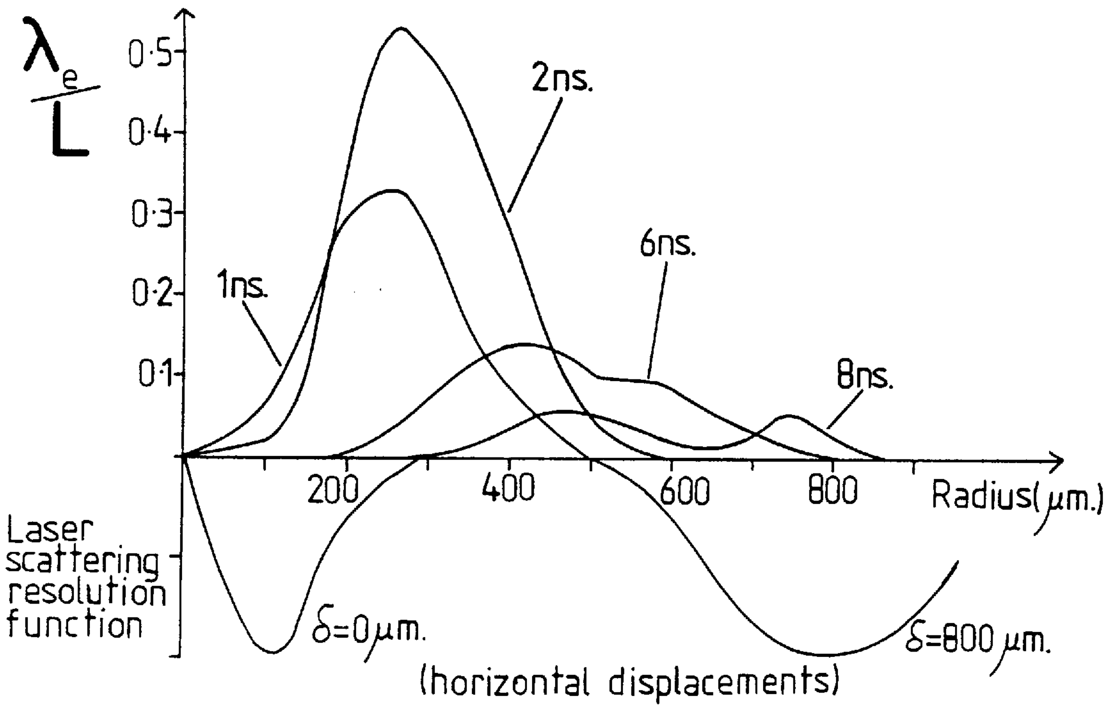
$\frac{\lambda_e}{L}$
0·5
0·4
0·3
0·2
0·1
1ns.
2ns.
6ns.
8ns.
200
400
600
800
Radius(μm.)
Laser scattering resolution function
δ=0μm.
δ=800 μm.
(horizontal displacements)

Fig. (7-2)

4. THE THERMAL CONDUCTIVITY

Fig. 7-3 summarises the results of the present experiment and that of M.S. White et al.[10] (here labelled Ref. (2)) and compares them with Spitzer's theory.

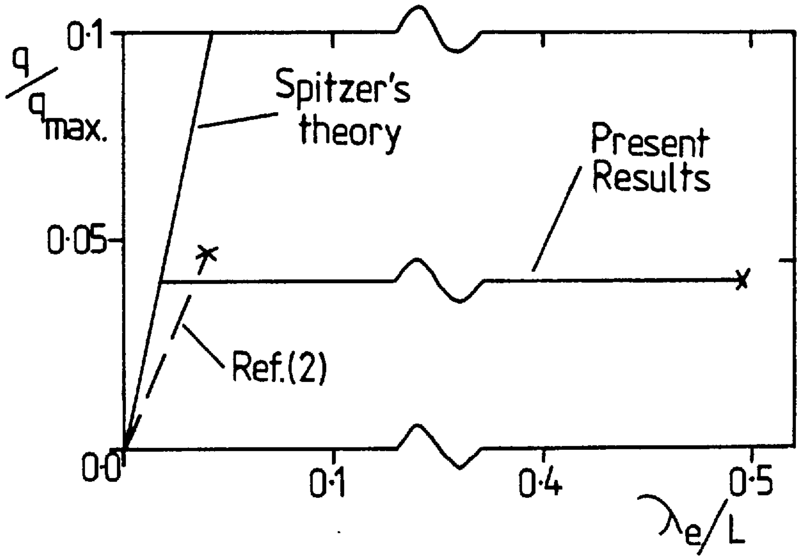

Fig. (7-3)

The deviation of the Ref. (2) experiment from Spitzer's theory is attributed to the failure of first-order theory as described. In that experiment no evidence for ion-acoustic turbulence was observed or expected since the 70ns long CO_2 laser pulse allowed equilibration of T_e and T_i to within 10%.

In the present experiment, the λ_e/L perturbation was increased from 0.04 to 0.5 but the normalized heat flux $q/q_{max.}$ was no higher than in the low power case. Although, an exact theory for large temperature gradients does not exist, it is reasonable to expect that in the absence of turbulence $q/q_{max.}$ would increase as λ_e/L increases. The fact that it does not is attributed to the observed ion-acoustic turbulence. Unfortunately, this observation was made at only one wave number namely $k_s \sim 2/\lambda_D$ (as $\alpha \sim \frac{1}{2}$). Measurements of the turbulence level in other parts of the wave spectrum by varying the laser scattering angle were not taken due to time constraints imposed on the experiment by A.W.R.E. Therefore, for the calculation of the flux limitation the shape of the spectral function has been taken from the simulation of current driven ion-acoustic turbulence by Dum, Chodura and Biskamp.[83] Manheimer[9] gives a value for the turbulence limited thermal conductivity in terms of the electric field fluctuations of the ion-acoustic waves. These electric field fluctuations may be related to the density fluctuations ($\delta n/n$) via the fluid equations. In turn $\delta n/n$ is directly related to the laser scattering cross-section. We may therefore check that the determined heat flux limitation is reasonable in the presence of the observed turbulence. The calculation proceeds as follows:-

(a) Relationship between $E_1(\underline{k}, \omega)$ and $n_1(\underline{k},\omega)$

The relationship between the first order fluctuation in the density- $n_1(\underline{k},\omega)$ - and the first order electric field of the ion-acoustic waves - $E_1(\underline{k},\omega)$ - may be evaluated from the fluid equations. We assume that all the energy involved in the compressions and expansions of the ion-acoustic waves leads to adiabatic heating and cooling. i.e. :-

$$p/_{\rho}\gamma = K \qquad \text{(a constant)}$$

Continuity

$$\partial n/_{\partial t} = -\nabla.(vn)$$

Mtum.

$$\partial/_{\partial t}\ (m\underline{v}n) = +ne\underline{E} - \nabla.\ (mn\ \underline{v}\ \underline{v}) - \nabla p$$

We take a periodic variation in 1D:-

$$T = T_o + T_1\ e^{i\ (\omega t + kx)}$$

$$v = v_o + v_1\ e^{i\ (\omega t + kx)}$$

$$n = n_o + n_1\ e^{i\ (\omega t + kx)} \qquad \text{N.B.}\ \ v_o = 0,\ \ T_o \neq n_o \neq 0.$$

We write the equations in first order and linearize. The continuity equation becomes:-

$$kv_1 \quad = \quad -\omega\, n_1/n_o \tag{7-1}$$

With $p = nk_BT$ and $\rho = n\ m$ the adiabatic equation becomes:

$$\frac{k_B\ (T_o + T_1)}{(n_o+n_1)^{\gamma-1} m^\gamma} \quad = \quad K \quad = \quad \frac{k_B\ T_o(1+{}^{T_1}/T_o)(1-(\gamma-1)^{n_1}/n_o)}{m^\gamma\ n_o^{\gamma-1}}$$

and using $\quad k_BT_o/n_o^{\gamma-1}\ m^\gamma = K$

$$\therefore \quad n_o\ T_1 + n_1\ T_o \quad = \gamma\ n_1\ T_o \tag{7-2}$$

The momentum equation becomes:-

$$\partial/_{\partial t} \quad (v_1) \quad + \quad \frac{k_B}{m(n_o+n_1)} \quad \nabla\ (n_o\ T_1 + n_1\ T_o) - eE_1/_m \quad = \quad 0$$

and substituting from (7-2) for $n_o\ T_1 + n_1\ T_o$ and from (7-1) for v_1:

$$\therefore \quad -\frac{i\omega^2}{k}\ {}^{n_1}/_{n_o} \quad + \quad \frac{i\ kk_B\ \gamma\ n_1\ T_o}{mn_o} \quad (1-{}^{n_1}/_{n_o}) \quad - \quad \frac{eE_1}{m} \quad = \quad 0$$

$$\therefore \quad i{}^{n_1}/_{n_o}\ (-\ {}^{\omega^2}/_k \quad + \quad \frac{\gamma k_B T_o}{m}\ k) \quad - \quad \frac{eE_1}{m} \quad = \quad 0$$

The electron thermal speed $v_e = (\gamma k_BT_o/m)^{\frac{1}{2}}$ is very much larger than the phase velocity of the ion acoustic waves (ω/k) and so:-

$${}^{n_1}/_{n_o} \quad = \quad i\ \frac{e}{m\ k\ v_e^2} \quad E_1(\underline{k},\omega) \tag{7-3}$$

(b) Relationship between W and S(k,ω)

The energy of the turbulent electric field W, is

$$W = \lim_{V,t\to\infty} \frac{1}{Vt} \iiiint \tfrac{1}{2}\, \varepsilon_0 E^2(\underline{r},t)\, d^3\underline{r}\, dt$$

which by Parseval's Theorem

$$= \left(\frac{1}{2\pi}\right)^4 \lim_{V,t\to\infty} \frac{1}{Vt} \iiiint \tfrac{1}{2}\, \varepsilon_0 E^2(\omega,\underline{k})\, d\,\omega\, d^3\underline{k}$$

and from (7-3)

$$= \left(\frac{1}{2\pi}\right)^4 \lim_{V,t\to\infty} \frac{1}{Vt} \iiiint \frac{n_1^2(\underline{k},\omega)}{n_0^{\,2}}\, \frac{m^2 v_e^{\,4}}{e^2}\, \frac{k^2 \varepsilon_0}{2}\, d^3\underline{k}\, d\omega$$

The plasma scattering cross-section at a given scattering vector $\underline{k}$ and at a frequency displacement ω from the incident laser beam is

$$\frac{d^2\sigma}{d\Omega\, d\omega} = \left(\frac{e^2}{4\pi\mu_0 m}\right) S^2(\underline{k},\omega)\, \sin^2\theta$$

S(k,ω) is the spectral power density of the fluctuations and is directly related to the wave density in the plasma by[6]

$$S(\underline{k},\omega) = \lim_{Vt\to\infty} \frac{1}{Vt} \frac{|n_1(\underline{k},\omega)|^2}{n_0}$$

Thus

$$W = \left(\frac{1}{2\pi}\right)^3 \frac{m_e}{\omega_{pe}^{\,2}}\, v_e^{\,4} \int_0^\infty S_i(k)\, k^4\, dk \tag{7-4}$$

where

$S_i(k) = \int_0^{\omega_{ia}} S(\underline{k},\omega)\, d\omega$ and assuming the turbulence is low

frequency.

(c) Relationship between the effective collision frequency ν^* and $S(\underline{k},\omega)$

From the numerical simulation[83] the effective collision frequency due to turbulence is:-

$$\nu^* \sim \omega_{pe} \frac{W}{n\,k_B\,T} = \omega_{pe} \left(\frac{1}{2\pi}\right)^2 \frac{2\gamma\,\lambda_{De}^5}{3\,N_D} \int_0^\infty S_i(k)\,k^4\,dk$$

where N_D is the number of particles in a Debye sphere.

The binary collision frequency is:-

$$\nu_{ei} = 8.79\;10^{-2}\;\omega_{pe}\;\ln\Lambda/N_D$$

Then, if $\gamma_e = 5/3$:

$$\nu^*/\nu_{ei} = 0.53\,\lambda_{De}^5 \int_0^\infty k^4\,S_i(k)\,dk \qquad (7\text{-}5)$$

where, ν^* is the collision frequency due to ion turbulence alone.

Using the spectral shape of $W(k)$ from the simulation and the experimental value for $S(k = 2/\lambda_D)$ we may now estimate ν^*/ν_{ei}. We measured $S_i(k)$ at $k = 2/\lambda_{De}$ (16eV, 4.10^{16} cm^{-3}) to be ~ 10 x thermal.

$$S_i(k) = Z\,\alpha^4/(1+\alpha^2)\,\{1+\alpha^2(1+z\,T_e/T_i)\}$$

The thermal level is thus 0.022 ($T_e = 4T_i$; $z = 1$, $\alpha = 0.5$) and therefore the observed level S_{io} $(k = 2/\lambda_{De}) = 0.22$. From equation 7-4:

$$W(k) \propto S_i(k)\,k^4 \qquad (7\text{-}6)$$

From Dum, Chodura and Biskamp[83] (Fig. 4):

$$W(k = 1/\lambda_{De})/W(k = 2/\lambda_{De}) = 10 \qquad (7\text{-}7)$$

(for $\omega_i\,t = 31$ i.e. $t \sim 5$ns)

Also note that for $k < 1/\lambda_{De}$, $W(k) \propto k$ and then we take this part as the major contribution to the integral of equation (7-5).

$$\therefore \frac{\Big[k^4 \, S_i(k)\Big]^{k = 1/\lambda_{De}}}{\Big[k^4 \, S_i(k)\Big]^{k = 2/\lambda_{De}}} = 10$$

$$\therefore \Big[k^4 \, S_i(k)\Big]^{k = 1/\lambda_{De}} = 10 \times \left({}^{2}/\lambda_{De}\right)^4 \times 0.22$$

Let $f(k) = k^4 \, S_i(k) = ak$ where a is a constant

Let $f(k = 1/\lambda_{De}) = V = a/\lambda_{De}$

$$\therefore f(k) = V\lambda_{De} \, k$$
$$= 2.2 \, (2/\lambda_{De})^4 \, \lambda_{De} \, k$$

$$\therefore \nu^*/\nu_{ei} = 0.53 \, \lambda_D^5 \int_{1/L}^{1/\lambda_{De}} f(k) \, dk$$

where L is the scale length $/2\pi$

$$\therefore \nu^*/\nu_{ei} = 0.53 \, \lambda_D^2 (2.2) \, 2^4 \Big[k^2/2\Big]_{1/L}^{1/\lambda_{De}}$$
$$= 9.33 \Big[1 - \lambda_{De}^2/L^2\Big]$$

If the scale length is 100μm, then L = 16μm and λ_{De} = .16μm

Thus ν^*/ν_{ei} has a peak value of ~ 10.

(d) Evaluation of the fractional fluctuation level

$$\left(\frac{\delta n}{n}\right)^2 = \lim_{V,t \to \infty} \iiiint \frac{n_1^2 \, (\underline{r},t) \, d^3\underline{r} \, dt}{n_o^{\,2} \, Vt}$$

which by Parseval's Theorem

$$= \left(\frac{1}{2\pi}\right)^4 \lim_{V,t\to\infty} \iiiint \frac{n_1^2\,(\omega,\underline{k})\; d^3\underline{k}\; d\omega}{Vt\; n_o^{\,2}}$$

$$= \left(\frac{1}{2\pi}\right)^3 \frac{2}{n_o} \int_0^\infty S_i\,(\underline{k})\; k^2 dk$$

Then using equations (7-6) and (7-7) we have

$$\frac{\left[k^2\, S_i(k)\right]\; k = 1/\lambda_{De}}{\left[k^2\, S_i(k)\right]\; k = 2/\lambda_{De}} = 40$$

Let $F(k) = k^2\, S_i(k)$, then

$$F(k = 1/\lambda_{De}) = 40 \times (2/\lambda_{De})^2 \times 0.22 = 35/\lambda_{De}^2$$

As before we integrate up to $1/\lambda_{De}$ with $W(k) \propto k$ and thus $F(k) \propto 1/_k$

$$\therefore \left(\frac{\delta n}{n}\right)^2 = \left(\frac{1}{2\pi}\right)^3 \frac{2}{n_o} \frac{35}{\lambda_{De}^3} \int_{1/_L}^{1/\lambda_{De}} \frac{1}{k}\, dk$$

$$= \left(\frac{1}{2\pi}\right)^3 \frac{70}{n_o\, \lambda_{De}^3} \ln\, (L/\lambda_{De})$$

And as before $L = 16\mu m$ and $\lambda_{De} = 0.16\mu m$.

$$\therefore \delta n/_n \sim 0.09.$$

If the ratio of $W(k = 1/\lambda_{De})$ to $W(k = 2/\lambda_{De})$ is only 2.5 then $\delta n/n \sim 0.05$. Clearly what is happening at low k is important in determining $\delta n/n$.

(e) The anomalous thermal conductivity

Manheimer[9] gives a value for the thermal conductivity in equation 20 of his paper:

$$K_{an} = \frac{2\sqrt{2\pi}}{\pi\,|k|} \quad V_e \; n \quad \left(\frac{e\,\phi(k)}{T_e}\right)^{-2}$$

where n has been added here to get it to the usual form. $\phi(k)$ is the coefficient in a Fourier series and Manheimer has simplified so that there is only one k value occuring. From Equation (7-3)

$$\frac{n_1\;(\underline{k},\omega)}{n_o} = i \quad \frac{e\;\phi(\underline{k},\omega)}{\gamma\;k_B T_e}$$

$$\therefore \quad \frac{e^2\;\phi^2(k)}{T_e^{\;2}} = 2\gamma^2 \quad \left(\frac{\delta n}{n}\right)^2$$

$$\therefore \quad K_{an} = \frac{2\sqrt{2\pi}}{\pi} \quad \frac{v_e n}{2\gamma^2} \quad \left(\frac{n}{\delta n}\right)^2 \; 2\;\lambda_{De}$$

where we have arbitrarily taken $k = 1/2\lambda_{De}$ and $v_e^2 = \gamma k_B T_e/m$

Now from Spitzer[3]:

$$K_{el} = \left(\frac{kT_e}{m_e}\right)^{\frac{1}{2}} \quad \lambda_{De}^4 \quad \frac{320\pi^2 n^2}{\ln\,\Lambda} \quad \left(\frac{2}{\pi}\right)^{3/2} \quad \delta\varepsilon$$

where $q_{el} = -K_{el}\;\nabla T_e$

$$\therefore \quad \frac{K_{an}}{K_{el}} = \frac{1}{\gamma^2\;n\;\lambda_{De}^3} \quad \left(\frac{n}{\delta n}\right)^2 \quad \frac{\ln\;\Lambda}{320\pi\delta\varepsilon}$$

where δ and ε are Spitzer's factors for a non-Lorentzian gas and zero current flow respectively.

So with $n\lambda_{De}^3 = 164 = N_D$

$$\therefore \quad K_{an}/K_{el} = (n/\delta n)^2 \;\; 2.25\;10^{-4}$$

$$\sim \;\; 0.03 \;\; \text{from section d.}$$

In fact, the computer program results were that if $q_{el} > (0.02 \rightarrow 0.04)q_{max}$. then flux is held to $(0.02 \rightarrow 0.04)q_{max}$.

With T_e in eV, ∇T_e in eV/cm and n_e in cm^{-3} we have

$$q_{e1} = 1.932\ 10^{21}\ T_e^{5/2}\ \nabla T_e/\ln\Lambda \quad eV\ cm^{-2}\ s^{-1}$$

$$q_{max} = \tfrac{1}{2}\ 6.692\ 10^{7}\ n_e\ T_e^{3/2} \quad eV\ cm^{-2}\ s^{-1}$$

From the best fit computer run used to generate Fig. 7.2 we have at a radius = 340μm and a time = 2ns a $\nabla T_{e\ max}$ = 700eV/cm at T_e = 12.7 eV and $n_e = 6.4\ 10^{16}$

$$\therefore\quad q_{e1} = 1.11\ 10^{26}\ eV\ cm^{-2}\ s^{-1}$$

and

$$q_{max} = 9.69\ 10^{25}\ eV\ cm^{-2}\ s^{-1}$$

Thus a 3% flux limit is certainly consistent with our observed turbulence level.

Note also that the method of limiting the flux in the regions of large temperature gradient is physically correct as it is in these regions where the turbulence level will be highest. Thus we would not expect a good fit in (w,s) space which has a blanket reduction in the conductivity constant.

5. THE ABSORPTION

From Figs. (5-5) and (5-9) it is seen that the inverse bremsstrahlung absorption used in the computer program fitted the experiment well. The saturation of inverse bremsstrahlung and the ponderomotive force were small corrections as described in Chapter 4 and thus the experiment confirmed the classical inverse bremsstrahlung coefficient to an accuracy ~ ±50%. The absorption coefficient is $\propto Z_{eff}$[76] and thus we have further evidence for the low impurity level in the plasma.

The fact that the ion-acoustic turbulence did not increase the absorption significantly agrees with the work of Faehl and Kruer[84] and of Manheimer, Colombant and Ripin[85]. This is because the plasma is about 2 orders of magnitude underdense for CO_2 laser light.

6. THE BACKSCATTERING

As described in Chapter 3, part 8, backscattered light was observed for plasma densities > 10^{17} cm^{-3}. The backscattered light was not spectrally resolved. In this section the thresholds and growth rates of the stimulated Brillouin and Raman instabilities are calculated and the rates of growth of the backscattering with incident power are compared with both a coherent wave theory[61,62] and a random phase theory[62,63].

(a) Thresholds for the instabilities

The thresholds calculated here are for an infinite homogeneous plasma pumped by an incident monochromatic wave. This approximation is reasonable since the z-pinch plasma is two orders of magnitude underdense for the CO_2 laser wavelength and the dominant density and temperature gradients are perpendicular to the incident $\underline{k}$ vector direction.

For these calculations, we use for the Landau damping rate:-

$$\gamma_{iaL} = \omega_{ia} \left(\frac{\pi}{2}\right)^{\frac{1}{2}} \left\{ \left(\frac{T_e}{T_i}\right)^{3/2} \exp\left[-\tfrac{1}{2} \left(\frac{T_e}{T_i} + 3\right)\right] + \left(\frac{m_e}{m_i}\right)^{\frac{1}{2}} \right\}$$

Forslund[8] gives the ion acoustic damping rate, for $v_{thi}^2 \ll v_{ia}^2 \ll v_{the}^2$, as:-

$$\omega_{ia} (\pi)^{-\frac{1}{2}} (1 + k^2\lambda_{De}^2)^{-1} \left\{ (m_e/2m_i)^{\frac{1}{2}} (1 + k^2\lambda_{De}^2)^{-\frac{1}{2}} + (2)^{-\frac{1}{2}} (T_e/T_i)^{3/2} \exp\left[-\tfrac{1}{2}(T_e/T_i + 3)\right]\right\}$$

in equation 15 of reference 8. For backscattering $k = 2k_{CO_2}$, where k_{CO_2} is the wave number of the incident CO_2 laser. Thus $k\lambda_{De} \sim 10^{-2}$. Tsytovich[63] gives the collisional damping rate for ion acoustic waves as:

$$\gamma_{coll} = \omega_{pe} (m_e/m_i) (\pi/2)^{\frac{1}{2}} v_{the}/c$$

Collisional damping was neglected in these calculations since $\gamma_{iaL} >> \gamma_{coll}$ in all cases.

Also for these calculations we take the initial plasma conditions as $n_e = 3.10^{17}$ cm^{-3} and T_e = 5eV. These conditions were measured using the multi-channel laser scattering system and a 20ns (FWHM) ruby pulse after completion of the backscattering measurements. The peak temperature at the focus of the CO_2 laser was taken as 20eV (as a reasonable estimate).

(i) Stimulated Brillouin Scattering

Lashmore-Davis[61] and Chen[86] both give the same coherent-wave threshold:-

$$v_o^2 / v_e^2 > 8 \;\; \gamma_s/\omega_{ia} \;\; {}^{\nu_{ei}}/\omega_o \qquad (7\text{-}8)$$

where $v_o = eE_o/m_e \, \omega_o$ and is the quiver velocity of an electron in the field of the pump wave, $v_e^2 = kT_e/m_e$, γ_s is the damping rate of the ion acoustic wave of frequency ω_{ia} and ν_{ei} is the electron collision frequency.

The threshold was calculated for three positions along the heating laser axis:- at the focal plane, between the focal plane and the edge of the plasma, and at the plasma edge; i.e. conditions of -

(α) $n_e = 3.10^{17}$ cm^{-3}, T_e = 20eV, T_i = 5eV;
(β) 3.10^{17} cm^{-3}, 10eV, 5eV;
(γ) 3.10^{17} cm^{-3}, 5eV, 5eV.

Landau damping dominated the collisional damping of the ion acoustic wave.

From equation (7-8) the thresholds for these conditions are:

(α) 1.2 10^9 Wcm^{-2};
(β) 1.3 10^9 Wcm^{-2}, and
(γ) 1.2 10^9 Wcm^{-2}.

(ii) Stimulated Raman Scattering

Lashmore-Davis gives the coherent wave threshold as:-

$$v_o^2/v_e^2 > \frac{4}{(k_e\lambda_{De})^2} \quad {}^{\nu_{ei}}/_{\omega_{pe}} \quad {}^{\nu_{ei}}/_{\omega_L} \tag{7-9}$$

where k_e is the wave number of the Langmuir wave, ω_L is the incident laser frequency and ν_{ei}, v_o and v_e are as equation (7-8). The thresholds for the above plasma conditions are: (α) 3.1 10^8 Wcm^{-2}; (γ) 1.5 10^{10} Wcm^{-2}.

(iii) The incident light intensities used

The laser light intensity incident on the plasma was determined as described in Chapter 2. The plasma was estimated to extend 5mms on either side of the focal plane. The peak flux density at the plasma edge was 4.3 ± 0.9 10^{10} Wcm^{-2} and at the focus 2.3 ± 0.5 10^{11} Wcm^{-2} when the above results were obtained. Both instabilities are therefore theoretically above threshold.

(b) Stimulated Brillouin Growth Rates

(i) Coherent wave theory

This theory defines a growth rate γ_o scaling as $I_o^{\frac{1}{2}} T_e^{-\frac{1}{4}}$ competing against an ion acoustic damping rate γ_{iaL} over a scale length l. Thus, we have:

$$P_B = P_N \; \exp \; \{ \, 2\gamma_o^2 \; l/\gamma_{iaL} c \, \} \tag{7-10}$$

This exponential was integrated over distance through the plasma as follows. The $T_e^{-\frac{1}{4}}$ dependence of γ_o was ignored. The focussing of the beam was modelled as a linear increase in intensity from the plasma edge to the focal plane:-

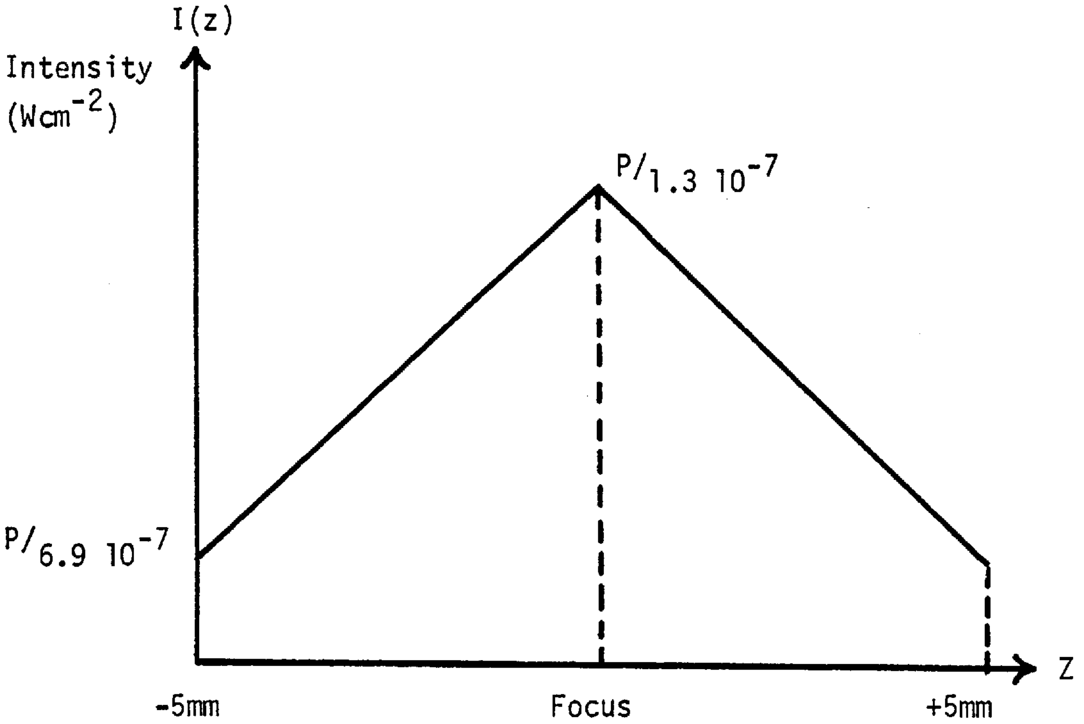

Fig. (7-4)

i.e. $I(z) = bz + a$ and P = incident laser power in watts.

$a = P/6.9\ 10^{-7}\ \mathrm{Wm}^{-2}$ and

$b = P(1.25\ 10^{9})\ \mathrm{Wm}^{-3}$.

The growth rate given by Offenburger[62] is:-

$\gamma_o = \frac{1}{2}\ {}^{v_o}/_{c}\ ({}^{\omega_o}/_{\omega_s})^{\frac{1}{2}}\omega_{pi}$ where ω_{pi} is the ion plasma frequency.

For $n_e = 3.10^{17}\ \mathrm{cm}^{-3}$;

$T_e = T_i = 5\mathrm{eV}$, then:-

$$\gamma_o^2 = A_1\ I(z) \quad \text{where } A_1 = 2.56\ 10^6\ \mathrm{MkS}. \tag{7-11}$$

The Landau damping rate γ_{iaL} was also modelled as a linear increase:

(Note that any rarefaction of the plasma electron density was ignored on the 1 → 2ns timescale of the backscattering.)

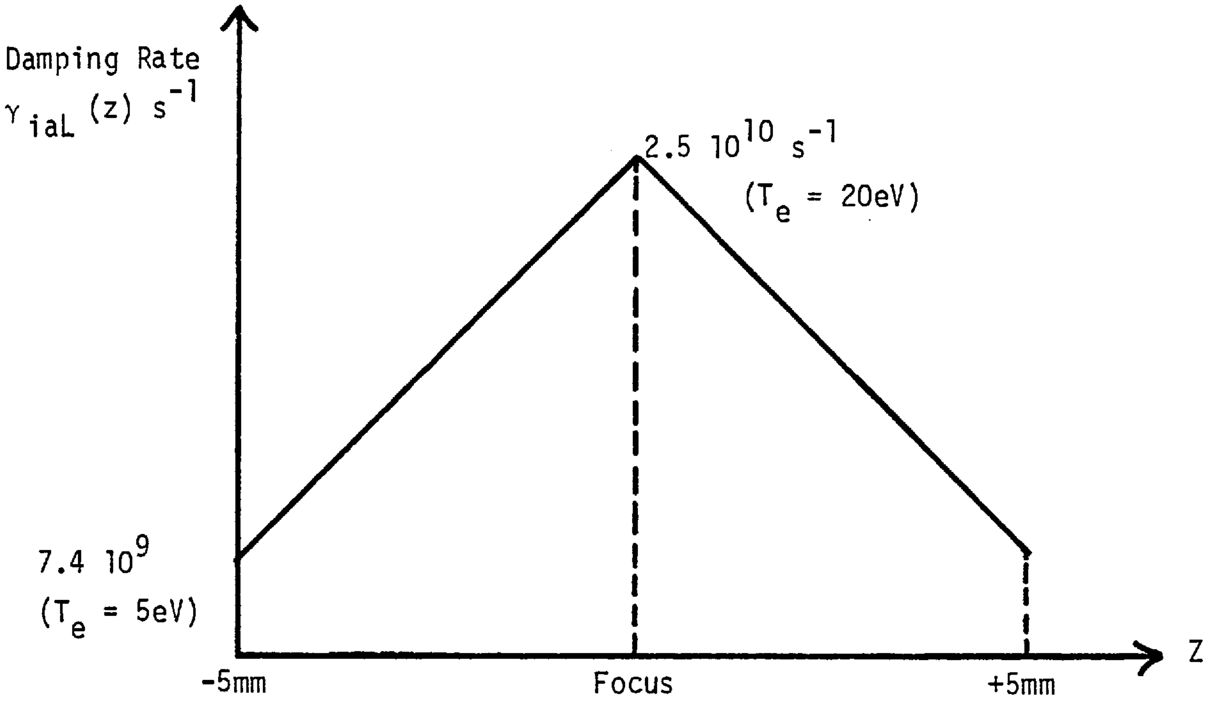

Fig. (7-5)

i.e. $\gamma_{iaL}(z) = fz + g$

where $g = 7.4\ 10^9\ s^{-1}$

and $f = 3.5\ 10^{13}\ s^{-1}\ m^{-1}$

$$\therefore \quad P_B/P_N = \exp\left\{ \frac{2A_1}{c}\ 2 \int_{\substack{\text{plasma}\\ \text{edge}}}^{\text{focus}} \frac{bz + a}{fz + g}\ dz \right\}$$

A standard integral:-

$$\int_0^z \frac{bz + a}{fz + g}\ dz = \left[\frac{bz}{f} + \left(\frac{af - bg}{f^2}\right) \ln (fz + g) \right]_0^z$$

Thus the value of the exponential may be evaluated theoretically. Experimentally, the exponential is evaluated from a plot such as Fig. (3-13). For a given incident power the exponential = $\ln P_B - \ln P_N$. Table (7-1) gives the theoretical/experimental comparisons of the exponential at peak power.

SHOT NUMBER	THEORY	EXP
1	2.7	7.9
2	2.6	5.2
3	3.6	4.8

Table (7-1)

From equation (7-11) the growth rates at the time of peak intensity are typically ~ 3 $10^{10} s^{-1}$ at the plasma edge and ~ 8 10^{10} s^{-1} at the focus.

(ii) Random Phase Theory

This theory gives a growth rate γ_k scaling as I and we have:

$$P_B = P_N \exp \{ \gamma_k l/c \}$$

The growth rate is given by Offenburger[62] as:

$$\gamma_k = \frac{(2\pi)^3 r_o^2 n_o I}{(k T_i) k_o^3} \times \frac{x\Gamma_\beta (x)}{\sqrt{\pi}}$$

where r_o is the classical electron radius, n_o is the plasma density T_i is the ion temperature and k_o is the incident laser wave number.

Fig. 1, of his paper was used to determine $x\Gamma_\beta (x)/\sqrt{\pi}$. As in (i) plasma conditions of ($n_e = 3.10^{17}$, T_e = 5eV, T_i = 5eV) at the plasma edge and (3.10^{17}, 20eV, 5eV) at the focus were assumed. Thus using curves a and d of Fig. 1 of that paper we have

$x\Gamma_\beta (x)/\sqrt{\pi} \simeq 0.2$ at the plasma edge

$x\Gamma_\beta (x)/\sqrt{\pi} \simeq 0.22$ at the focus

for the waves of maximum growth.

Now writing

$$\gamma_k(z) = A_2\, I(z) \quad \frac{x\Gamma_\beta(x)}{\sqrt{\pi}} \quad (z) \qquad (7\text{-}12)$$

where $A_2 = 3.54\ 10^{-3}$ (MkS) for the above plasma conditions and I(z) is as Fig. (7-4). The growth rate was then approximated as a linear increase to the focus:-

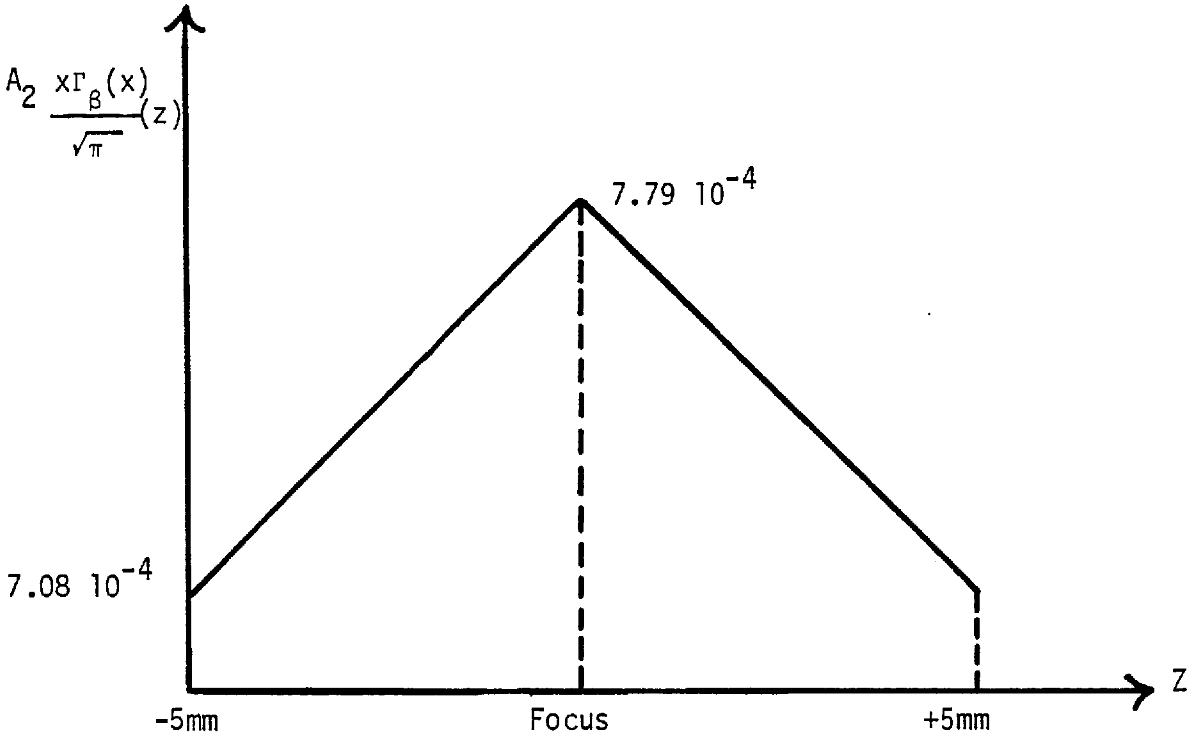

i.e. $A_2 \times \Gamma_\beta\ (x)/\sqrt{\pi}\ (z) = pz + q$

where $q = 7.08\ 10^{-4}$

$p = 0.014.$

$$\therefore\quad P_B/P_N = \exp\left\{\frac{2}{c}\int_{\substack{\text{plasma}\\ \text{edge}}}^{\text{focus}} (bz + a)(pz + q)\ dz\right\}$$

$$\therefore\quad \text{Exponential} = \frac{2}{c}\left[\,bpz^3/3 + \frac{bq + ap}{2}\ z^2 + aqz\right]_{\substack{\text{plasma}\\ \text{edge}}}^{\text{focus}}$$

Table (7-2) gives the theoretical/experimental comparisons for the random phase exponential.

SHOT NUMBER	THEORY	EXP
1	32	7.9
2	31	5.2
3	42	4.8

Table (7-2).

From Equation (7-12) the growth rates at the time of peak intensity are typically ~ 3 10^{11} at the plasma edge and 2.10^{12} at the focus.

(c) Stimulated Raman Growth Rates

In this case, only the coherent wave growth rate given by Lashmore-Davis[61] was calculated. As before:-

$$P_B = P_N \exp \{ 2\gamma_0{}^2 \, 1/\gamma_s \, c \}$$

where

$$\gamma_0 = \frac{K_1\lambda_{De}}{4} \left(\frac{\omega_{pe}}{\omega_0}\right)^{\frac{1}{2}} {}^{v_0}/{}_{v_{th}} \quad \omega_{pe}$$

Note that this is T_e independent. For our plasma conditions:-

$$\gamma_0(z) = 218.2 \;\; I^{\frac{1}{2}}(z) \; s^{-1} \qquad (7\text{-}13)$$

For Langmuir waves, collisional damping is here dominant over Landau damping and is approximated by a linear fall-off to the focal plane:

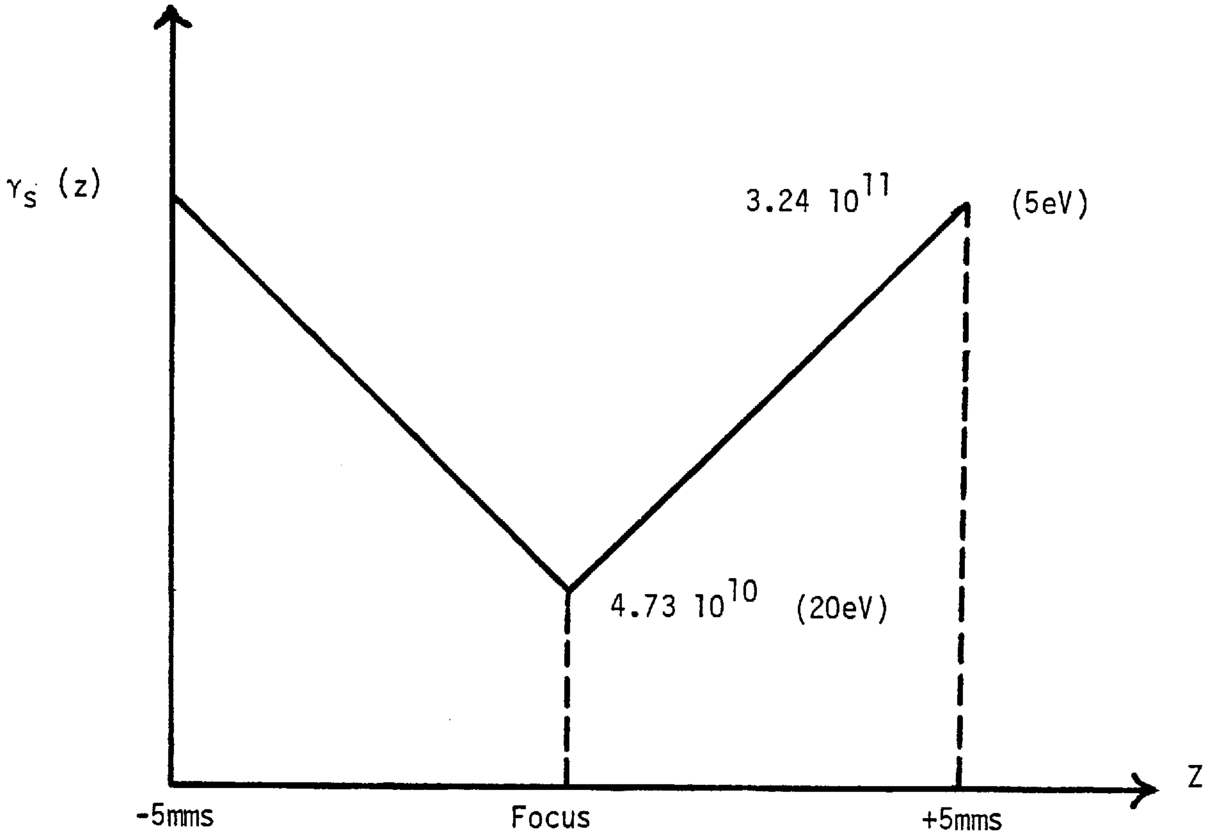

i.e. $\gamma_s(z) = fz + g$

where $g = 3.24\ 10^{11}\ s^{-1}$

and $f = -5.53\ 10^{13}$.

Then as before:

$$\ln\ (P_B/P_N) = 6.35\ 10^{-4}\left[\frac{bz}{a} + \frac{af - bg}{f^2}\ \ln\ (fz + g)\right]_{\text{plasma edge}}^{\text{focus}}$$

Table (7-3) gives the theoretical/experimental comparisons of the exponential.

SHOT NUMBER	THEORY	EXPERIMENT
1	0.057	7.9
2	0.055	5.2
3	0.074	4.8

Table (7-3)

From Equation (7-13) the growth rates at the time of peak intensity are typically ~ 4 10^9 s^{-1} at the plasma edge and ~ 1 10^{10} s^{-1} at the focus.

(d) Discussion of the backscattering results

From Tables (7-1), (7-2) and (7-3) it is seen that the growth rates with intensity agree best with a coherent wave theory of stimulated Brillouin scattering.

It could be argued that the temporal shape of the backscattered pulse is limited by the bandwidth of the Tektronix 7844 oscilloscope and that Fig. (3-13) represents the detector response. However, further evidence for agreement with a coherent wave theory comes from the Thomson scattering results at the lower plasma density of ~ 8 10^{16} cm^{-3} which indicated little change in the electron density for ~ 2ns. Furthermore, a low pressure continuous discharge cell was also used in the CO_2 laser oscillator cavity to reduce the bandwidth giving the laser a coherence length greater than 1 metre (i.e. >> the interaction length). These conditions imply a coherent wave interaction.

7. FUTURE WORK

The experiment of M.S. White et al.[10] investigated laminar heat flow with a λ_e/L of up to 0.04. His determination of a conductivity coefficient half that calculated by Spitzer has been here attributed to a failure of the theory. There is an obvious need to extend the theory to include the higher order terms which become important for large λ_e/L.

In the present experiment λ_e/L was extended to ~ 0.5 but with $T_e \sim 5T_i$ the heat flow was dominated by turbulence.

A successful SRC application has already been made for an experiment to measure the heat flux at $\lambda_e/L \sim 0.1$ to 0.2 with $T_e \sim T_i$. The value of λ_e/L is well into the region where Spitzer theory fails and $T_e \sim T_i$ ensures that the ion-acoustic instability is not excited. It is proposed to obtain the above conditions with a 150MW CO_2 laser pulse of 100ns duration. The above estimated value for λ_e/L was obtained by running the computer program with conductivity coefficients of one half and one quarter that given by Spitzer. Table (7-4) lists the results of these two runs.

TABLE (7-4)

S	Max. T_e(eV)	T_e/T_i	$q/q_{max.}$	λ_e/L	v_o/v_{the}
0.25	14.4	1.5	0.07	0.12	0.97
0.50	12.7	1.3	0.09	0.08	1.03

The ratios: T_e/T_i and v_o/v_{the} are calculated at the time when T_e is a maximum. A 150MW peak power CO_2 laser pulse was used which had a triangular temporal shape with a maximum at 60ns and a total duration of 140ns. A Gaussian focal spot intensity distribution was assumed with a $^{1}/_{e}$ point at a radius of 200μm. A hydrogen plasma was assumed with initial $n_e = 8.10^{16}$ cm^{-3} and T_e = 5eV.

As mentioned in Chapter 4, the coding of the fluid equations used in the computer program becomes inexact in the presence of an appreciable $\nabla \underline{T}_i$ ($\nabla . \underline{\underline{P}}_i \neq 0$ in equation 4-5). For accurate modelling in (w,s) space the equations should therefore be corrected.

Note that with a heating timescale ≥ the equilibration/conduction timescale a lower maximum T_e is obtained and we get a maximum $v_o/v_e \sim 1$ for a 150MW peak CO_2 laser power. This compares with $v_o/v_e \leq 0.3$ in the present experiment and therefore saturation of the inverse bremsstrahlung absorption coefficient may be further investigated. It should also be possible to look at the difference in the absorption coefficient for linearly and circularly polarised radiation[87].

The computer output for s = 0.25 is shown in Fig. (7-6) where the plasma parameters are shown as functions of time and radial distance R from the axis of the CO_2 laser heating pulse. Note that plasma is expelled from the heated region due to a rarefaction wave. This is because the heating timescale is comparable with the time taken for a sound wave to propagate across the heated region. The maximum electron temperature occurs on axis at 60ns, the time at which the CO_2 laser peaks. The ion temperature lags behind due to the finite electron ion equilibration time.

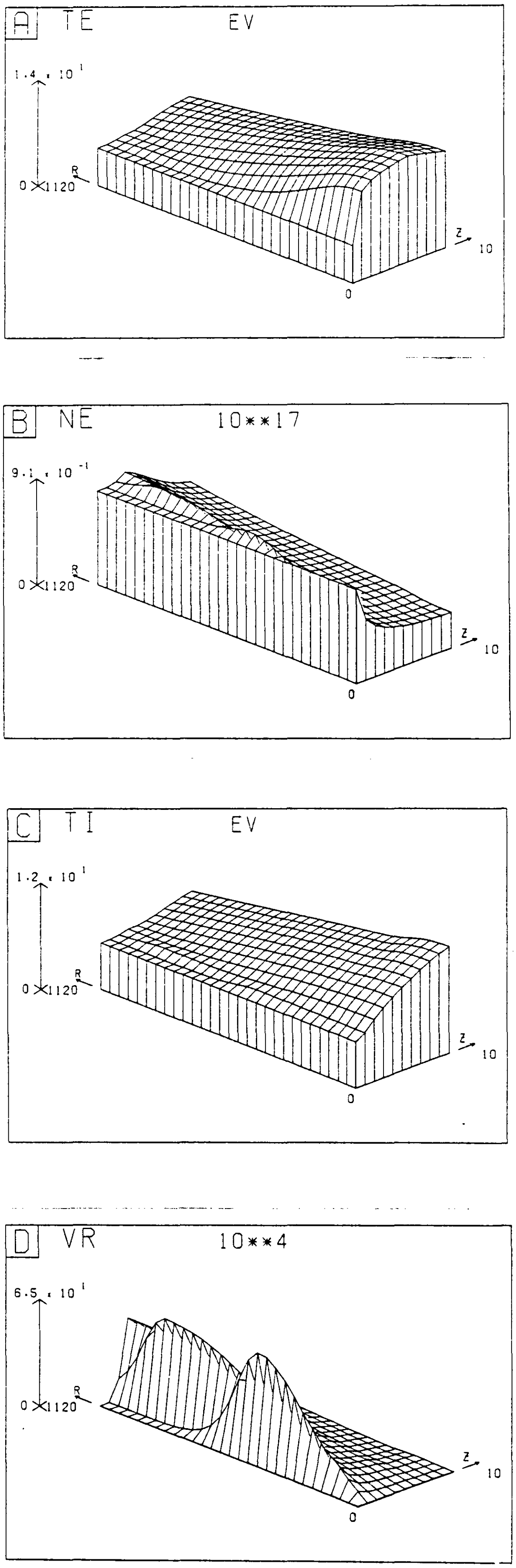

Fig. (7-6) Computer output for future experiment. Time varies with z from 1 to 10ns and the radial distance from the CO_2 laser beam axis with R from 0 to 1120μm.

Plot A.....T_e (eV)
Plot B.....n_e (10^{17} cm^{-3})
Plot C.....T_i (eV)
Plot D.....Radial velocity (10^4 cm s^{-1})

8. CONCLUSION

In the experiment described in this thesis, the thermal conduction down a laser-induced temperature gradient in a high density plasma was definitively measured. As discussed in Chapter 1 previous measurements[34,35,36] of the thermal conduction down large temperature gradients have been indirect and complicated by other phenomena.

The dominant restriction on the heat flux was ion acoustic turbulence driven by the return current. This had been predicted by Forslund[8] in the context of the solar wind. The inverse bremsstrahlung absorption was also shown to be consistent with the measurements and calculations of other workers[75]. Thus, it is felt that the results of this experiment represent confirmation of theories of the important processes of thermal conduction and absorption of light in high density plasmas.

Breakdown of the first order theory of thermal conduction in the presence of a large λ_e/L was masked in the present experiment by the ion-acoustic turbulence. A further experiment is under way in which the heating timescale > the electron-ion equilibration timescale so that the ion-acoustic turbulence will be Landau damped and laminar flow investigated. This experiment coupled with an extension of the theory to include higher order terms should extend further our knowledge of thermal conduction in plasmas.

APPENDIX A

Computer Program for Abel Inversion.

```
      PROGRAM DAVID(INPUT,OUTPUT,TAPE5=INPUT,TAPE6=OUTPUT)
      DIMENSION AI(21),AID(21)
      COMMON AID,FY,D
 500   CONTINUE
      WRITE(6,210)
 210  FORMAT(*ENTER 21 VALUES FOR INTENSITY*)
      READ,AI
      WRITE(6,120)
 120  FORMAT(*ENTER STEP BETWEEN INTENSITY VALUES,DELTAY*)
      READ,D
C
C         20  SPACE STEPS USED
C
      RMAX=20.0*D
C         CALCULATE DERIVATIVES OF INTENSITY
      AID(1)=0.0
      AID(21)=(AI(21)-AI(20))/D
      DO 3 I=2,20
      AID(I)=(AI(I+1)-AI(I-1))/(2.0*D)
    3 CONTINUE
C
C       LOOP FOR INCREASING R-VALUES
      WRITE(6,300)
 300  FORMAT(21X,*RADIUS   INTENSITY*)
       DO 1 I=1,20
      R=FLOAT(I-1)*D
       IF(I.EQ.1) R=D/2.0
      SUM=0.0
      DELTA=(RMAX-R)/1000.0
      DO 2 J=1,1000
      Y=R+FLOAT(J-1)*DELTA
      CALL DIDY(Y+DELTA/2.0)
      SUM=SUM+(ALOG(Y+DELTA+SQRT((Y+DELTA)**2-R**2))-
     +ALOG(Y+SQRT(Y**2-R**2+1.0E-20)))*FY*(-1.0/(4.0*ATAN(1.0)))
 2    CONTINUE
      WRITE(6,100) R,SUM
 100  FORMAT(21X,F6.2,F10.4)
 1    CONTINUE
      WRITE(6,600)
 600  FORMAT(X,*TYPE 1 FOR RERUN,2 FOR EXIT*)
      READ,K
       IF(K.EQ.1) GO TO 500
      STOP
      END
C
C---------------------------------------------------------------
C
      SUBROUTINE DIDY(Y)
      DIMENSION AID(21)
      COMMON AID,FY,D
      A=Y/D-FLOAT(INT(Y/D))
      N=INT(Y/D)
      FY=AID(N+1)+(AID(N+2)-AID(N+1))*A
      RETURN
      END
```

APPENDIX B

Computer Program to integrate laser scattering electron feature spectra for use in Rayleigh calibrations.

```
      PROGRAM SPECTRA(TAPE8,INPUT,OUTPUT,TAPE6)
      DIMENSION A(20,232),SPM(100),STM(100)
 500  CONTINUE
      REWIND 8
      READ(8) A,SPM
      DO 1 I=1,20
      I1=I
      ALPHA=A(I,231)
      WRITE(6,18)A(I,231),A(I,232)
   18     FORMAT(1H1,10X,*ALPHA=*,F5.2,19X,*NCAL=*,E8.2)
           WRITE(6,19)
  19  FORMAT(X,11X,*SHIFT*,13X,*SUM*,10X,*SUM X 1.035E17/SEK*,
     +7X,*SHIFT DENSITY*,7X,*ELECTRON TEMP.*)
      WRITE(6,191)
  191 FORMAT(X,11X,*-----*,13X,*---*,10X,*------------------*,
     +7X,*-------------*,7X,*--------------*)
C
      DO 2 J=0,50
      SHIFT=FLOAT(J-25)
      SHF=SHIFT/100,0
      DO 33 K=1,100
  33  STM(K)=SPM(K)-SHIFT
C            - SINCE SHIFTING BASELINE NOT ALPHA CURVE
      SUM=0.0
C              SUM OVER SPECTRUM
      DO 99 K=2,100
      L=IFIX(STM(K))
      DIFF=STM(K)-FLOAT(L)
      SUM=SUM+A(I1,L)+(A(I1,L+1)-A(I1,L))*DIFF
  99  CONTINUE
C           SPECTROMETER BANDWIDTH=13.0 A↑S
C           COUNTING INTERVAL=3.25 A↑S
C           SO ADD CENTRAL + ALLOW BOTH SIDES SPECTRUM
C           2.0*A(I1,1) SINCE STARTED DO 99 AT 2 TO 100
      SUM=(SUM+A(I1,1))/2.0+A(I1,1)
      SEK=1.0/(1.0+ALPHA**2)
      DEN1=(SUM*1.035E17)/(SEK)
      TE=(8.60)*(10**(2.0*SHF))
      DEN2=(A(I1,232))*(10**(2.0*SHF))
      WRITE(6,21) SHF,SUM,DEN1,DEN2,TE
  21  FORMAT(X,11X,F6.2,13X,F6.3,12X,E9.3,9X,E9.3,9X,F6.3)
  2    CONTINUE
  1    CONTINUE
      STOP
      END
```

APPENDIX C

The two-temperature 1-D fluid code used to model the experiment (A complete listing).

```
       PROGRAM MALK(INPUT,OUTPUT,TAPE5=INPUT,TAPE6=OUTPUT,TAPE7,
     A     TAPE60=300)
        COMMON DEN,T,T1,TK,V,U,P,XX,YY,A,B,C,DD,ELAS,I,UI
         COMMON WDEN,WT,WTI,WV,AWV,AWH,SUMH,SUMV
C  LASER HEATED PLASMA
C   TWO FLUID MODEL-----------------
C======================================
         DIMENSION DEN(2,320),T(320),T1(320),TK(320),V(2,320),U(2,320)
     +             P(2,320),WDEN(12,320),WV(12,320),WT(12,320),WTI(12,
     +2),                   XX(320),YY(320),A(320),B(320),C(320),DD(32
     +,                                ELAS(320),TIMES(20),UI(2,320)
         DIMENSION RR(320),AWV(26,100),AWH(26,100),SUMV(26),SUMH(26)
         DIMENSION QTOT(15),AZ(3,3),SATURO(15),UL(15)
       REAL LL(15)
         REAL LAVER,MODJM,MODJP
         REAL I(320)
         REAL LOL,LOLMIN,MODFAC(320)
         REAL KB,LOLA,IO,IN,IND
         DATA NEXTRA/10/
          DATA IONE/1/
           HRUN=3HR62
C
         WRITE(6,417)
          WRITE(6,468)
 468       FORMAT(20H THIS IS MOD.SAT.           )

  417 FORMAT(1X,*TWO FLUID FLUX LIMITED MODEL*)
C  K=1 AUX  K=2 MAIN MESH
C     ALL UNITS  MKS
C  DEN =NO DENSITY   P=MOMENTUM
C   SET SPACE AND TIME STEPS
         D=2.E-5
          DT=4.E-12


          KB=1.38E-23
          AMI=1.66E-27
         PLSUM=0.
          PIE=3.14159
          EPS=(1.E-9)/(36.*PIE)
          AME=9.1E-31
          CHAR=1.602E-19
         CRDN=1.E+25
C  CRITICAL DEN. FOR CO2
         LOLA=7.5
         ARTLIM=1.
          WL=10.6E-6
          SPLI=3.E+8
          CA=((WL/(2.0*PIE))**2)/(SPLI**3)
         CB=2.6E-6*(CHAR**2)/(AME*EPS)
           ALASER=10.6
            BLASER=ALOG10(ALASER)
            AZ(1,1)=1.1750
            AZ(1,2)=0.0789
            AZ(1,3)=0.1842
            AZ(2,1)=0.1812
            AZ(2,2)=0.5586
            AZ(2,3)=0.0304
            AZ(3,1)=0.3305
            AZ(3,2)=0.0203
            AZ(3,3)=-0.0657
C     MATRIX FOR CALCULATING GAUNT FACTOR
         CC=(1.9702E-41)*(ALASER**2)
C  SET INITIAL BUFFER LIMITS TO FLF VARIABLES
```

```
      JMIN=250
      LOLMIN=1.E+6
      RMAX=1.E-5
      DO 484 II=1,15
  484 QTOT(II)=0.
C-=-=-=-=-=-=-=-=-=-=-=-=-=-=-=-=-=-=-=-=-=-=-=-=-=-=-=-=-==-
      DENSET=.63E+23
      VSET=0.
      TSET=3.6
C  UNITS OF TEMP ARE EV. FOR INPUT +OUTPUT ONLY
      SPIFAC=.1
      SIGMO=1.84E-10
      SIGMO=SIGMO*SPIFAC
      SIGMA=SIGMO/LOLA
      WRITE(6,224)
      WRITE(6,231)SIGMO,SPIFAC
  231 FORMAT(1X,*SIGMO=*,E12.4,2X,*SPIFAC=*,F6.2)
      WRITE(6,3847)ARTLIM
 3847  FORMAT(1X,*ARTIFICIAL LIMITING AT*,2X,F6.3,1X,
   +        *TIMES FREE STREAMING LIMIT*)
      WRITE(6,224)
      CON=0.
      PO=2.36E+8
      MMO=12
      THETA=0.9
      WRITE(6,403)THETA
  403 FORMAT(1X,*THETA=*,F8.4)
      JJJ=100
      JV=JJJ-30
      JSMOOTH=JJJ-5
      JWRI=JJJ
      JINT=2
      JM1=JJJ-1
      JM2=JJJ-2
      JP3=JJJ+3
      JP1=JJJ+1
C ------------------------------
C TO SET +NORMALISE INTENSITY DISTRIBN. FROM INPUT POWER
C==========================
      JZERO=11
      ASUM=1.*PIE*(D**2)/4.
      DO 788 J=2,JJJ
      Z=FLOAT(J-1)*1.22*PIE/FLOAT(JZERO-1)
      ASUM=ASUM+(2.*PIE*FLOAT(J-1)*(D**2))*((2.*S17ABF(Z)/Z)**2)
      IF(J.GE.JZERO) GO TO 622
  788 CONTINUE
  622 CONTINUE
      IO=PO/ASUM
        IO=PO/3.1415/(FLOAT(JZERO)*D)**2
C     THIS IS FOR A GAUSSIAN BEAM PROFILE
      WRITE(6,224)
      WRITE(6,560)ASUM
  560 FORMAT(1X,*VOL UNDER INTENS.DISTRIBN.=*,E14.4)
C--------------------------------
      JP1=JJJ+1
      NP=500
      NM=1000
C   SET INITIAL VALUES  PLASMA PARAMETERS
       DO 1 K=1,2
      DO 2 J=1,JP3
      DEN(K,J)=DENSET
      V(K,J)=VSET
       P(K,J)=AMI*DEN(K,J)*V(K,J)
    2 CONTINUE
```

```
      1 CONTINUE
C    CALCULATE INITIAL TOTAL PARTICLES
          SUM=0.25*PIE*(D**2)*DEN(2,1)
          DO 121 J=2,JJJ
          FJM1=FLOAT(J-1)
    121   SUM=SUM+2.*PIE*FJM1*(D**2)*DEN(2,J)
    303 FORMAT(1X,*INITIAL TOTAL PARTICLES=*,E12.4)
          DO 49 J=1,JP3
          T(J)=TSET*1.16E+4
          T1(J)=T(J)
          TK(J)=T1(J)
          A(J)=0.
          B(J)=0.
          C(J)=0.
          DD(J)=0.
          U(2,J)=DEN(2,J)*T(J)*KB*1.5
          UI(2,J)=U(2,J)
          UI(1,J)=UI(2,J)
          U(1,J)=U(2,J)
          ELAS(J)=0.
          RR(J)=0.0
     49 CONTINUE
C-----------------------------------------
C   CALCULATE INITIAL TOTAL ENERGY
C========================================
          ESIMO=0.25*PIE*(D**2)*(UI(2,1))
          ESUMO=0.25*PIE*(D**2)*(U(2,1)+0.5*AMI*DEN(2,1)*(V(2,1)**2))
          DO 99 J=2,JJJ
          FJM1=FLOAT(J-1)
          ESUMO=ESUMO+2.*PIE*FJM1*(D**2)*
     +                (U(2,J)+0.5*AMI*DEN(2,J)*(V(2,J)**2))
          ESIMO=ESIMO+2.*PIE*(D**2)*FJM1*UI(2,J)
     99 CONTINUE
          ETOT=ESUMO+ESIMO
C-----------------------------------------
C
          ELASUM=0.
          ELOSUM=0.
          DO 431 M=1,MMO
          DO 432 J=1,JP3
           WDEN(M,J)=0.
          WTI(M,J)=0.0
           WT(M,J)=0.
           WV(M,J)=0.
    432 CONTINUE
    431  CONTINUE
         DO 1110 J=1,15
   1110    SATURO(J)=0.
          DO 402 M=1,MMO
          TIMES(M)=0.
    402 CONTINUE
          WRITE(6,224)
          WRITE(6,224)
          WRITE(6,472)PO
          WRITE(6,603)IO,JZERO
           M=0
           TIME=0.0
C   START MAIN TIME LOOP -------------------------
          NF=2500
          NSMOOTH=NF
          WRITE(6,473)DT,D
          WRITE(6,474)JJJ,NF
          WRITE(6,475)NP,NM
    472 FORMAT(1X,*INPUT POWER WATTS=*,E14.4)
```

```
  603 FORMAT(1X,*MAX INTENS. W/M2=*,E14.4,2X,*JZERO=*,I4)
  473  FORMAT(1X,*TIME STEP =*,E10.3,5X,*SPACE STEP =*,E10.3)
  474 FORMAT(1X,I5,*SPACE STEPS*,8X,I5,*TIME STEPS*)
  475 FORMAT(1X,I5,*=CO2 MAX T. STEP*,8X,I5,*=CO2 OFF*)
          WRITE(6,224)
         WRITE(6,151)
         WRITE(6,152)
  151 FORMAT(1X,*INNER BCS. 1ST DERIVS OF N,T=0,, V=0  *)
  152 FORMAT(1X,*OUTER BCS.  CONDITIONS(A)   *)
         WRITE(6,224)
         WRITE(6,303) SUM
         WRITE(6,224)
         WRITE(6,801)ESUMO,ESIMO,ETOT
  801 FORMAT(1X,*INIT.ENERGIES   E+V*,E12.4,2X,*IONS*,E12.4,
     +         2X,*TOTAL*,E12.4)
C-----------------------------------------------------------
C========================================
         DO 5 N=1,NF
C-----------------------------------------------------------
         J=1
          L5=N/50
          A6=FLOAT(L5)
          Q1 =FLOAT(N)/50.0-A6
        IF(Q1.NE.0.) GO TO 738
         WRITE(6,224)
         WRITE(6,743)N,JMIN,LOLMIN
  743 FORMAT(1X,* N= *,I4,1X,* JMIN= *,I3,2X,*LOLMIN=*,E10.4)
         WRITE(6,9843) (RR(J),J=1,40)
 9843 FORMAT(1X,20(1X,F5.3))
  738  CONTINUE
          TIME=FLOAT(N)*DT
          J=1
C-----------------------------------------------------
C  LENGTH AVERAGING FOR ABSORPTION OENERGY EQUATS
C  ARE PER UNIT VOL.DUMP ENERGY OVER LENGTH LAVER,
C  AND SCALE UP LINEARLY
C  THEN ENERGY EQUATS. UNCHANGED..I.E. ARE WRITING ABSORPTION
C ENERGY UNIT VOL DEPOSITED=IO/L *(1.-EXP(-KL)) WHICH AVERAGES
C OVER L RATHER THAN OLD IO(1-EXP(-K)) WHICH AVERAGES OVER
C  UNIT LENGTH=1M.
       LAVER=0.01
         IF(N.EQ.1)WRITE(6,9988)LAVER
 9988 FORMAT(1X,*AVERAGING LENGTH METRES=*,F6.4)
C  INSERT TIME SHAPE GENERATOR FOR CO2
C--------------------------------------------------------
          FM=FLOAT(NM)
          FN=FLOAT(N)
          FP=FLOAT(NP)
          IF(N.GE.NP) GO TO 143
          IN=IO*(FN-1.)/FP
  143 CONTINUE
          IF(N.LT.NP) GO TO 744
        IN=IO*(1.-1./FP)*(FM-FN)/(FM-FP)
  744 CONTINUE
        IF(N.GT.NM) IN=0.
C ALTERNATIVELY I CAN USE A TIME PROFILE GENERATOR
          IN=IO*PTIME(TIME)
C-------------------------------------
C   INSERT SPACE SHAPE GENERATOR FOR CO2
         I(1)=IN
         DO 774 J=2,JJJ
         Z=FLOAT(J-1)*1.22*PIE/FLOAT(JZERO-1)
         I(J)=IN*((2.*S17ABF(Z)/Z)**2)
         IF(J.GE.JZERO) I(J)=0.
```

```
         Z=FLOAT(J-1)/FLOAT(JZERO-1)
          I(J)=IN*EXP(-Z*Z)
C    THIS IS FOR A GAUSSIAN BEAM PROFILE
  774 CONTINUE
C    DEFN. OF ELAS(J)
C-----------------------------------------------------------
        DO 579 J=1,JJJ
         BTEMP=(T(J))/(1.16E+4)
           GAUNT=0.
          DO 444 IK=1,3
          DO 444 JK=1,3
           IIK=IK-1
           JJK=JK-1
 444    GAUNT=GAUNT+(AZ(IK,JK))*((ALOG10(BTEMP))**IIK)*(BLASER**JJK)
        ABSCO=CC*GAUNT*((DEN(2,J)**2)/(T(J)**1.5))*
     +            (1./SQRT(1.-DEN(2,J)/CRDN))
        ABSV=(I(J)/LAVER)*(1.-EXP(-ABSCO*LAVER))
         ABSV=ABSV/(1.+6.24E-15*I(J)/T(J)*1.16E+4)
  579 ELAS(J)=ABSV*DT
         IF(Q1.NE.0.) GO TO 9152
         DO 9150 J=1,JZERO,2
 9150     SATURO(J)=1. + 6.24E-15*I(J)/T(J)*1.16E+4
         WRITE(6,224)
         WRITE(6,9151) (SATURO(J),J=1,JZERO,2)
 9151    FORMAT(1X,*SAT. OF I.B. EVERY ODD SPACE STEP TO *,
     +*1 UPON E POINT*,6(1X,F6.4))
 9152    CONTINUE
C======================================
C  SUM ELAS(J) IN TIME AND SPACE FOR CONSERVATION TEST=========
        ELASUM=ELASUM+0.25*PIE*(D**2)*ELAS(1)
        DO 508 J=2,JJJ
        FJM1=FLOAT(J-1)
        ELASUM=ELASUM+2.*PIE*FJM1*(D**2)*ELAS(J)
  508 CONTINUE
          CONJ=3.35E-34/D/(FLOAT(JZERO))**2
C================================
C  AXIAL AUX CALCS
C-------------------------------
        J=1
        DEN(1,1)=0.5*(DEN(2,2)+DEN(2,1))-((DT/D)*DEN(2,2)*V(2,2))
        GRAVD=(V(2,3)-V(2,1))/(2.*D)
         AP= DEN(2,2)*GRAVD*ABS(GRAVD)
       P(1,1)=0.5*(P(2,2)+P(2,1))-(DT/D)*(P(2,2)*V(2,2))
     +          -(DT*0.5*KB/D)*(DEN(2,2)*T(2)-DEN(2,1)*T(1))
     +                    -(DT/(3.*D))*(UI(2,2)-UI(2,1))
     +                           +0.5*DT*CON*AMI*D*AP
     ++    (DEN(2,1)+DEN(2,2))*CONJ*DT/4.*.5*I(J)
C THIS LAST LINE IS FOR THE PONDEROMOTIVE FORCE
         V(1,1)=P(1,1)/(AMI*DEN(1,1))
C  SMOOTH
        IF(V(1,1).LT.0.)V(1,1)=0.
C------------------------------------------
        TOP=37.E+6*((T(1)+T(2))**1.5)
        BOT=(2.**0.5)*(DEN(2,2)+DEN(2,1))
        TEQ=TOP/BOT
       EQ=0.25*DT*(U(2,J)+U(2,J+1)-UI(2,J)-UI(2,J+1))/TEQ
C
        FIRST=0.5*(U(2,2)+U(2,1))-(5./3.)*(DT/D)*(U(2,2)*V(2,2))
        SEKAND=0.25*(ELAS(1)+ELAS(2))
        THIRD=-EQ
        U(1,1)=FIRST+SEKAND+THIRD
C    AXIAL AUX ION ENERGY
C-------------------------------
        FIRST=0.5*(UI(2,1)+UI(2,2))+EQ
```

```
         SEKAND=-((5.*DT)/(3.*D))*(UI(2,2)*V(2,2))
         UI(1,1)=FIRST+SEKAND
C========================================
C DIAGNOSTIC  PRINT I(J) AT N=NP OR NF
         IF(NF.LT.NP) GO TO 901
        J22=JZERO+10
        IF(N.EQ.NP) WRITE(6,902)  (I(J),J=1,J22)
  902 FORMAT(1X,5(E12.4,1X))
  901 CONTINUE
         IF(NF.GE.NP)GO TO 644
        IF(N.EQ.NF) WRITE(6,902)  (I(J),J=1,J22)
  644 CONTINUE
C-------------------------------------------------------
C   AXIAL MAIN CALCS-----------------
          DEN(2,1)=DEN(2,1)-(4.*DT*DEN(1,1)*V(1,1))/D
          P(2,1)=P(2,1)-(4.*DT*P(1,1)*V(1,1))/D
          V(2,1)=P(2,1)/(AMI*DEN(2,1))
          DP=(V(1,2)-V(1,1))/(2.*D)
C   SMOOTH
         IF(V(2,1).LT.0.)  V(2,1)=0.
C
         TEQ=37.E+6*(T(1)**1.5)/DEN(1,1)
         EQ=DT*(U(1,1)-UI(1,1))/TEQ
         FIRST=(4.*DT/D)*(5./3.)*U(1,1)*V(1,1)
         SEKAND=ELAS(1)
         THIRD=-EQ
         U(2,1)=U(2,1)-FIRST+SEKAND+THIRD
         T(1)=U(2,1)/(1.5*KB*DEN(2,1))
        IF(T(1).LT.0.)  WRITE(6,907)N,T(1)
         IF(T(1).LT.0.)  GO TO 904
  907 FORMAT(1X,I3,3X,F10.2)
C-------------------------------
C AXIAL MAIN ION ENERGY
C=============================
        UI(2,1)=UI(2,1)+EQ-(4.*DT/D)*(5./3.)*UI(1,1)*V(1,1)
C----------------------------------------------------------
C  NOW LOOP THRO WHOLE RAD ---------------
C======================================================
         DO 10 J=2,JM1
C
         FJ=FLOAT(J)
C  DENSITY AUX CALCS-----------------
          Z=(DT*0.5)/(D*(FJ-0.5))
          ZZ=(DT*0.5)/D
         TOP=37.E+6*((T(J)+T(J+1))**1.5)
         BOT=(2.**0.5)*(DEN(2,J)+DEN(2,J+1))
         TEQ=TOP/BOT
         EQ=(0.25*DT/TEQ)*(U(2,J)+U(2,J+1)-UI(2,J)-UI(2,J+1))
           AA=FJ*DEN(2,J+1)*V(2,J+1)-FLOAT(J-1)*DEN(2,J)*V(2,J)
           DEN(1,J)=0.5*(DEN(2,J+1)+DEN(2,J))-AA*Z
C
C  MOMM AUX CALCS-------
           AB=FJ*P(2,J+1)*V(2,J+1)-(FJ-1.)*P(2,J)*V(2,J)
         AC=DEN(2,J+1)*T(J+1)-DEN(2,J)*T(J)
           GRAV1=(V(2,J+2)-V(2,J))/(2.*D)
           GRAV2=(V(2,J+1)-V(2,J-1))/(2.*D)
           AM=DEN(2,J+1)*ABS(GRAV1)*GRAV1-DEN(2,J)*ABS(GRAV2)*GRAV2
           P(1,J)=0.5*(P(2,J+1)+P(2,J))-Z*AB-ZZ*KB*AC
     +              -(DT/(3.*D))*(UI(2,J+1)-UI(2,J))
     +                     +0.5*DT*CON*AMI*D*AM
     +      +CONJ*(DEN(2,J+1)+DEN(2,J))*DT*.25*I(J)*(FLOAT(J)-.5)
           V(1,J)=P(1,J)/(AMI*DEN(1,J))
          IF((V(1,J).LT.0.0).AND.(J.GT.JV).AND.(N.LT.NP)) V(1,J)=0.
           VC=D/DT
```

```
          IF(V(1,J).GE.VC) GO TO 904
C  ENERGY AUX CALCS ----------------------
         FIRST=FJ*U(2,J+1)*V(2,J+1)-(FJ-1.)*U(2,J)*V(2,J)
         SEKAND=0.25*(ELAS(J+1)+ELAS(J))
         DA=FJ*V(2,J+1)*GRAV1*ABS(GRAV1)*DEN(2,J+1)
         DB=(FJ-1.)*V(2,J)*DEN(2,J)*GRAV2*ABS(GRAV2)
         THIRD=-EQ
        U(1,J)=0.5*(U(2,J+1)+U(2,J))-(5./3.)*Z*FIRST+SEKAND+THIRD
C   AUX ION ENERGY-----------------
         FIRST=0.5*(UI(2,J)+UI(2,J+1))+EQ
         SEKAND=(5.*DT)/(6.*D*(FJ-0.5))
         SECAND=FJ*UI(2,J+1)*V(2,J+1)-(FJ-1.)*UI(2,J)*V(2,J)
         UI(1,J)=FIRST-SEKAND*SECAND
C=-=-=-=-=-=-=-=-=-=-=-=-=-=-=-==-=-=-=-=-=-
C  END OF AUX CALCS LOOP 10
   10  CONTINUE
C=-=-=-=-=-=-=-=-=-=-=-=-=-=-=-=-=-=-=-=-=-=-=-
         IF(DEN(1,1).NE.DEN(1,2))DEN(1,1)=DEN(1,2)
         DEN(1,JJJ)=2.*DEN(1,JM1)-DEN(1,JM2)
        IF(DEN(1,JJJ).GT.DEN(1,JM1))  DEN(1,JJJ)=DEN(1,JM2)
         V(1,JJJ)=(FLOAT(JM1)-0.5)*DEN(1,JM1)*V(1,JM1)/
     +             ((FLOAT(JJJ)-0.5)*DEN(1,JJJ))
        IF(V(1,JJJ).LT.V(1,JM1))  V(1,JJJ)=V(1,JM2)
         P(1,JJJ)=V(1,JJJ)*AMI*DEN(1,JJJ)
         IF(UI(1,JJJ).NE.UI(1,JM1))UI(1,JJJ)=UI(1,JM1)
         IF(UI(1,1).NE.UI(1,2))  UI(1,1)=UI(1,2)
C
C   NOW DO MAIN CALCS  -----------
         DO 12 J=2,JM1
         FJ=FLOAT(J)
C
C  DENSITY MAIN   ----------
           Y=DT/((FJ-1.)*D)
          BA=(FJ-0.5)*DEN(1,J)*V(1,J)-(FJ-1.5)*DEN(1,J-1)*V(1,J-1)
          DEN(2,J)=DEN(2,J)-Y*BA
C   MOMM MAUN
C   ----------
          BB=P(1,J)*V(1,J)*(FJ-0.5)-P(1,J-1)*V(1,J-1)*(FJ-1.5)
         BC=(U(1,J)+UI(1,J)-U(1,J-1)-UI(1,J-1))/(1.5*KB)
          IF(J.NE.2)  GO TO 344
          GRAVB=(V(2,J)-V(2,J-1))/(2.*D)
  344  CONTINUE
          IF(J.EQ.2)  GO TO 331
          GRAVB=(V(1,J)-V(1,J-2))/(2.*D)
  331  CONTINUE
          GRAVA=(V(1,J+1)-V(1,J-1))/(2.*D)
          AN=DEN(1,J)*GRAVA*ABS(GRAVA)-DEN(1,J-1)*GRAVB*ABS(GRAVB)
          P(2,J)=P(2,J)-Y*BB-BC*KB*(DT/D)
     +            +DT*CON*AMI*D*AN
C  THIS LAST LINE IS THE PONDEROMOTIVE FORCE
     + +CONJ*DT*.5*I(J)*(FLOAT(J)-1.)*(DEN(1,J-1)+DEN(1,J))
          V(2,J)=P(2,J)/(AMI*DEN(2,J))
        IF((V(2,J).LT.0.0).AND.(J.GT.JV).AND.(N.LT.NP))V(2,J)=0.
          IF(V(2,J).GE.VC)  PRINT 807
  807 FORMAT(2H /,*  GONE UNSTAB.  V(2,J)   *)
          IF(V(2,J).GE.VC)  GO TO 904
C
C=-=-=-=-=-=-=-=-=-=-=-=-=-=-=-=-=-=-=-=
C  MAIN ENERGY CALCS
C--------------------------------------
         TEQ=74.E+6*(T(J)**1.5)/(DEN(1,J)+DEN(1,J-1))
         EQ=0.5*DT*(U(1,J)+U(1,J-1)-UI(1,J)-UI(1,J-1))/TEQ
         FIRST=(FJ-0.5)*U(1,J)*V(1,J)-(FJ-1.5)*U(1,J-1)*V(1,J-1)
         SEKAND=ELAS(J)
```

```
      DC=(FJ-0.5)*V(1,J)*DEN(1,J)*GRAVA*ABS(GRAVA)
     DDD=(FJ-1.5)*V(1,J-1)*DEN(1,J-1)*GRAVB*ABS(GRAVB)
C
      THIRD=-EQ
      U(2,J)=U(2,J)-(5./3.)*Y*FIRST+SEKAND+THIRD
      T(J)=U(2,J)/(1.5*KB*DEN(2,J))
     IF(T(J).LT.0.) WRITE(6,907)N,T(J)
     IF(T(J).LT.0.) WRITE(6,907)J,T(J)
      IF(T(J).LT.0.) GO TO 904
C
C   ION ENERGY MAIN CALCS
C-----------------------------
      FIRST=UI(2,J)+EQ
      SEKAND=(5./3.)*(DT/(D*(FJ-1.)))
      SECAND=(FJ-0.5)*UI(1,J)*V(1,J)-(FJ-1.5)*UI(1,J-1)*V(1,J-1)
      UI(2,J)=FIRST-SEKAND*SECAND
C-------------------------------
C  END OF MAIN CALCS LOOP 12
   12 CONTINUE
C------------------------------
      IF(UI(2,1).NE.UI(2,2)) UI(2,1)=UI(2,2)
      IF(UI(2,JJJ).NE.UI(2,JM1)) UI(2,JJJ)=UI(2,JM1)
      IF(DEN(2,1).NE.DEN(2,2)) DEN(2,1)=DEN(2,2)
      DEN(2,JJJ)=2.*DEN(2,JM1)-DEN(2,JM2)
     IF(DEN(2,JJJ).GT.DEN(2,JM1)) DEN(2,JJJ)=DEN(2,JM2)
    V(2,JJJ)=FLOAT(JM2)*DEN(2,JM1)*V(2,JM1)/(FLOAT(JM1)*DEN(2,JJJ))
     IF(V(2,JJJ).LT.V(2,JM1)) V(2,JJJ)=V(2,JM2)
      DO 172 J=1,JJJ
  172 P(2,J)=AMI*DEN(2,J)*V(2,J)
C
C=-=-=-=-=-=-=-=-=-=-=-=-=-=-=-=
C  PARTICLE CONSERVATION TESTS
C--------------------------------
      PLSUM=PLSUM+2.*PIE*D*FLOAT(JM1)*DT*DEN(2,JJJ)*V(2,JJJ)
      SUM=0.25*PIE*(D**2)*DEN(2,1)
      DO 83 J=2,JJJ
      FJ=FLOAT(J)
   83 SUM=SUM+2.*PIE*(FJ-1.)*(D**2)*DEN(2,J)
      PARTN=SUM+PLSUM
C
      TO=FLOAT(NF/10)
      ITO=10*N/NF
      Q=FLOAT(N)/TO-FLOAT(ITO)
      IF(Q.NE.0.) GO TO 532
      WRITE(6,531)N,SUM,PLSUM,PARTN
C
  531 FORMAT(1X,I3,3X,*NMESH=*,E12.4,3X,*NLOST=*,E12.4,3X,*TOT.=*,E12.4)
     +
  532 CONTINUE
C
C-=-=-=-=-=-=-=-=-=-=-=-=-=-=-=-=-=-=-=-=-=-=-=-=-=-=-=-
C  SOLUTION OF THERMAL DIFFUSION BY SEPARATED IMPLICIT ROUTINE
C -=-=-=-=-=-=-=-=-=-=-=-=-=-=-=-=-=-=-=-=-=-=-=-=-=-=-=-=-=-=-=-=-=-=-=-=-=-=-=
     CALL LIMTER(DEN,T,MODFAC,JJJ,D,LOLMIN,JMIN,ARTLIM)
      CALL FLMOD(DEN,T,SIGMA,MODFAC,RR,JJJ,D,QTOT,RMAX,LL,UL)
      ALP=DT/(1.5*KB*(D**2))
      ITT=0
      DO 656 J=1,JJJ
      T1(J)=T(J)
  656 CONTINUE
  654 CONTINUE
      DO 655 J=2,JJJ
      TK(J)=(T1(J)+T1(J-1))/2.
  655 CONTINUE
```

```
       ITT=ITT+1
C   DOWNSCAN------------------------
       DO 442 K=2,JM1
       J=JJJ+1-K
C    J GOES JM1-2 DOWN
      IF((N.EQ.1).AND.(J.EQ.2)) WRITE(6,777)SIGMA,LOLA
       FJ=FLOAT(J)
  777 FORMAT(1X,*AT 1,2 SIGMA AND LOLA=*,E12.4,2X,E12.4)
       FJM1=FLOAT(J-1)
       FJM2=FLOAT(J-2)
       FJM32=FLOAT(J)-1.5
       FJP1=FLOAT(J+1)
       FJMH=FJ-0.5
       ALPHA=ALP*SIGMA/(DEN(2,J)*FJM1)
       MODJP=0.5*(MODFAC(J+1)+MODFAC(J))
       MODJM=0.5*(MODFAC(J-1)+MODFAC(J))
       BETA=(1.-THETA)*(T(J-1)-T(J))*(((T(J-1)+T(J))/2.)**2.5)
    +            *MODJM
       GAMMA=(1.-THETA)*(T(J)-T(J+1))*(((T(J)+T(J+1))/2.)**2.5)
    +              *MODJP
       A(J)=-ALPHA*THETA*FJMH*(TK(J+1)**2.5)
    +            *MODJP
       B(J)=1.+THETA*MODJM*(TK(J)**2.5)*FJM32*ALPHA
    +           +ALPHA*THETA*MODJP*FJMH*(TK(J+1)**2.5)
       C(J)=-ALPHA*THETA*(TK(J)**2.5)*FJM32
    +            *MODJM
       DD(J)=T(J)+ALPHA*(FJM32*BETA-FJMH*GAMMA)
       XX(JM1)=1.
       YY(JM1)=0.
C----------------------------------------------
       BOT=A(J)*XX(J)+B(J)
       TOP=DD(J)-A(J)*YY(J)
       XX(J-1)=-C(J)/BOT
       YY(J-1)=TOP/BOT
  442 CONTINUE
       T1(1)=YY(1)/(1.-XX(1))
       DO 557 J=1,JM2
       T1(J+1)=XX(J)*T1(J)+YY(J)
  557 CONTINUE
       T1(JJJ)=T1(JM1)
       IF(T1(1).NE.T1(2)) T1(1)=T1(2)
       MMM=0
       DO 599 J=2,JM1
       TEST=((T1(J)+T1(J-1))/2.)-TK(J)
       TIST=0.001*TK(J)
       IF(TEST.GT.TIST)  MMM=MMM+1
  599 CONTINUE
       IF(ITT.GT.10) WRITE(6,676)N
  676 FORMAT(1X,*CONVERGENCE FAILURE *,2X,I5)
       IF(ITT.GT.10)GO TO 379
       CALL CHKT(T1,JJJ)
       IF(MMM.NE.0)GO TO 654
  379 CONTINUE
       TO=FLOAT(NF/10)
  873 FORMAT(1X,I5,5X,I5)
       ITO=10*N/NF
       Q=FLOAT(N)/TO-FLOAT(ITO)
       IF(Q.NE.0.) GO TO 849
       WRITE(6,873) N,ITT
  849 CONTINUE
C------------------------------
C  PUT NEW TEMPS IN ARRAY T(J)
       DO 598 J=1,JJJ
       T(J)=T1(J)
```

```
      U(2,J)=1.5*KB*DEN(2,J)*T(J)

  598 CONTINUE
      CALL CHKT(T,JJJ)
C
C
C     ENERGY CONSERVATION TEST--------------------------
C============================
      EPLAS=0.25*PIE*(D**2)*U(2,1)
      EPLASI=0.25*(D**2)*PIE*UI(2,1)
      EKSUM=0.25*PIE*(D**2)*0.5*(AME+AMI)*DEN(2,1)*(V(2,1)**2)
      DO 695 J=2,JJJ
      FJM1=FLOAT(J-1)
      EPLAS=EPLAS+U(2,J)*2.*PIE*FJM1*(D**2)
      EKSUM=EKSUM+2.*PIE*(D**2)*FJM1*
     +           0.5*(AME+AMI)*DEN(2,J)*(V(2,J)**2)
      EPLASI=EPLASI+2.*PIE*(D**2)*FJM1*UI(2,J)
  695 CONTINUE
C      SUM ENERGY LOST=======================
      ELOSUM=ELOSUM+2.*PIE*D*FLOAT(JM1)*DT*
     +           (U(2,JJJ)*V(2,JJJ)+UI(2,JJJ)*V(2,JJJ)+
     +                  0.5*AMI*DEN(2,JJJ)*(V(2,JJJ)**3))
      ETOT=EPLAS+EPLASI+EKSUM+ELOSUM-ELASUM
      TO=FLOAT(NF/10)
      ITO=10*N/NF
      Q=FLOAT(N)/TO-FLOAT(ITO)
      IF(Q.NE.0.) GO TO 289
      WRITE(6,299) N,ETOT
      WRITE(6,300)EPLAS,EPLASI,EKSUM
      WRITE(6,304)ELOSUM,ELASUM
  299 FORMAT(1X,I3,2X,*ENERGIES-PLASMA+LOSS-LASER IN=*,E12.4)
  300 FORMAT(1X,*ENERGIES   PLASE*,E12.4,2X,*PLASI*,E12.4,
     +      2X,*KE*,E12.4)
  304 FORMAT(1X,*LOSS*,E12.4,2X,*LASER IN*,E12.4)
  289 CONTINUE
C
C------------------------------
      SO=FLOAT(N/5)
      SOO=FLOAT(N)/5.
      TEST5=ABS(SO-SOO)
      SB=0.000001
C
C
C
C
C  PRINTOUT  INSTRUCTIONS
      IF(N.EQ.1) GO TO 437
      L8=NF/10
      Q5=FLOAT(L8)
      L4=N/L8
      Q=FLOAT(N)/Q5-FLOAT(L4)
      IF(Q.NE.0.0) GO TO 22
  437  CONTINUE
       M=M+1
      MMAX=M
     TIMES(M)=TIME*1.E+9
      DO 900 J=1,JP3
       WDEN(M,J)=DEN(2,J)/1.E+23
C  DEN READ OUT IN CM-3 /E17
       WV(M,J)=V(2,J)/1.E+2
C  VEL READOUT IN CM/SEC /E+4
      WT(M,J)=T(J)/1.16E+4
C    TEMP READOUT IN EV.
      WTI(M,J)=UI(2,J)/(1.5*KB*DEN(2,J)*1.16E+4)
```

```
  900  CONTINUE
          WRITE(6,6840) TIME,IN
 6840      FORMAT(6H TIME    ,E13.2,6H POWER,E13.3)

           WRITE(6,6841)  (WDEN(MMAX,KL),KL=2,70,2)
 6841      FORMAT(1X,20(1X,F5.1))

   22  CONTINUE
         TTM=1750.0
         CALL SECOND(TTT)
         IF(TTT.GT.TTM) WRITE(6,312)
         IF(TTT.GT.TTM) GO TO 314
  312  FORMAT(1X,*    TIMEDROP   *)
C----------------------------------
C----------------------------------
C----END OF MAIN TIME LOOP----
C------------------------------
    5 CONTINUE
  314  CONTINUE
C    END OF LOOPS
C  OUTPUT INSTRUCTIONS     HAVE STORED FOR DESIRED PRESENTATION
  904 CONTINUE
         WRITE(6,609) (TIMES(MN),MN=1,MMAX)
  609 FORMAT(2X,*TIMES IN NS.   *,5(F8.3,1X))
         WRITE(6,224)
         WRITE(6,224)
          WRITE(6,750)
  750 FORMAT(1X,*   NE/CC/E17       *)
          WRITE(6,224)
  224 FORMAT(1X,*-----------------------------------*)
         DO 956 J=1,JWRI,JINT
         WRITE(6,220)  (WDEN(M,J),M=1,MMAX),J
  220 FORMAT(1X,11(F5.3,1X),2X,I3)
  956  CONTINUE
         WRITE(6,224)
         WRITE(6,224)
         WRITE(6,223)
  223 FORMAT(1X,//)
          WRITE(6,751)
  751 FORMAT(1X,*TEMP IN EV.   *)
          WRITE(6,224)
         WRITE(6,224)
         DO 957 J=1,JWRI,JINT
         WRITE(6,221)  (WT(M,J),M=1,MMAX),J
  221 FORMAT(1X,11(F5.2,1X),2X,I3)
  957  CONTINUE
         WRITE(6,224)
         WRITE(6,223)
         WRITE(6,752)
  752 FORMAT(1X,*  VEL/CM/E+4    *)
         WRITE(6,224)
         DO 958 J=1,JWRI,JINT
         WRITE(6,222)  (WV(M,J),M=1,MMAX),J
  222 FORMAT(1X,11(F5.1,1X),2X,I3)
  958  CONTINUE
         WRITE(6,224)
         WRITE(6,223)
         WRITE(6,394)
  394 FORMAT(1X,*PRESSURE  ARB UNITS *)
         WRITE(6,224)
  215 FORMAT(1X,11(F5.2,1X),2X,I3)
         WRITE(6,224)
         WRITE(6,223)
         WRITE(6,395)
```

```
  395 FORMAT(1X,*     ION TEMPERATURE IN EV.   *)
         WRITE(6,224)
         DO 821 J=1,JWRI,JINT
         WRITE(6,221)  (WTI(M,J),M=1,MMAX),J
  216 FORMAT(1X,11(F5.3,1X),2X,I3)
  821 CONTINUE
          REWIND60
         WRITE(6,224)
          ISIGN=1
           IAV=0
          IGRAPH=0
           ZTIME=1.
           FSCALE=1.

C *************************
C**************************
C    INSERT FOR MICROFILM
             NREC60=0
 1050        CONTINUE
          NREC60=NREC60+1
          J1=1
          J2=57
          J3=2
          NR60=29
          NZ60=11
           ZTIME=0.
          ZDAT=0.
          ZTIM=0.

          NSTEP=1
          ZRMX=FLOAT(NR60-1)*2.*D*1.00001E+6
          ZMX=10.0001
C CMX IS IN NANOSECONDS
          HEAD=2HTE
          HUNIT=3H EV
          ILOOK=1
          WRITE(60) IONE,NREC60,NR60,NZ60,((WT(M,J)
      1  ,J=J1,J2,J3),M=1,11),ZDAT,ZTIM,HRUN,NEXTRA,
      1  NSTEP,ZTIME,ZRMX,ZMX,HEAD,HUNIT,ILOOK,ISIGN,
      1   IAV,FSCALE

          HEAD=2HNE
          HUNIT=6H10**17
          WRITE(60) IONE,NREC60,NR60,NZ60,((WDEN
      1    (M,J),J=J1,J2,J3),M=1,11),ZDAT,ZTIM,HRUN,
      2   NEXTRA,NSTEP,ZTIME,ZRMX,ZMX,HEAD,HUNIT,ILOOK
      3   ,ISIGN,IAV,FSCALE
          HEAD=2HTI
          HUNIT=3H EV
          WRITE(60) IONE,NREC60,NR60,NZ60,((WTI
      1    (M,J),J=J1,J2,J3),M=1,11),ZDAT,ZTIM,HRUN,
      2   NEXTRA,NSTEP,ZTIME,ZRMX,ZMX,HEAD,HUNIT,ILOOK
      3   ,ISIGN,IAV,FSCALE
          HEAD=2HVR
          HUNIT=5H10**4
          WRITE(60) IONE,NREC60,NR60,NZ60,((WV
      1    (M,J),J=J1,J2,J3),M=1,11),ZDAT,ZTIM,HRUN,
      2   NEXTRA,NSTEP,ZTIME,ZRMX,ZMX,HEAD,HUNIT,ILOOK
      3    ,ISIGN,IAV,FSCALE

          ITWR=3
          WRITE(6,337)RMAX
   337 FORMAT(1X,*MAX VALUE OF RATIO R=*,F12.4)
          WRITE(6,407)
```

```
  407 FORMAT(1X,*LL,UL,QTOT*)
         WRITE(6,224)
         DO 93 J=1,10
   93 WRITE(6,406)LL(J),UL(J),QTOT(J)
  406 FORMAT(1X,F10.3,2X,F10.3,2X,E12.4)
        CALL RUBY(AWV,AWH,SUMV,SUMH)
C
C       THIS DIAGNOSTIC SPATIAL RESOLUTION CORRECTION
      WRITE(6,224)
       WRITE(6,920)
920    FORMAT(1X,*LASER SCATT. CORRECTED FOR HORIZ. DISPLS.*)
       WRITE(6,224)
       DO 931 JKJ=1,19
       DO 921 M=1,MMAX
       SUMB=SUMD=SUMI=0.
       DO 922 IWR=1,100
       SUMD=SUMD + AWH(JKJ,IWR)*WDEN(M,IWR)
       SUMI=SUMI +AWH(JKJ,IWR)*WTI(M,IWR)
922    SUMB=SUMB + AWH(JKJ,IWR)*WT(M,IWR)
       ANS=SUMB/SUMH(JKJ)
       ANSD=SUMD/SUMH(JKJ)
       ANSI=SUMI/SUMH(JKJ)
       TETI=ANS/ANSI
       MB=M-1
        ISPL=(JKJ-1)*50
      WRITE(6,923)MB,ISPL,ANS,ANSD,ANSI,TETI
923   FORMAT(1X,*TIME(NS)= *,I2,*  HORIZ. DISPL. = *,I4,*  EL. TEMP.= *,
     +F6.3,*  EL. DENSITY= *,F5.3,*  ION TEMP.= *,F6.3,*  TEOTI= *,F6.3)
921    CONTINUE
        WRITE(6,224)
931      CONTINUE
C
       WRITE(6,224)
       WRITE(6,924)
924      FORMAT(1X,*LASER SCATT. CORRECTED FOR VERT. DISPLS.*)
       WRITE(6,224)
       DO 935 JKJ=1,19
       DO 925 M=1,MMAX
       SUMB=SUMD=SUMI=0.
       DO 926 IWR=1,100
         SUMD=SUMD+AWV(JKJ,IWR)*WDEN(M,IWR)
         SUMI=SUMI + AWV(JKJ,IWR)*WTI(M,IWR)
926     SUMB=SUMB + AWV(JKJ,IWR)*WT(M,IWR)
        ANS=SUMB/SUMV(JKJ)
        ANSD=SUMD/SUMV(JKJ)
        ANSI=SUMI/SUMV(JKJ)
        TETI=ANS/ANSI
        MB=M-1
        ISPL=(JKJ-1)*50
        WRITE(6,927)MB,ISPL,ANS,ANSD,ANSI,TETI
927   FORMAT(1X ,*TIME(NS)= *,I2,*  VERT. DISPL.= *,I4,*  EL.TEMP.= *,
     +F6.3,*  EL. DENSITY= *,F5.3,*  ION TEMP.= *,F6.3,*  TEOTI= *,F6.3)
925       CONTINUE
        WRITE(6,224)
935      CONTINUE

       IF(ITWR.EQ.1)CALL TAPO(WDEN,WT,WTI,WV)
       STOP
       END
C
C==================================
C--      ---------         ----------
C  SUBROUTINE TO CHECK FOR -VE TEMPS
         SUBROUTINE CHKT(T,N)
```

```
      DIMENSION T(320)
      DO 100 I=1,N
      IF(T(I).LT.0.) GO TO 200
 100 CONTINUE
      RETURN
 200 WRITE(6,201)T
 201 FORMAT(1X,*T NEGATIVE *,//(5E13.5))
     STOP
     END
C------------------------------
C  SUBROUTINE TO SMOOTH EARLY PROFILES
C=====================================
      SUBROUTINE SMOOTH(F,N)
      DIMENSION F(2,320),G(320)
      DO 199 K=1,N
      G(K+1)=0.5*(F(2,K)+F(2,K+2))
 199 CONTINUE
      G(1)=F(2,1)
      G(N+2)=F(2,N)
      NMN=N+2
      DO 200 I=1,NMN
 200 F(2,I)=G(I)
     RETURN
     END
C    ------------------------------
C  SUBROUTINE TO SPATIALLY AVERAGE DEN AND TEMP
C   AROUND POINTS USED IN EXPT..
C    WEIGHTED FOR VOLUME AND SCATT.PARAMETER
C=-=-=-=-=-=-=-=-=-=-=-=-=-=-=-=-=-=-=
      SUBROUTINE SPAV(DEN,T,JJJ,N,D)
      DIMENSION DEN(2,320),T(320),BTF(5),BNF(5)
      REAL MWAFAC
       DO 5 IC=1,4
       IF(IC.EQ.1)J1=1
       IF(IC.EQ.1)J2=21
       IF(IC.EQ.2) J1=71
       IF(IC.EQ.2)J2=111
       IF(IC.EQ.3)J1=101
       IF(IC.EQ.3)J2=141
      IF(IC.EQ.4)J1=155
    IF(IC.EQ.4)J2=195
      JNT=J2-J1+1
      FJINT=FLOAT(JNT)
    WASUM=0.
       DO 55 J=J1,J2
       AR902=(1.05**2)*(1.E-18)*1.16*DEN(2,J)/T(J)
       WAFAC=1./(1.+AR902)
       WASUM=WASUM+WAFAC
  55 CONTINUE
      PIE=3.14159
       MWAFAC=WASUM/FJINT
      IF(IC.NE.1) GO TO 499
     DV=PIE*(D**2)*((FLOAT(J2)-0.5)**2)
 499 CONTINUE
      IF(IC.EQ.1) GO TO 500
      DV=PIE*(D**2)*((FLOAT(J2)-0.5)**2)-
    +           PIE*(D**2)*((FLOAT(J1)-1.5)**2)
 500 CONTINUE
      DA=2.*PIE*(D**2)
       SUMT=0.
       SUMN=0.
       DO 66 J=J1,J2
      FJM1=FLOAT(J-1)
       AR902=(1.05**2)*(1.E-18)*1.16*DEN(2,J)/T(J)
```

```
          WAFAC=1./(1.+AR902)
         VOLJ=DA*FJM1
         SUMN=SUMN+WAFAC*DEN(2,J)*VOLJ
         SUMT=SUMT+WAFAC*T(J)*VOLJ
   66 CONTINUE
         BTF(IC)=SUMT/(MWAFAC*DV*1.16E+4)
         BNF(IC)=SUMN/(MWAFAC*DV)
    5 CONTINUE
          WRITE(6,44)N,(BNF(K),K=1,4)
          WRITE(6,33)N,(BTF(K),K=1,4)
   44 FORMAT(1X,*TSTEP*,I4,2X,*DEN.SPAT.AVS=*,4(E12.4,2X))
   33 FORMAT(1X,*TSTEP*,I4,2X,*TEMP SPAT.AVS.*,4(F12.4,2X))
        RETURN
        END
C---------------------------------------------
C  SUBROUTINE TO PUT OUTPUT ON MAG TAPE--------
C==============================================
        SUBROUTINE TAPO(WDEN,WT,WTI,WV)
        DIMENSION WDEN(12,320),WT(12,320),WV(12,320)
         DIMENSION WTI(12,320)
        WRITE(7) WDEN,WT,WTI,WV
C
         RETURN
         END
C-------------------------------------------
C  SUBROUTINE TO CALC LOCAL VALUE LOLA
C============================
         SUBROUTINE LOLOL(DEN,T,J,LOLA)
         DIMENSION DEN(2,320),T(320)
         REAL LOLA,LAMBDA,KB
         PIE=3.14159
C ALL UNITS ARE C.G.S. IN THIS SUB
         DIN=DEN(2,J)*1.E-6
         KB=1.38E-16
         CHAR=4.803E-10
         A=1.5/(CHAR**3)
         B=(KB**3)*(T(J)**3)/(PIE*DIN)
         C=SQRT(B)
         LAMBDA=A*C
         LOLA=ALOG(LAMBDA)
       RETURN
       END
       SUBROUTINE SCALEN(DEN,T,D,JJJ,LOLMIN,JMIN,SCALMIN)
C  TO EVALUATE MIN SCALENGTH OF T/ELEC MFP
C==============================================
         DIMENSION DEN(2,320),T(320)
         REAL LOLMIN,LOL,MFP
C  BUFFER MAXIMA
         JMIN=1
         LOLMIN=1.E+9
         SCALMIN=1.E+9
         JM1=JJJ-1
         DO 5 J=1,JM1
         I=J+1
           T1=T(J)-T(I)
            DTDL=(ABS(T1)+10.)/D
         ADTDL=ABS(DTDL)

C    THE FACTOR 1.E-8 ISTO AVOID INFINITE RESULT AT 4375
         IF(ADTDL.LT.1.E-8)ADTDL=1.E-8
         TAV=(T(J)+T(I))/2.
         DENAV=(DEN(2,J)+DEN(2,I))/2.
         SCAL=TAV/ADTDL
         MFP=(2.276/1.16**2)*1.E+8*(TAV**2)/DENAV
```

```
      LOL=SCAL/MFP
      IF(LOLMIN.GT.LOL)JMIN=J
      IF(LOLMIN.GT.LOL)LOLMIN=LOL
      IF(SCALMIN.GT.SCAL)SCALMIN=SCAL
    5 CONTINUE
      RETURN
      END
      SUBROUTINE FLMOD(DEN,T,SIGMA,MODFAC,RR,JJJ,D,QTOT,
     +          RMAX,LL,UL)
C -----------------------------------------------------
C======================================================
C   TO EVALUATE FLUX IN VARIOUS REGIMES OF R
C============================================
      DIMENSION DEN(2,320),T(320),QTOT(15),UL(15)
      DIMENSION RR(320)
      REAL MODFAC(320)
      REAL KB,LL(15)
      KB=1.38E-23
      PIE=3.14159
      AME=9.1E-31
C
C
      LL(1)=0.
      LL(2)=0.0001
      LL(3)=0.001
      LL(4)=0.002
      LL(5)=0.005
      LL(6)=0.01
      LL(7)=0.05
      LL(8)=0.1
      LL(9)=0.5
      LL(10)=1.
      LL(12)=0.07
      DO 6 JJ=1,10
    6 UL(JJ)=LL(JJ+1)
      UL(10)=2.
C
      GO TO 909
C  TO SEE HOW FAR T(J)  CHANGES
      ITC=1
      DO 12 J=1,JJJ
      TDIF=ABS(T(J)-T(J+1))
      IF(TDIF.LT.1.)ITC=ITC+1
      IF(ITC.GT.6)JT=J
      IF(ITC.GT.6) GO TO 15
   12 CONTINUE
   15 CONTINUE
      IF(JT.LT.3)JT=3
  909 CONTINUE
C
      DO 9001 J=1,JJJ
 9001  RR(J)=0.0
C   TO EVALUATE HEAT FLUXES
C================================
      JM1=JJJ-1
      DO 1 J=2,JM1
      Q=-SIGMA*(T(J)**2.5)*(T(J+1)-T(J-1))/(2.*D)
      AQ=MODFAC(J)*Q
      QMAX1=SQRT(2./PIE)*DEN(2,J)*KB*T(J)
      QMAX2=SQRT(KB*T(J)/AME)
      QMAX=QMAX1*QMAX2
C  MODIFIEDFREE STREAMING LIMIT ; 2 NOT 1.5)
      R=AQ/QMAX
      IF(R.GT.RMAX) RMAX=R
```

```
         LTYPE=11
         DO 4 L=1,10
         IF((R.GE.LL(L)).AND.(R.LE.UL(L))) LTYPE=L
    4 CONTINUE
         QTOT(LTYPE)=QTOT(LTYPE)+AQ
         RR(J)=R
    1 CONTINUE
C
C
         RETURN
       END
         SUBROUTINE LIMTER(DEN,T,MODFAC,JJJ,D,LOLMIN,
     +             JMIN,ARTLIM)
C  TO EVALUATE FREE STREAMING REDUCTION TO CLASSICAL THERAL
C   CONDUCTIVITY ACCORDING TO L/LAMBDAE ON THIS STEP FOR
C   USE ON NEXT STEP
C-=-=-=-=-=-=-=-=-=-=-=-=-=-=-==-=-=-=-=-=-=-=-=-=-=-=-=-=-=-=-=-
         DIMENSION DEN(2,320),T(320),RR(320)
         REAL MODFAC(320),LOL,LOLMIN,MFP
         DO 93 J=1,JJJ
   93 MODFAC(J)=1.
         ONLIM=3.6363/ARTLIM
         JM1=JJJ-1
         JMIN=250
         LOLMIN=1.E+9
         SCALMIN=1.E+9
         DO 5 J=1,JM1
         I=J+1
         ADTDL=(1.E-8+T(J)-T(I))/D
          T1=T(J)-T(I)
           ADTDL=ABS(T1)+10.
           ADTDL=ADTDL/D
         TAV=0.5*(T(J)+T(I))
         DENAV=0.5*(DEN(2,J)+DEN(2,I))
         SCAL=TAV/ADTDL
C   SCAL=TEMPERATURE GRADIENT SCALE LENGHT
         MFP=(2.276/(1.16**2))*1.E+8*(TAV**2)/DENAV
         LOL=SCAL/MFP
C  LOL=LOCAL RATIO OF SCALE LENGTH OVER ELECTRON MEAN FREE PATH
         IF(LOLMIN.GE.LOL)LOLMIN=LOL
         IF(LOLMIN.GE.LOL)JMIN=J
         IF(LOL.GE.ONLIM)GO TO 12
         IF(LOL.LT.0.)GO TO 12
         MODFAC(J)=(LOL/ONLIM)
   12 CONTINUE
    5 CONTINUE
       RETURN
       END
            FUNCTION PTIME(T)
C THIS FUNCTION FORMS A NORMALISED POWER
         TRISE=1.E-9
           TFALL =2.E-9
              TEXT=4.2E-9
            PPLAT=.1
            TZERO=6.E-9
          IF(T.GT.TRISE)  GO TO 100
           PTIME=T/TRISE
            RETURN
 100       IF(T.GT.TFALL)  GO TO 200
          PTIME=1.
          RETURN
 200      PTIME=1.-(T-TFALL)/(TEXT-TFALL)
          IF(PTIME.LT.PPLAT)  PTIME=PPLAT
          IF(T.GT.TZERO)  PTIME=0.
```

```
            RETURN
            END
C
        SUBROUTINE RUBY(AWV,AWH,SUMV,SUMH)
        DIMENSION AWV(26,100),AWH(26,100),SUMH(26),SUMV(26)
C
C        CLEAR ARRAYS
C
            DO 1 J=1,26
            DO 1 I=1,100
           AWV(J,I)=AWH(J,I)=0.
1          SUMV(J)=SUMH(J)=0.
           DO 99 JJJ= 1,19
            DELTA=(FLOAT(JJJ-1))*50.
        KN=11
        KNZ=31
        RKN=FLOAT(KN-1)
C       IRBIN IS SPATIAL RESOLUTION IN MICROMETRES

        IRBIN=20

         TW=414.
         TH=255.
         TZ=288.
         DH=TH/RKN
         DW=TW/RKN
         DZ=TZ/RKN

         DO 2 IX=1,KN
         DO 2 IY=1,KN
         DO 2 IZ=1,KNZ
C     FROM 3X -1/E TO 3X +1/E

         Z=-(TZ/2.0)*3.0 + (FLOAT(IZ)-1.)*DZ

C      Y SCANNED IN KN STEPS FROM RHS OF BOX

        Y=-TW/2.0 + (FLOAT(IY)-1.)*DW


C       X SCANNED IN KN STEPS FROM BOTTOM OF BOX


         X=-TH/2.0 + (FLOAT(IX)-1.)*DH
C       RADIUS FOR VERTICAL DISPL.

         RV=SQRT((((Z+Y)**2)/2.) + (DELTA-X)**2)

C     RADIUS FOR HORIZ. DISPLS.

          RH=SQRT(X*X + (DELTA -(Z+Y)/1.4142)**2)
         RLR= (X*X + Z*Z)/((TZ/2.0)**2)
C
C        ASSUME GAUSSIAN FALL OF FOR RUBY
C
         JRV= IFIX(RV)/IRBIN +1
         JRH=(IFIX(RH))/IRBIN +1
C
C       INDEX OF ARRAY FOR THIS RADIUS
C
         AWV(JJJ,JRV)=AWV(JJJ,JRV)  +EXP(-RLR)
         AWH(JJJ,JRH)=AWH(JJJ,JRH)  +EXP(-RLR)
2        CONTINUE
```

```
        SUMH(JJJ)=SUMV(JJJ)=0.
       DO 54 LL=1,100
       SUMV(JJJ)=SUMV(JJJ)+AWV(JJJ,LL)
54     SUMH(JJJ)=SUMH(JJJ)+AWH(JJJ,LL)
99     CONTINUE
       RETURN
       END
```

APPENDIX D

Computer Program used to look at the perturbed distribution functions of Spitzer et al.[5]

```
      PROGRAM FLUX(TAPE5,INPUT,OUTPUT,TAPE6,TAPE88)
      DIMENSION DTX(51),FLUXE(51),FLUXT(51),SUMFLUX(51)
     +,DE(51),DT(51),TOTFLUX(51),TNTFLUX(51),DSN(51),
     +DTN(51),FACT1(51),DTQN(51),ANSS(51),ANST(51),ANSTQ(51)
     +,DISTN(51),DISTP(51),TX(102),TFLUX(102),ANS(102),DIST(102)
      READ(5,10) (DTX(I),I=1,51)
   10 FORMAT(F10.0)
      READ(5,11) (DE(I),I=1,51)
   11 FORMAT(F10.0)
      READ(5,11) (DT(I),I=1,51)
C
      DO 29 KK=1,8
      K=KK-1
      T=2.**FLOAT(K)
      B=.01*T
      A=.3517*B
      DO 13 I=1,51
      FACT1(I)=EXP(-(DTX(I))**2)
      FACT2=((DTX(I))**5)*FACT1(I)
      FLUXE(I)=B*0.3517*FACT2*DE(I)
      FLUXT(I)=B*FACT2*DT(I)
      SUMFLUX(I)=FLUXE(I)  + FLUXT(I)
      TOTFLUX(I)=FACT2 + SUMFLUX(I)
      TNTFLUX(I)=FACT2 - SUMFLUX(I)
   13 CONTINUE
      AINT1=AINT2=AINT3=0.0
      DSN(1)=DTN(1)=DTQN(1)=0.0
      DO 14 I=2,51
      DEN=(DTX(I)-DTX(I-1))/2.0
      JJJ=I
      DSN(JJJ)=(SUMFLUX(I)+SUMFLUX(I-1))*DEN
      AINT1=AINT1+DSN(JJJ)
      DTN(JJJ)=(TOTFLUX(I)+TOTFLUX(I-1))*DEN
      AINT2=AINT2+DTN(JJJ)
      DTQN(JJJ)=(TNTFLUX(I)+TNTFLUX(I-1))*DEN
      AINT3=AINT3+DTQN(JJJ)
   14 CONTINUE
      ANSS(1)=ANST(1)=ANSTQ(1)=0.0
      DO 15 I=2,51
      SUMS=SUMT=SUMTQ=0.0
      JJ=I
      DO 16 J=2,JJ
      SUMS=SUMS + DSN(J)
      SUMT=SUMT + DTN(J)
      SUMTQ=SUMTQ + DTQN(J)
   16 CONTINUE
      ANSS(I)=SUMS/1.
      ANST(I)=SUMT/1.
      ANSTQ(I)=SUMTQ/1.
   15 CONTINUE
      DO 20 J=1,51
      FACTP=1.+B*DT(J)+A*DE(J)
      DISTP(J)=FACTP*FACT1(J)
      FACTN=1.-B*DT(J)-A*DE(J)
   20 DISTN(J)=FACTN*FACT1(J)
      DO 30 I=1,51
      KN=52-I
      TX(I)=-DTX(KN)
      TFLUX(I)=TNTFLUX(KN)
      ANS(I)=ANSTQ(KN)
   30 DIST(I)=DISTN(KN)
      DO 31 I=1,51
      KN=51 + I
      TX(KN)=DTX(I)
```

```
      TFLUX(KN)=TOTFLUX(I)
      ANS(KN)=ANST(I)
31    DIST(KN)=DISTP(I)
      ID=KK
      N=102
      WRITE(88) ID,N,(TX(I),TFLUX(I),I=1,N)
      ID=ID+8
      WRITE(88) ID,N,(TX(I),DIST(I),I=1,N)
29       CONTINUE
      STOP
      END
```

APPENDIX E

A PLASMA FOCUS DEVICE

1. INTRODUCTION

I constructed this device in the first year of my Ph.D. with a view to obtaining a plasma of super-critical density for the CO_2 laser (i.e. $n_e > 10^{19}$ cm^{-3}). Laser-plasma interactions at the critical density were to be investigated. However, with similar work under way at the Culham Laboratory[89] the project was terminated.

2. DESCRIPTION OF THE DEVICE

The focus was a co-axial Mather-type device[90] with a 5cm. diameter cathode and a 10cm. diameter outer electrode. Both electrodes were 22cm. long and an insulator covered the first 5cm. of the inner electrode. A base pressure of better than 5.10^{-5} Torr was achieved. A 2.5kJ, 10kV capacitor bank powered the device.

3. MEASUREMENTS

(i) Time integrated photographs

Fig. (E-1) shows two shots at 10kV in 100mT of hydrogen. The restricted light emission over the centre electrode confirmed that some pinching was taking place.

(ii) Measurement of the rundown velocity

The current sheath moves down the electrodes under the action of a $\underline{j} \wedge \underline{B}$ force and "snowploughs" the gas ahead of itself.

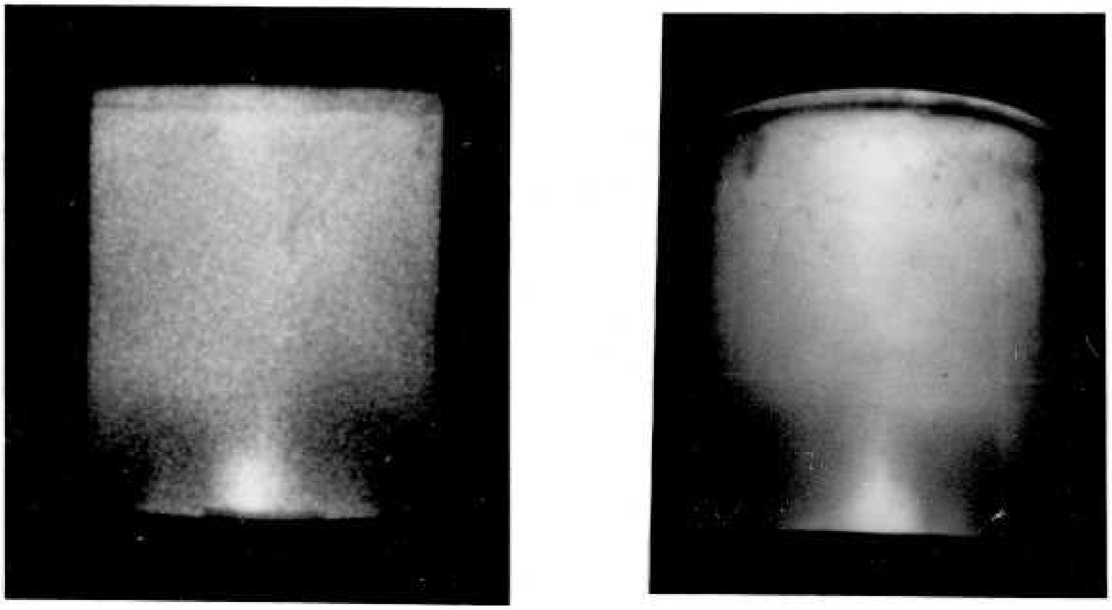

Fig. (E-1)

Rosenbluth and Garwin[91] have calculated this velocity as,

$$v_s = (c^2E^2/4\pi\rho_0)^{\frac{1}{4}} \text{ cms}^{-1} \qquad \text{(E-1)}$$

where E_0 and ρ_0 are, respectively, the applied electric field and initial mass density (in cgs units). With ~ 5kV over 2.5 cm in 1 Torr of hydrogen this gives v_s ~ 1.1 10^7 cms^{-1}.

This velocity was measured by drilling 3mm. diameter holes in the outer electrode and observing the light emission from the passing sheath. This is shown in Fig. (E-2).

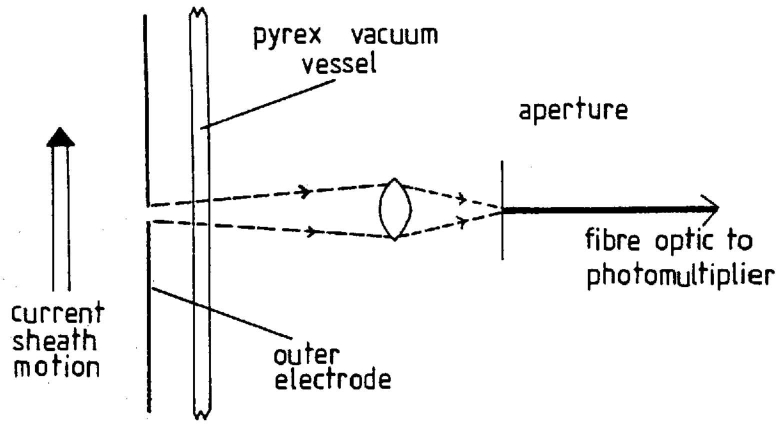

Fig. (E-2)

The start of the current pulse observed on a Rogowski coil was used as time zero. A number of shots were taken for each hole and reproducibility was good. The results for 1 Torr hydrogen and 10kV in the capacitor bank are shown in Fig. (E-3).

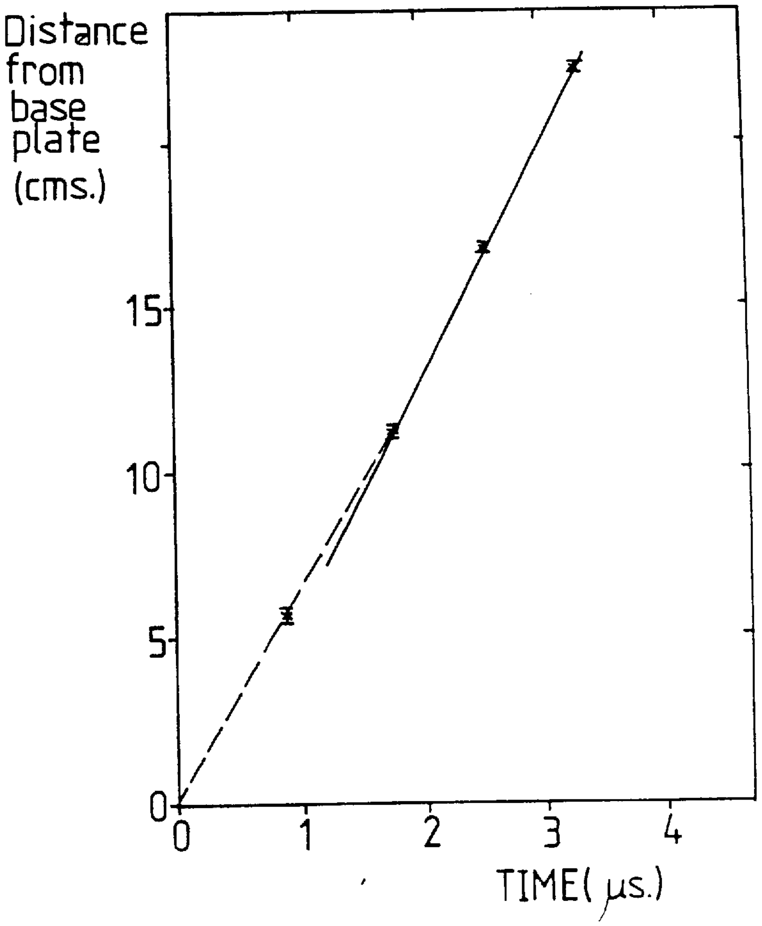

Fig. (E-3)

The shown straight line gave a velocity of 7.1 10^{6} cms^{-1}. For optimum operation, the focus should be designed such that the rundown time matches the LCR risetime of the device so that the pinch phase occurs at maximum current. A velocity of 7.10^{6} cms^{-1} down 22cm. electrodes gave a rundown time of 3.1μs compared with a 3.8μs current risetime. In part (iv) with 4 Torr hydrogen the expected rundown time is ~ 4.4μs from equation E-1.

(iv) Pinch phase

A Hadland image convertor camera was used in the framing mode to observe the collapse and pinch phase at the end of the electrodes. In all the pictures shown, each frame is exposed for 10ns with 50ns between frames. The framing sequence is shown in Fig. (E-4).

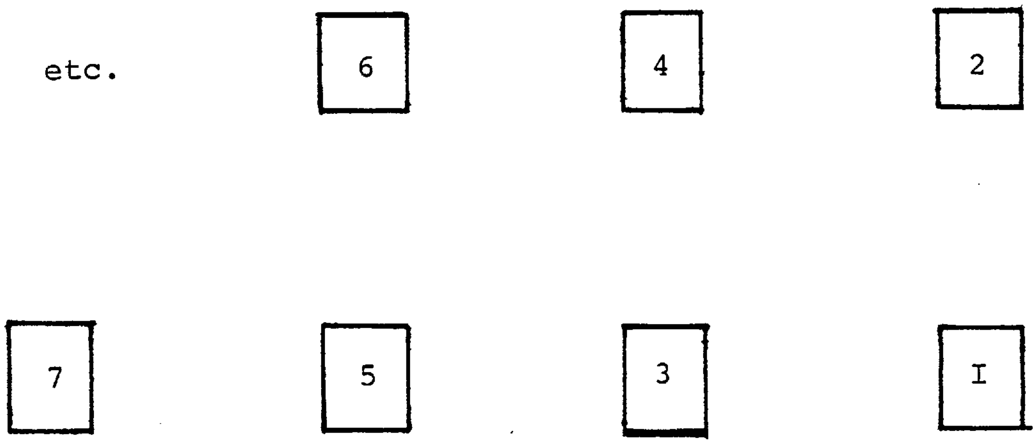

Fig. (E-4)

Fig. (E-5) shows the results. Fig. (E-5)(a) is a focus mode picture. The black tape mask gives the scale for the inner electrode (5cms.). Fig. (E-5)(b) shows a pinch phase in 4T of pure hydrogen lasting 50 to 100ns. Fig. (E-5)(c) shows a subsequent shot with 0.2% Ar doping.

Here, the pinch lasts 150 to 200ns. Fig. (E-5)(d) shows a collapse phase with 0.2% Ar doping. Measuring from the centre of the collapsing sheath in each frame we get from frames 1, 2 and 3 an interpolated collapse velocity of $6.8 \pm 0.2\ 10^{6}$ cms^{-1} and from frames 3 and 4 a velocity of $1.1 \pm 0.2\ 10^{7}$ cm s^{-1}.

Also visible in Figs. (E-5)(b) and (c) is the break-up of the pinch phase due to the m = 0 instability.

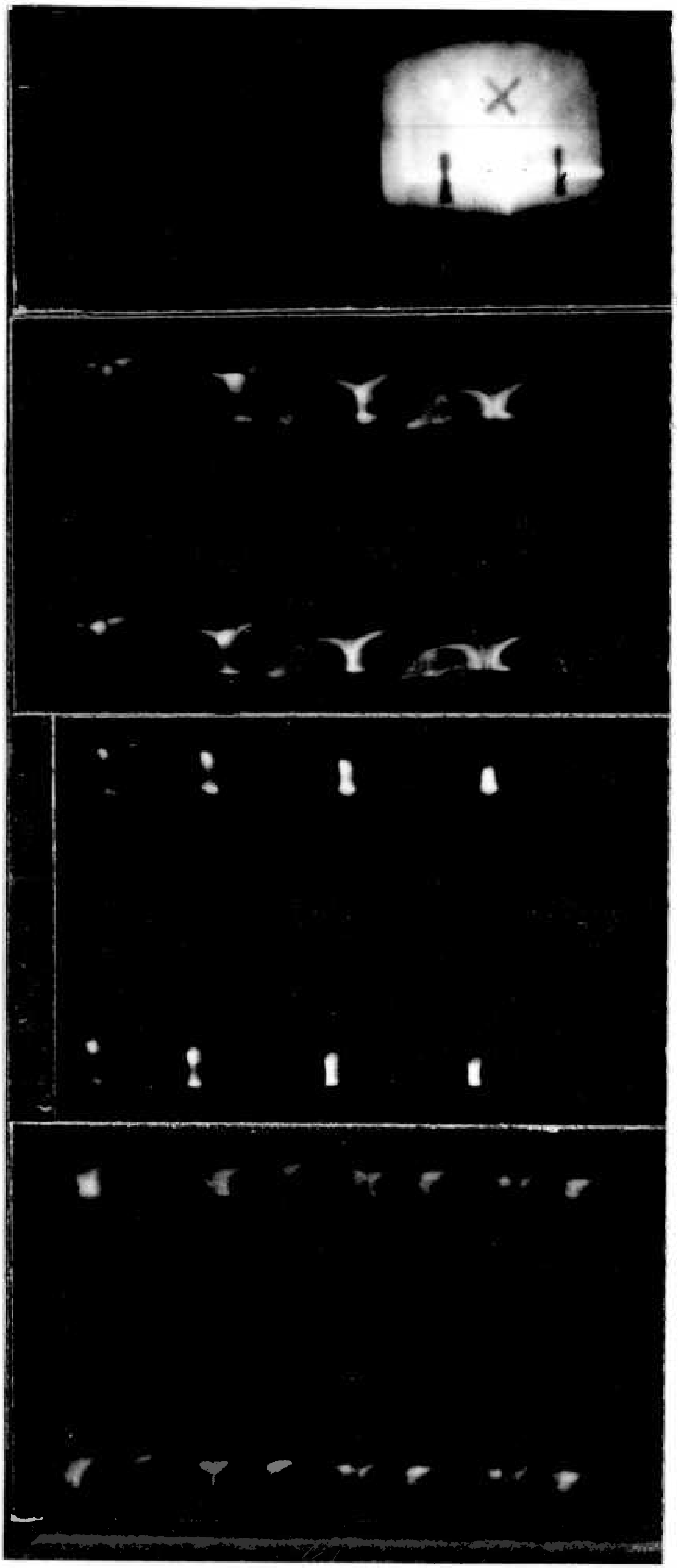

(a)
FOCUS MODE

(b)
4 Torr hydrogen

(c)
4 Torr hydrogen with
0.2% argon

(d)
4 Torr hydrogen with
0.2% argon

Fig. (E-5)

REFERENCES

1. Landshoff, R. Phys. Rev. 76, 904 (1949).
2. Braginskii, S.I. Sov. Phys. JETP, 6(33), 358 (1958).
3. Spitzer, L. Physics of fully ionized gases, Interscience Inc., New York (1956).
4. Shkarofsky, I.P. Can. J. Phys. 39, 1619 (1961).
5. Spitzer, L. and Harm, R. Phys. Rev. 89, 977 (1953).
6. Sheffield, J. Plasma Scattering of electromagnetic radiation, New York, Academic (1975).
7. Jackson, D.J. Classical Electrodynamics (p.340) J. Wiley and Sons. (1962).
8. Forslund, D.W. J. Geophys. Res. 75, 17 (1970).
9. Manheimer, W.M. Phys. Fluids, 20, 265 (1977).
10. White, M.S. et al. Phys. Rev. Lett. 35, 524 (1975).
11. Athay, R.G. Solar Phys. 29, 357 (1973).
12. Lawson, J.D. Proc. Phys. Soc. B70, 6-10, 137 (1957).
13. Nuckolls, J. et al. Nature, 239, 139 (1972).
14. Brueckner, K.A. and Jorna, S. Rev. of Mod. Phys. 46, 325 (1974).
15. Haas, R.A. et al. Phys. Fluids 20, 322, Fig. 10(b) (1977).
16. Perkins, F.W. and Flick, J. Phys. Fluids 14, 2012 (1971).
17. Stamper, J.A. Phys. Fluids 18, 735 (1975).
18. Attwood, D.T. et al. Phys. Rev. Lett. 40, 184 (1978).
19. Fedosejeos, R. et al. Phys. Rev. Lett. 39, 932 (1977).
20. Haas, R.A. et al. Phys. Fluids 20, 322 (1977).
21. Thomson, J.J. et al. Phys. Fluids 21, 707 (1978).
22. Ginzburg, V.L. The propagation of E-M waves in plasmas, 2nd ed., Oxford (1970) - Pergamon (Pages 252 - 277).
23. Forslund, D.W. et al. Phys. Rev. A. 11, 679 (1975).

24. Manes, et al. Phys. Rev. Lett. 39, 281 (1977).

25. Bodner, et al. 6th Int. Conf. of Plasma Phys. and Controlled Nuc. Fusion. (I.A.E.A. - Berchtesgaden, 1976) Paper F9, 217.

26. Ripin, B.H. Appl. Phys. Lett. 30, 134 (1977).

27. Ripin, B.H. NRL internal report no. 3684 (1977), Naval Research Laboratory, Washington D.C., U.S.A.

28. Mead, W.C. et al. Phys. Rev. Lett. 37, 489 (1976).

29. Key, M.H. et al. Paper WA7, Topical meeting on inertial confinement fusion, San Diego (1978).

30. Gurevich, A.V. et al. J.E.T.P. 22, 449 (1966).

31. Storm, E.K. and Larsen, J.T. A simple scaling model for exploding pusher targets. Lawrence Livermore Lab. Report No: UCRL - 79788 (1977).

32. Corman, E.G. et al. Nucl. Fusion, 15, 377 (1975).

33. Anisimov et al. Sov. J. Plasma Phys. 3(4), 409 (1977).

34. Malone et al. Phys. Rev. Lett. 34, 721 (1975).

35. Pearlman, J.S. and Anthes, J.P. App. Phys. Lett. 27, 581 (1975).

36. Yaakobi, B. and Bristow, T.C. Phys. Rev. Lett. 38, 350 (1977).

37. Campbell, P.M. et al. Phys. Rev. Lett. 39, 274 (1977).

38. Ripin, B.H. et al. Phys. Rev. Lett. 34, 1313 (1975).

39. Stamper, J.A. and Ripin, B.H. Phys. Rev. Lett. 34, 138 (1975).

40. Stamper, J.A. et al. Phys. Rev. Lett. 40, 1177 (1978).

41. Raven, A. et al. Phys. Rev. Lett. 41, 554 (1978).

42. Stamper, J.A. et al. Phys. Rev. Lett. 35, 663 (1975).

43. Colombant, D.G. and Winsor, N.K. Phys. Rev. Lett. 38, 697 (1977).

44. Craxton, R.S. and Haines, M.G. Phys. Rev. Lett. 35, 1336 (1975).

45. Thomson, J.J. et al. Phys. Rev. Lett. 35, 663 (1975).

46. Bezzerides, B. et al. Phys. Rev. A. 16, 1678 (1977).

47. Bickerton, R.J. Nuc. Fusion, 13, 457 (1973).

48. Mishin, E.V. Sov. Phys. Dokl. 19, 140 (1974).

49. Morse, R.L. and Nielson, C.W. Phys. Fluids 16, 909 (1973).

50. Mason, R.J. Los Alamos internal report LA-UR-78-2776 (1978).

51. Dumanchin, R., Farcy, J.C. et al. Proc. 6th Int. Quantum Elec. Conf. Kyoto, Japan 1970. Also J. Quant. Elec. Feb. (1972).

52. Craig, A.D. and Perkin, R.M. Optics Communications, 12, 256 (1974

53. Ireland C.L.M. Journal Phys. E. 8, 1007 (1975).

54. Lochte-Holtgreven, W. (ed). "Plasma Diagnostics" (North-Holland, Amsterdam) (1968).

55. White, M.S. Ph.D. Thesis, Univ. London (1976).

56. Thornton, E. Journal Phys. E. 3, 862 (1970).

57. Evans, D.E., and Katzenstein, J. Rep. Prog. Phys. 32, 207 (1969).

58. Salpeter, E.E. Phys. Rev. 120, 1528 (1960).

59. Kunze, H.J. Z. Naturf. A, 20, 801 - 13 (1965).

60. Kegel, W. Garching Internal rep. no. IPP6/34 (1965). Note - unpublished but available in Culham Library.

61. Lashmore-Davis, C. Plasma Phys. 17, 281 (1975).

62. Offenberger, A.A. et al. J. App. Phys. 47, 1451 (1976).

63. Tsytovich, V.N. Nonlinear effects in Plasma (Plenum, New York, 1970).

64. White, M.S. Ph.D. Thesis, Univ. London (1976) Pages 90 and 119.

65. Drawin, H. and Felenbok, P. Data for Plasmas in Local Thermodynamic Equilibrium (Gauthier-Villars, Paris, 1965).

66. McWhirter, R.W.P. and Hearn, A.G. J. Phys. Soc. 82, 641 (1963).

67. Jordan, C. Mon. Not. R. Astr. Soc. 142, 501 - 521 (1969).

68. Johnson, L.C. and Hinnov, E. J. Quant. Spectrosc. Radiat. Transfer. 13, 333 - 358 (1973).

69. Griem, H.R. Plasma Spectroscopy (1964), McGraw-Hill Inc. Page 163.

70. Evans, D.E. Plasma Phys. 12, 573 (1970).

71. Boyd, T.J.M. and Sanderson, J.J. "Plasma Dynamics", (Nelson, London 1969) Section 3 - 6.

72. Potter, D. "Computational Physics" (Wiley, London 1973).

73. Heald, M. and Wharton, C. "Plasma Diagnostics with Microwaves" (Wiley, London 1965).

74. Hora, H. and Wilhelm, H. Nuc. Fusion 10, 111 (1970).

75. Billman, K.W. and Stallcop, J.R. App. Phys. Lett. 28, 704 (1976).

76. Johnston, T.W. and Dawson, J.M. Phys. Fluids 16, 722 (1973).

77. Silin, V.P. Sov. Phys. JETP, 20, 1510 (1965).

78. Cohen, R.S., Spitzer, L. and McR.Routly, P. Phys. Rev. 80, 230 (1950).

79. Robinson, B.B. and Berstein, I.B. Ann. Phys. (N.Y.) 18, 110 (1962).

80. Shkarofsky, I.P., Berstein, I.B. and Robinson, B.B. Phys. Fluids, 6, 40 (1963).

81. Chapman, S. and Cowling, T.G. "The Mathematical Theory of Non-Uniform Gases" (Cambridge University Press, London 1939).

82. Chandrasekhar, S. Revs. Mod. Phys. 15, 31 (1943).

83. Dum, C.D., Chodura, R. and Biskamp, D. Phys. Rev. Lett. 32, 1231 (1974).

84. Faehl, R.J. and Kruer, W.L. Phys. Fluids, 20, 55 (1977).

85. Manheimer, W.M., Colombant, D.G. and Ripin, B.H. Phys. Rev. Lett. 38, 1135 (1977).

86. Chen, F.F. In 'Laser interaction and related plasma phenomena' ed. H.J. Schwarz and H. Hora. Plenum, New York Vol. 3A, P.291 (1973).

87. Catto, P.J. and Speziallе, T. Phys. Fluids, 20, 167 (1977).

88. Cooper, R. "Motion of Solid D_2 under Laser Irradiation", AIAA Paper 72 - 721 (1972).

89. Forrest, M.J. et al. Phys. Rev. Lett. 37, 1681 (1976).

90 "Methods of Experimental Physics" (Plasma Physics) Vol. 9B, Ed. R.H. Lovberg and H.R. Griem, Academic Press, New York and London 1971.

91. Rosenbluth, M. and Garwin, R. Los Alamos Sci. Lab. Rep. LA-1850, Los Alamos Sci. Lab., Los Alamos, New Mexico, 1954.

92. Gondhalekar, A. et al. IEEE J. Quantum Electron (U.S.A.), QE-11, 103 (1975).

OBSERVATION OF SEVERE HEAT-FLUX LIMITATION AND ION-ACOUSTIC TURBULENCE IN A LASER-HEATED PLASMA

D. R. Gray, J. D. Kilkenny, M. S. White, P. Blyth, D. Hull

Reprinted from PHYSICAL REVIEW LETTERS Vol. 39, No. 20, 14 November 1977
1270

Observation of Severe Heat-Flux Limitation and Ion-Acoustic Turbulence in a Laser-Heated Plasma

D. R. Gray, J. D. Kilkenny, and M. S. White[a]
Blackett Laboratory, Imperial College, London, United Kingdom

and

P. Blyth and D. Hull
Atomic Weapons Research Establishment, Aldermaston, United Kingdom

(Received 12 September 1977)

The thermal conductivity of a plasma of density 6×10^{16} cm^{-3} is measured when it is heated by a 300-MW, 3-ns CO_2 laser pulse. The data are best represented using a heat flux which is limited to ~ 4% of the free-streaming limit. Low-frequency turbulence is observed of sufficient intensity to cause this flux limit.

In this Letter we report definitive measurements of the thermal conductivity of a laser-heated plasma when the temperature gradient is large and an ion-acoustic instability is excited. The classical treatment of thermal conductivity[1] has been by a first-order perturbation to a Maxwellian. However, when λ_e/L (the ratio of the electron mean free path to the temperature-gradient scale length) is greater than 0.02, second-order terms dominate and there seems to be no rigorous theory. Here we use

$$\lambda_e/L = 2.292\times10^{13} T_e\,|\nabla T_e|\, n_e \ln\Lambda\,, \qquad (1)$$

with T_e in eV and n_e in inverse cubic centimeters. We have previously measured the thermal conductivity[2] with $T_e=T_i$ and $\lambda_e/L\sim0.04$ and found a reduction by a factor of 2 from Spitzer's value. When $T_e\gg T_i$, the return current from the heat flow can drive an ion-acoustic instability, which would decrease the heat flux.[3,4] Here we have increased λ_e/L to 0.5 (from Ref. 2) and with $T_e \sim 5T_i$ have seen a very low thermal conductivity accompanied by low-frequency turbulence.

As before, our measurement is based on ruby-laser light scattering. We have extended this technique to spatial and temporal resolutions of 200 μm and 1 ns. Other experiments on laser-produced plasmas[5-7] have used much less direct diagnostics to measure thermal conductivity. Many other phenomena (magnetic-field generation, resonant absorption, atomic physics, fast-electron transport) complicate these experiments. In contrast, our experiment has to our knowledge none of these extraneous phenomena.

The plasma used has been described previously.[2] It was a weak hydrogen Z pinch with initial density and temperature of 6×10^{16} cm^{-3} and 4 eV, respectively. The center of this plasma was heated by a 300-MW, 3-ns CO_2 laser pulse, focused to a measured spot size of 350 ± 50 μm. Ruby-laser light scattering at 90° was performed with the differential scattering vector ($\vec{k}_s$) both parallel and perpendicular to ∇T_e. The scattering parameter α was in the range $0.5<\alpha<1.5$. The electron density and temperature were obtained by fitting shifted Salpeter curves for different α's to the electron features. This method is described by Kunze.[8] The error bars on density and temperatrue were determined by the range of the values of α which would fit within the experimental error bars. These values of n_e agreed with those obtained using a Rayleigh calibration of the system. A fast photomultiplier (RCA C31024A) gave a 1.2-ns time resolution. Reproducibility was good enough to plot spectra on a shot-to-shot basis. The spatial resolution

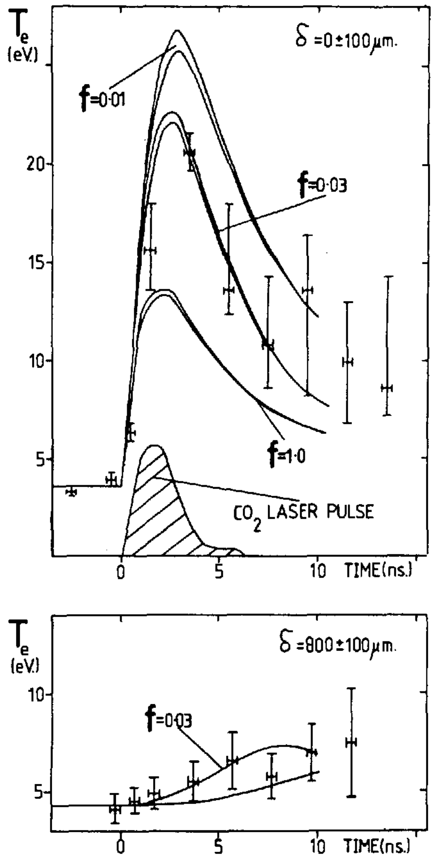

FIG. 1. Examples of experimental data and simulation results with $s = 1$ and $w = 1$. For each simulation the two solid lines indicate the band of temperature possible within the ± 100-μm alignment setting error. At $\delta = 0$, the best fit of $f = 0.03$ is shown together with $f = 1.0$ and $f = 0.01$. At $\delta = 800$ μm the band is for displacements between 700 and 900 μm and simulation results are only shown for $f = 0.03$.

(~200 μm) was defined by the spectrometer entrance-slit height and width, and the measured ruby-laser focal-spot size. Data were taken for different displacements (δ) between the CO_2- and ruby-laser foci.

On the length and time scale of the laser heating, the plasma was homogeneous, constant, and unmagnetized. As the plasma was so underdense, refraction and variation along the laser beam were negligible, and the experiment could be modeled by a one-dimensional, two-temperature fluid code with symmetry about the CO_2 laser axis.

In the simulation, the absorption coefficient K_I for CO_2 laser radiation was taken from Billman and Stallcop[9]:

$$K_I = w C_2 \lambda^2 n_e^2 T_e^{-1.5}(1 - C_3 n_e \lambda^2)^{-0.5} g, \qquad (2)$$

where w was an additional factor allowing for artificial variation of K_I. The ponderomotive force and the saturation of inverse bremsstrahlung were included although their effect was small. The electron heat flux q was defined in the normal way:

$$\vec{q} = -s\sigma T_e^{2.5} \nabla T_e / \ln\Lambda, \qquad (3)$$

where s is a factor allowing for an artificial variation in the conductivity. When $s = 1$ the conductivity corresponds to Spitzer's value.[1] Additionally, simulations were run in which $\vec{q}$, as defined by Eq. (3), was constrained not to exceed some fraction (f) of the free-streaming limit, $q_{\max} = nkT_e(2kT_e/\pi m_e)^{0.5}$. Experiments were performed with CO_2-laser-pulse durations of 3 and 20 ns. An example of the results for $\delta = 0 \pm 100$ and $\delta = 800 \pm 100$ μm is shown in Fig. 1. Results were also obtained at $\delta = 100 \pm 100$ and 1200 ± 100 μm. On the rising edge of the heating there are large error bars due to the 1-ns instrumental time resolution. Late in time the power of the diagnostic laser is decreasing and the error bars again become large. Simulation results with $w = 1$ (classical absorption) and varying f are also shown on Fig. 1. A good fit at both displacements, where the band of simulation results fits within all the experimental errors, is obtained for $f = 0.03$, but not for $f = 1$ or $f = 0.01$. Under no conditions can $f = 1$ fit the experimental data. If, for example, the absorption coefficient is doubled for $f = 1$ the temperature at $\delta = 0$, $t = 3.5$ ns is only 14 eV compared with a measured 20.6 ± 1 eV (Fig. 1, top), and at $\delta = 800 \pm 100$ μm, $t = 3.7$ ns it is 8 ± 1 eV compared with 5.5 ± 1 eV (Fig. 1, bottom). Thus by requiring the simulations to fit the experiment at all four positions, and also for runs with the two different pulse lengths, both absorption and thermal conductivity were determined. The accuracy of the measurements of thermal conductivity and absorption is shown in Fig. 2. The hatched area shows the only regions of absorption/conductivity space where the simulation fits all the data.

Computations were also carried out in ($s, w, f = 1$) space but the fits to the experimental data were poor. (The nearest fit was actually with $s = 0.065$, $w = 1.4$, and $f = 1$). So the comparison of experimental and simulation results for the high-intensity experiment unambiguously show best agreement for classical inverse bremsstrahlung absorption with thermal conduction modeled classically up to a (2–5)% flux limiter.

In constrast, the lower-power experiment[2] gave

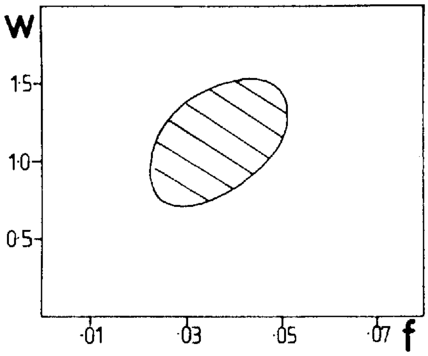

FIG. 2. Hatched area shows region of $(f, w, s=1)$ space allowed by results. The factors w and f vary the absorption and flux limit, respectively.

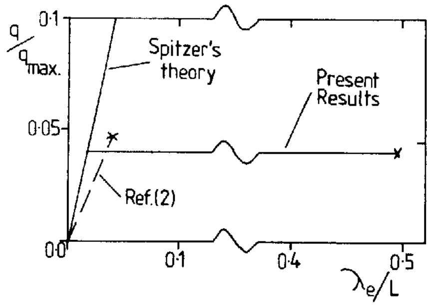

FIG. 4. Normalized heat flux vs normalized temperature gradient showing strong heat-flux limitation.

good agreement between experiment and simulation for classical absorption and a heat flux of 0.4 times Spitzer's value without using a flux limiter ($s=0.4$, $w=1$, and $f \geqslant 0.05$). Attempts to use a model with classical ($s=1$) thermal conduction and a flux limiter gave much poorer fits, the least bad being with $s=1$, $w=1$, and $f=0.06$.

The measured n_e and T_e defined a thermal level $S_{i,\mathrm{th}}$ for scattering in the ion feature.[8] At $\delta=0$, where the scattered electron spectra were symmetric and thermal, the height of the observed ion feature (S_{i0}) is enhanced to $\sim 14 S_{i,\mathrm{th}}$ as shown in Fig. 3. S_{i0} was obtained from the measured scattering in a 13-Å-bandwidth channel centered at the ruby wavelength, after the small stray-light and the electron-feature contributions had been subtracted.

The results of the two experiments are summarized and compared with Spitzer's theory in Fig. 4. In the low-power experiment,[2] matching of experimental and computational results showed that, for temperature gradients characterized by $\lambda_e/L \lesssim 0.04$, the heat flux was best modeled by reducing the classical thermal conduction coefficient to 0.4 ± 0.2 times Spitzer's value. The discrepancy is attributed to the failure of Spitzer's first-order perturbation theory for $\lambda_e/L \gtrsim 0.02$. The simulation could not be made to fit the experiment well for reduced thermal conduction based on a flux limiter. No evidence of ion-acoustic turbulence was observed or expected since the long (70-ns) CO_2-laser pulse allowed equilibration of T_e and T_i to within about 10%.

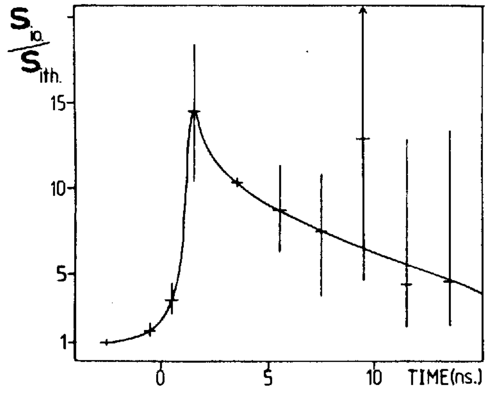

FIG. 3. Enhancement above thermal of scattering in the ion feature. The 3-ns CO_2-laser pulse starts at time zero.

In the high-power experiment the temperature gradient λ_e/L was increased from 0.04 to 0.5 but the normalized heat flux q/q_{max} was no higher than in the low-power case. The experiment was best modeled by the simulation using classical thermal conduction up to $\lambda_e/L \simeq 0.02$, then a flux limiter of 0.02 to 0.05 times the free-streaming limit. Although a theory for large temperature gradients does not exist, it would be reasonable to expect that in the absence of turbulence q/q_{max} would increase as λ_e/L increases. The fact that it did not we attribute to ion-acoustic turbulence because we observe an enhanced ion feature (Fig. 3).

Unfortunately, this observation was with $k_s \sim 2/\lambda_{\mathrm{D}}$ (as $\alpha \sim \frac{1}{2}$). From simulations of current-driven ion-acoustic turbulence,[10] the spectral function $S(k)$ peaks at $1/\lambda_{\mathrm{D}}$ and is much smaller at $2/\lambda_{\mathrm{D}}$. Using our measurement at $2/\lambda_{\mathrm{D}}$ and the shape of $S(k)$ from simulations, a fluctuation level $\delta n/n$ of 9% was deduced. From Ref. 4 this would severely limit the heat flux. It is interesting that although ion-acoustic turbulence reduces the thermal conductivity it does not increase the absorption. This is in agreement with theory[11] and is because the density is so much below critical.

The turbulence is presumed to be driven by the return current. We rule out Brillouin backscatter as the source of the turbulence because no backscattered light was observed at these densities and the enhancement (Fig. 3) lasted for longer than the CO_2-laser pulse (Fig. 1). The threshold for the heat-flux instability is $\lambda_e/L = 0.6$ for $T_e = 5T_i$[3], which is close to our observed maximum, $\lambda_e/L \sim 0.5$. However the distribution functions[1] on which this theory is based are unphysical since they become negative on one side in the region of velocity space where the net heat flux occurs ($1.5v_{\rm th} < v < 3v_{\rm th}$) when $\lambda_e/L > 0.02$.

In conclusion we have observed a (2–5)% flux limit to heat flow when $T_e \sim 5T_i$, which can be explained by the observed low-frequency turbulence.

This work was supported by the Science Research Council and the Northern Ireland Department of Education.

---

[a] Present address: Rutherford Laboratory, Chilton, Didcot, Oxon, United Kingdom.

[1] L. Spitzer, *Physics of Fully Ionized Gases* (Wiley, London, 1962).

[2] M. S. White, J. D. Kilkenny, and A. E. Dangor, Phys. Rev. Lett. 35, 524 (1975).

[3] D. W. Forslund, J. Geophys. Res. 75, 17 (1970).

[4] W. M. Manheimer, Phys. Fluids 20, 265 (1977).

[5] P. M. Campbell *et al.*, Phys. Rev. Lett. 39, 274 (1977).

[6] R. C. Malone, R. L. McCrory, and R. L. Morse, Phys. Rev. Lett. 34, 721 (1975).

[7] B. Yaakobi and T. C. Bristow, Phys. Rev. Lett. 38, 350 (1977).

[8] H. J. Kunze, in *Plasma Diagnostics*, edited by W. Lochte-Holtgreven (North-Holland, Amsterdam, 1968), p. 594.

[9] K. W. Billman and J. R. Stallcop, Appl. Phys. Lett. 28, 704 (1976).

[10] C. Dum, R. Chodura, and D. Biskamp, Phys. Rev. Lett. 32, 1231 (1974).

[11] R. J. Faehl and W. L. Kruer, Phys. Fluids 20, 55 (1977).